

1-1-2008

Aerodynamic optimization for low Reynolds number flight of a solar unmanned aerial vehicle

Louis Dube

University of Nevada, Las Vegas

Follow this and additional works at: <https://digitalscholarship.unlv.edu/rtds>

Repository Citation

Dube, Louis, "Aerodynamic optimization for low Reynolds number flight of a solar unmanned aerial vehicle" (2008). *UNLV Retrospective Theses & Dissertations*. 2398.

<http://dx.doi.org/10.25669/ziey-32pi>

This Thesis is protected by copyright and/or related rights. It has been brought to you by Digital Scholarship@UNLV with permission from the rights-holder(s). You are free to use this Thesis in any way that is permitted by the copyright and related rights legislation that applies to your use. For other uses you need to obtain permission from the rights-holder(s) directly, unless additional rights are indicated by a Creative Commons license in the record and/or on the work itself.

This Thesis has been accepted for inclusion in UNLV Retrospective Theses & Dissertations by an authorized administrator of Digital Scholarship@UNLV. For more information, please contact digitalscholarship@unlv.edu.

AERODYNAMIC OPTIMIZATION FOR LOW REYNOLDS NUMBER
FLIGHT OF A SOLAR UNMANNED AERIAL VEHICLE

by

Louis Dube

Bachelor of Science
University of Nevada, Las Vegas
2006

A thesis submitted in partial fulfillment
of the requirements for the degree of

**Master of Science Degree in Aerospace Engineering
Department of Mechanical Engineering
Howard R. Hughes College of Engineering**

**Graduate College
University of Nevada, Las Vegas
December 2008**

UMI Number: 1463501

INFORMATION TO USERS

The quality of this reproduction is dependent upon the quality of the copy submitted. Broken or indistinct print, colored or poor quality illustrations and photographs, print bleed-through, substandard margins, and improper alignment can adversely affect reproduction.

In the unlikely event that the author did not send a complete manuscript and there are missing pages, these will be noted. Also, if unauthorized copyright material had to be removed, a note will indicate the deletion.

UMI[®]

UMI Microform 1463501

Copyright 2009 by ProQuest LLC.

All rights reserved. This microform edition is protected against unauthorized copying under Title 17, United States Code.

ProQuest LLC
789 E. Eisenhower Parkway
PO Box 1346
Ann Arbor, MI 48106-1346



Thesis Approval
The Graduate College
University of Nevada, Las Vegas

November 21, 2008

The Thesis prepared by

Louis Philippe Dube

Entitled

Aerodynamic Optimization for Low Reynolds Number Flight of a Solar
Unmanned Aerial Vehicle

is approved in partial fulfillment of the requirements for the degree of

Master of Science in Aerospace Engineering

Harrell W. Pepper

Examination Committee Chair

Adrian S. ...

Dean of the Graduate College

Brendan J. ...

Examination Committee Member

William Cullis

Examination Committee Member

...

Graduate College Faculty Representative

ABSTRACT

Aerodynamic Optimization for Low Reynolds Number Flight of a Solar Unmanned Aerial Vehicle

By

Louis Dube

Dr. Darrell Pepper, Examination Committee Chair
Professor of Mechanical Engineering
University of Nevada, Las Vegas

A study has been conducted to optimize the aerodynamics of a solar powered unmanned aerial vehicle for low Reynolds number flight. In this study, three areas of the airframe, namely the fuselage, wing-fuselage junction and wingtips, were analyzed, tested, evaluated and developed in an iterative design process. A numerical analysis method was employed to complete the aerodynamic study, the purpose of which was to minimize adverse flow conditions occurring near or about the aforementioned areas under most flight conditions and to maximize their aerodynamic usefulness. The results were benchmarked internally through the iterative process using the initial design as a control and externally by comparing with collected empirical figures characterizing solar airplanes of the past and present. The results showed that with careful design practices, wingtip devices can be made to improve flight characteristics at low Reynolds number flight significantly enough to offset their structural disadvantages, providing a substantial drag decrease over the entire flight envelope. It was also shown that fuselage shape can be modified to accommodate the airplane's mission and fulfill a greater role than solely being a payload carrier by using this body to generate and control aerodynamic forces. Finally it was illustrated that careful design of the wing-fuselage junction could lead to significant improvements in both lift and drag characteristics.

TABLE OF CONTENTS

ABSTRACT	iii
LIST OF TABLES	vii
LIST OF FIGURES.....	x
NOMENCLATURE	xiii
ACKNOWLEDGEMENTS	xiv
CHAPTER 1 INTRODUCTION	1
1.1 General Information.....	1
1.2 Motivation	5
1.3 Problem Description	7
CHAPTER 2 LITERATURE SURVEY.....	8
2.1 Wingtip Devices – History and Research	8
2.2 Fuselage – History and Research	12
2.3 Wing-Fuselage Junction – History and Research	13
CHAPTER 3 SET-UP AND PROCEDURE	17
3.1 Introduction.....	17
3.2 Winglet and Wingtip Design Parameters.....	17
3.3 Fuselage and Wing-Fuselage Junction Design Parameters	20
3.4 Resources	22
3.5 Model Set-Ups.....	23
3.5.1 Computational Method	24
3.5.2 Computational Domain Modeling.....	30
3.5.3 Other Considerations Regarding the Computational Domain	32
3.6 Test Section Calibration	32
CHAPTER 4 WINGTIP DEVICE SIMULATION ANALYSIS	35
4.1 Introduction.....	35
4.2 Wing Control Specimen.....	35
4.3 Planar Device 01 (PD-01).....	37
4.4 Planar Device 02 (PD-02).....	39
4.5 Non-Planar Device 01 (NPD-01).....	41
4.6 Non-Planar Device 02 (NPD-02).....	43
4.7 Non-Planar Device 03 (NPD-03).....	47
4.8 Non Planar Device 04 (NPD-04)	49
4.9 Final Candidates Discussion	52
4.9.1 Drag Coefficient versus Angle-of-Attack	52
4.9.2 Lift Coefficient versus Angle-of-Attack	53

4.9.3	Lift-to-Drag Ratio versus Angle-of-Attack.....	54
4.9.4	Lift Coefficient versus Drag Coefficient	55
CHAPTER 5 WING-FUSELAGE JUNCTION SIMULATION ANALYSIS		56
5.1	Introduction.....	56
5.2	Wing-Fuselage Junction Control Specimen	56
5.3	Linear Wing-Fuselage Junction 01 (LWJ-01).....	58
5.4	Linear Wing-Fuselage Junction 02 (LWJ-02).....	61
5.5	Non-Linear Wing-Fuselage Junction 01 (NLWJ-01)	63
5.6	Non-Linear Wing-Fuselage Junction 02 (NLWJ-02)	67
5.7	Final Candidates Discussion	69
CHAPTER 6 CONCLUSION		71
6.1	Overview.....	71
6.2	Recommendations.....	72
APPENDICES		74
A	Virtual Wind Tunnel Calibration and Wing Control Specimen Data.....	74
B	Wingtip Device Simulations – Collected Data and Model Information.....	79
C	Wing-Fuselage Junction Control Specimen Data	116
D	Wing-Fuselage Junction Simulations – Collected Data and Model Information.....	121
E	On the Induced Drag of Real Wings	141
F	On the Use of Thin-Film Solar Cells to Power an Unmanned Aerial Vehicle	149
G	Copyright Permission Form.....	152
BIBLIOGRAPHY		154
VITA		157

LIST OF TABLES

3.1	Model constants for Equations 3.5, 3.6 and 3.7	25
3.2	Model closure constants and variables for Equations (3.8), (3.9) and (3.10)	26
3.3	Comparison for values acquired using COMSOL to various popular panel methods	33
4.1	Wing Control Specimen dimensions and attributes	36
4.2	Wing Control Specimen aerodynamic properties	37
4.3	Basic geometric parameters for Planar Device 01	38
4.4	Planar Device 01 results – loiter, level flight (root chord $Re = 330141$)	39
4.5	Basic geometric parameters for Planar Device 02	40
4.6	Planar Device 02 results – loiter, level flight (root chord $Re = 330141$)	41
4.7	Non-Planar Device 01 – geometric parameters	42
4.8	Non-Planar Device 01 results – loiter, level flight (root chord $Re = 330141$)	43
4.9	Non-Planar Device 02 – geometric parameters	44
4.10	Non-Planar Device 02 results – loiter, level flight (root chord $Re = 330141$)	45
4.11	Non-Planar Device 02 results – loiter, -2° AOA (root chord $Re = 330141$)	46
4.12	Non-Planar Device 02 results – loiter, $+2^\circ$ AOA (root chord $Re = 330141$)	46
4.13	Non-Planar Device 02 results – loiter, $+4^\circ$ AOA (root chord $Re = 330141$)	46
4.14	Non-Planar Device 03 – geometric parameters	48
4.15	Non-Planar Device 03 results – loiter, level flight (root chord $Re = 330141$)	48
4.16	Non-Planar Device 04 – geometric parameters	50
4.17	Non-Planar Device 04 results – loiter, level flight (root chord $Re = 330141$)	50
4.18	Non-Planar Device 04 results – loiter, -2° AOA (root chord $Re = 330141$)	51
4.19	Non-Planar Device 04 results – loiter, $+2^\circ$ AOA (root chord $Re = 330141$)	51
4.20	Non-Planar Device 04 results – loiter, $+4^\circ$ AOA (root chord $Re = 330141$)	51
5.1	Wing-Fuselage Junction Control Specimen data, loiter speed (root $Re = 330141$)	58
5.2	Basic geometric parameters for Linear Wing-Fuselage Junction 01	59
5.3	Linear Wing-Fuselage Junction 01 - loiter, level flight (root $Re = 330141$)	60
5.4	Linear Wing-Fuselage Junction 01 - loiter, $+2^\circ$ AOA (root $Re = 330141$)	60
5.5	Linear Wing-Fuselage Junction 01 - loiter, $+4^\circ$ AOA (root $Re = 330141$)	61
5.6	Basic geometric parameters for Linear Wing-Fuselage Junction 02	62
5.7	Linear Wing-Fuselage Junction 02 - loiter, level flight (root $Re = 330141$)	63
5.8	Basic geometric parameters for Non-Linear Wing-Fuselage Junction 01	64
5.9	Non-Linear Wing-Fuselage Junction 01 - loiter, level flight (root $Re = 330141$)	65
5.10	Non-Linear Wing-Fuselage Junction 01 - loiter, $+2^\circ$ AOA (root $Re = 330141$)	66
5.11	Non-Linear Wing-Fuselage Junction 01 - loiter, $+4^\circ$ AOA (root $Re = 330141$)	66
5.12	Basic geometric parameters for Non-Linear Wing-Fuselage Junction 02	68
5.13	Non-Linear Wing-Fuselage Junction 02 - loiter, level flight (root $Re = 330141$)	68
A.1	Mesh statistics for Wing Control Specimen in loiter, level flight.	74
A.2	Raw and processed data from the Wing Control Specimen, loiter and level flight.	74
A.3	Mesh statistics for Wing Control Specimen in loiter, -2° angle-of-attack.	76
A.4	Raw and processed data from the WCS in loiter, -2° angle-of-attack.	76
A.5	Mesh statistics for Wing Control Specimen in loiter, $+2^\circ$ angle-of-attack.	77

A.6	Raw and processed data from the WCS in loiter, +2° angle-of-attack.....	77
A.7	Mesh statistics for Wing Control Specimen in loiter, +4° angle-of-attack.....	78
A.8	Raw and processed data from the WCS in loiter, +4° angle-of-attack.....	78
B.1	Model statistics for PD-01 in loiter, level flight.....	79
B.2	Collected data from the model simulation for Planar Device 01 in loiter, level flight	80
B.3	PD-02 Model statistics for loiter, level flight	83
B.4	Collected data from the model simulation for Planar Device 02 in loiter, level flight	84
B.5	NPD-01 model statistics for loiter, level flight.....	87
B.6	Collected data from the model simulation for NPD-01	88
B.7	Model statistics for NPD-02 in loiter, level flight.....	92
B.8	Collected data from the model simulation for NPD-02 in loiter, level flight	93
B.9	Model statistics for NPD-02 in loiter, -2° angle-of-attack.....	96
B.10	Collected data from the model simulation for NPD-02 in loiter, -2° AOA	97
B.11	Model statistics for NPD-02 in loiter, +2° angle-of-attack.....	98
B.12	Collected data from the model simulation for NPD-02 in loiter, +2° AOA	99
B.13	Model statistics for NPD-02 in loiter, +4° angle-of-attack.....	100
B.14	Collected data from the model simulation for NPD-02 in loiter, +4° AOA	101
B.15	Model statistics for NPD-03 in loiter, level flight	102
B.16	Collected data from the model simulation for NPD-03 (loiter, level flight).....	103
B.17	Model statistics for NPD-04 in loiter, level flight	106
B.18	Collected data from the model simulation for NPD-04 (loiter, level flight).....	107
B.19	Model statistics for NPD-04 in loiter, +2° angle-of-attack.....	110
B.20	Collected data from the model simulation for NPD-04 in loiter, -2° AOA	111
B.21	Model statistics for NPD-04 in loiter, +2° angle-of-attack.....	112
B.22	Collected data from the model simulation for NPD-04 in loiter, +2° AOA	113
B.23	Model statistics for NPD-04 in loiter, +4° angle-of-attack.....	114
B.24	Collected data from the model simulation for NPD-04 in loiter, +4° AOA	115
C.1	Mesh statistics for Wing-Fuselage Junction Control Specimen in loiter, level flight.	116
C.2	Raw and processed data from the WFJCS, loiter and level flight.....	117
C.5	Mesh statistics for Wing-Fuselage Junction Control Specimen in loiter, +2° AOA.	119
C.6	Raw and processed data from the WFJCS in loiter, +2° AOA.....	119
C.7	Mesh statistics for Wing-Fuselage Junction Control Specimen in loiter, +4° AOA.	120
C.6	Raw and processed data from the WFJCS in loiter, +4° AOA.....	120
D.1	Mesh statistics for Linear Wing-Fuselage Junction 01 in loiter, level flight.....	121
D.2	Raw and processed data from the LWJ-01, loiter and level flight.....	122
D.3	Mesh statistics for Linear Wing-Fuselage Junction 01 in loiter, +2° AOA.....	124
D.4	Raw and processed data from the LWJ-01 in loiter, +2° AOA.....	125
D.5	Mesh statistics for Linear Wing-Fuselage Junction 01 in loiter, +4° AOA.....	126
D.6	Raw and processed data from the LWJ-01 in loiter, +4° AOA.....	127
D.7	Mesh statistics for Linear Wing-Fuselage Junction 02 in loiter, level flight.....	128
D.8	Raw and processed data from the LWJ-02, loiter and level flight.....	129
D.9	Mesh statistics for Non-Linear Wing-Fuselage Junction 01 in loiter, level flight.	131
D.10	Raw and processed data from the NLWJ-01, loiter and level flight.	132
D.11	Mesh statistics for Non-Linear Wing-Fuselage Junction 01 in loiter, +2° AOA.....	134
D.12	Raw and processed data from the NLWJ-01 in loiter, +2° AOA.	135
D.13	Mesh statistics for Non-Linear Wing-Fuselage Junction 01 in loiter, +4° AOA.....	136
D.14	Raw and processed data from the NLWJ-01 in loiter, +4° AOA.	137
D.15	Mesh statistics for Non-Linear Wing-Fuselage Junction 02 in loiter, level flight.	138
D.16	Raw and processed data from the NLWJ-02 in loiter, level flight.	139

LIST OF FIGURES

1.1	NASA's Pathfinder Plus and AC Propulsion's SoLong	2
1.2	The Great Flight Diagram completed with solar airplane data	4
1.3	Schleicher ASH-26E competition sailplane	5
1.4	Wingtip wake vortices from NASA Study "Wake Vortex Study at Wallops Island"	6
2.1	KC-135 tanker retrofitted with Whitcomb winglets (1980)	9
2.2	A front view of Richard Vogt's winglet patent, circa 1949 [43]	10
2.3	Ishimitsu's 1977 winglet design for the Boeing Company [16]	10
2.4	Jupp's 1987 wing "fence" design for British Aerospace PLC [17]	10
2.5	Louis Gratzner's "Blended Winglet" design, 1993 [12]	10
2.6	Heller et al.'s "Wing Tip Extension for a Wing" for Fairchild Dornier, 2002 [14]	11
2.7	Irving's winglet design, filed for in 2007, for Airbus UK Limited [15]	11
2.8	Picture of Global Hawk	12
2.9	Underside view of the Airbus A380	14
2.10	Detail of wing fillet for P-51D	16
2.11	Detail of wing fillet for unidentified sailplane on cover of Soaring Magazine	16
3.1	Winglet geometry parameters	19
3.2	Whitcomb winglet	20
3.3	Local pressure coefficient for 63-206 at $Re = 2,700,000$	21
3.4	Typical boundary conditions set in two dimensions	23
3.5	Typical problem set-up	24
3.6	Deformed velocity slices around an object in freestream	29
3.7	Wingtip device testing environment dimensions	31
3.8	Wing-fuselage junction testing environment dimensions	32
4.1	Wing control specimen diagram	35
4.2	Planar Device 01 configuration	37
4.3	Planar Device 02 configuration	39
4.4	Non-Planar Device 01 configuration	41
4.5	Non-Planar Device 02 configuration	43
4.6	Non-Planar Device 03 configuration	47
4.7	Non-Planar Device 04 configuration	49
4.8	Drag coefficient versus angle-of-attack	52
4.9	Lift coefficient versus angle-of-attack	53
4.10	Lift-to-drag ratio versus angle-of-attack	54
4.11	Lift coefficient versus drag coefficient	55
5.1	Wing-Fuselage Junction Control Specimen diagram	57
5.2	Linear Wing-Fuselage Junction 01 configuration	59
5.3	Linear Wing-Fuselage Junction 02 configuration	62
5.4	Non-Linear Wing-Fuselage Junction 01 configuration	64
5.5	Non-Linear Wing-Fuselage Junction 02 configuration	67
5.6	Overall drag coefficient versus angle-of-attack	69
5.7	Overall lift coefficient versus angle-of-attack	70

A.1	Mesh arrangement over wing surface	75
A.2	Comparison of COMSOL 3.5 and XFLR5 pressure distributions.....	75
B.1	Mesh overview for PD-01	79
B.2	Mesh arrangement over PD-01	80
B.3	Boundary pressure distribution over PD-01	81
B.4	Boundary velocity distribution with streamlines over PD-01's bottom surface.....	81
B.5	Streamline detail over PD-01	82
B.6	Mesh arrangement over PD-02	83
B.7	Mesh overview for PD-02	83
B.8	Boundary pressure distribution over PD-02	85
B.9	Boundary velocity distribution with streamlines over PD-02's bottom surface.....	85
B.10	Streamline detail over PD-02	86
B.11	Mesh arrangement over NPD-01	87
B.12	Mesh overview for NPD-01	87
B.13	Boundary pressure distribution over NPD-01's main wing surfaces	89
B.14	Boundary pressure distribution over NPD-01's non-planar faces	89
B.15	Boundary velocity distribution over NPD-01's main wing surfaces	90
B.16	Boundary velocity distribution and streamline detail over NPD-01's top surface.....	91
B.17	Boundary velocity distribution and streamline detail over NPD-01's bottom surface.....	91
B.18	Mesh arrangement over NPD-02	92
B.19	Mesh overview for NPD-02	92
B.20	Boundary pressure distribution over NPD-02's main wing surfaces	94
B.21	Boundary pressure distribution over NPD-02's non-planar faces	94
B.22	Boundary velocity distribution and streamline detail over NPD-02	95
B.23	Boundary velocity distribution and streamline detail over NPD-02	95
B.24	Boundary pressure distribution and streamline detail near NPD-02 at -2° AOA.....	96
B.25	Boundary pressure distribution and streamline detail near NPD-02 at +2° AOA.....	98
B.26	Boundary pressure distribution and streamline detail near NPD-02 at +4° AOA.....	100
B.27	Mesh arrangement over NPD-03	102
B.28	Mesh overview for NPD-03	102
B.29	Boundary pressure distribution over NPD-03's main wing surfaces	104
B.30	Boundary pressure distribution over NPD-03's non-planar faces	104
B.31	Streamline detail around NPD-03 in loiter, level flight.....	105
B.32	Mesh arrangement over NPD-04	106
B.33	Mesh overview for NPD-04	106
B.34	Boundary pressure distribution over NPD-04's main wing surfaces	108
B.35	Boundary pressure distribution over NPD-04's non-planar faces	108
B.36	Boundary pressure distribution and streamline detail near NPD-04 in loiter, level flight .	109
B.37	Boundary pressure distribution and streamline detail near NPD-04 in loiter at -2° AOA .	110
B.38	Boundary pressure distribution and streamline detail near NPD-04 in loiter at -2° AOA .	112
B.39	Boundary pressure distribution and streamline detail near NPD-04 in loiter at -2° AOA .	114
C.1	Mesh detail for Wing-Fuselage Junction Control Specimen	116
C.2	Streamline detail and boundary pressure distribution for loiter, level flight.....	118
D.1	Mesh detail for LWJ-01	121
D.2	Mesh overview for LWJ-01	121
D.3	Boundary pressure distribution and streamline detail for LWJ-01 in loiter, level flight.....	123
D.4	Boundary velocity distribution and streamline detail for LWJ-01 at +2° AOA	124
D.5	Boundary pressure distribution and streamline detail for LWJ-01 at +4° AOA	126
D.6	Mesh detail for LWJ-02.....	128

D.7	Mesh overview for LWJ-02	128
D.8	Boundary pressure distribution and streamline for LWJ-02	130
D.9	Mesh detail for NLWJ-01	131
D.10	Mesh overview for NLWJ-01	131
D.11	Boundary pressure distribution and streamline detail for NLWJ-01	133
D.12	Boundary velocity distribution and streamline detail for NLWJ-01 at +2° AOA.....	134
D.13	Boundary pressure distribution and streamline detail for NLWJ-01 at +4° AOA.....	136
D.14	Mesh detail for NLWJ-02	138
D.15	Mesh overview for NLWJ-02	138
D.16	Boundary pressure distribution and streamline detail for NLWJ-02	140
E.1	Wingtip vortices diagram	141
E.2	Picture of the Supermarine Spitfire.....	143
E.3	Local lift distribution and taper ratio relationship	145
E.4	Close-up of a Hoerner wingtip on a general aviation aircraft	147

NOMENCLATURE

AR	aspect ratio	T_∞	ambient temperature
a	measurement plane cross-sectional area	\bar{U}	averaged velocity field
b	wingspan	U_∞	freestream velocity
C	chord length	u	x-direction velocity
C_D	coefficient of drag	u_0	in-bound or initial x-velocity
$C_{D,i}$	coefficient of induced drag	u_τ	friction velocity
C_L	coefficient of lift	\bar{u}'	velocity field fluctuation vector
D	drag force	V	volume
e	Oswald efficiency factor	\bar{u}, \bar{V}	velocity field vector
\bar{F}_e	outside force vector	δ_w, δ_w^+	logarithmic wall distance
\vec{g}	gravity	ε	dissipation rate of turbulent energy
k	turbulent energy or induced drag factor	λ	taper ratio
L	lift force	λ_α	maximum eigenvalue of strain rate tensor
l^*	viscous length scale	η	absolute viscosity
\vec{n}	normal direction	η_T	turbulent viscosity
p	pressure	ρ	density
S	surface area (generally of the wing)	τ_w	shear stress at the wall
T	temperature	ω	dissipation per unit turbulent
t	time	\otimes	outer vector product

ACKNOWLEDGMENTS

I would like to sincerely express my gratitude to Dr. Darrell W. Pepper, my committee chair and mentor through my years at UNLV. His dedication to the growth of his students, both as engineers and human beings, is reflected in the ones of us who are lucky enough to be under his tutelage. The completion of this work would not have been possible without his insightful guidance and his unique professionalism and friendship.

In the same vein, I would like to extend my appreciation to Mr. John L. Vogt, who has shown relentless interest in the development of his students, even long after they have left his classroom. Mr. Vogt is one of the most genuine human beings I know and I am thankful for his continued input through the years.

I also would like to thank Dr. Culbreth, Dr. O'Toole and Dr. Yfantis for agreeing to sit in on my thesis committee.

I must also thank Dr. Noth from the Autonomous Systems Lab at ETH Zurich for his gracious allowance to reproduce a figure he had published.

Additionally, I would like to thank undergraduate classman Wade McElroy for the work he concluded with me, especially with regards to the fuselage design, and allowing me to briefly discuss his work within this document.

Last but not least, I thank my closest friends, Cortnie and Gabe, as well as my parents, Richard and Suzanne, for their endless patience, support and understanding.

CHAPTER 1

INTRODUCTION

1.1 General Information

Solar powered or assisted flight has been around since the 1970s but has seen a steady growth in interest over the past two decades due to the development of two separate technologies, namely progress in photovoltaic cells and the mainstream advent of unmanned flight. It remains a niche area of the aviation industry and consists almost entirely of experimental crafts but recent trends in the development of flying platforms that utilize renewable or environmentally-friendly energy sources point to a future where these machines will be common and to a present where the market eagerly awaits their arrival.

Historically, aerodynamic optimization has been an on-going learning process. The UNLV Howard H. Hughes College of Engineering possesses a marvelous testament to this in the HR-1 replica hung in the Great Hall of the Thomas Beam Engineering 'A' Building. The aerodynamic properties of an aircraft and its manageable power dictate its flight performance. In certain cases, such optimization will establish the platform's viability and determine its success.

Solar flight does not enjoy the privilege of internal combustion. Photovoltaic cells have been fragile, cumbersome and sometimes heavy, while yielding a very limited amount of power. Simply put, solar flight is one of the most underpowered forms of flying and to this day remains a close second to human powered flight in terms of performance [35]. However, with the coming of new solar technology such as thin-film solar cells and nanotechnology, solar flight is starting to move from dream to reality and is seeing more funding than ever in its relatively new life [25].

The motivation for solar flight is clear. In the mid-1970's, modelers and scientists were eager to prove that solar flight was possible. A perhaps premature jump to manned solar flight occurred in the latter parts of that decade but all this work pointed to one common goal: sustainable flight.

The benefit of solar flight is then the defunct need for fuel. The harvesting of energy while airborne theoretically announces the onset of “eternal” flight. Thus, starting in the late-1990’s, and in a trend that is still ongoing, several unmanned High Altitude Long Endurance (HALE) projects have come and gone, from NASA’s Pathfinder [23], a variant of which is shown in Figure 1.1, to lesser known but equally successful airframes such as AC Propulsion’s SoLong [1].



Figure 1.1 NASA’s Pathfinder Plus (1998, [23]) and AC Propulsion’s SoLong (2005, inset [1])

Thin-film solar cells offer many advantages over their predecessors, the main of which is most certainly the cost per watt. This reduction in price makes the cells more competitive to other forms of energy. From a strictly aerodynamic point of view this has no bearing, but from a business mindset it has a profound impact on the profitability of such a system. The photovoltaic cells used on Pathfinder and SoLong are high-grade, high cost ones, but the developers of SoLong knew that more affordable technology was on the horizon.

Another serious ramification of progress in thin-film solar cells is the increase in efficiency. Over the authoring of this document, from August 2007 to August 2008, the maximum reported

efficiency of thin-film photovoltaic cells has gone from 17.4% to 19.9%, according to Solarbuzz.com, a popular website monitoring the solar cell business. This increase in efficiency allows an aircraft designer to obtain a similar amount of power for a smaller surface area, which in turn allows airframes like SoLong, eight times smaller than Pathfinder Plus' 121 foot wingspan, to fly for much longer periods of time.

In many instances, surface area is the main parameter that will dictate the viability of a solar platform because it is directly correlated to the power available. Brandt and Gilliam [6] used this approach to present a design methodology for solar-powered aircraft. With increased photovoltaic efficiency, designers can start to worry less about how much surface area they have available for cells and more about fine-tuning the platform for various legs of flight the craft will be operating in.

Empirically, sailplanes have the highest aspect ratio and lowest wing loading of any manned, powered flying platform [28]. Because of these characteristics, it is a configuration that lends itself well to solar-powered aircraft. Figure 1.2 illustrates this statement brilliantly. Tennekes [35] published The Great Flight Diagram and its entries can be viewed as the light entries. Tennekes surveyed several species of birds, insects and even prehistoric flyers, along with flying machines from today such as the Boeing 747 and the Beech Bonanza. The Tennekes Curve was his way of showing that the science of flight was a natural evolution, from insects to jumbo jets.

Noth [23, 24] gathered a gargantuan amount of sailplane data and was able to extrapolate two regression lines, shown in Figure 1.2 as the Top 5% Model and Mean Model lines, which accurately represent the majority of the data he gathered. Also noteworthy, as Noth [24] wrote: "A model from B.W. McCormick for the estimation of the wing loading of manned airplanes, also based on square-cubing scaling laws, is also represented. One remarkable point is its asymptote at a weight of 1000 N which corresponds to the weight of a single human person in an incredibly lightweight airplane. The airplane approaching the most this asymptote is the Gossamer Albatross, the human powered aircraft built by Mcready that crossed the English Channel in 1979." Noth then proceeds to plot the data for 86 different solar airplanes, both manned and unmanned.

Figure 1.2 leads to the appreciation that solar-powered flight has assumed the sailplane configuration factor and has barely deviated from it. At the top of the plot are Helios, Centurion and company, due to their peculiar flying wing configuration, followed by a few manned solar planes and finally, in the large cluster, the majority of the unmanned solar-powered crafts. Coincidentally, this author's first foray into solar flight (Howie Mk. III, [7]) is found on this figure.

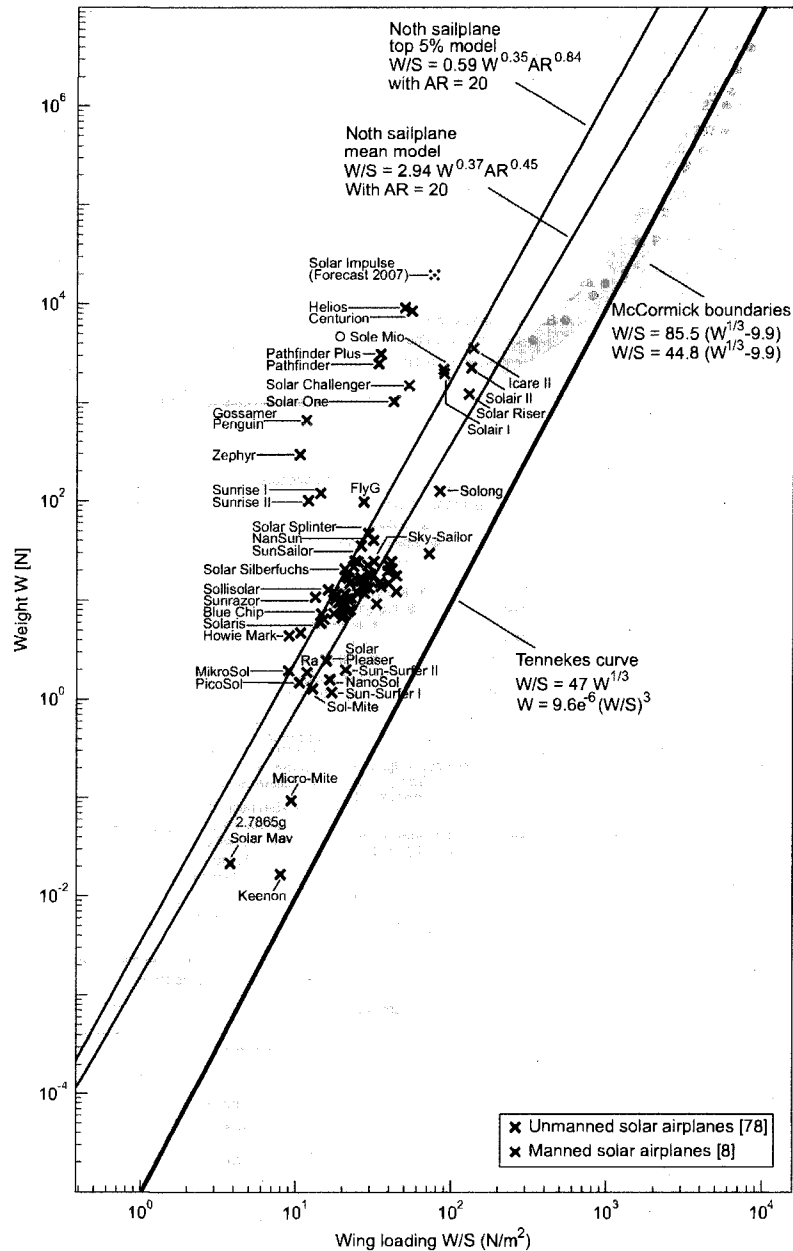


Figure 1.2 The Great Flight Diagram completed with 62 solar airplanes [24].

A survey of many of these unmanned solar aircrafts (including Howie Mk. III) reveals rather crude aerodynamics, which is surprising considering the careful flow studies engaged when developing sailplanes. Generally speaking, modern competition sailplanes are highly refined machines and quite possibly some of the most aerodynamically optimized flying objects in the subsonic regime. Some cues could definitely be taken from these aircrafts, especially if solar unmanned aerial vehicles seem to be emulating this form factor, as shown by Figure 1.2.

Solar airplanes categorically have a low wing loading due to their lack of power and their requirement for increased surface area for solar cells. Still, even with their high aspect ratio and the fact that they operate in a low Reynolds number regime (relative to other flying machines), sailplanes are the subject of numerous flow studies, including the benefit of winglets, interference drag between the wing and the fuselage, and the fuselage shape itself. The Schleicher ASH-26E is a prime example of current sailplane technology and is depicted in Figure 1.3.

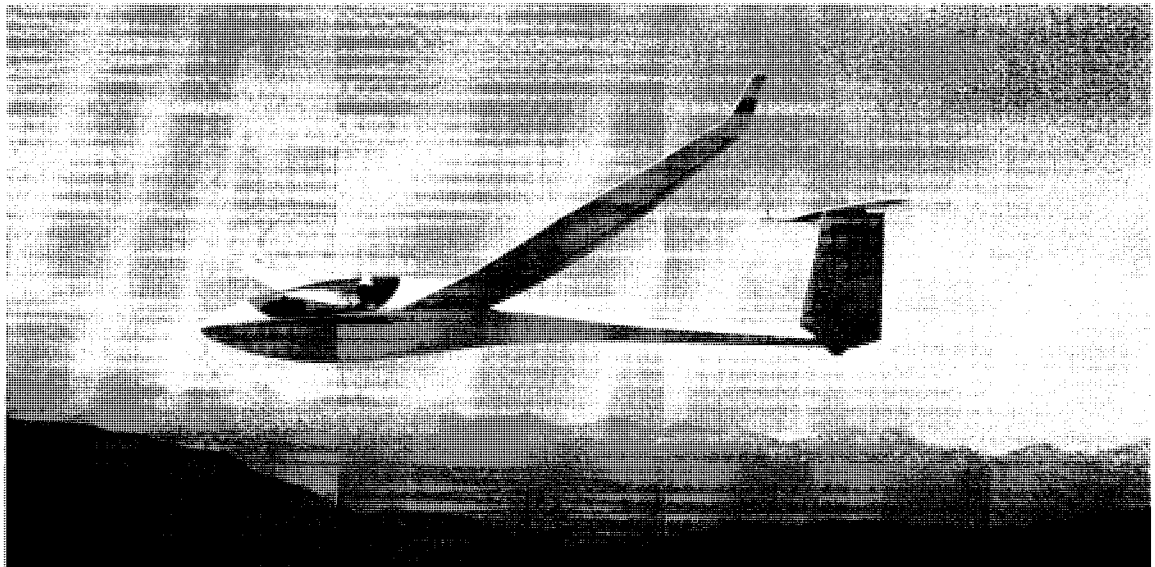


Figure 1.3 Schleicher ASH-26E competition sailplane.

1.2 Motivation

Several sources (e.g. [33]) state that the incorporation of winglets or wingtip devices for low Reynolds number flight may be futile but it should be stated that the field of wingtip devices and

winglets is still very active. The direct benefit of utilizing such a system is the reduction of, or clever usage of wingtip vortices, a typical case of which is illustrated in Figure 1.4. This in turn would lead to a reduction in induced drag and in some cases an increase in lift or other useful aerodynamic forces [17]. Winglets often supersede wing extensions in terms of performance [28], although earlier literature seems divided on this issue.



Figure 1.4 Wingtip wake vortices, illustrated here by material from a NASA study titled "Wake Vortex Study at Wallops Island" [22].

Moreover the literature concerning the study of wingtip devices specifically for low Reynolds number flight, such as encountered for solar-powered flight, is scarce. The majority of the published material is either proprietary or acknowledges the fact that such devices are useful in high subsonic or transonic regimes. Further investigation on whether such devices may be worthwhile was deemed necessary.

Interference drag between the wing and body of the plane accounts for a significant portion of the overall drag [3]. Once again, a lot of the literature found on this subject deals with transonic or even supersonic regimes but it should be noted that comparatively fewer papers were found on this subject than on winglets. This is likely due to the complexity of the problem, the problem's proprietary nature to a system and the great need for a large amount of computing power. Nonetheless, several efforts have been made to try to explain this still not fully understood problem, particularly by Boermans [2, 3, 38].

That these areas were of interest were spurred from two different personal experiences, which are separate from the literature survey but were supported by the later. The design, development and testing of the Howie Mk. III solar UAV at UNLV [7] was the first of such experiences. The aircraft flew at a significantly lower airspeed than what it had been designed for, specifically due to the lack of aerodynamic optimization ensued by last-minute change in manufacturing and construction technique. The second such experience was the design and development of the Howie Mk. IV, this time under the UAV umbrella supported by the United States Air Force and General Dynamics.

1.3 Problem Description

Aerodynamic behavior of different wingtip devices was analyzed. Using an iterative design process, these devices were refined until significant aerodynamic gains could be appreciated. An extensive literature survey was conducted for the duration of the design process to quantify the design decisions. The designs were benchmarked against a control wing (no wingtip devices) and also against their previous iteration. The results were obtained using various computational tools.

Aerodynamic behavior of different wing-fuselage junction configurations was also analyzed, using a similar reiterative design process and the same set of tools. The monitored output for these studies was primarily the drag and lift produced by the various arrangements.

CHAPTER 2

LITERATURE SURVEY

2.1 Wingtip Devices – History and Research

The advent of winglets can be traced back to nearly a hundred years ago when such Prandtl recognized that with lift production on a finite wing came spanwise flow and tip vortices [38]. Prandtl's lifting line theory led way to his famous 1918 solution for optimum lift distribution, which was an elliptical spanload [32]. This results in the minimum wing root bending moment for a given lift and a given span. Prandtl published another interesting paper, *Über Tragflügel kleinsten induzierten Widerstandes*, which translates to "The Minimum Induced Drag of Wings", in 1933 [32]. Prandtl revisited his work to determine if a spanload could provide the same wing root bending moment but yield less induced drag, if the span was taken as a variable. A bell-shaped spanload was found to have this desirable quality; however, most modern textbooks refer to the optimum spanload as elliptical, an explanation which may lie on the structural side of aircraft design.

The elliptical planform, according to all classical sources except the Horten brothers [32], is the optimum lift distribution. However, few airplanes have been manufactured with such a wing geometry due mainly to difficulties in the construction process. The Hortens argued that the bell-shaped spanload was optimal and some engineers still agree for this but the structural ramifications remain a question mark, and their flying examples suffered from control problems [32]. For a more complete discussion on induced drag, its causes and the subsequent benefits of wingtip devices, please refer to Appendix E or [34].

Prandtl's lifting-line theory needs to be adapted to handle non-planar lifting surfaces, such as winglets. As such, most wingtip devices until the 1970s came in other (planar) forms, such as rounded, sharp, drooped, or even the popular Hoerner wingtip [30], to only name a few, and

these are still widely today. A chart showcasing some of the more popular types can be viewed in [32]. Very little literature can be found on such wingtips but it is widely recognized that a designer can't do much worse than rounding off the wing and calling it quits.

The early work of Munk [21] on lift distribution is seen as the catalyst that led to several papers devoted to discussions revolving around wingtip devices, endplates and winglets. His often cited paper, *The Minimum Induced Drag of Aerofoils*, led to modern breakthroughs from which emerged what are contemporarily considered to be winglets. While Vogt [40] filed the first patent for a winglet design, Whitcomb's work [42] deserves special interest as he was the first to demonstrate that winglets could be retrofitted to an existing airplane to provide real benefits. His winglet design methodology and the implementation thereof [20], in 1980, on a KC-135 tanker (Figure 2.1) showed a seven percent overall drag reduction.



Figure 2.1 KC-135 tanker retrofitted with Whitcomb winglets (1980).

While the full potential of winglets has yet to be seen, it is being probed. Over the past two decades, several patents have been filed over winglet types, such as those by Ishimitsu [12],

Jupp [13], Gratzner [8], Heller [10] and Irving [11]. It is interesting to note that many of the patents filed on the subject in the early 1980s were held by The Boeing Company. Indeed it may have been the airliner builders of the world who initially took notice and saw winglets as a way to reduce fuel consumption for an aircraft of a given wingspan, with little to no modification to the existing design. To this day, research on the subject is heavily pursued by airliner builders, such as the M-DAW Project [15] funded by Airbus, which investigates “Novel Wing Tip Device Design”, blending together a study of planar and non-planar wingtip devices to achieve the same goal.

Figures 2.2 through 2.7 illustrate the winglets designed by the above-mentioned names, showing the technology’s evolution. These figures come from the patents their inventors have filed. As computing power and man’s understanding of fluid flow progresses, so too does winglet technology. Natural curves and shapes that flow into one another seemingly replace planar faces, which lent themselves more easily to fluid flow analysis in the past. Complex, compound aerodynamic components are now being patented, and the amount of patents filed related to winglets has gradually increased since Vogt [40], again as illustrated through the figures.

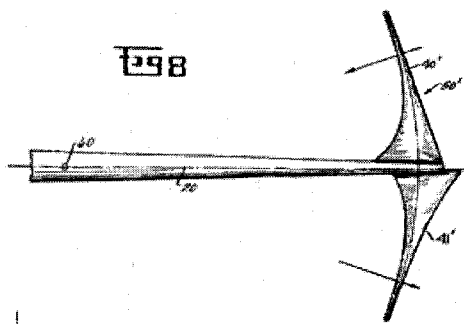


Figure 2.2 A front view of Richard Vogt's winglet patent, circa 1949 [40]

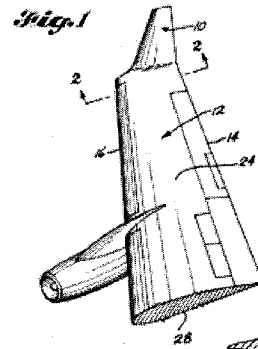


Figure 2.3 Ishimitsu's 1977 winglet design for the Boeing Company [12]

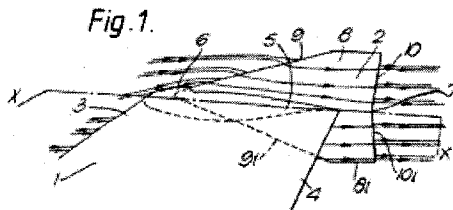


Figure 2.4 Jupp's 1987 wing "fence" design for British Aerospace PLC [13]

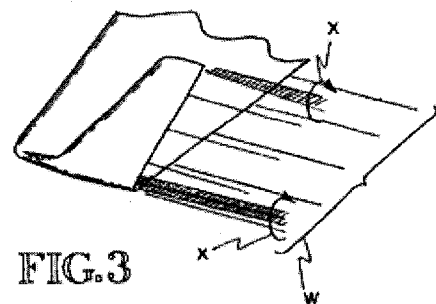


Figure 2.5 Louis Gratzner's "Blended Winglet" design, 1993 [8]

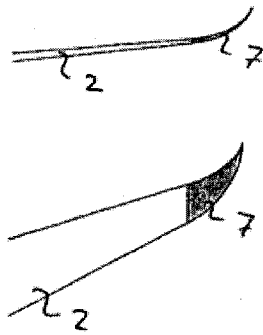


Figure 2.6 Heller et al.'s "Wing Tip Extension for a Wing" for Fairchild Dornier, 2002 [10]

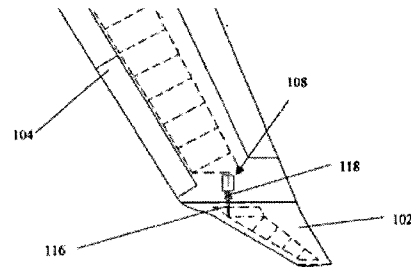


Figure 2.7 Irving's winglet design, filed in 2007, for Airbus UK Limited [11]

Airliners operate at high subsonic or nearly transonic speeds and their gains are different from aircraft flying at lower speeds, and thus lower Reynolds numbers. The field of winglet design has not been dormant for such applications. Maughmer of Pennsylvania State University has been a forerunner on the design, research and development of winglets for high-performance sailplanes [18], a configuration factor which solar-powered airplanes empirically mimic.

Maughmer perhaps best summed the evolution of winglets and the current state of the art when he wrote: "The design goal is clearly to minimize the overall drag, not just the induced drag" [19]. While Munk [21] and the Hortens [32] may have been concerned with reducing the induced drag, Whitcomb [42] saw potential in harnessing the wingtip vortices but recognized that such tip devices would only be optimized for a particular flying condition. For most aircraft, such as airliners or tankers, this may not be of concern; however, for aircraft such as sailplanes or fighters, where the flight envelope is not on the straight-and-narrow, a different approach must be utilized to successfully utilize winglets. The focus must then be to reduce the overall drag in all flight conditions.

Evidently, the design of such devices is inherently proprietary to any aircraft. This may explain why most published sources either glance over the subject, or why most developments are filed as patents. Some papers have tried to shed light on common design practices for winglets (such as [18]). Nonetheless, winglet design should remain a function of the aircraft for which it is implemented: there simply isn't one design that will fit all.

2.2 Fuselage – History and Research

Fuselage design has and always will be largely dictated by the aircraft's mission. The Wright brothers, in their first foray into manned flight, were more concerned with becoming airborne than providing creature comforts to the sole passenger they could carry. Later, it would be passenger flight; military combat; high-speed and high-altitude flight; and with each step came new requirements, new demands, the designs evolving organically through technological progress.

In the case of an unmanned aerial vehicle, the design requirements are alleviated to a certain degree by the removal of the human factor. With humans gone, so are the principles of ergonomics and in some cases the factor of safety can now be reduced significantly. UAV's are payload-centric devices: their only mission is to carry their payload and enable it [28].

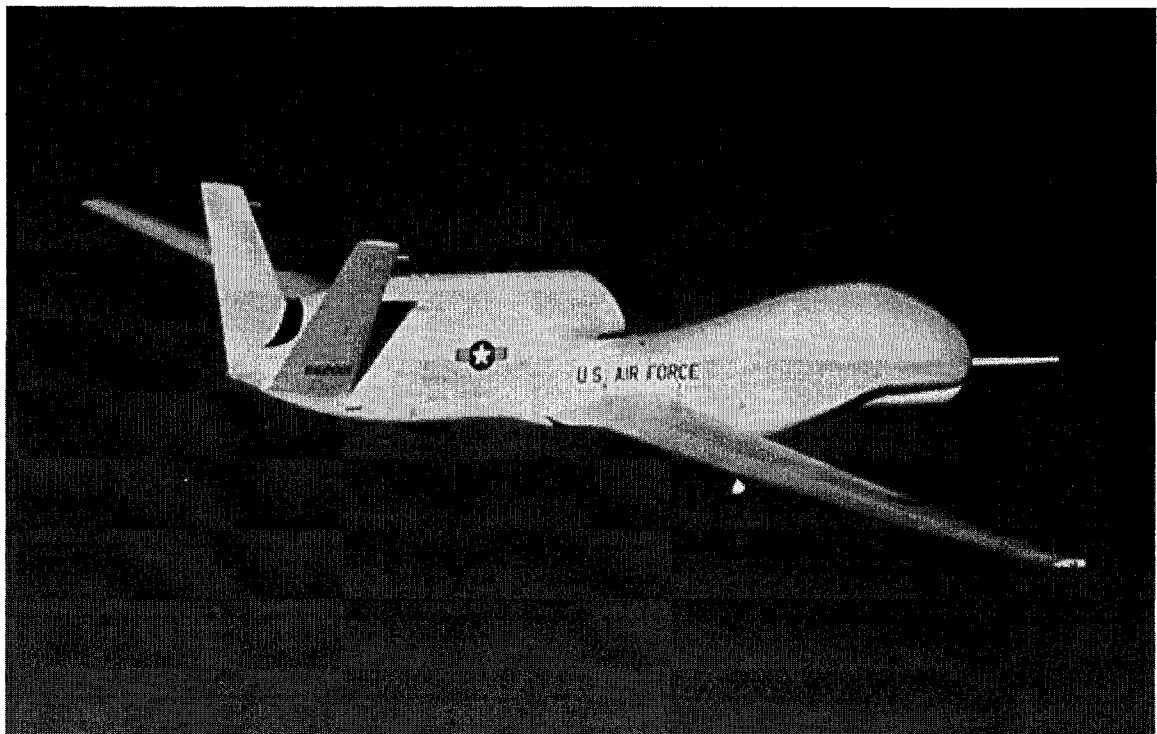


Figure 2.8 Global Hawk, one of the USAF's newest UAV's, designed for high-altitude reconnaissance. The bulge at the front is housing for a large radar array.

Much research has been completed over the years on the subject of fuselage design and while it must be covered in the discussion of this study, it was not a central point of the work presented here. Instead, a large amount of research was conducted, both in literature and in

gathering empirical data of related aircraft types. The design of the fuselage would thus not be part of the iterative design process but rather a starting block for the wing-fuselage junction study.

In this particular case, the fuselage only has two basic tasks, to carry its payload and to form a structural link between the lifting surfaces and the control surfaces. Given that the payload can be shifted around as will, the only design guideline then become ones to minimize drag and to delay separation in the boundary layer in normal flight conditions [36].

To achieve this goal, it is suggested that the fuselage be initially modeled after an airfoil section which fulfills these initial requirements [26]. An ensuing contraction near the wing root section (either at the quarter chord or the trailing edge) should help smooth flow in the area, but equally importantly, a wing-fuselage junction should be designed at this point to keep the flow attached for as long as possible and to prevent the mixing of adverse pressure gradients [36].

2.3 Wing-Fuselage Junction – History and Research

Like wingtip device design, the study of wing-fuselage interference is inherently proprietary to a particular aircraft and as such, very few publications can be found on the subject. For example, Raymer [28] dedicates two short paragraphs to it and mentions it later when he discusses various CFD success stories. Simons [33] discusses interference drag in his “Parasite Drag” chapter, giving the former a one-page sub-section (but not much else) and noting that “the gain is too slight to justify the effort”. How is it that this form of drag, which may account for a large percentage of the drag on a streamlined body, is given such little attention?

Aside from its proprietary nature, wing-fuselage junction design is also a very complicated problem. As Raymer points out, recent advances in CFD have helped in the understanding of interference drag and allowed designers to optimize their designs. Boermans [3] states that the interference drag problem can be split into inviscid and viscous cases, the dominant case being dictated by the Reynolds number regime: lower Reynolds numbers will point to a dominant viscous case, whereas higher Reynolds numbers point to a dominant inviscid case. Whitcomb’s Area Rule [14], a product of shock formation in transonic flow, alleviates the latter by contraction or waisting of the fuselage. While the resulting “coke bottle” shape is no longer as prominent as it

once was, the area rule is still being used and is directly related to interference drag. The new Airbus A380 uses this shaping rule but it can only be appreciated from under the aircraft, as depicted in Figure 2.9.

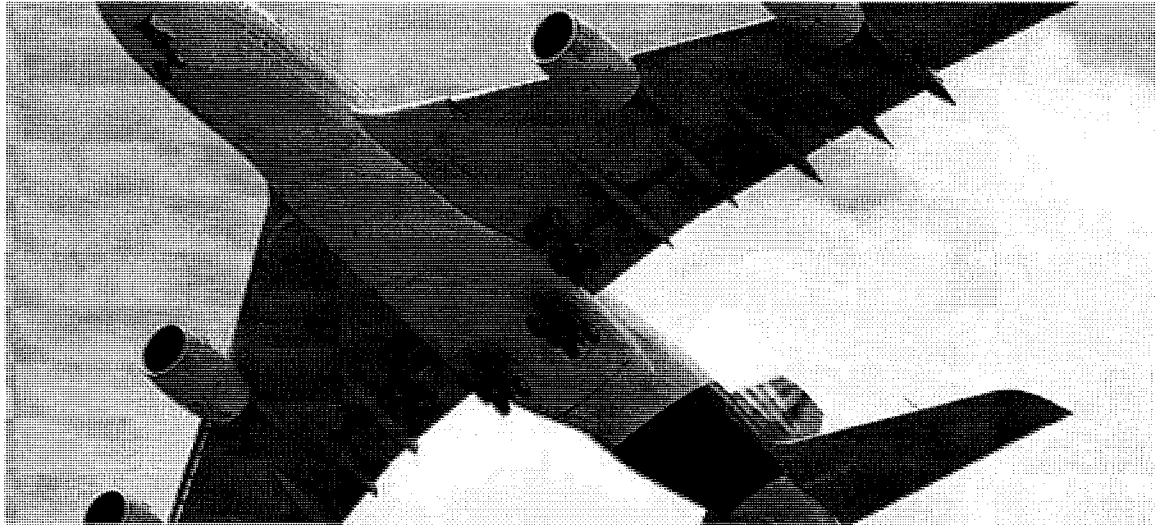


Figure 2.9 The Airbus A380 uses the area rule around its massive wing root.

The complex interaction of boundary layers makes the interference problem a complicated one at any Reynolds number. Early texts shied away from the subject. Tietjens [38] does not explicitly cover the material in *Applied Hydro- and Aeromechanics* but hints at it. Von Mises [41] acknowledges that for a body with an appendage, “the resultant drag is considerably larger than the sum of the two drag forces that are found when each part is tested independently.” In terms of theory, one of the most complete discussions on the matter comes from Schlichting’s *Boundary Layer Theory* [29], where all matters of boundary layer interaction are covered. Specifically in terms of aerodynamics, Thwaites [37] offers a complete chapter on the subject under the title “Uniform Flows Past Joined Bodies”. Both works require a great deal more engineering insight than other textbooks which may cover similar subjects.

It can be safely generalized here that while designers understood there were interference effects, they did not have the tools required to properly optimize a design until computational-fluid dynamics had evolved to a state where the flows could be approximated to an appropriate level of accuracy and reality (according to [3], not until the late 1980’s). Instead, generalizations could be

made based on empirical results and specific implementations could be made after wind-tunnel testing and subsequent flight-testing.

It is difficult to track the history of wing-root design simply due to the lack of cohesive documents which may detail the design of such devices, even if it were on a proprietary basis. A chronological review of various aircrafts can reveal some advances in the design process for such devices. For example, consider Figures 2.9 and 2.10. Figure 2.9 shows a P-51D's wing root, arguably the United States' finest fighter of World War II. The Mustang is famous for its NACA 6-series laminar flow airfoil. The wing root shows a crude transition, a mere set of fillets to the contour of the wing. Figure 2.10 shows an unidentified sailplane on the January, 1992 cover of *Soaring Magazine*. The shaping around the wing root here is considerably more complex. It is easy to dismiss the differences in terms of flight mission and requirements but it is also important to recall that both of these examples illustrate (to a point) the state-of-the-art in terms of aerodynamics at their respective periods in time.

In the late 1980's, advancements in available computing power made the study of complex juncture flows more reasonable. While generalizations still cannot be made to this day, research by Maughmer [19] and Green [9], among several others, have shown that general guidelines can be drawn in the designing of fillets for leading and trailing edges, which may be specific to the application. Of particular interest for this study, [19] states that a linear planform (fairing) at the leading edge obtained a "3-5% drag reduction over much of the polar" and that "the linear planform yields superior performance to the parabolic one in every case". Finally, this report also states that "the benefits of the integration fairing are even greater as the Reynolds number is decreased", clearly a promising claim for a UAV that operates at Reynolds numbers in the range of the tests conducted in [19], namely between $Re = 230,000$ and $400,000$.



Figure 2.9 North American's P-51D. Notice the crude fillet-style transition.

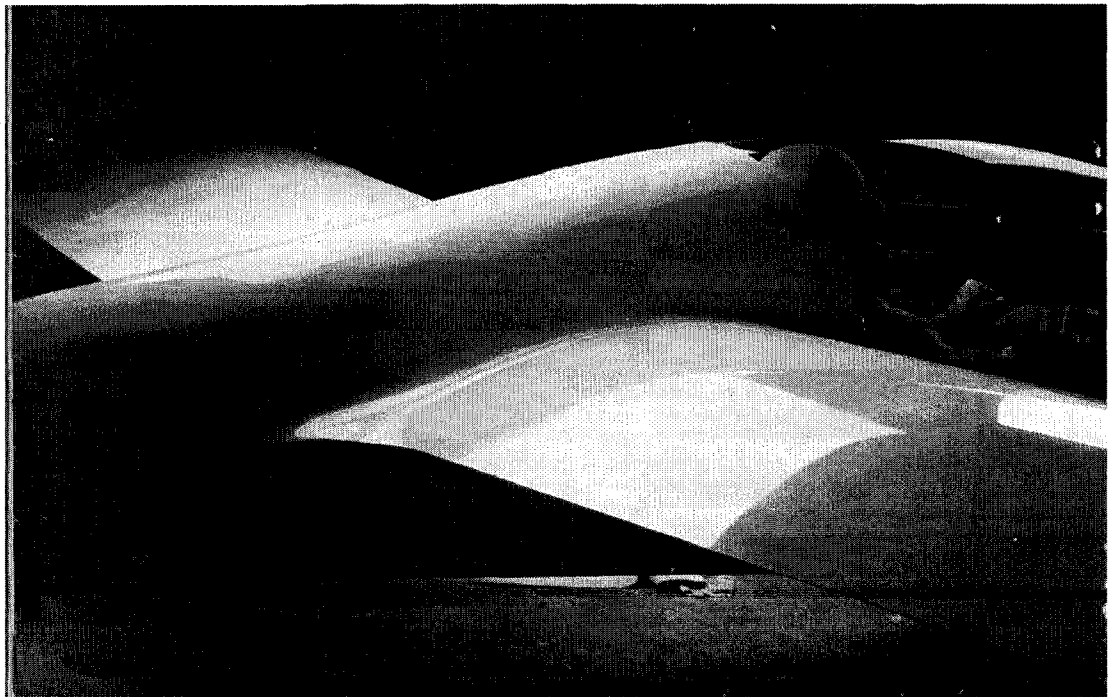


Figure 2.10 Unidentified sailplane on the cover of Soaring Magazine, January 1992. Observe here the intricate fairing arrangement at the wing root. At the fuselage a specialized airfoil is used, which is then hybridized into the wing's root airfoil.

CHAPTER 3

SET-UP AND PROCEDURE

3.1 Introduction

At the most basic level, the premise of this study was to decrease the overall drag of the airframe. The key areas which were studied were the wingtips, the wing-fuselage junction and to a lesser extent, the fuselage itself. While some of the design aspects could be parameterized, some cannot and thus no global generalization can be made about which aspects of the geometries could be changed. However, in some cases, such as with the winglets, some aspects can be clearly defined.

3.2 Winglet and Wingtip Design Parameters

Winglets have basic geometric parameters that are widely recognized: toe and twist angles, sweep angle, cant angle, root chord, root position and winglet span or height. Additionally, the airfoil selection for these devices is not trivial. The physical meaning of these parameters are illustrated in Figure 3.1. Newer types of winglets, such the blended kind as shown in Chapter Two, tend to have more organic qualities and as such become more difficult to parameterize; nonetheless some of these categories still apply.

Given the smaller chord lengths of non-planar lifting devices, the operational Reynolds number becomes significantly lower than that of the wing's and thus one must take special consideration in the selection of the airfoil profile. Avoiding laminar separation bubbles is imperative but it still must provide good low-drag performance over the entire operating range, which usually translates into some sort of compromise in the thickness of the airfoil. In this study, the airfoil designed in [20] was utilized due to its already proven wingtip performance and the fact that it was a good match to the flight polars of the main wing.

The toe and twist angles of the winglet are not directly related. Usually, one of the two will be held constant while the other is set as a variable. The twist angle is more closely related to the sweep angle since changing the amount of sweep will have the same effect on the load distribution as changing the toe angle and it is the tip's physical connection to the root of the winglet. By setting the toe angle as the variable (essentially the winglet's initial angle of attack), the overall load on the winglet can be varied as required by the design. Testing has shown that a higher toe angle will lead to an increase in climbing or turning performance with a decrease in performance at higher speeds. An increase in toe and twist angle can contribute to the generation of thrust in cases where a forward component in lift is produced. In general, most winglet designers take these two angles to be the key to a successful non-planar wingtip device, most probably because the results are most sensitive to their values (though, in this particular case, not by much as [18] would lead most to believe).

It is beneficial to readily acknowledge that a winglet has its own planform efficiency (the Oswald Efficiency Factor, see Appendix E) and that all the parameters usually being monitored for a wing should also be monitored for a winglet, such as winglet loading and load distribution. The increase in span due to a cant angle of less than 90° can be offset by removing a section of the wingtip. This also alleviates part of the issue regarding the increase in wetted area. However this technique was not used in this study because the surface area provided by the wing was already at the minimum required by the solar array. The winglet root chord determines the initial operating Reynolds number. The ensuing chord distribution (or a measure of the taper ratio, see Appendix E) will dictate the winglet's ability to produce a suitable spanwise loading which will enable it to favorably affect the flowfield at the wingtip. The winglet's span (or height) can thus be determined after the taper ratio is set.

The cant angle can be a major player in the efficiency of the winglet as it can be used to regulate the wing bending moment provided by the surface. In some cases the cant angle has to be limited due to wingspan requirements, but in instances where there is some room for play in this area, it can strongly affect the efficiency of the winglet. An increase in wing bending moment at the root usually translates into a natural dihedral during in-flight conditions, which will vary with

airspeed. As such it is also one of the qualities which is most readily affected by the flight condition.

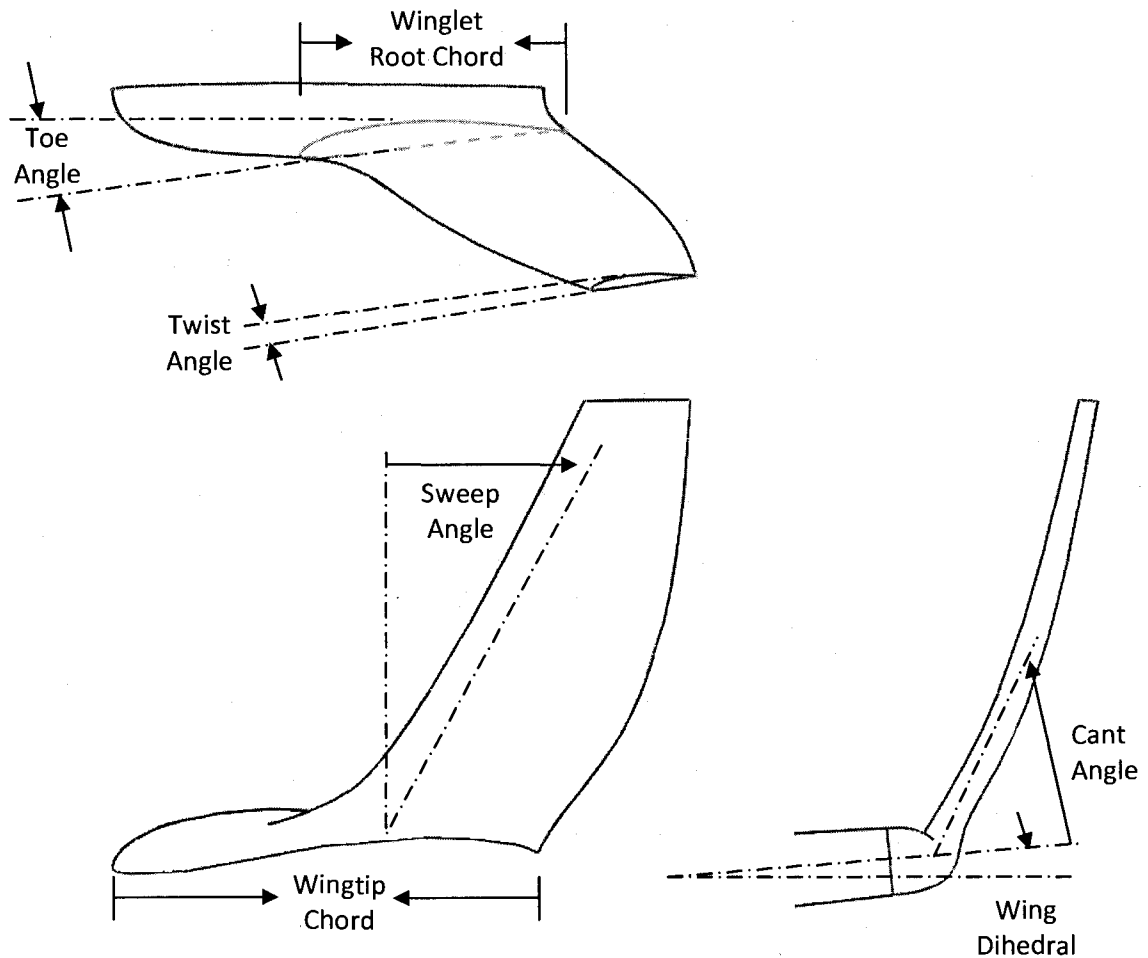


Figure 3.1 Winglet geometry parameters.

Finally, the root position is generally set as matching up the trailing edges, for the simple fact that the vortices usually originate at the trailing edge. However, in some cases there are two or more non-planar devices on the wingtip, such as on the modified Whitcomb winglet, as shown in Figure 3.2. The forward winglet on the Whitcomb design is optional [40] and as such the inclusion of the forward, “primer” winglets was ruled out in this study. This forward winglet is dubbed “primer” because it is used to trip a separate set of vortices prior to the main non-planar surface, a process that becomes increasingly efficient as vortex-strength (and thus airspeed) increases.

For planar wingtip devices, there are no widely recognized design parameters. An attempt was made to make the wingtip designs in this study easily scalable and reproducible. In some instances, features commonly found in planar devices were incorporated into the winglet designs. In these cases, the design dimensions are well presented and thoroughly explained. All of the designs will be outlined in Chapter Four.

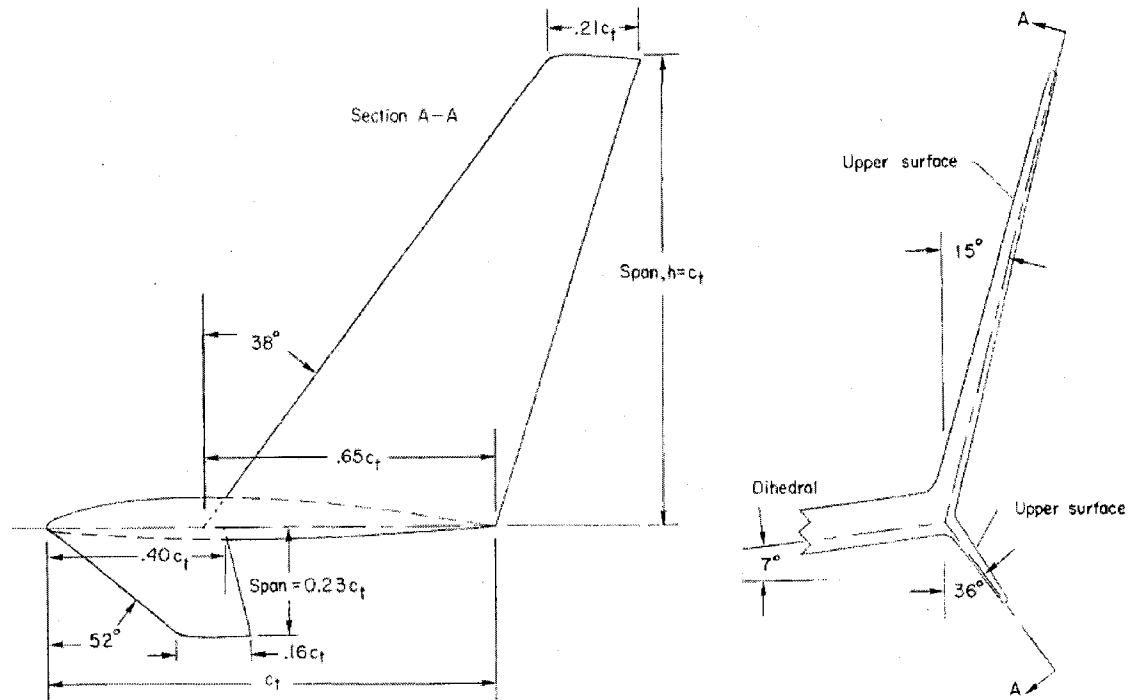


Figure 3.2 Whitcomb winglet, as presented in NASA Technical Note D-8260 [44].

3.3 Fuselage and Wing-Fuselage Junction Design Parameters

The fuselage design was not part of the iterative study but a large amount of research was conducted on fuselage design practice and the initial design was used as a building block for the other pieces, such as the wing-fuselage junction. In this particular case, the fuselage's profile was modeled as a six-series NACA airfoil, known for their laminar flow qualities. By studying the surface speed as a function of the chord length, or the pressure distribution over the airfoil section (as in Figure 3.3), the placement of the wing section can be chosen for optimum performance. After the trailing edge, or a bit before it, the airfoil profile can be discarded or modified to include a

contraction which will enable smoother flow after the wing root. The wing section dominates the flowfield because of the adverse pressure gradients it causes, so the fuselage must be designed to accommodate this feature. In this particular case, the fuselage's third dimension is dictated by the components it has to carry and not much else. Sailplane fuselages usually employ a mid-wing configuration and use the top half of the fuselage as an additional buffer between the previously-mentioned adverse pressure gradient, but such a layout was not applicable for this design as interior space was paramount.

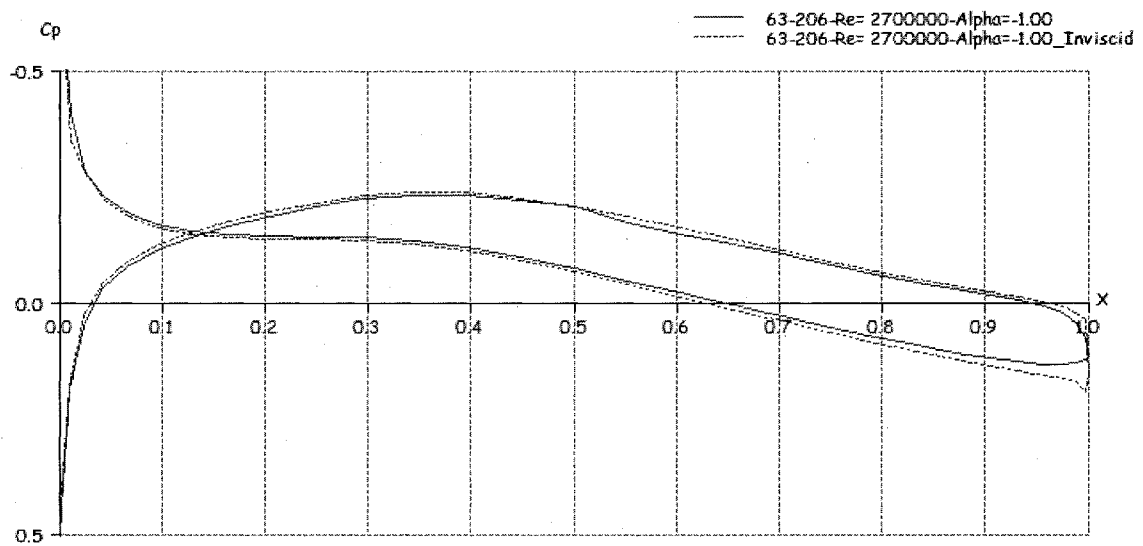


Figure 3.3 Local coefficient of pressure for the base airfoil used in the fuselage design effort. Solid line shows the viscous case. Based on this analysis, proper placement of the fuselage contraction and subsequent design decisions could be made.

The fuselage design was kept constant since its shape directly affects the design of the wing-fuselage junction, which is one of the factors in this study. By keeping the fuselage design intact, the wing-fuselage junction can be more easily parameterized, thus enabling reproducible results. However, wing-fuselage junction design does not have its own set of geometric parameters as winglets do. An effort was made to standardize the designs within this study, from one to the next.

All measurements for the junctions were taken from the fuselage's nose, a value which would not change through the study since the fuselage design would be kept constant. This gave a fixed point of reference around which the geometries could be built. In this part of the study, the main

focus was to evaluate the overall drag for the airframe as changes in the junction are made, primarily for loitering, level flight.

Ideally, the shape should be as simple as possible. Lofting between two profiles, while using start and end conditions, would be the best way to construct the junctions. Thus, the importance of the wing-fuselage junction design is in designing a profile which lays on the centerline plane, primarily its shape and its position, and determining the best way in which it should be lofted over to the wing's root profile.

3.4 Resources

To characterize the flow over the various parts of the airframe being analyzed, a dedicated simulation workstation was built which would meet the requirements for solving problems within the scope of this project. This machine was built with output visualization, upgradeability and ease of use.

The following is a list of the components outfitted to the machine:

- Q9450 Intel Core 2 Quad Processor, rated at 2.66GHz/core, running at 3.20GHz/core
- P43 Intel Chipset motherboard with 1600Mhz FSB
- 8GB RAM rated at 1066MHz, running with tighter timings for faster calculation times
- GeForce 9600GT graphic card for high-end 3-D visualization

The software used for these simulations was COMSOL Multiphysics 3.5 [6], a popular commercial package used in a multitude of professions. COMSOL has several built in physics "modules" and is designed in such a way that these modules can speak to one another, allowing the user to modify his or her model as required for any number of relationships between the different modes.

COMSOL's graphic output capabilities and the fact that boundaries can easily be integrated for any variable provided a quick and accurate way of judging results and interpreting data. These results could then supplement initial estimates acquired through panel methods. Plotting velocity fields or pressure fields over boundaries or through isosurface distribution enabled for intuitive understanding of what was happening in three dimensions.

COMSOL has been sparsely used in fields similar to this study's, and to the author's knowledge, this study is one of the few (if not the only one) of its kind using COMSOL. This can most likely be attributed to a variety of issues, such as the weakness of the CAD Import feature or the slow-footed fluid solvers, many of which were fixed in version 3.5 and thus allowed the work to be pushed forward using this software.

3.5 Model Set-Ups

In general, all of the problems were set up the same way as to minimize the need for changes from one problem to the next. Furthermore, only one "wind tunnel" was constructed for a particular set of assets (e.g. winglet testing) and all geometries pertinent to that study would be imported into that testing environment. This ensured that the results would be comparable and that the constraints put upon the results by the environment would be the same. COMSOL was utilized to simulate the wind tunnel without the limitations associated with physical wind tunnels. Figure 3.4 illustrates a typical boundary configuration in two dimensions. The geometries tested could usually be halved about a plane of symmetry in the longitudinal direction and incorporating a symmetry boundary, effectively halving the computational time. Figure 3.5 illustrates a typical problem configuration, this particular one pertaining to the assessment of drag on a wing model. All of these studies assumed incompressible, isothermal flow.

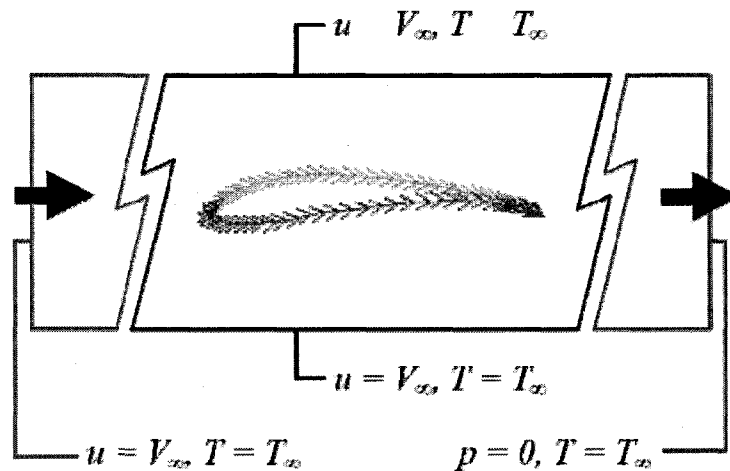


Figure 3.4 Typical boundary conditions set in two dimensions.

A fluid box is constructed around the object. One face has a normal flow velocity boundary assigned to it, while the face directly opposite of this has a no pressure, no viscous stress outlet condition. The faces surrounding the object are slip surfaces, while the plane of symmetry is modeled as a symmetry boundary. The advantage to modeling the surfaces as slip as opposed to non-slip is so that the fluid box can be made smaller as the boundary effects are drastically reduced, albeit still present. The interior boundaries created by the object being nested inside of the fluid box are no slip surfaces. Interior planes, such as the ones observed in Figure 3.5, can be inserted in the fluid box as continuity interior boundaries, for the purpose of integrating over these boundaries.

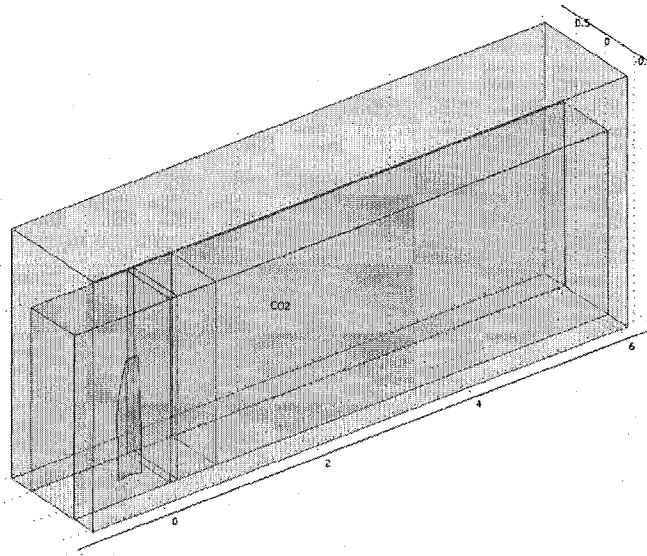


Figure 3.5 Typical problem setup. Notice the inserted measurement planes.

3.5.1 Computational Method

The fluid domain was initially modeled using the direct Navier-Stokes equations (Eq. (3.1), (3.2)). After several iterations of the design it was found that the Reynolds Number, while relatively low for flying machines, was too high for the particular physics module being utilized for the simulation. A move over to the turbulent $k-\epsilon$ and $k-\omega$ models [5, 41] was eventually made. The models of the wind tunnel remained unchanged with the migration. COMSOL uses the Reynolds Average Navier-Stokes (RANS) equations [6] for its implementation of the $k-\epsilon$ and $k-\omega$ models, as presented in Eq. (3.3) and (3.4).

$$\rho \frac{\partial \vec{u}}{\partial t} + \rho(\vec{u} \cdot \nabla) \vec{u} = \nabla[-p\vec{I} + \eta(\nabla \vec{u} + (\nabla \vec{u})^T)] + \vec{F} \quad \text{Eq. (3.1)}$$

$$\nabla \cdot \vec{u} = 0 \quad \text{Eq. (3.2)}$$

$$\rho \frac{\partial \vec{U}}{\partial t} + \rho \vec{U} \cdot \nabla \vec{u} + \nabla \cdot (\overline{\rho \vec{u}' \otimes \vec{u}'}) = -\nabla p + \nabla \cdot \eta (\nabla \vec{U} + (\nabla \vec{U})^T) + \vec{F} \quad \text{Eq. (3.3)}$$

$$\nabla \cdot \vec{U} = 0 \quad \text{Eq. (3.4)}$$

For the k - ε model, Eq. (3.5) illustrates the turbulent kinetic energy k . Equations (3.6) and (3.7) describe the dissipation rate of turbulent energy ε and the turbulent viscosity η_T for the k - ε model, respectively. The model constants in these equations are determined from experimental data and their values are given in Table 3.1.

$$\rho \frac{\partial k}{\partial t} - \nabla \cdot \left[\left(\eta + \frac{\eta_T}{\sigma_k} \right) \nabla k \right] + \rho \vec{U} \cdot \nabla k = \frac{1}{2} \eta_T (\nabla \vec{U} + (\nabla \vec{U})^T)^2 - \rho \varepsilon \quad \text{Eq. (3.5)}$$

$$\rho \frac{\partial \varepsilon}{\partial t} - \nabla \cdot \left[\left(\eta + \frac{\eta_T}{\sigma_\varepsilon} \right) \nabla \varepsilon \right] + \rho \vec{U} \cdot \nabla \varepsilon = \frac{1}{2} C_{\varepsilon 1} \frac{\varepsilon}{k} \eta_T (\nabla \vec{U} + (\nabla \vec{U})^T)^2 - \rho C_{\varepsilon 2} \frac{\varepsilon^2}{k} \quad \text{Eq. (3.6)}$$

$$\eta_T = \rho C_\mu \frac{k^2}{\varepsilon} \quad \text{Eq. (3.7)}$$

Constant	Value
C_μ	0.09
$C_{\varepsilon 1}$	1.44
$C_{\varepsilon 2}$	1.92
σ_k	1.0
σ_ε	1.3

Table 3.1 Model constants for Equations 3.5, 3.6 and 3.7.

The modified Wilcox k - ω model COMSOL uses can be described by Eq. (3.8) (turbulent energy k), (3.9) (dissipation per unit turbulent kinetic energy ω) and (3.10) (turbulent viscosity). The closure constants and functions used by these equations can be found in Table 3.2.

$$\rho \frac{\partial k}{\partial t} + \rho \vec{U} \cdot \nabla k = \nabla \cdot [(\eta + \sigma_k \eta_T) \nabla k] + \frac{1}{2} \eta_T (\nabla \vec{U} + (\nabla \vec{U})^T)^2 - \rho \beta_k k \omega \quad \text{Eq. (3.8)}$$

$$\rho \frac{\partial \omega}{\partial t} + \rho \vec{U} \cdot \nabla \omega = \nabla \cdot [(\eta + \sigma_\omega \eta_T) \nabla \omega] + \frac{\alpha}{2} \eta_T \frac{\omega}{k} \eta_T (\nabla \vec{U} + (\nabla \vec{U})^T)^2 - \rho \beta \omega^2 \quad \text{Eq. (3.9)}$$

$$\eta_T = \rho \frac{k}{\omega} \quad \text{Eq. (3.10)}$$

Variable	Relationship
α	$\alpha = \frac{13}{25}$
β	$\beta = \beta_0 f_\beta$
β_k	$\beta_k = \beta_{0,k} f_{\beta,k}$
β_0	$\beta_0 = \frac{9}{125}$
$\beta_{0,k}$	$\beta_{0,k} = \frac{9}{100}$
f_β	$f_\beta = \frac{1 + 70\chi_\omega}{1 + 80\chi_\omega}$
$f_{\beta,k}$	$f_{\beta,k} = \begin{cases} 1, & \chi_k \leq 0 \\ \frac{1 + 680\chi_k^2}{1 + 400\chi_k^2}, & \chi_k > 0 \end{cases}$
σ_ω, σ_k	$\sigma_\omega = \sigma_k = \frac{1}{2}$
χ_k	$\chi_k \equiv \frac{1}{\omega^3} \nabla k \cdot \nabla \omega$
χ_ω	$\chi_\omega \equiv \left \frac{\Omega_{ij} \Omega_{jk} S_{ij}}{(\beta_{0,k} \omega^3)} \right $
Ω_{ij}	$\Omega_{ij} = \frac{1}{2} \left(\frac{\partial U_i}{\partial x_j} - \frac{\partial U_j}{\partial x_i} \right)$
S_{ij}	$S_{ij} = \frac{1}{2} \left(\frac{\partial U_i}{\partial x_j} + \frac{\partial U_j}{\partial x_i} \right)$

Table 3.2 Model closure constants and variables for Equations (3.8), (3.9) and (3.10).

It is generally more difficult to get convergence from the $k-\omega$ model. A method suggested in [6] to help convergence of the model is to first solve the problem with the $k-\varepsilon$ model and then use that solution as the initial value to the $k-\omega$ setup. While one would expect such a procedure to cut down computational time, it was not so, as the $k-\varepsilon$ and $k-\omega$ models generally took the same amount of time to reach a solution.

As is common knowledge, a good wall function dictates the validity of the $k-\varepsilon$ and $k-\omega$ models. In COMSOL Multiphysics, the logarithmic wall function is prescribed as a distance from the wall in unit length or in viscous units. This value is usually guessed by the user at first and COMSOL promptly adjusts its solver settings to acquire a converging solution. However, the user may adjust his or her guess by following these steps. Equation (3.11) defines the friction velocity u_τ , which can be used in Eq. (3.12) to find the viscous length scale, l^* ,

$$u_\tau = \sqrt{\frac{\tau_w}{\rho}} \quad \text{Eq. (3.11)}$$

$$l^* = \frac{\eta}{\rho u_\tau} \quad \text{Eq. (3.12)}$$

where τ_w is the shear at the wall and can be approximated, ρ is the fluid density and η is the fluid's absolute viscosity. Knowing these values, Eq. (3.13) and its attached relationship can be used to find δ_w , the logarithmic wall distance. For lower Reynolds number ranges on the turbulent scale, a lower δ_w^+ value is recommended.

$$\delta_w^+ = \frac{\delta_w}{l^*}, \text{ where } 30 \leq \delta_w^+ \leq 300 \quad \text{Eq. (3.13)}$$

Additionally, COMSOL Multiphysics allows the logarithmic wall function to be specified in terms of h , the local element diameter. The logarithmic wall distance δ_w can thus be specified as some function of h , usually a fraction [6]. Both approaches were initially tested and for this particular

problem, a logarithmic wall distance of 0.01 yielded nearly exactly the same solution as if it was specified by $h/2$. The latter option was subsequently used in all simulations.

One specific assumption made in the turbulence modeling of the k - ε and k - ω models is that the turbulence is in equilibrium in the boundary layers. This assumption is not always true, and in the modeling of these geometries the stagnation point at the wing's leading edge produces an instability in regards to this assumption. To remedy this situation, a realizability constraint must be utilized. This constraint is described in 3-D in Eq. (3.14) and (3.15) for the k - ε and k - ω models, respectively and specifically affects the turbulent viscosity, where λ_α is the largest eigenvalue of the strain rate tensor.

$$\eta_T = \min \left(\rho C_\mu \frac{k^2}{\varepsilon}, \frac{\rho k}{3 \cdot \max(\lambda_\alpha)} \right) \quad \text{Eq. (3.14)}$$

$$\eta_T \leq \frac{\rho k}{\sqrt{6} \sqrt{S_{ij} S_{ij}}} \quad \text{Eq. (3.15)}$$

The drag being measured in this study is the overall drag, which includes the following, in any combination: skin friction, interference drag, induced and parasitic drag, along with other 3-D effects which cannot be accounted for by simply integrating the pressure distribution over the surface of the object. Various methods for measuring the drag directly are suggested at this point: pressure integration over the geometry's boundaries, shear stress integration over the computational domain walls, a virtual force-balance system and finally the momentum theorem.

While a virtual force-balance system would do the job, such an implementation was not possible with COMSOL Multiphysics. Pressure integration over the wing surface would have given only a portion of the drag (that which is not associated with the 3-D effects) and shear stress integration over the domain's walls proved to be highly suspect in terms of its outputs, especially since the computational domain was designed as a virtual wind tunnel, as to have minimal effect on the results. Therefore these methods were shown from the onset to either miss some vital drag components or not be accurate enough. The momentum method would be the

simplest and most efficient way of obtaining accurate results. This method is regularly used in the wind tunnel testing industry when more expensive equipment is not available. A measurement tool called a wake rake is used to take pressure readings in a specific plane and then compares the pressures recorded with the known tunnel static pressure. Figure 3.3 illustrates the basic premise of this method.

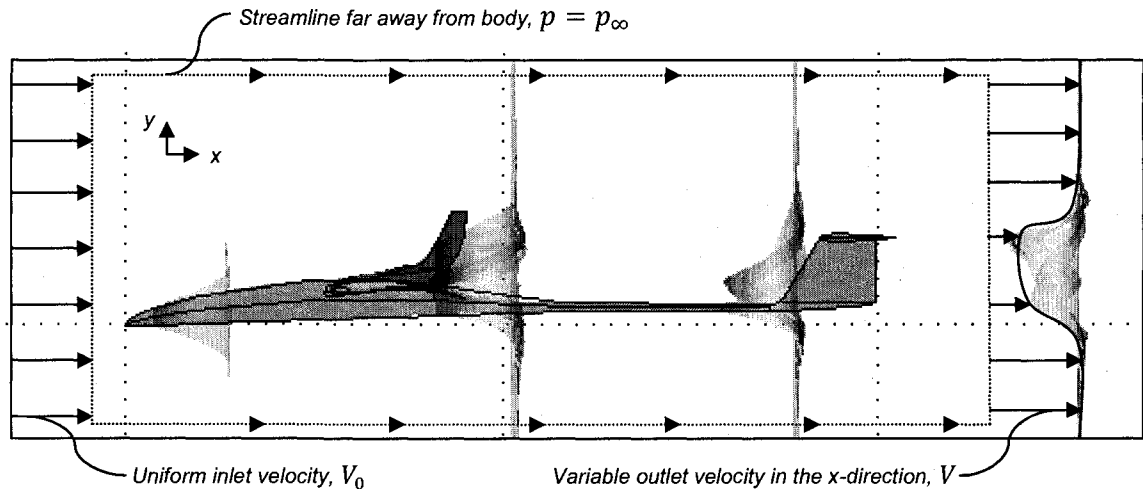


Figure 3.6 Deformed velocity slices around an object, illustrating the basis for the momentum method.

There are various ways of deriving the drag equation resulting from the momentum method. Although far downstream the flow would return to its original state, the fluid does lose some momentum after flowing around an object. By integrating over a measurement plane we can find the total drag imparted on the object as the loss in momentum in the fluid. From the momentum theorem, we can write:

$$\frac{d}{dt} \iiint_v \rho \vec{V} dV + \iint_s \rho \vec{V} (\vec{V} \cdot \vec{n}) dS = -\vec{F}_e - \iint_s p \vec{n} dS + \iiint_v \rho \vec{g} dV \quad \text{Eq. (3.16)}$$

Assuming incompressible flow and neglecting gravity, one can apply the starting and ending conditions as shown in Figure 3.3, to obtain:

$$D = \iint \rho u da (u_0 - u) \quad \text{Eq. (3.17)}$$

$$D = \iint (\rho u u_0 da - \rho u^2 da) \quad \text{Eq. (3.18)}$$

Kuethé and Chow [14] refer to Goldstein's *Modern Developments in Fluid Dynamics*, stating that the location of the measurement plane should be 0.12 chord lengths behind the trailing edge, where "pressure variation is small enough so that [the reading] gives the drag within a few percents of its correct value". In contrast, *Low-Speed Wind Tunnel Testing* [27] states that a wake rake should be used *at least* 0.7 chord lengths behind the trailing edge of the wing "so that the wake has returned to tunnel static pressure, since a difference in static pressure across the wake will void the values for" the wake's dynamic pressure. For the purpose of this study, an airfoil with known aerodynamic properties would be used to calibrate the test section and to find where the plane of measurement should be placed. After these results were found, it was shown that for this study, the measurement plane should be placed at 2.35 chord lengths away from the trailing edge. The calibration results can be found in Section 3.6. Good agreement was found between this data and other panel methods, also shown in Section 3.6. One major downfall of the momentum method is that it is not valid near stall angles due to separation [13, 26], and as thus limited the range of data available for this study.

3.5.2 Computational Domain Modeling

The environment modeled around the geometries was kept constant. Minimum dimensions for the test sections were taken from [27] and the test sections were subsequently made larger to accommodate for boundary layer effects. Good testing practice, as outlined in [27], requires that the test section width be at least 1.2 times the span of the model. Concurrently, the model chord should not exceed 0.4 times the tunnel height. Finally, the test section should be long enough that the flow outlet conditions do not affect the flowfield around the geometry itself.

The dimensions for the test section outlined in Figure 3.5 are shown in Figure 3.7. This test section was developed for the analysis of the winglet designs, using the basic guidelines outlined

in [27] for proper testing practice. For reference, the root chord of the test sections measured approximately 0.3 meters.

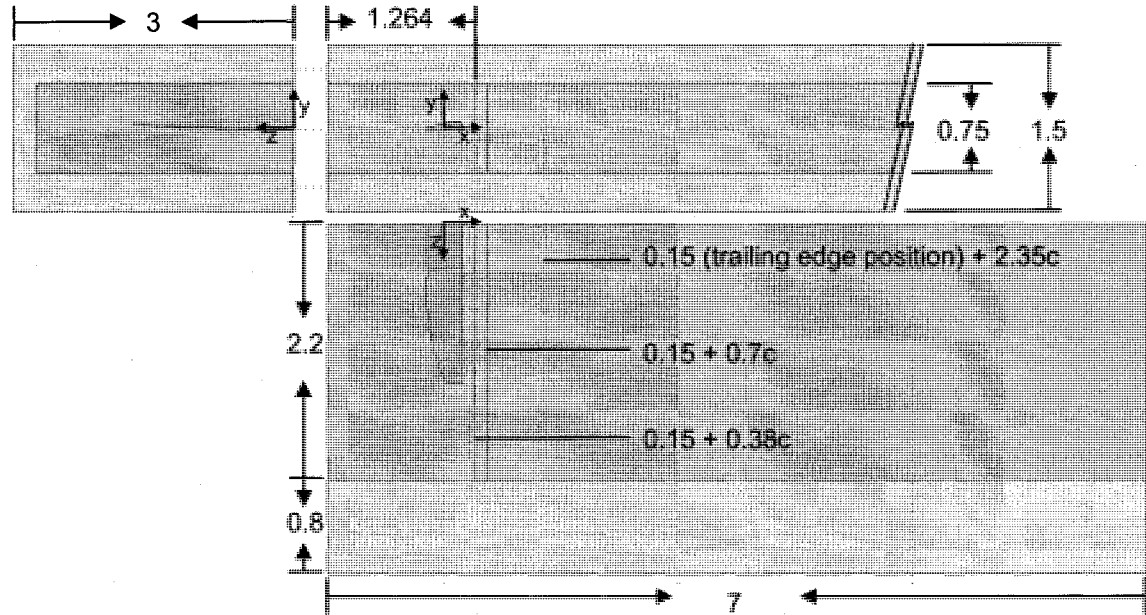


Figure 3.7 Test section dimensions for winglet analysis (0.12 chord measurement plane not shown). All measurements in meters.

The dimensions for the test section used in the analysis of the wing-fuselage junction can be found in Figure 3.8. According to [19], the test section needed only to be 0.15 times the wingspan of the airplane since the remaining amount of the wing does not affect the flow in the region of interest. The model allowed for a significantly greater portion of the wingspan to be included, along with a slip condition at that boundary to minimize all boundary effects.

In cases where the structural aspect was not considered, the geometry of the object being studied was hollowed to minimize the amount of elements produced in the mesh. The mesh was constructed using a hybrid of mapped and free mesh parameters. The mesh around the object of interest would be mapped along the edges of the geometry, followed by a free mesh used to fill in the subdomain. Meshing the geometries proved to be particularly tricky due to the highly curved surfaces commonly associated with airfoils and fuselage structures. A beneficial side-effect of the

partitions created by the measurement planes is that they act as separation zones where the mesh can become less dense.

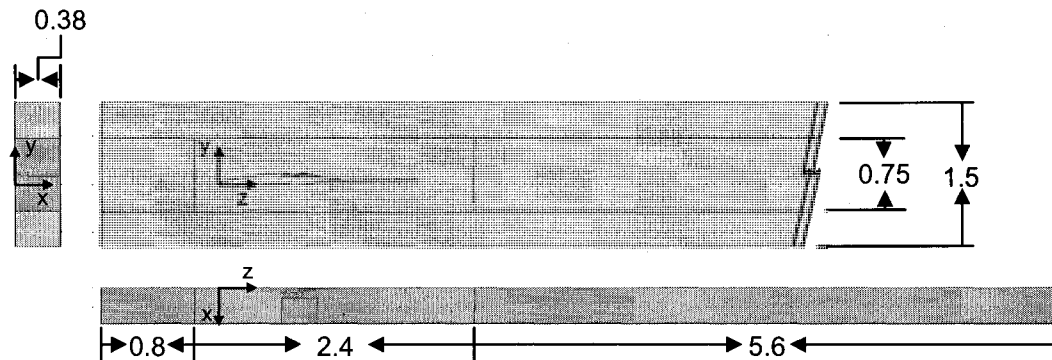


Figure 3.8 Wing-fuselage junction testing environment dimensions. All dimensions in meters.

3.5.3 Other Considerations Regarding the Computational Domain

The fluid domain properties were set for air at 3,000 feet above mean-sea level (MSL), which roughly corresponds to about 1,000 feet above-ground level (AGL) in Las Vegas.

All simulations were run at the cruise speed. Designs that showed more promise were run at various angles-of-attack, corresponding to different flight legs. In varying the angle of attack, the flow was kept constant and the geometry was rotated about its lateral axis to simulate the attitude of the object in the flow.

The tolerance (or convergence criteria) for the flow solvers was set at 0.0001 for the values of \bar{V} and p , and 0.00001 for the values of k , ϵ , and ω . This ensured timely convergence of the problems with a relatively efficient memory usage and a good solution quality.

3.6 Test Section Calibration

A calibration test was devised to benchmark the accuracy of the virtual wind tunnel opposite to some popular numerical methods used in aeronautical design. The panel methods utilized to solve the problem included lifting-line theory (LLT) and vortex lattice method (VLM, using both

horseshoe and quad vortices). Due to the geometry of the test section, marginally better results should be expected from the VLM than from LLT, although LLT should still converge. The results from these panel methods were obtained from XFLR5, a freeware frontend for the well-known and well-established X-Foil program, developed by Drela [44].

A more detailed description of the model used in this test can be found in Appendix A, along with the data collected and processed. The results for this test are shown in Table 3.3. Output from the virtual wind tunnel agrees fairly well with these standard, time-proven methods.

	Test Section FEM ($k-\epsilon$)	Test Section FEM ($k-\omega$)	Test Section LLT	Test Section VLM, Quads	Test Section VLM, Horseshoes
C_D	0.0386	0.0382	0.0352	0.0358	0.0359
C_L	0.8762	0.8780	0.8259	0.8486	0.8493
C_D , % error ($k-\epsilon$)	-	-	9.61%	7.77%	7.47%
C_L , % error ($k-\epsilon$)	-	-	6.10%	3.26%	3.17%
C_D , % error ($k-\omega$)	-	-	8.40%	6.58%	6.28%
C_L , % error ($k-\omega$)	-	-	6.31%	3.47%	3.38%

Table 3.3 Comparison for values acquired using the COMSOL environment to various popular panel methods.

The error found in Table 3.3 can be readily associated with a variety of factors. The geometries of the two test planforms are not exactly the same. XFLR5 is limited to linear sections from one airfoil cross-section to another while the wing design calls for a smooth transition between airfoil profiles. These minute differences can be viewed in Figure A.3. While the coefficients of lift and drag should scale appropriately with the small change in area, it can be more directly affected by the small differences in geometry. Furthermore, the mesh constructed around the geometry may generate error in the output due to the complex nature of the objects

being modeled. Other 3-D effects associated with lift and drag production may not be completely accounted for in the panel methods. The error may also be related directly to the limitations of the $k-\epsilon$ and $k-\omega$ models. The $k-\omega$ model seemed to better approximate the drag and it is well known that this model is generally better near walls.

CHAPTER 4

WINGTIP DEVICE SIMULATION ANALYSIS

4.1 Introduction

Some of the data recorded in Appendix B is presented here in a format that allows quick assessment of the winglet designs as they evolved. Appendix B also includes several additional illustrations of each model. For a more detailed overview of the models, it is recommended that Appendix B be viewed along with the descriptions carried within this chapter. As outlined in Chapter Three, the momentum method was used to compute the overall drag acting upon the system. Lift was obtained by integrating the pressure distribution over the boundary of the lifting surfaces. The data from both the $k-\epsilon$ and $k-\omega$ models is presented but it was generally observed that the $k-\omega$ model represented the flow around the object more accurately. All figures depicting pressure or velocity fields in Appendix B are taken from the $k-\omega$ simulations. The benchmarks for all of these designs were in primary fashion the control specimen, and in secondary fashion the previous iteration of the design.

4.2 Wing Control Specimen

The control specimen for the wingtip device analysis is the wing without wingtip devices. This particular wing employs two different airfoils, both of which were designed for high-lift operation at low Reynolds numbers: S1223 and S1220 (S stands for Selig) [30]. The design of this wing will not be explored as it is not the subject of this document but the performance of this planform must be covered in order to give the results presented here some relevance. Figure 4.1 and Table 4.1 outline the design parameters of the initial wing. All subsequent modifications in terms of adding planar or non-planar devices would be made onto this wing. Of particular interest are the lift and drag coefficients, along with the lift-to-drag ratio (also known as the glide ratio). The results from

the control specimen were also pit against various panel methods as described in Chapter Three. These results, along with the ones discussed in this sub-section, are presented in Appendix A.

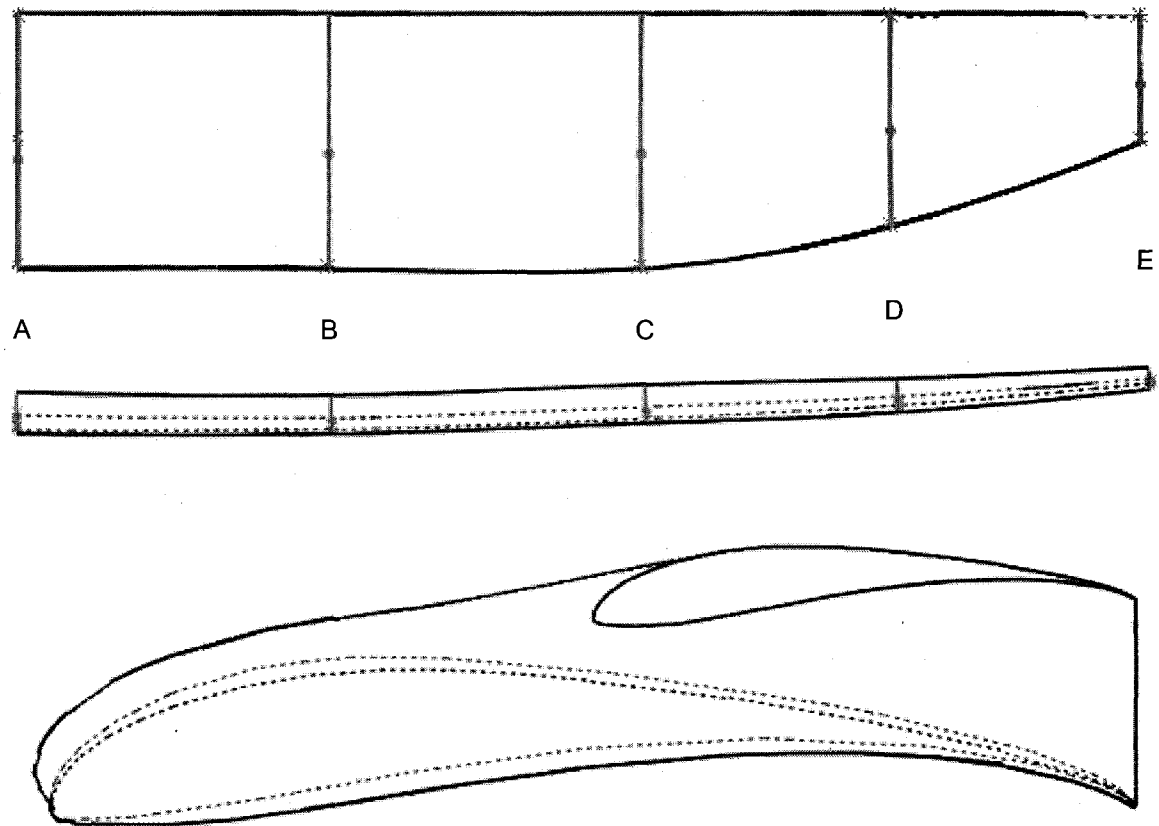


Figure 4.1 Wing Control Specimen diagram (top, front and side views) with station placement.

WING CONTROL SPECIMEN ATTRIBUTES	Station A	Station B	Station C	Station D	Station E
Airfoil Type	S1223	S1210			
Station Location (Z-Axis) [in]	0"	15"	30"	42"	54"
Local Station Chord [in]	12"	12"	12"	10"	6"
Local Station Dihedral [degrees]	0°	0°	2°	3°	5°
Local Station Twist [degrees]	0°	0°	0°	-1°	-2°
Local Station Alignment	-	Trailing Edge			

Table 4.1 Wing Control Specimen dimensions and attributes.

As illustrated in Appendix A, data gathered from this control model accurately followed predicted values from various panel methods. Consequently, data from this model was gathered in several flight attitudes, namely -2, 0, +2 and +4 degrees angle-of-attack, all of which are associated with a certain phase of the UAV's flight profile. Since loiter will be the main mode of transportation for this aircraft, it was natural to focus this study upon this particular flight condition. The wingtip designs would initially be tested at 0 degrees angle-of-attack. If the design showed promise, it would be run through the complete gamut of tests so that its behavior may further be studied. Table 4.2 lists the values of interest gathered from the control tests: the values gathered from the $k-\epsilon$ and $k-\omega$ models are very close in this case, as they remained throughout the study for all simulation runs.

WING CONTROL SPECIMEN		C_L	C_D	L/D
-2° AOA	($k-\epsilon$)	0.6907	0.0387	17.8397
	($k-\omega$)	0.6925	0.0383	18.0930
	Average	0.6916	0.0385	17.9656
0° AOA	($k-\epsilon$)	0.8762	0.0386	22.7117
	($k-\omega$)	0.8780	0.0382	23.0110
	Average	0.8771	0.0384	22.8605
+2° AOA	($k-\epsilon$)	1.0616	0.0407	26.0589
	($k-\omega$)	1.0632	0.0403	26.3955
	Average	1.0624	0.0405	26.2263
+4° AOA	($k-\epsilon$)	1.2182	0.0517	23.5460
	($k-\omega$)	1.2214	0.0511	23.9211
	Average	1.2198	0.0514	23.7323

Table 4.2 Wing control specimen aerodynamic properties.

4.3 Planar Device 01 (PD-01)

Planar Device 01 is a Hoerner-inspired planar wingtip device [28]. It was the first wingtip device designed for this study and is depicted in Figure 4.2. This particular device used a single

shaping feature (an extruded cut) to reach the desired results. This feature is highlighted in Figure 4.2 as well. By creating a pair of sharp edges and a recirculation seat for the vortices, it was hoped that the vortex strength could be harnessed while at the same time slightly delaying the merging of the pressure gradients. Table 4.3 outlines the basic geometric parameters for such a feature to be reproduced.

Wingtip Geometry Parameter (PD-01)	Magnitude
Spline Point 01: x_1 [in]	49.109
Spline Point 01: y_1 [in]	0.382
Spline Point 02: x_2 [in]	54.001
Spline Point 02: y_2 [in]	2.139
Spline Point 03: x_3 [in]	55.706
Spline Point 03: y_3 [in]	2.261

Table 4.3 Basic geometric parameters for Planar Device 01. All measurements given stem from the wing root airfoil's center of gravity. A natural cubic spline is used to link up the points listed.

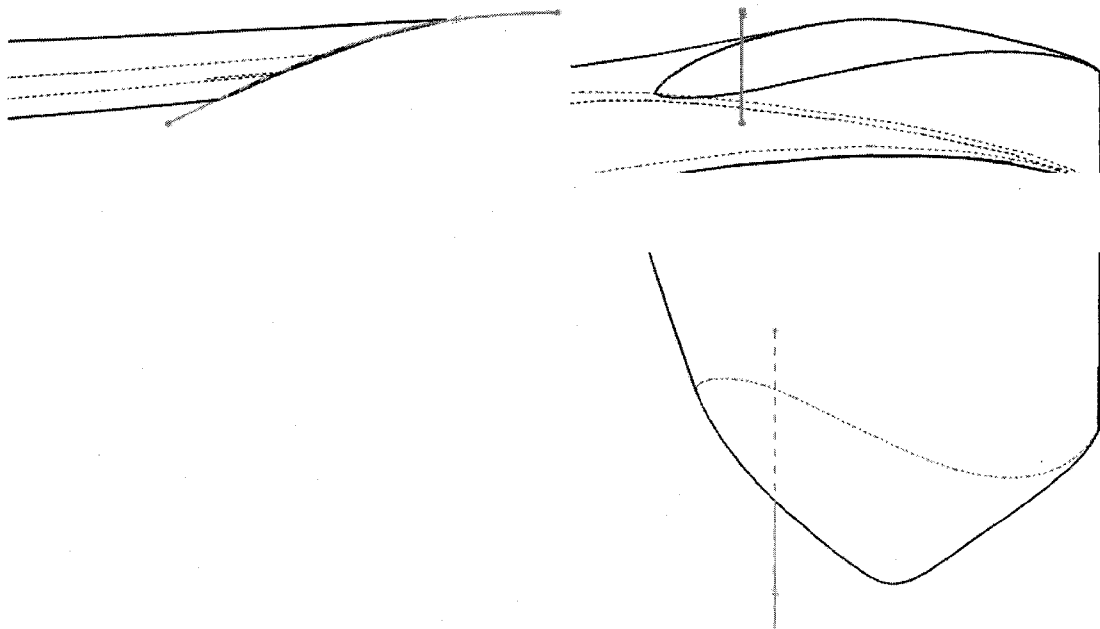


Figure 4.2 Planar Device 01 configuration (front, side and top views).

Unfortunately, the results did not prove to be as positive as hoped. In fact, the device had a negative impact on all categories of interest. One other important factor became quickly apparent: such a wingtip configuration would cut down on the precious surface area available to lay solar cells on, which also shows up as a loss in lift. The changes in performance hardly justified the loss of surface area. Table 4.4 illustrates the data gathered in the simulation run for loiter, level flight of Planar Device 01.

PLANAR DEVICE 01	Test Section ($k-\epsilon$)	Test Section ($k-\omega$)	Control Specimen ($k-\epsilon$)	Control Specimen ($k-\omega$)	Average Percent Change Over Control
Drag Force [N]	2.2109	2.1853	2.2352	2.2106	0.30%
Drag Coefficient	0.0387	0.0383	0.0386	0.0382	
Lift Force [N]	49.3053	49.4001	50.7654	50.8676	-1.49%
Lift Coefficient	0.8632	0.8648	0.8762	0.8780	
Lift-to-Drag Ratio	22.3013	22.6056	22.7117	23.0110	-1.78%

Table 4.4 Planar Device 01 results – loiter, level Flight (root chord $Re = 330141$).

As seen in section B.1, Planar Device 01 destroyed any useful pressure gradient at the tip. This resulted in an overall failure to make the wing more efficient. As noted previously, the implementation of such a wingtip usually translates into a decrease in surface area, but one more attempt would be made to design a planar device before moving on to the more promising winglets.

4.4 Planar Device 02 (PD-02)

A different approach would be taken for PD-02. A single sharp edge would be constructed as the bottom of the airfoil would be brought up to meet the top, a configuration more akin to the Hoerner wingtip. This planar device once again uses a single shaping feature (an extruded cut) and creates a curved surface in an attempt to propel the vortices up slightly, in an effort to counter downwash and more importantly, outwards, to delay the effect of this adverse pressure

gradient. Also as per the experience gathered in Planar Device 01, an effort was made to keep the overall surface area of the wing intact, which turned out to be quite successful (Table B.3 reveals that only 0.002 m^2 was lost by the inclusion of PD-02). Planar Device 02 is illustrated in Figure 4.3 and the geometric parameters for the spline which dictates the extruded cut, highlighted in Figure 4.3, are given in Table 4.5.

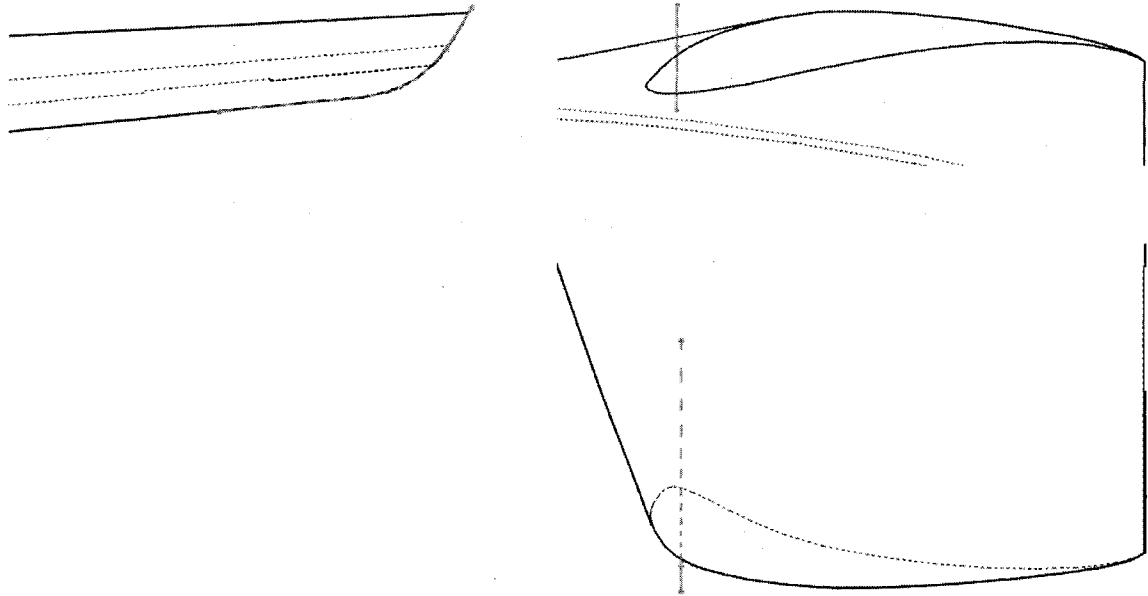


Figure 4.3 Planar Device 02 configuration (front, side and top views). A natural cubic spline is used to link up the points listed.

Wingtip Geometry Parameter (PD-02)	Magnitude
Spline Point 01: x_1 [in]	50.736
Spline Point 01: y_1 [in]	0.856
Spline Point 02: x_2 [in]	53.645
Spline Point 02: y_2 [in]	1.665
Spline Point 03: x_3 [in]	53.984
Spline Point 03: y_3 [in]	2.198

Table 4.5 Basic geometric parameters for Planar Device 02. All measurements given stem from the wing root airfoil's center of gravity. A natural cubic spline is used to link up the points listed.

Planar Device 02 fared much better than PD-01. Performance gains were observed in both drag and lift coefficients and subsequently a decent improvement in lift-to-drag ratio was made. Table 4.6 outlines the results obtained from the simulations.

PLANAR DEVICE 02	Test Section ($k-\epsilon$)	Test Section ($k-\omega$)	Control Specimen ($k-\epsilon$)	Control Specimen ($k-\omega$)	Average Percent Change Over Control
Drag Force [N]	2.1778	2.1544	2.2352	2.2106	-2.89%
Drag Coefficient	0.0377	0.0373	0.0386	0.0382	
Lift Force [N]	50.9815	51.0810	50.7654	50.8676	0.64%
Lift Coefficient	0.8818	0.8836	0.8762	0.8780	
Lift-to-Drag Ratio	23.4097	23.7102	22.7117	23.0110	3.06%

Table 4.6 Planar Device 02 results – loiter, level Flight (root chord $Re = 330141$).

A nice reduction in drag can be appreciated here. As a side-effect the lift was bumped up slightly, most likely due to the fact that the device deflected the vortices outwards and thus delayed the merging of the pressure gradients at the tip. This enabled the wing to produce lift more efficiently, plainly observed in the boundary pressure distribution over the wing (section B.2). However, at this point it was felt that a non-planar device would more efficiently serve the airframe and thus planar devices were abandoned.

4.5 Non-Planar Device 01 (NPD-01)

This winglet design was the initial non-planar study. It used data from [17] and [18] as a starting point. The winglet is depicted in Figure 4.4 and the associated geometric parameters are listed in Table 4.7. This initial design was conceived with a middle chord plane that could create a compound toe, twist, sweep and cant angle. This feature will be more evident in Non-Planar Device 02 but can already be seen here, especially in the cant angle. In Table 4.8, processed output for Non-Planar Device 01 at zero-degree angle of attack, in loitering flight conditions, can be viewed. A small planform was utilized at first and it would gradually be built-up in order to find

a general surface area for which the profile drag trade-off is optimal. It should be noted here that some concern had been brought up with the winglet surfaces possibly getting in the way of incident sunlight. This could be partially remedied by the inclusion of solar concentrators on the inside surface of the device but is the subject for another study.

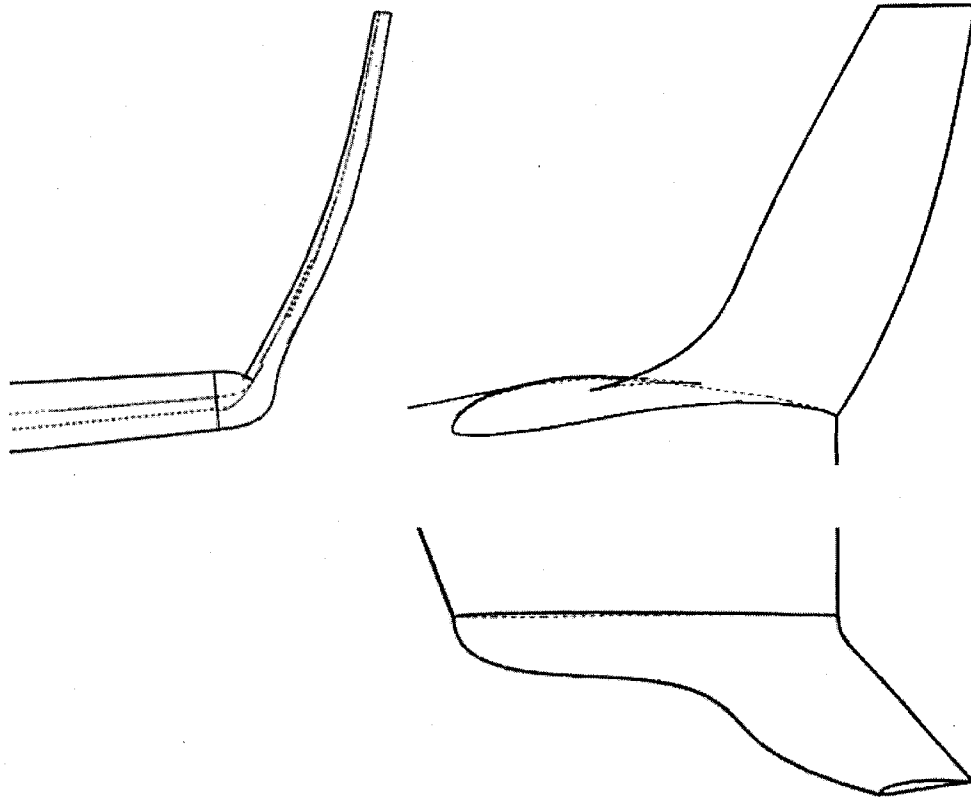


Figure 4.4 Non-Planar Device 01 configuration (front, side and top views).

Winglet Geometry Parameter (NPD-01)	Magnitude
Winglet Root Chord [in]	6
Toe Angle [degrees]	3
Twist Angle [degrees]	3
Sweep Angle [degrees]	25
Cant Angle [degrees]	15
Winglet Span [in]	6
Winglet Tip Chord [in]	2
Winglet Surface Area [m ²]	0.012940

Table 4.7 Non-Planar Device 01 – geometric parameters.

NON-PLANAR DEVICE 01	Test Section ($k-\epsilon$)	Test Section ($k-\omega$)	Control Specimen ($k-\epsilon$)	Control Specimen ($k-\omega$)	Average Percent Change Over Control
Drag Force [N]	2.2835	2.2613	2.2352	2.2106	0.59%
Drag Coefficient	0.0388	0.0384	0.0386	0.0382	
Lift Force [N]	52.7911	52.8893	50.7654	50.8676	2.32%
Lift Coefficient	0.8966	0.8983	0.8762	0.8780	
Lift-to-Drag Ratio	23.1184	23.3884	22.7117	23.0110	1.71%

Table 4.8 Non-Planar Device 01 results – loiter, level flight (root chord $Re = 330141$).

Non-Planar Device 01 showed some hope with only a minor increase in drag and a more significant increase in lift, resulting in a coupled increase in the lift-to-drag ratio. With the pressure distribution found around the root of the winglet, it was thought that perhaps greater changes could be achieved by adjusting the cant angle. Also, by modifying the sweep of the winglet and somewhat increasing the overall surface area by modifying the chord distribution, it was thought that a greater moment could be generated at the tip to provide a sufficient amount of force to positively affect the tip vortices and perhaps generate useful aerodynamic forces. Non-Planar Device 01 was only tested in loiter, level flight before the design process moved on.

4.6 Non-Planar Device 02 (NPD-02)

As a direct follow-up design, a greater cant angle was sought to provide an added bit of wing bending moment [26]. This can be desirable if the designer seeks to slightly increase the amount of dihedral in the wing, among other things (as long as the design remains deeply seated within the structural envelope of the materials used in the fabrication process). Furthermore, the chord distribution would be altered in an effort to produce a greater amount of force over the winglet. The design is depicted in Figure 4.5 and the geometric parameters are given in Table 4.9. Some parameters are given two values: the first is the value nearest the winglet's root, the second value coming after the "break" evident in Figure 4.5. These compound values are due to a mid-chord station, positioned approximately two inches above the winglet's root.

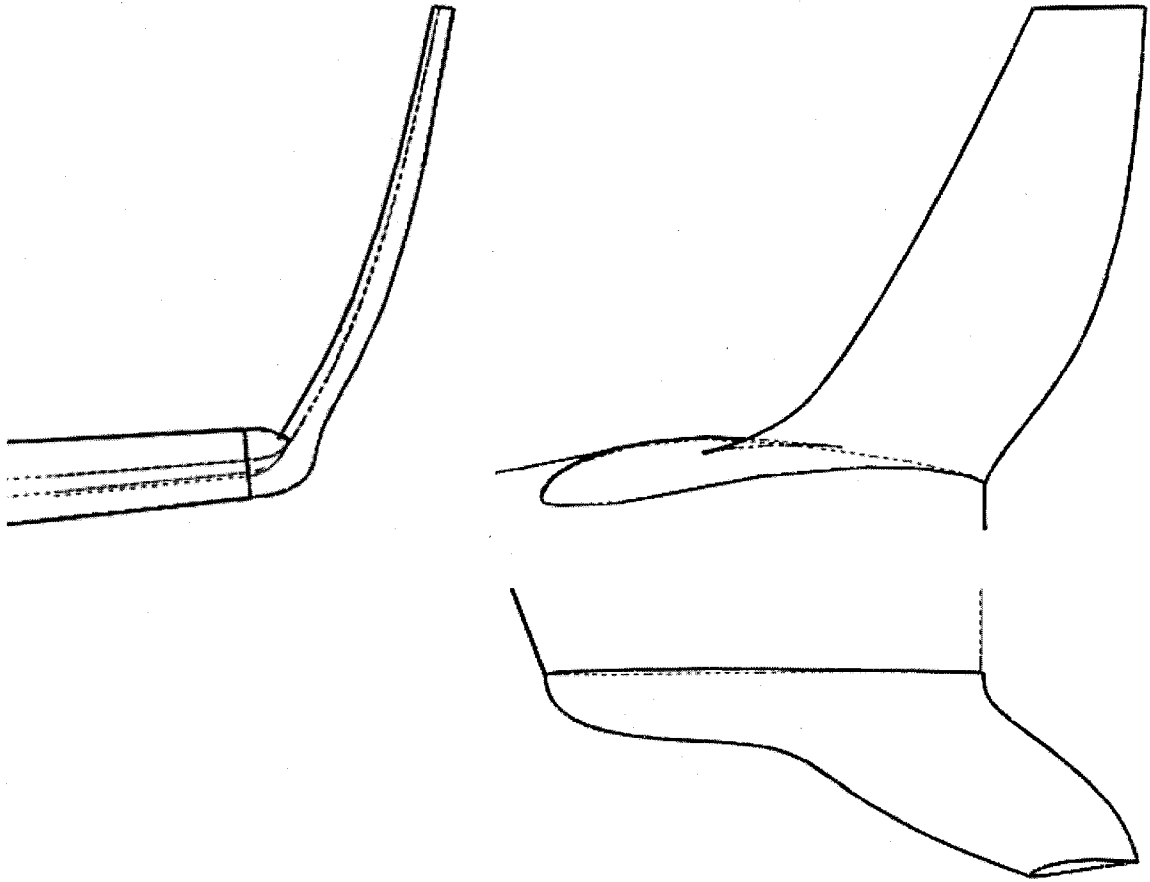


Figure 4.5 Non-Planar Device 02 configuration.

Winglet Geometry Parameter (NPD-02)	Magnitude
Winglet Root Chord [in]	6
Toe Angle [degrees]	3
Twist Angle [degrees]	3
Sweep Angle [degrees]	25
Cant Angle [degrees]	20, 15
Winglet Span [in]	6
Winglet Tip Chord [in]	2
Winglet Surface Area [m ²]	0.013764

Table 4.9 Non-Planar Device 02 – geometric parameters.

NON-PLANAR DEVICE 02	Test Section ($k-\epsilon$)	Test Section ($k-\omega$)	Control Specimen ($k-\epsilon$)	Control Specimen ($k-\omega$)	Average Percent Change Over Control
Drag Force [N]	2.1264	2.1040	2.2352	2.2106	-6.46%
Drag Coefficient	0.0361	0.0357	0.0386	0.0382	
Lift Force [N]	53.1357	53.2448	50.7654	50.8676	2.89%
Lift Coefficient	0.9016	0.9034	0.8762	0.8780	
Lift-to-Drag Ratio	24.9883	25.3070	22.7117	23.0110	10.00%

Table 4.10 Non-Planar Device 02 results – loiter, level Flight (root chord $Re = 330141$).

Non-Planar Device 02 truly exemplified what this study was after: proof that a non-planar device would be useful on a slow-moving craft such as a solar-powered UAV. In many cases it would be stated that the effort required to design such a device would outweigh the benefits from the start, but the numbers in Table 4.10 point to a very significant 10% increase in lift-to-drag ratio and a 6.46% decrease in drag. This design was selected to go through the next batch of tests, namely at -2, +2 and +4 degrees angle-of-attack at loiter speed. The results from these tests are outlined in Tables 4.11, 4.12 and 4.13.

Table 4.11 shows that NPD-02's performance gains are still valid at a shallow negative angle of attack, a desirable feature. While such an attribute may increase approach speed, the benefits outweigh the disadvantages. A -4.8% decrease in drag while moving from one thermal to another or as the plane aims to trade some energy height for distance would really pay off.

Table 4.12 and 4.13 show still an improvement over the control specimen, but not the same type of gains as in level flight. This was a bit of a disappointment but considering the winglet was designed for level flight, it is respectable. Revisiting the flight profile reveals that nearly 70% of the flight profile is predicted to occur in level, loitering flight. The designer should be reminded that the main aim is to minimize drag in a particular flight condition, and over the entire flight profile, or more importantly, to not incur any penalties by the adoption of a non-planar lifting device. NPD-02 succeeds in this respect.

NON-PLANAR DEVICE 02	Test Section ($k-\epsilon$)	Test Section ($k-\omega$)	Control Specimen ($k-\epsilon$)	Control Specimen ($k-\omega$)	Average Percent Change Over Control
Drag Force [N]	2.1704	2.1486	2.2432	2.2173	-4.82%
Drag Coefficient	0.0368	0.0365	0.0387	0.0383	
Lift Force [N]	40.8781	40.9329	40.0181	40.1176	0.35%
Lift Coefficient	0.6936	0.6945	0.6907	0.6925	
Lift-to-Drag Ratio	18.8343	19.0513	17.8397	18.0930	5.43%

Table 4.11 Non-Planar Device 02 results – loiter at -2° AOA (root chord Re = 330141).

NON-PLANAR DEVICE 02	Test Section ($k-\epsilon$)	Test Section ($k-\omega$)	Control Specimen ($k-\epsilon$)	Control Specimen ($k-\omega$)	Average Percent Change Over Control
Drag Force [N]	2.3282	2.2793	2.3601	2.3336	-3.51%
Drag Coefficient	0.0395	0.0387	0.0407	0.0403	
Lift Force [N]	63.8449	64.0498	61.5031	61.5969	2.13%
Lift Coefficient	1.0833	1.0867	1.0616	1.0632	
Lift-to-Drag Ratio	27.4229	28.1007	26.0589	26.3955	5.85%

Table 4.12 Non-Planar Device 02 results – loiter at +2° AOA (root chord Re = 330141).

NON-PLANAR DEVICE 02	Test Section ($k-\epsilon$)	Test Section ($k-\omega$)	Control Specimen ($k-\epsilon$)	Control Specimen ($k-\omega$)	Average Percent Change Over Control
Drag Force [N]	2.9472	2.8948	2.9974	2.9580	-3.57%
Drag Coefficient	0.0500	0.0491	0.0517	0.0511	
Lift Force [N]	73.0102	74.2135	70.5781	70.7610	2.39%
Lift Coefficient	1.2388	1.2592	1.2182	1.2214	
Lift-to-Drag Ratio	24.7725	25.6364	23.5460	23.9211	6.20%

Table 4.13 Non-Planar Device 02 results – loiter at +4° AOA (root chord Re = 330141).

4.7 Non-Planar Device 03 (NPD-03)

Non-Planar Device 03 sought to expand on NP-02's success. It was thought that perhaps a slightly greater chord distribution and, more importantly, a refined winglet tip might benefit the pressure distribution over the device. However, this had to be approached carefully since the local Reynolds number over the winglet was already quite low, but this was effectively countered by the increased chord distribution. It was initially thought that the aspect ratio of the winglet itself had gone down and that this would adversely affect the results. The geometry for Non-Planar Device 03 is outlined in Figure 4.6 and the parameters are given in Table 4.14.

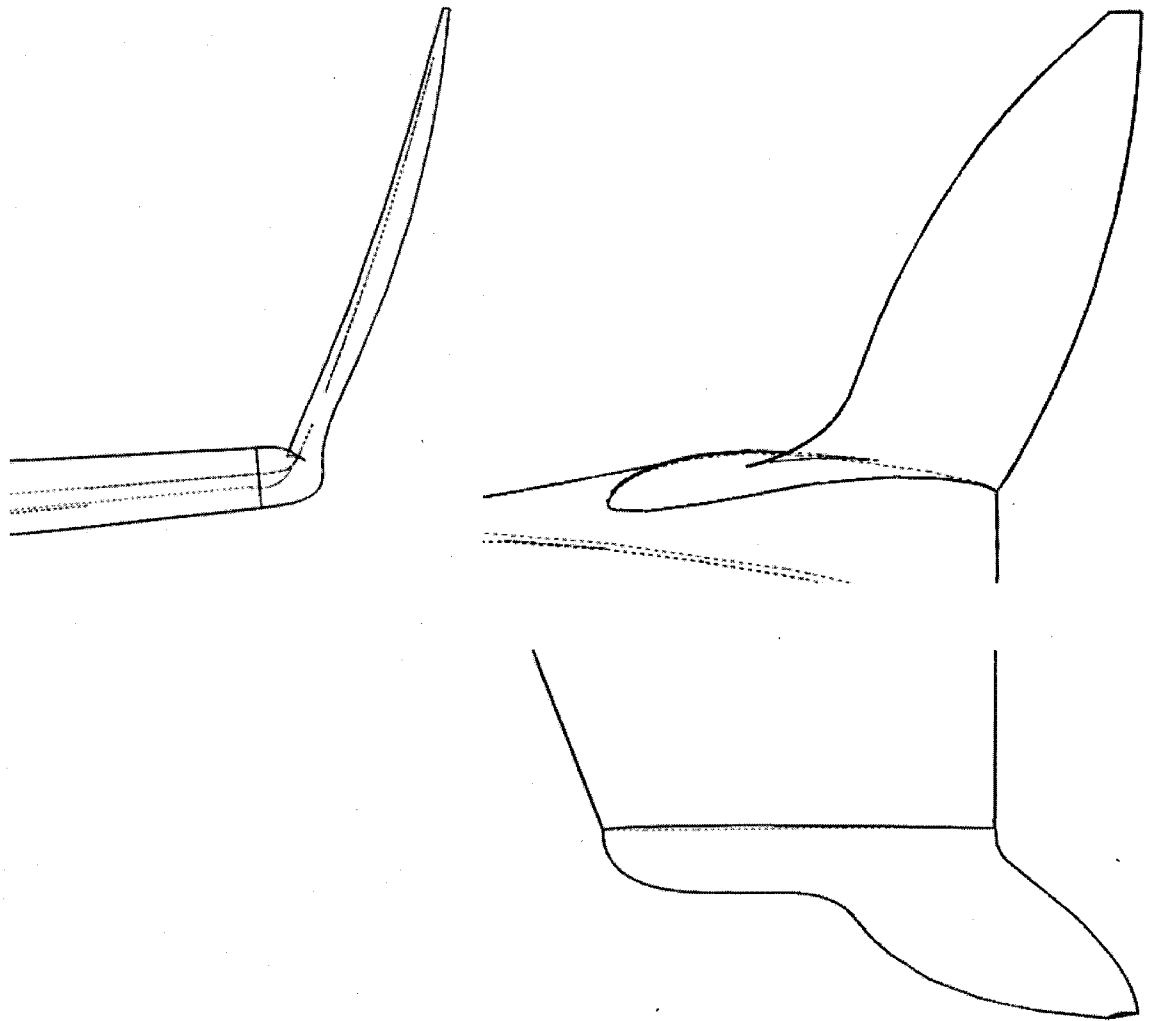


Figure 4.6 Non-Planar Device 03 configuration.

Winglet Geometry Parameter (NPD-03)	Magnitude
Winglet Root Chord [in]	6
Toe Angle [degrees]	3
Twist Angle [degrees]	3
Sweep Angle [degrees]	20
Cant Angle [degrees]	15
Winglet Span [in]	7
Winglet Tip Chord [in]	0.6
Winglet Surface Area [m ²]	0.015403

Table 4.14 Non-Planar Device 03 – geometric parameters.

The mid-chord was slightly enlarged and this resulted in a decrease in overall cant angle. While the changes made with NPD-03 were touted to improve performance, the overall surface area increase was greater than what was optimal. Also, it was found that although the winglet span had been increased, the aspect ratio had gone up because of the drastic increase in surface area. The boundary had been pushed a bit too far, as the results in Table 4.15 illustrate. The performance was a decrease from the previous iteration so it would be back to NPD-02 and with less drastic changes.

NON-PLANAR DEVICE 03	Test Section ($k-\epsilon$)	Test Section ($k-\omega$)	Control Specimen ($k-\epsilon$)	Control Specimen ($k-\omega$)	Average Percent Change Over Control
Drag Force [N]	2.1865	2.1601	2.2352	2.2106	-4.09%
Drag Coefficient	0.0370	0.0366	0.0386	0.0382	
Lift Force [N]	53.1284	53.1215	50.7654	50.8676	2.56%
Lift Coefficient	0.8996	0.8995	0.8762	0.8780	
Lift-to-Drag Ratio	24.2984	24.5917	22.7117	23.0110	6.93%

Table 4.15 Non-Planar Device 03 results – loiter, level Flight (root chord $Re = 330141$).

Non-Planar Device 03 illustrates how sensitive these devices can be to very subtle changes and perhaps best exemplifies why there are very few papers on the overall design practice of

such devices. While Raymer [29] is especially deft at drawing empirical relationships to prime a conceptual design, it would be much more difficult to establish such relationships for these non-planar devices, which are practically tailored to the wing's needs.

4.8 Non-Planar Device 04 (NPD-04)

Non-Planar Device 04 would be the last winglet design explored in the context of this study. NPD-03 showed that the aspect ratio of the winglet was a significant factor in its performance but the fact still remained that NP-02 could probably be improved by improving the taper ratio, or more specifically by refining the winglet's wingtip. Therefore, Non-Planar Device 02 was taken verbatim and was enhanced with a one inch span extension that would culminate in a similar tip as found on NPD-03, but without the chord redistribution. Figure 4.7 describes the configuration of the winglet while Table 4.16 lists the geometric parameters of NPD-04.

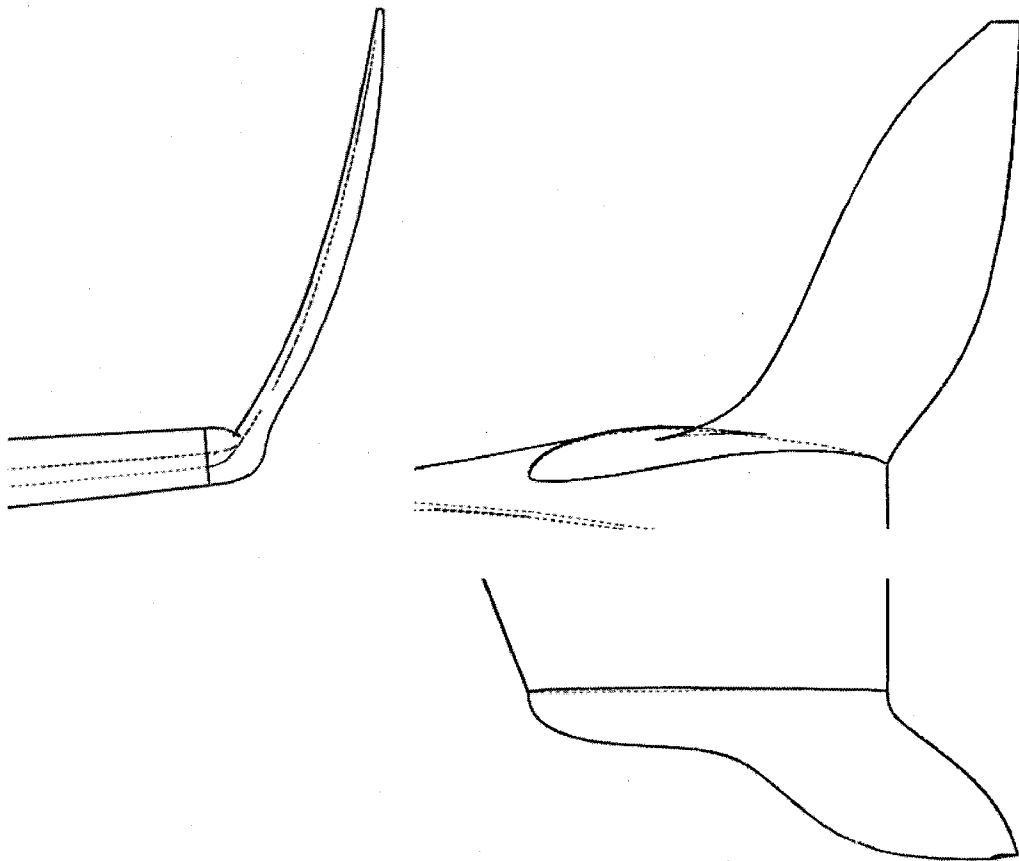


Figure 4.7 Non-Planar Device 04 configuration.

Winglet Geometry Parameter (NPD-04)	Magnitude
Winglet Root Chord [in]	6
Toe Angle [degrees]	3
Twist Angle [degrees]	3
Sweep Angle [degrees]	25
Cant Angle [degrees]	20, 15
Winglet Span [in]	7
Winglet Tip Chord [in]	0.6
Winglet Surface Area [m ²]	0.014391

Table 4.16 Non-Planar Device 04 – geometric parameters.

NON-PLANAR DEVICE 04	Test Section ($k-\epsilon$)	Test Section ($k-\omega$)	Control Specimen ($k-\epsilon$)	Control Specimen ($k-\omega$)	Average Percent Change Over Control
Drag Force [N]	2.1615	2.1232	2.2352	2.2106	-5.34%
Drag Coefficient	0.0366	0.0360	0.0386	0.0382	
Lift Force [N]	52.8974	53.0911	50.7654	50.8676	2.43%
Lift Coefficient	0.8968	0.9001	0.8762	0.8780	
Lift-to-Drag Ratio	24.4727	25.0050	22.7117	23.0110	8.21%

Table 4.17 Non-Planar Device 04 results – loiter, level Flight (root chord $Re = 330141$).

In loiter and level flight, NPD-04 offered similar performance increases to NPD-02, albeit not providing as great a difference. After analyzing the local Reynolds numbers over the winglet, it was found that the winglet tip Reynolds number was around 16,000, a value simply too low for the airfoil selected to produce any useful aerodynamic force. As a result, much of the tip extension translated into dead wetted area. Nonetheless, NPD-04 moved on to the next batch of testing. Tables 4.18, 4.19 and 4.20 outline the results obtained from these tests.

NPD-04 showed an overall decrease in performance and technically failed in reducing the overall drag in all flight profiles, although it did boost lift in all conditions. The inconsistency in percent change of the results from 0, to +2, to +4 degrees angle-of-attack is a bit suspect, but considering the range of the values, the simulation output is relatively well congregated.

NON-PLANAR DEVICE 04	Test Section ($k-\epsilon$)	Test Section ($k-\omega$)	Control Specimen ($k-\epsilon$)	Control Specimen ($k-\omega$)	Average Percent Change Over Control
Drag Force [N]	2.3427	2.2934	2.2432	2.2173	2.09%
Drag Coefficient	0.0397	0.0389	0.0387	0.0383	
Lift Force [N]	41.2520	41.6166	40.0181	40.1176	1.57%
Lift Coefficient	0.6994	0.7056	0.6907	0.6925	
Lift-to-Drag Ratio	17.6087	18.1459	17.8397	18.0930	-0.50%

Table 4.18 Non-Planar Device 04 results – loiter at -2° AOA (root chord Re = 330141).

NON-PLANAR DEVICE 04	Test Section ($k-\epsilon$)	Test Section ($k-\omega$)	Control Specimen ($k-\epsilon$)	Control Specimen ($k-\omega$)	Average Percent Change Over Control
Drag Force [N]	2.4438	2.3762	2.3601	2.3336	0.86%
Drag Coefficient	0.0414	0.0403	0.0407	0.0403	
Lift Force [N]	63.7398	63.8146	61.5031	61.5969	1.78%
Lift Coefficient	1.0806	1.0819	1.0616	1.0632	
Lift-to-Drag Ratio	26.0820	26.8562	26.0589	26.3955	0.92%

Table 4.19 Non-Planar Device 04 results – loiter at +2° AOA (root chord Re = 330141).

NON-PLANAR DEVICE 04	Test Section ($k-\epsilon$)	Test Section ($k-\omega$)	Control Specimen ($k-\epsilon$)	Control Specimen ($k-\omega$)	Average Percent Change Over Control
Drag Force [N]	3.0386	2.9864	2.9974	2.9580	-0.63%
Drag Coefficient	0.0515	0.0506	0.0517	0.0511	
Lift Force [N]	73.4231	74.0668	70.5781	70.7610	2.50%
Lift Coefficient	1.2448	1.2557	1.2182	1.2214	
Lift-to-Drag Ratio	24.1637	24.8018	23.5460	23.9211	3.16%

Table 4.20 Non-Planar Device 04 results – loiter at +4° AOA (root chord Re = 330141).

4.9 Final Candidate Discussion

Based on the preliminary runs, which was to run all design candidates at zero degree angle-of-attack, Non-Planar Devices 02 and 04 were chosen as the likeliest iterations to most benefit the aircraft's performance. Simulations were then run at -2, +2 and +4 degrees angle-of-attack to emulate various phases of flight projected for this particular airframe. The data collected in these tests was presented earlier but there is yet one final way to appreciate these results. By plotting the data against the original flight polars we can see how the flight dynamics of the plane are changed, if at all. We can also discern areas of concern, if there are any, and go back to the design to try to remedy these issues.

4.9.1 Drag Coefficient versus Angle-of-Attack

The main aim of this study was to decrease overall drag in all flight conditions. By plotting the averaged drag coefficients from the $k-\epsilon$ and $k-\omega$ models for the control and the candidates, we can appreciate the degree to which a reduction has been achieved, if at all, as in Figure 4.8.

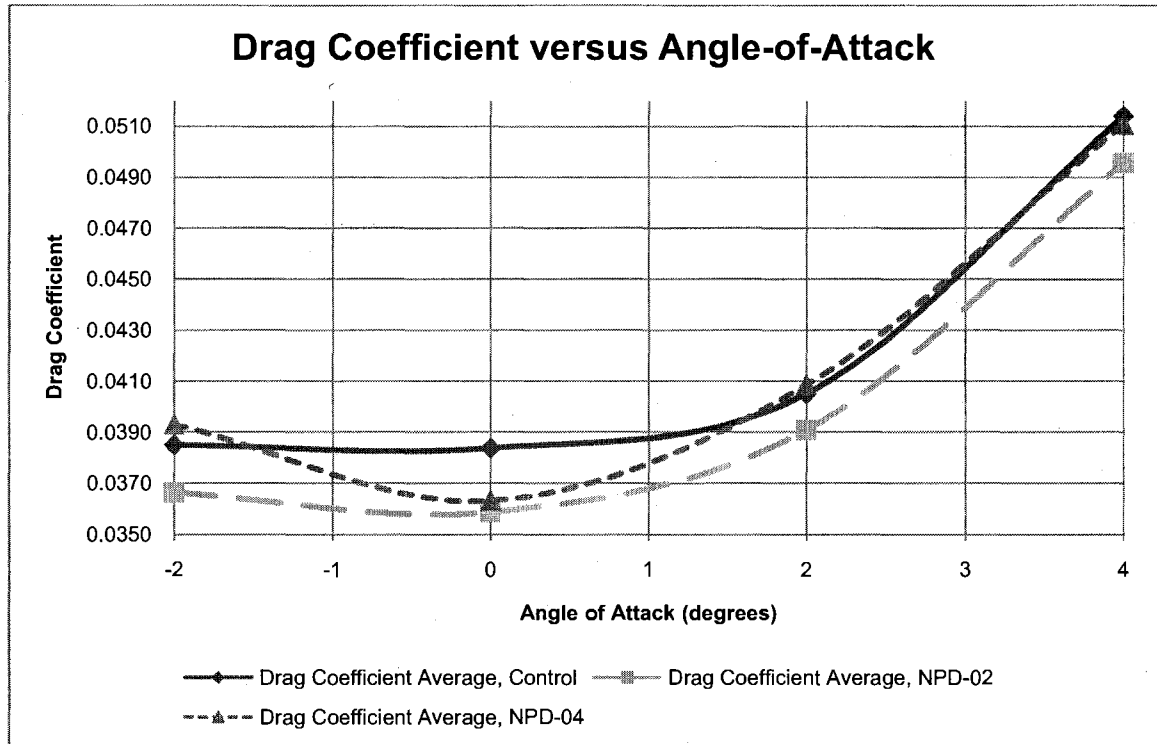


Figure 4.8 Drag coefficient versus angle-of-attack. While NPD-04's performance isn't bad, NPD-02 clearly surpasses it in all flight attitudes.

Non-Planar Device 04 offered the bulk of its drag improvement around zero degrees angle-of-attack, while Non-Planar Device 02 offered a similar drag improvement over the entire flight envelope tested for. In retrospect, the increase in drag in NPD-04 with respect to NPD-02 is most likely attributable to the winglet's tip extension. The extra one inch of span seems to make a significant difference here, and while this may seem a bit extreme it must be reminded that the winglet's original span was only six inches.

4.9.2 Lift Coefficient versus Angle-of-Attack

Another side-effect of the decrease in induced drag, or the harnessing of the wingtip vortices, is an increase in lift production over the main wingspan. While the winglet itself also generates lift, the component which it contributes to the overall lift force of the airplane is minute. The real benefit is in the increase in the main span efficiency. Figure 4.9 illustrates the averaged lift coefficients gathered from the $k-\epsilon$ and $k-\omega$ models.

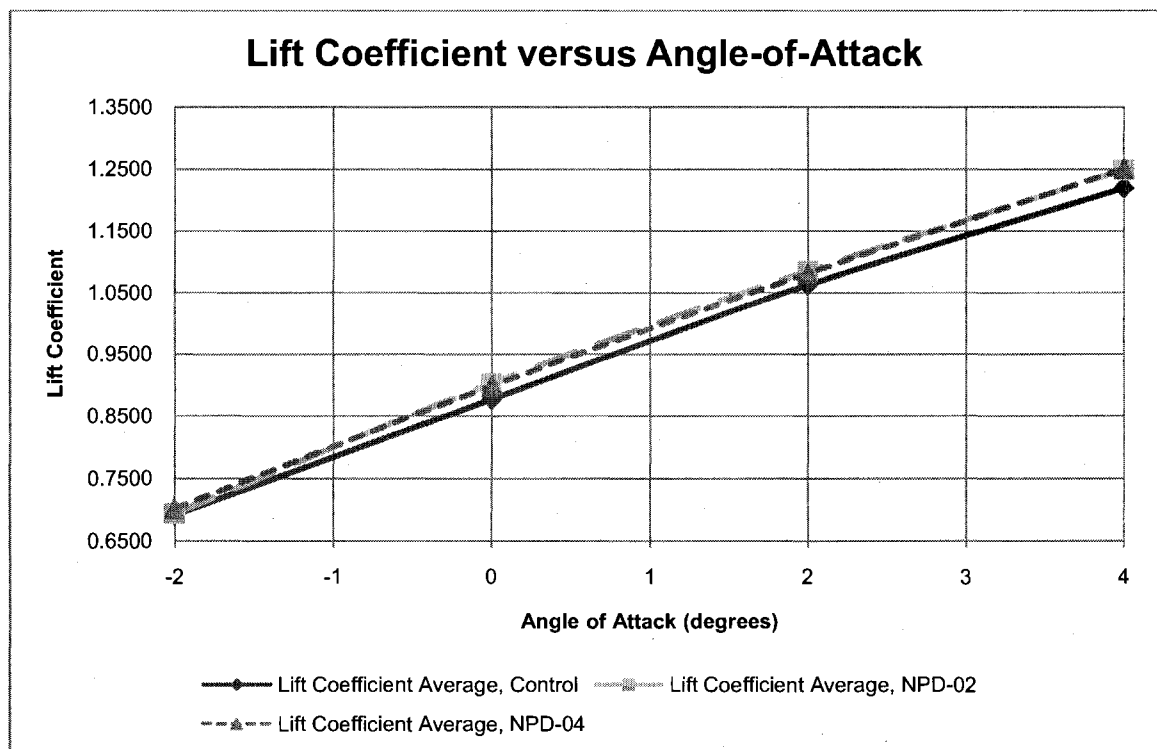


Figure 4.9 Lift coefficient versus angle-of-attack for the Wing Control Specimen along with NPD-02 and NPD-04.

In this case, both NPD-02 and NPD-04 see similar gains over the control. The reason for this is that both non-planar devices are practically identical at the root, providing the main wing with a similar type of support. In this respect, the two devices are nearly identical.

4.9.3 Lift-to-Drag Ratio versus Angle-of-Attack

The lift-to-drag ratio is a quantity of particular interest in the case of this aircraft due to its mission requirements. The lift-to-drag ratio is also widely known as the glide ratio and factors in strongly to the aircraft's sink rate. Figure 4.10 illustrates the lift-to-drag ratio as averaged from the $k-\epsilon$ and $k-\omega$ models for the control specimen along with the two candidates.

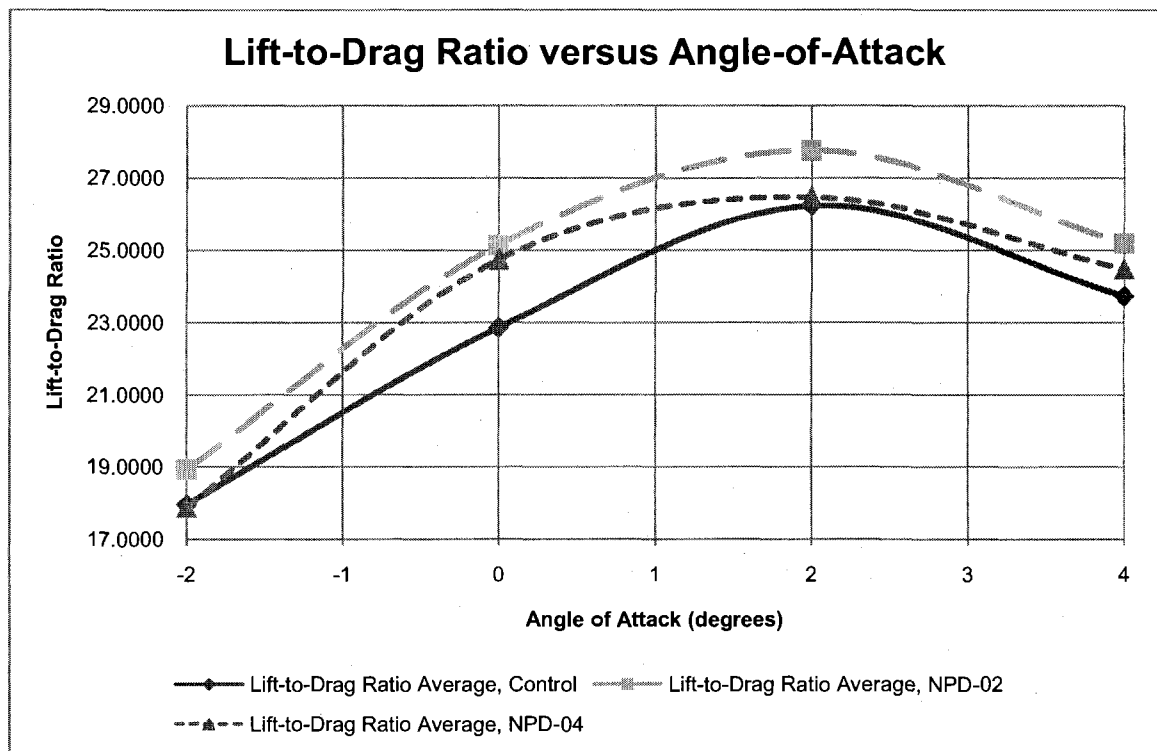


Figure 4.10 Lift-to-drag ratio versus angle-of-attack. Notice the significant improvements for NPD-02 over the control.

In this case, NPD-02 is the clear winner. With a 10% increase at 0 degree angle-of-attack, the device provides a significant improvement over the control specimen and this roughly translates in a 10% increase in allowable loiter time. This value alone should qualify NPD-02 to be incorporated into the aircraft, as the UAV's goal is to stay aloft for as long as possible

4.9.4 Lift Coefficient versus Drag Coefficient

The final category of interest is perhaps one of the more meaningful ones. By plotting the averaged lift and drag coefficients obtained from the $k-\epsilon$ and $k-\omega$ models against one another, we can easily visualize the gains made by incorporating these non-planar devices into the airframe with respect to the two main variables recorded during the study. Figure 4.11 represents this plot.

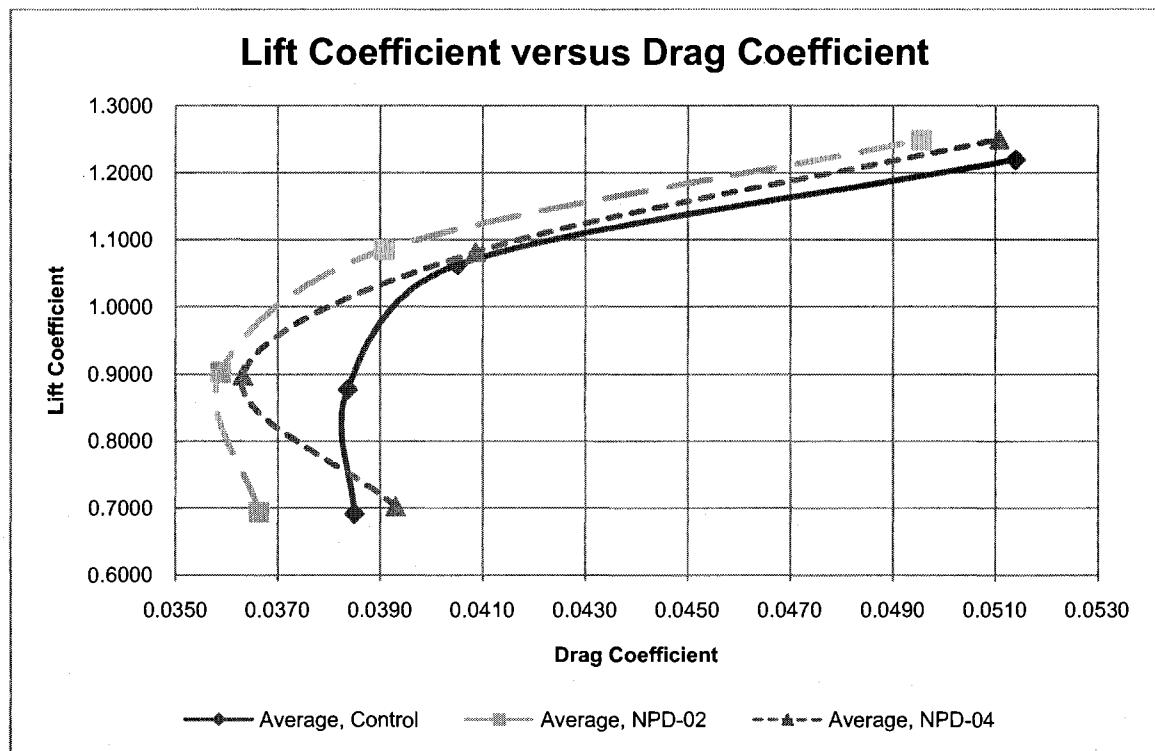


Figure 4.11 Lift coefficient versus drag coefficient. Again, NPD-02 emerges as the clear-cut winner. NPD-04 shows signs of brilliance at its maximum L/D but its advantage dissipates further on.

As with the previous plot, NPD-02 comes through and performs brilliantly over the entire flight envelope. As such, without any further iterations and barring additional testing, NPD-02 should be cleared for incorporation into the UNLV solar-powered UAV. The structural ramifications of incorporating this device should be nearly trivial: the overall added surface area is 0.027 m^2 per winglet, translating in roughly 0.144 kg of added mass at the tip, assuming a particularly sloppy composite job.

CHAPTER 5

WING-FUSELAGE JUNCTION SIMULATION ANALYSIS

5.1 Introduction

The data recorded in Appendix D is presented here in an abbreviated format that allows quick assessment of the wing-fuselage junction designs as they evolved. Appendix D also includes several additional illustrations of each model and for a more detailed overview of the models it is recommended that Appendix D be viewed along with the descriptions carried within this chapter. As outlined in Chapter Three, the momentum method was used to compute the overall drag acting upon the system. Lift production was computed by integrating the boundary pressure distributions over the lifting surfaces. The data from both the $k-\varepsilon$ and $k-\omega$ models is presented but it was generally observed that the $k-\omega$ model represented the flow around the object more accurately. All figures depicting pressure or velocity fields in Appendix D are taken from the $k-\omega$ simulations. The benchmarks for all of these designs were in primary fashion the control specimen, and in secondary fashion the previous iteration of the design.

5.2 Wing-Fuselage Junction Control Specimen

The control specimen for the wing-fuselage junction is the fuselage and wing configuration with no wing-fuselage junction fairing of any kind: the wing simply protrudes from the body of the plane. This is a simple but common arrangement, especially at the scale at which this particular airframe is built. The results from the control will act as the benchmark for the future designs but whereas the data from the wingtip device analysis was initially validated by other methods, it is not the case here and as such is a purely comparative analysis. Figure 5.1 illustrates the arrangement of the control specimen for the wing-fuselage junction testing. Appendix C covers the results gathered from the wing-fuselage junction control specimen simulations.

The origin for all the wing-fuselage junction designs is at the plane's nose, a point which also coincided with the origin for all the subsequent assemblies for the project. Since the fuselage design would not be changed during the wing-fuselage junction study, this seemed a natural choice. The fuselage itself is 70 inches long and the wing's root chord is 12 inches. A length of four inches spanning from the centerline has been allocated for the development and design of the wing-fuselage junction.

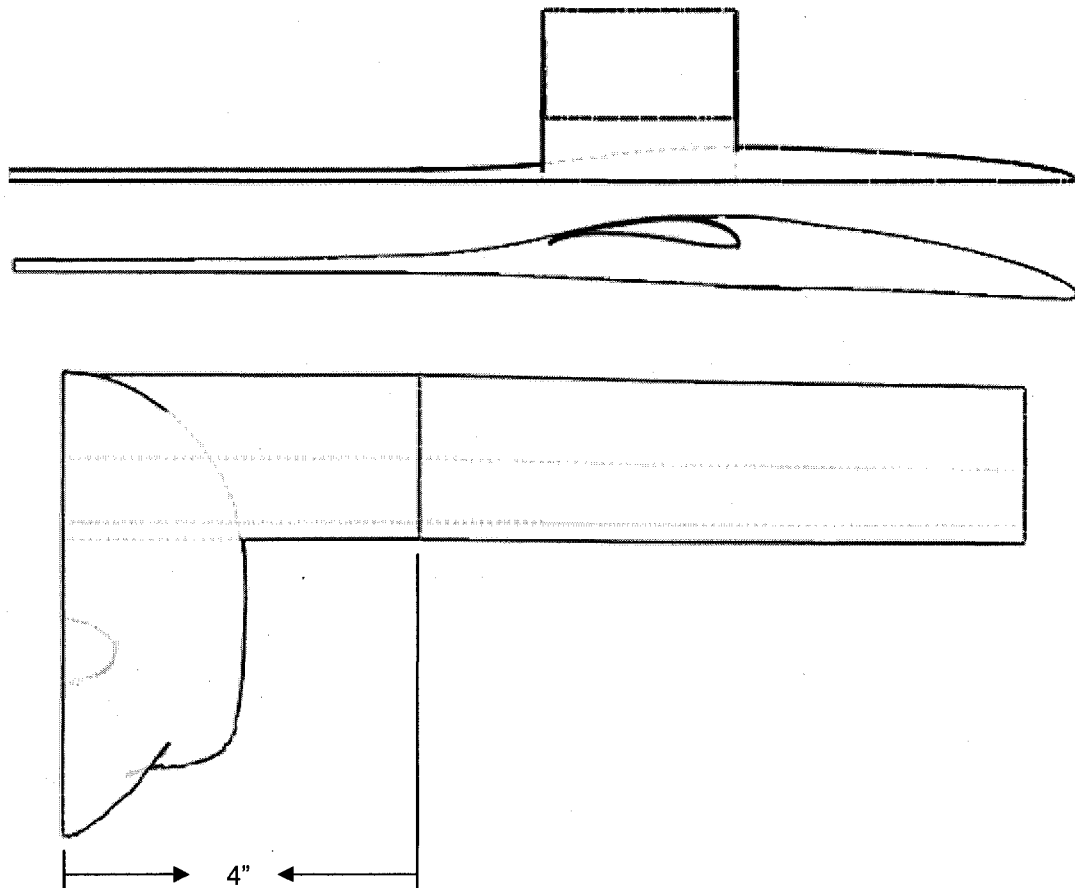


Figure 5.1 Wing-fuselage junction control specimen diagram (top, side and front views). The linear demarcation in the wing denotes the allocated space for the wing-fuselage junction (four inches from the fuselage centerline). In the control case, the wing's root is not faired to the fuselage in any way.

Table 5.1 outlines the key values recorded in the control specimen tests. In effect, the main value of interest was the drag coefficient although other important values would also be recorded. The lift coefficient near the root is directly affected by the design of the fuselage and furthermore,

the wing-fuselage junction. Both of these values are simultaneously affected by the junction's surface area. Data from this model was gathered in several flight attitudes, namely 0, +2 and +4 degrees angle-of-attack, all of which are associated with a certain phase of the UAV's flight profile. Data from -2° angle-of-attack was omitted due to a bug in the COMSOL software in which the geometry could not properly be imported, an issue which still remains unresolved. In Table 5.1, the coefficient of lift is given for the junction and its surface area, the wing section and its corresponding surface area, and finally the total lift is used to find the overall lift coefficient for the model, which includes the fuselage's wetted area and explains the significantly lower figures. This measure was in an effort to provide consistency with the drag coefficient, a reading which accounts for the entire model as well.

WING-FUSELAGE JUNCTION CONTROL SPECIMEN		$C_{L, \text{ junction}}$	$C_{L, \text{ wing section}}$	$C_{L, \text{ model}}$	$C_{D, \text{ model}}$
0° AOA	$(k-\varepsilon)$	0.5786	1.1477	0.3527	0.0114
	$(k-\omega)$	0.5802	1.1522	0.3539	0.0113
	<i>Average</i>	0.5794	1.1500	0.3533	0.0114
+2° AOA	$(k-\varepsilon)$	0.6370	1.3534	0.4098	0.0128
	$(k-\omega)$	0.6374	1.3608	0.4116	0.0127
	<i>Average</i>	0.6372	1.3571	0.4107	0.0128
+4° AOA	$(k-\varepsilon)$	0.7083	1.5455	0.4654	0.0159
	$(k-\omega)$	0.7102	1.5457	0.4657	0.0158
	<i>Average</i>	0.7093	1.5456	0.4655	0.0159

Table 5.1 Wing-Fuselage Junction Control Specimen data, loiter speed (root Re = 330141).

5.3 Linear Wing-Fuselage Junction 01 (LWJ-01)

The first wing-fuselage junction designed would be a linear fairing of the most extreme simplicity. The S1223 airfoil profile of the wing root was transposed onto the centerline plane and scaled accordingly. The coordinates for this airfoil section and thousands of others are available

through [30]. Figure 5.2 illustrates the configuration of LWJ-01. The centerline profile is highlighted. This particular design aimed to get an overall feel for the information relayed in [23], in particular, although the junction is not smoothly faired to the wing and the fuselage as it is in Maughmer's study [19].

The placement of LWJ-01 and other geometric parameters are listed in Table 5.2. The performance of LWJ-01 is outlined in Table 5.3. While these numbers were thought to be quite respectable, it was hoped that further progress could be made with the next iterations.

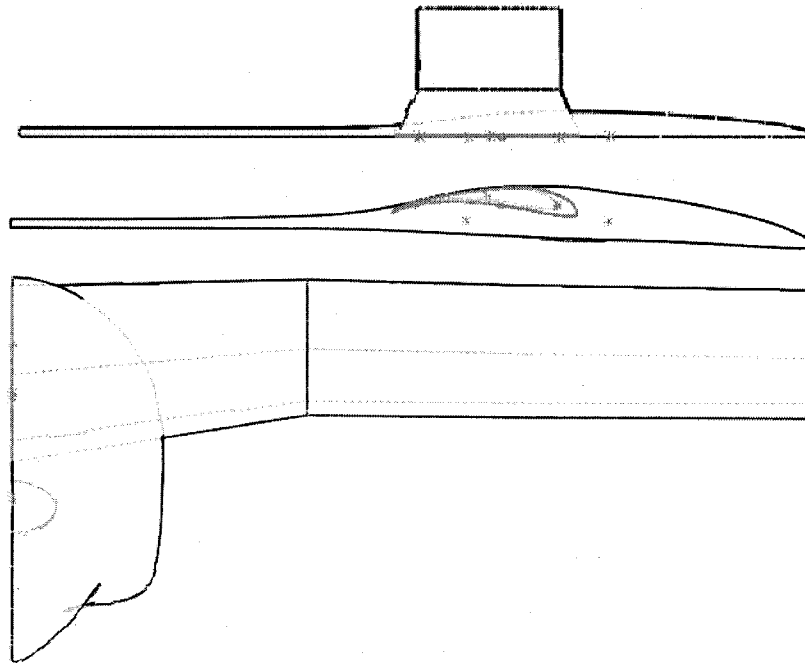


Figure 5.2 Linear Wing-Fuselage Junction 01's configuration. Notice the deliberate placement of the centerline profile, sitting slightly lower than the wing.

LWJ-01 Geometry Parameters	Value
Junction Type	Linear
Junction Centerline Profile	S1223
Centerline Chord Length [in]	15.6
Centerline Profile Twist Angle [degrees]	0
Centerline Profile Leading Edge Z-Position [in]	19.84
Centerline Profile Leading Edge Y-Position [in]	2.63
Surface Area Increase Over Control [m ²]	0.004283

Table 5.2 Basic geometric parameters for Linear Wing-Fuselage Junction 01.

LINEAR WING-FUSELAGE JUNCTION 01	Test Section ($k-\epsilon$)	Test Section ($k-\omega$)	Control Specimen ($k-\epsilon$)	Control Specimen ($k-\omega$)	Average Percent Change Over Control
Junction Lift Force [N]	4.4754	4.4973	4.1736	4.1853	-1.21%
Junction Lift Coefficient	0.5710	0.5738	0.5786	0.5802	
Wing Section Lift Force [N]	15.2255	15.2846	14.7667	14.8246	3.11%
Wing Section Lift Coefficient	1.1834	1.1880	1.1477	1.1522	
Overall Lift Force [N]	19.7010	19.7819	18.9403	19.0099	4.04%
Overall Lift Coefficient	0.3647	0.3662	0.3527	0.3539	
Drag Force [N]	0.6087	0.6032	0.6140	0.6078	-1.89%
Drag Coefficient	0.01127	0.01117	0.01143	0.01132	

Table 5.3 Linear Wing-Fuselage Junction 01 - loiter, level flight (root Re = 330141).

The increase in lift came from the increase in chord near the root, allowing for a higher Reynolds number and thus increased lift. There was a decrease in drag in this case and it was believed that a yet greater decrease in drag coefficient, and more importantly in drag force, could be attained. Nonetheless, this configuration was studied in further detail at +2 and +4 degrees angle-of-attack, the results of which are presented in Tables 5.4 and 5.5.

LINEAR WING-FUSELAGE JUNCTION 01	Test Section ($k-\epsilon$)	Test Section ($k-\omega$)	Control Specimen ($k-\epsilon$)	Control Specimen ($k-\omega$)	Average Percent Change Over Control
Junction Lift Force [N]	4.9477	4.9467	4.5954	4.5976	-0.95%
Junction Lift Coefficient	0.6312	0.6311	0.6370	0.6374	
Wing Section Lift Force [N]	17.7523	17.7804	17.4125	17.5083	1.75%
Wing Section Lift Coefficient	1.3798	1.3820	1.3534	1.3608	
Overall Lift Force [N]	22.7000	22.7270	22.0079	22.1059	2.98%
Overall Lift Coefficient	0.4202	0.4207	0.4098	0.4116	
Drag Force [N]	0.7352	0.7298	0.6893	0.6832	5.64%
Drag Coefficient	0.01361	0.01351	0.01283	0.01272	

Table 5.4 Linear Wing-Fuselage Junction 01 - loiter, +2° AOA (root Re = 330141).

LINEAR WING-FUSELAGE JUNCTION 01	Test Section ($k-\epsilon$)	Test Section ($k-\omega$)	Control Specimen ($k-\epsilon$)	Control Specimen ($k-\omega$)	Average Percent Change Over Control
Junction Lift Force [N]	5.4987	5.5231	5.1094	5.1234	-0.87%
Junction Lift Coefficient	0.7015	0.7046	0.7083	0.7102	
Wing Section Lift Force [N]	20.0936	20.1455	19.8845	19.8871	1.18%
Wing Section Lift Coefficient	1.5618	1.5658	1.5455	1.5457	
Overall Lift Force [N]	25.5923	25.6685	24.9939	25.0105	2.51%
Overall Lift Coefficient	0.4737	0.4751	0.4654	0.4657	
Drag Force [N]	0.9123	0.9068	0.8550	0.8488	5.76%
Drag Coefficient	0.01689	0.01678	0.01592	0.01580	

Table 5.5 Linear Wing-Fuselage Junction 01 - loiter, +4° AOA (root Re = 330141).

An increase in angle-of-attack yielded a very substantial increase in lift. This can most likely be attributed to two factors. The first is the increased projected frontal area when the aircraft is at some angle-of-attack other than zero. The second is the increased chord length. While nearly all the lift categories see some type of increase, with an unoptimized increased lift production will come with a greater drag component (at least in this particular case). LWJ-01 was subsequently discarded, but not before it had achieved final candidacy based on its early performance.

5.4 Linear Wing-Fuselage Junction 02 (LWJ-02)

In an attempt to improve on LWJ-01, the same centerline profile used in Linear Wing-Fuselage Junction 01 would be used but brought forward slightly in an effort to smooth out the flow before it reaches the wing's leading edge while eliminating the trailing edge fairing. Figure 5.3 illustrates LWJ-02's configuration.

This design again employed the S1223 profile on the centerline. Essentially, the only design difference between LWJ-01 and LWJ-02 is the placement of fairing on the centerline plane. The geometric parameters can be found in Table 5.6. Moving the fairing forward resulted in a minute

increase in overall surface area for the junction. Table 5.7 outlines the recorded performance of LWJ-02 in loiter, level flight.

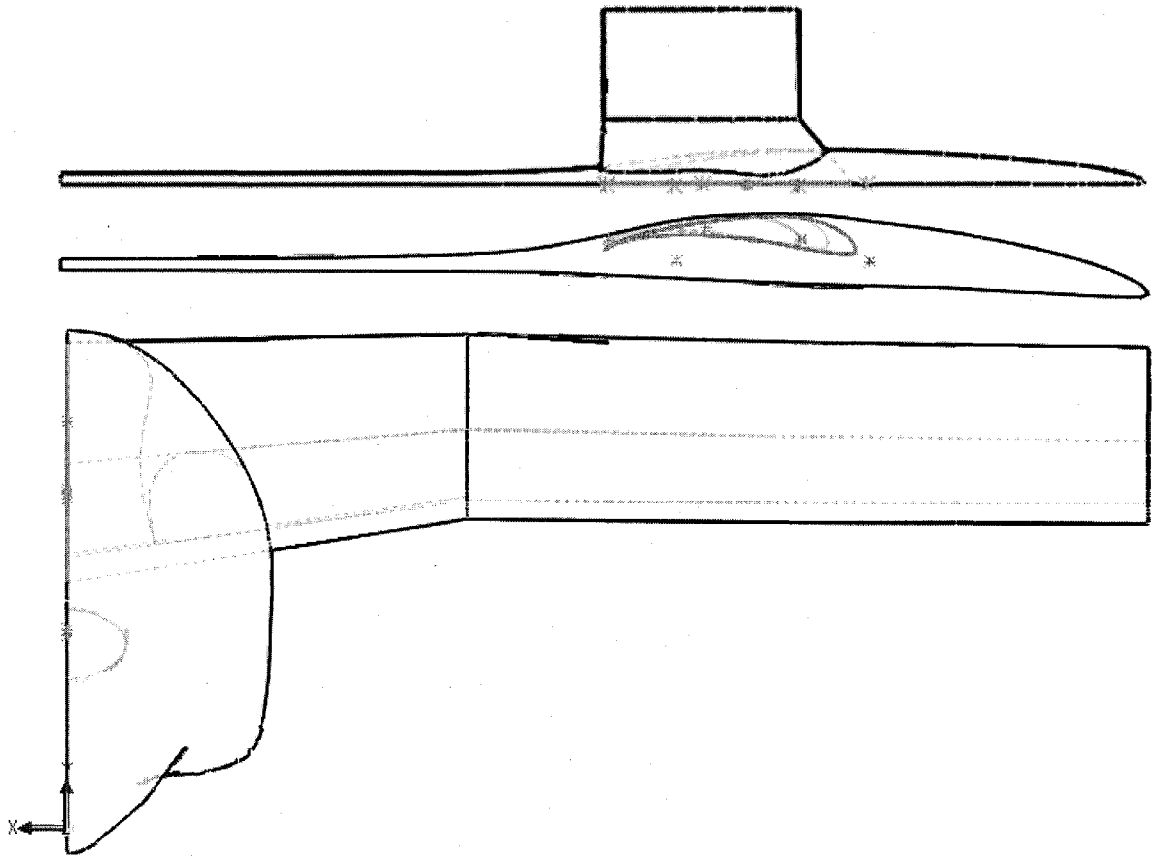


Figure 5.3 Linear Wing-Fuselage Junction 02 configuration.

LWJ-02 Geometry Parameters	Value
Junction Type	Linear
Junction Centerline Profile	S1223
Centerline Chord Length [in]	15.6
Centerline Profile Twist Angle [degrees]	0
Centerline Profile Leading Edge Z-Position [in]	18.12
Centerline Profile Leading Edge Y-Position [in]	2.63
Surface Area Increase Over Control [m ²]	0.001189

Table 5.6 Basic geometric parameters for Linear Wing-Fuselage Junction 02.

LINEAR WING-FUSELAGE JUNCTION 02	Test Section ($k-\epsilon$)	Test Section ($k-\omega$)	Control Specimen ($k-\epsilon$)	Control Specimen ($k-\omega$)	Average Percent Change Over Control
Junction Lift Force [N]	4.2801	4.3000	4.1736	4.1853	0.24%
Junction Lift Coefficient	0.5794	0.5821	0.5786	0.5802	
Wing Section Lift Force [N]	15.3336	15.3892	14.7667	14.8246	3.82%
Wing Section Lift Coefficient	1.1918	1.1961	1.1477	1.1522	
Overall Lift Force [N]	19.6136	19.6892	18.9403	19.0099	3.56%
Overall Lift Coefficient	0.3652	0.3666	0.3527	0.3539	
Drag Force [N]	0.6068	0.6024	0.6140	0.6078	-1.52%
Drag Coefficient	0.01130	0.01122	0.01143	0.01132	

Table 5.7 Linear Wing-Fuselage Junction 02 – loiter, level flight (root $Re = 330141$).

The second iteration of the linear junction design did not yield the expected results. While the performance of LWJ-02 was close to its predecessor's, the design was dropped in favor of exploring future designs. If the planform was to be linear, LWJ-01 simply performed better and would be a better candidate for the next iteration. At this point in the design study, the first non-linear planform would be developed and tested.

5.5 Non-Linear Wing-Fuselage Junction 01 (NLWJ-01)

While [13] and [23] both stated that non-linear planforms were detrimental to the overall drag performance, such a configuration was still sought for testing purposes. NLWJ-01 was the result of the first of such a design, which started with the same arrangement as LWJ-01 but used a constraint on the ending face of the loft, by specifying a “normal-to-profile” condition on the wing's root airfoil profile. This gave a non-linear loft but it is not parabolic in nature, as opposed to [23] where the shape of the leading edge fairing is parabolic in top-down projected view. Nonetheless, this should allow for a direct comparison between two otherwise similar configurations. Figure 5.4 illustrates the configuration for Non-Linear Wing-Fuselage Junction 01. Table 5.8 outlines the geometric parameters that describe the junction.

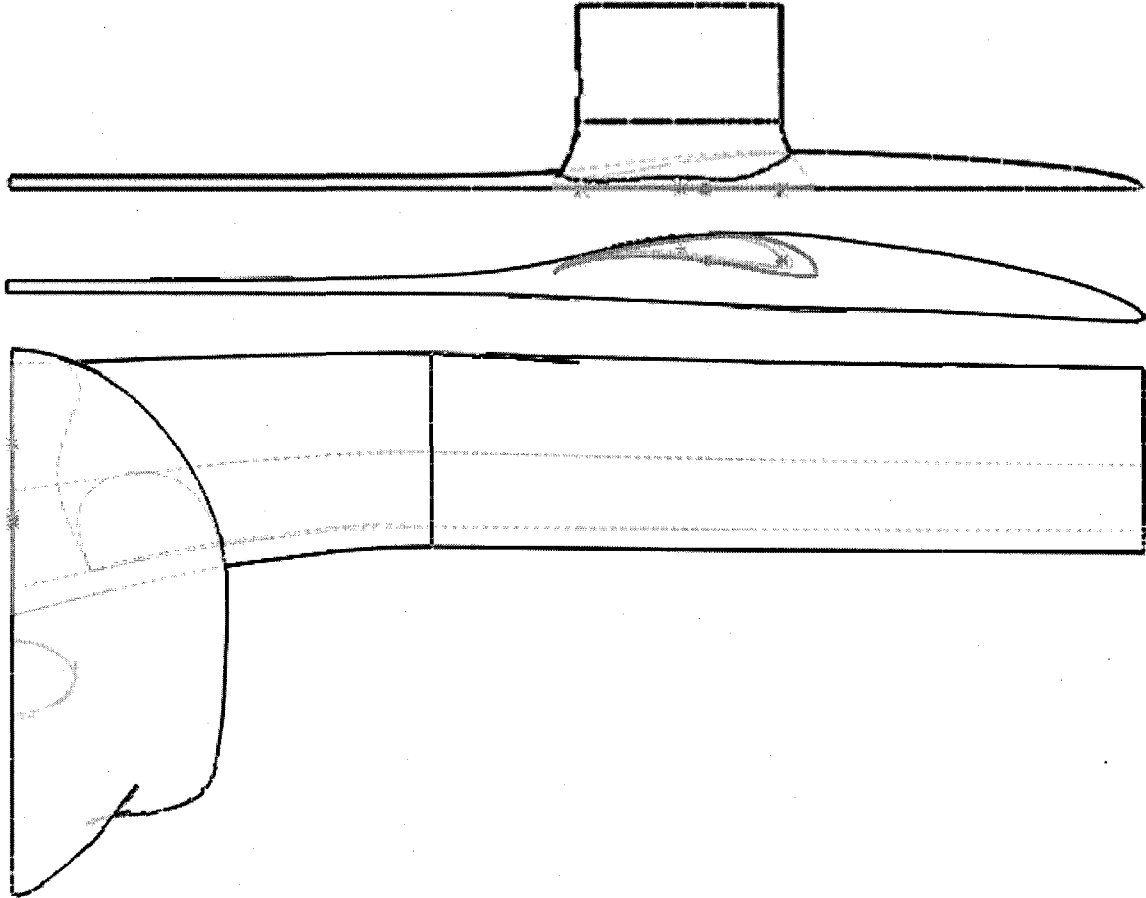


Figure 5.4 Non-Linear Wing-Fuselage Junction 01 configuration.

NLWJ-01 Geometry Parameters	Value
Junction Type	Non-Linear
Loft Starting Constraint (Loft starts at the centerline)	None
Loft Ending Constraint	Normal to Profile
Junction Centerline Profile	S1223
Centerline Chord Length [in]	15.6
Centerline Profile Twist Angle [degrees]	0
Centerline Profile Leading Edge Z-Position [in]	19.43
Centerline Profile Leading Edge Y-Position [in]	2.61
Junction Surface Area Increase Over Control [m ²]	0.000979

Table 5.8 Basic geometric parameters for Non-Linear Wing-Fuselage Junction 01.

Since LWJ-02 showed no gains with respect to placing the centerline profile forward, NLWJ-01 used the centered profile placement as LWJ-01 did. Table 5.9 lists the performance attributes obtained from the simulation for this design.

NON-LINEAR WING-FUSELAGE JUNCTION 01	Test Section ($k-\epsilon$)	Test Section ($k-\omega$)	Control Specimen ($k-\epsilon$)	Control Specimen ($k-\omega$)	Average Percent Change Over Control
Junction Lift Force [N]	4.3547	4.3745	4.1736	4.1853	2.40%
Junction Lift Coefficient	0.5920	0.5947	0.5786	0.5802	
Wing Section Lift Force [N]	15.2483	15.3013	14.7667	14.8246	3.24%
Wing Section Lift Coefficient	1.1852	1.1893	1.1477	1.1522	
Overall Lift Force [N]	19.6030	19.6757	18.9403	19.0099	3.50%
Overall Lift Coefficient	0.3640	0.3653	0.3527	0.3539	
Drag Force [N]	0.5930	0.5889	0.6140	0.6078	-4.01%
Drag Coefficient	0.01101	0.01094	0.01143	0.01132	

Table 5.9 Non-Linear Wing-Fuselage Junction 01 – loiter, level flight (root Re = 330141).

This particular wing-fuselage junction performed better than the previous attempts and certainly better than expected. While the literature would not agree with these results, there are some glaring differences which categorically eliminate the ability to compare between studies. Most importantly, the fairing only operates on the leading and trailing edges and not on the top and bottom surfaces of the airfoil against the fuselage's surface. Additionally, the linear planforms presented in [23] are smoothly blended into the wing and fuselage. In other words, the method presented here is only a leading and trailing edge fillet, as in [13]. Fairing against the fuselage's body was deemed unnecessary primarily because it would increase projected frontal area. Observations were noted as these tests progressed: for example, it was observed in the testing for LWJ-02 that a greater sweep angle on the fairing resulted in a decrease in overall performance, this probably due to the low operating Reynolds number. In light of the satisfactory

performance of NLWJ-01, an additional battery of tests was desired, the results of which are presented in Tables 5.10 and 5.11.

NON- LINEAR WING-FUSELAGE JUNCTION 01	Test Section ($k-\epsilon$)	Test Section ($k-\omega$)	Control Specimen ($k-\epsilon$)	Control Specimen ($k-\omega$)	Average Percent Change Over Control
Junction Lift Force [N]	4.7704	4.7912	4.5954	4.5976	1.99%
Junction Lift Coefficient	0.6485	0.6513	0.6370	0.6374	
Wing Section Lift Force [N]	17.6250	17.6402	17.4125	17.5083	0.99%
Wing Section Lift Coefficient	1.3699	1.3711	1.3534	1.3608	
Overall Lift Force [N]	22.3954	22.4314	22.0079	22.1059	1.62%
Overall Lift Coefficient	0.4158	0.4165	0.4098	0.4116	
Drag Force [N]	0.6807	0.6736	0.6893	0.6832	-2.03%
Drag Coefficient	0.01264	0.01251	0.01283	0.01272	

Table 5.10 Non-Linear Wing-Fuselage Junction 01 – loiter, +2° AOA (root Re = 330141).

NON- LINEAR WING-FUSELAGE JUNCTION 01	Test Section ($k-\epsilon$)	Test Section ($k-\omega$)	Control Specimen ($k-\epsilon$)	Control Specimen ($k-\omega$)	Average Percent Change Over Control
Junction Lift Force [N]	5.3261	5.3300	5.1094	5.1234	2.12%
Junction Lift Coefficient	0.7240	0.7245	0.7083	0.7102	
Wing Section Lift Force [N]	19.9801	19.9815	19.8845	19.8871	0.48%
Wing Section Lift Coefficient	1.5529	1.5531	1.5455	1.5457	
Overall Lift Force [N]	25.3061	25.3115	24.9939	25.0105	1.23%
Overall Lift Coefficient	0.4699	0.4700	0.4654	0.4657	
Drag Force [N]	0.8646	0.8557	0.8550	0.8488	0.33%
Drag Coefficient	0.01605	0.01589	0.01592	0.01580	

Table 5.11 Non-Linear Wing-Fuselage Junction 01 – loiter, +4° AOA (root Re = 330141).

The results within the previous two tables show an increasing drag coefficient with angle-of-attack with a coinciding lift gain, again contributable to the increase in chord length at the root.

The explanation for the still desirable drag decrease, as opposed to LWJ-01, is in the decreased amount of surface area of the leading edge fillet and thus the overall decreased projected frontal area due to the shaping of the fairing itself.

5.6 Non-Linear Wing-Fuselage Junction 02 (NLWJ-02)

For the second non-linear iteration, the centerline profile would be given a slight amount of negative twist in an attempt to lessen the drag produced by the junction. The direct disadvantage to this approach is a loss in lift production and an increased root-stall tendency, but it was thought that these minuses could be outweighed by a potentially significant drag decrease. Additionally, a slightly different centerline profile placement would be used to give the junction some dihedral. Figure 5.5 outlines the configuration for NLWJ-02.

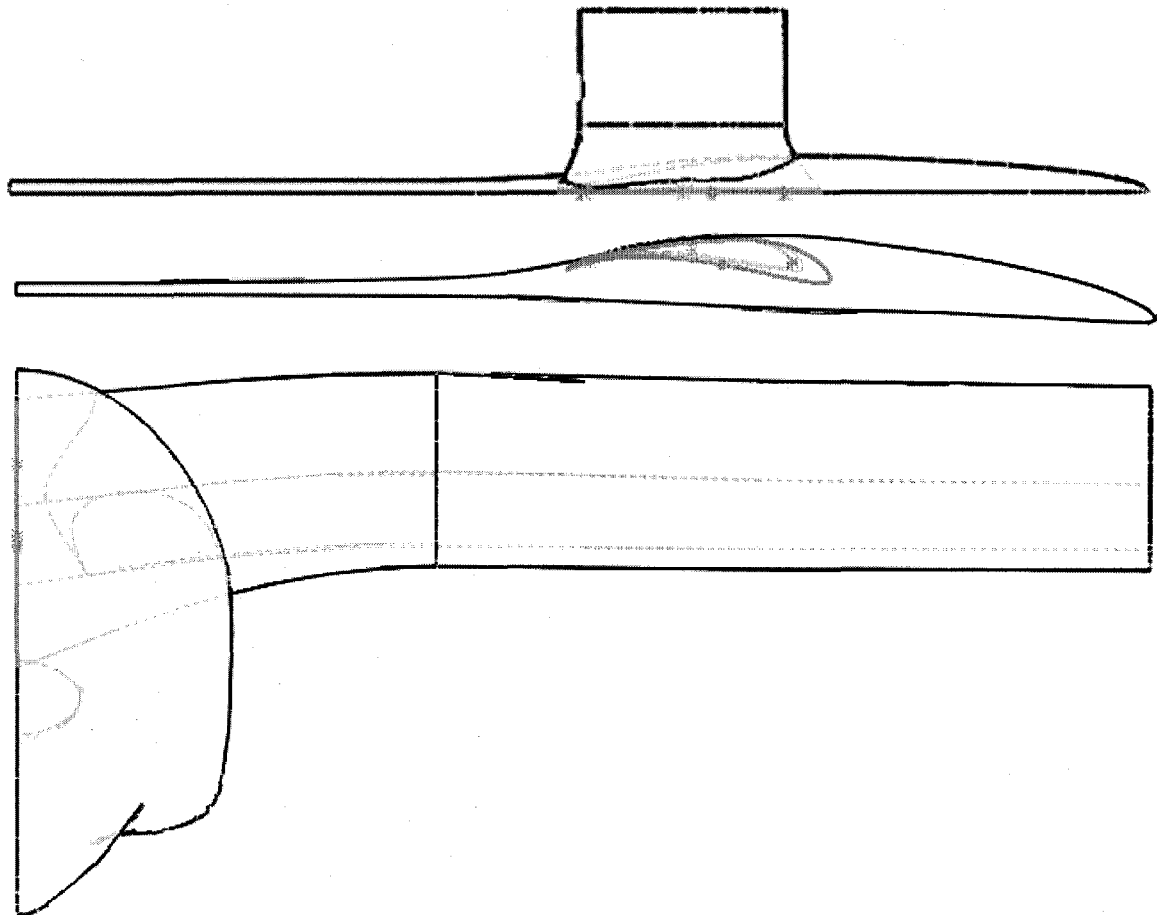


Figure 5.5 Non-Linear Wing-Fuselage Junction 02 configuration.

Table 5.12 outlines the geometric parameters used to create NLWJ-02. The most significant change from NLWJ-01 is the negative twist angle, as described previously. Table 5.13 lists the performance values recorded for this particular design.

NLWJ-02 Geometry Parameters	Value
Junction Type	Non-Linear
Loft Starting Constraint (Loft starts at the centerline)	None
Loft Ending Constraint	Normal to Profile
Junction Centerline Profile	S1223
Centerline Chord Length [in]	15.6
Centerline Profile Twist Angle [degrees]	-2
Centerline Profile Leading Edge Z-Position [in]	19.28
Centerline Profile Leading Edge Y-Position [in]	2.30
Junction Surface Area Increase Over Control [m ²]	0.000640

Table 5.12 Basic geometric parameters for Non-Linear Wing-Fuselage Junction 02.

NON-LINEAR WING-FUSELAGE JUNCTION 02	Test Section (<i>k-ε</i>)	Test Section (<i>k-ω</i>)	Control Specimen (<i>k-ε</i>)	Control Specimen (<i>k-ω</i>)	Average Percent Change Over Control
Junction Lift Force [N]	4.2272	4.2457	4.1736	4.1853	0.07%
Junction Lift Coefficient	0.5785	0.5811	0.5786	0.5802	
Wing Section Lift Force [N]	15.0956	15.1480	14.7667	14.8246	2.20%
Wing Section Lift Coefficient	1.1733	1.1774	1.1477	1.1522	
Overall Lift Force [N]	19.3229	19.3937	18.9403	19.0099	2.02%
Overall Lift Coefficient	0.3577	0.3590	0.3527	0.3539	
Drag Force [N]	0.6126	0.6087	0.6140	0.6078	-1.13%
Drag Coefficient	0.01134	0.01127	0.01143	0.01132	

Table 5.13 Non-Linear Wing-Fuselage Junction 02 – loiter, level flight (root Re = 330141).

The performance gains from the loiter, level flight values obtained with NLWJ-02 were not significant enough to warrant an additional battery of tests. NLWJ-02 would also be the last

junction design explored: more complicated shapes were not desired but they were the next evolution step for this study, at that point, and thus the design process was terminated. Therefore, the two final candidates for the wing-fuselage junction would be LWJ-01 and NLWJ-01.

5.7 Final Candidates Discussion

As the results in Table 5.4 and 5.5 showed, LWJ-01's performance at angle-of-attack left a lot to be desired. NLWJ-01 showed considerable performance gains in loiter and level flight but these seemed to fade away as the angle-of-attack was increased. It is safe to assume that at even greater angles-of-attack, NLWJ-01's performance drops off from the control, but not at the same rate as LWJ-01. Figure 5.6 plots the averaged drag coefficients from the $k-\epsilon$ and $k-\omega$ models against the angle of attack for the control specimen, LWJ-01 and NLWJ-01.

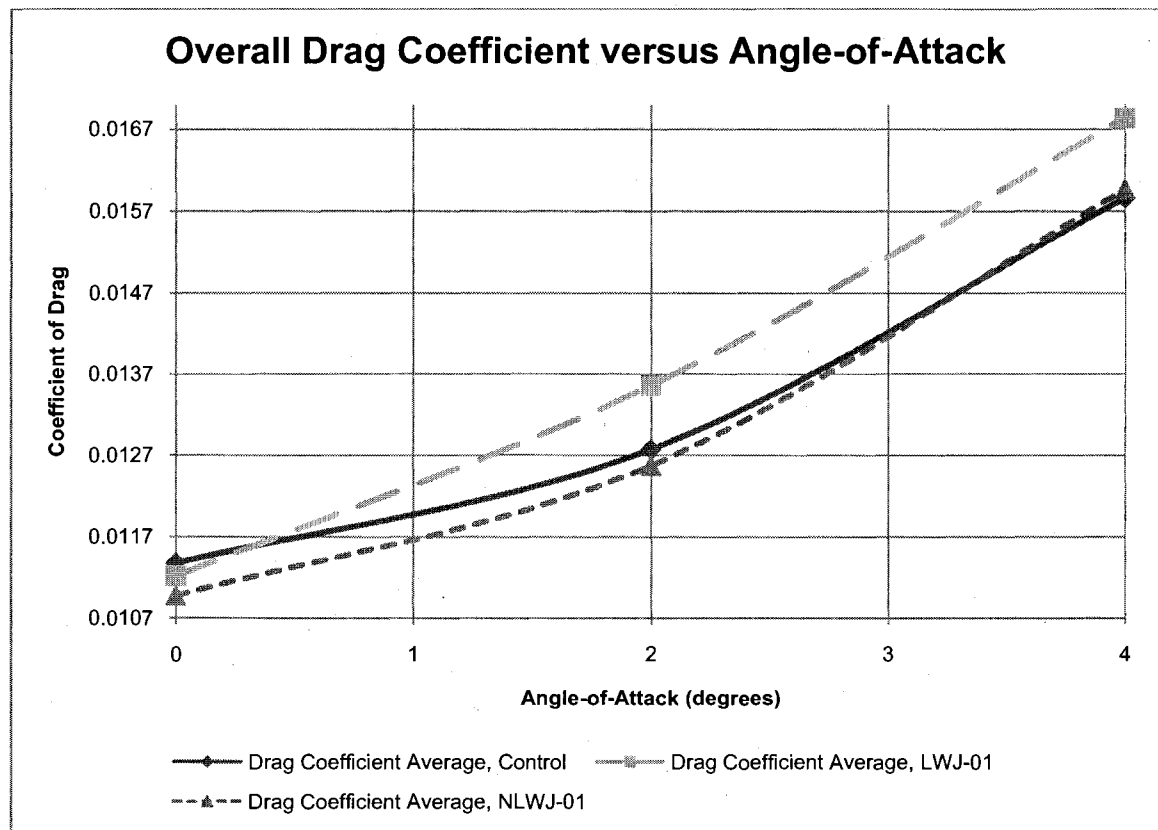


Figure 5.6 Overall drag coefficient versus angle-of-attack for selected wing-fuselage junctions.

All of the designs showed some type of lift improvement but it should be interesting to plot the development of these performance gains against the angle-of-attack. Figure 5.7 shows such a plot. All three plotted sections show a linear trend, a normal occurrence for lifting bodies in low angles-of-attack. NLWJ-01 seems to settle comfortably between the control case and LWJ-01 in terms of lift gains.

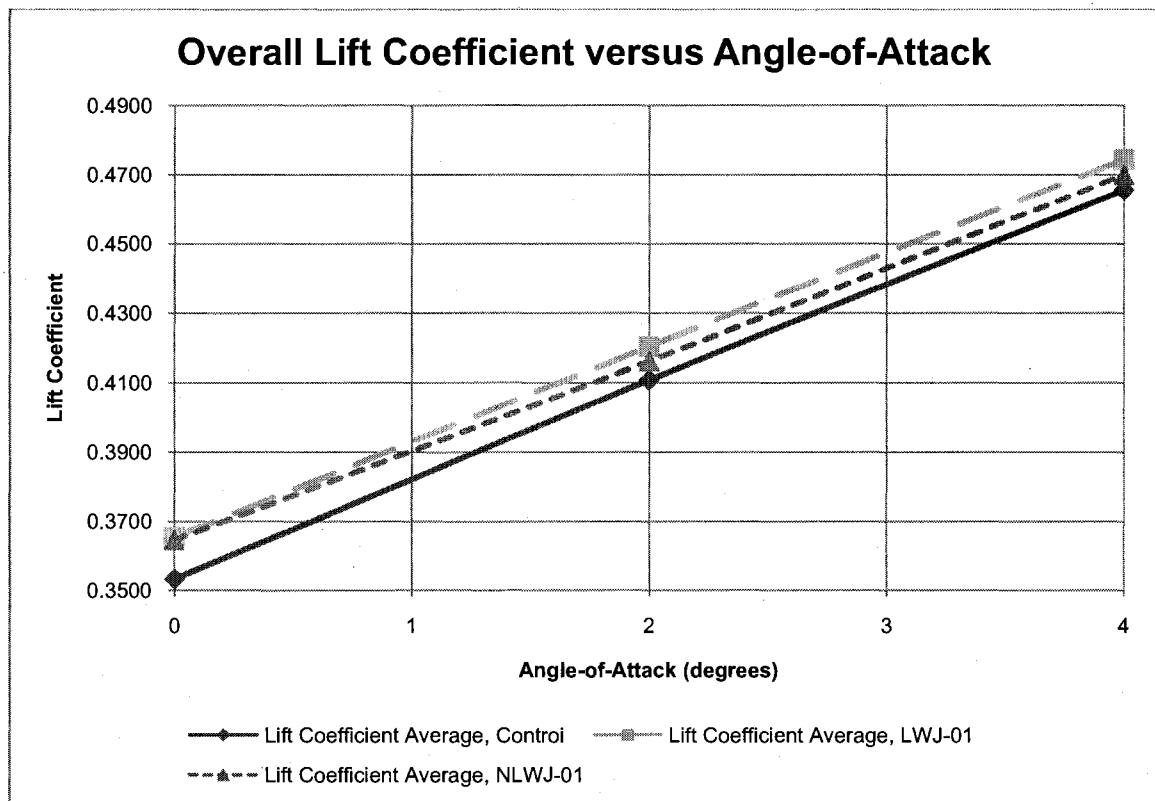


Figure 5.7 Overall lift coefficient versus angle-of-attack for selected wing-fuselage junctions.

While the ultimate goal of decreasing drag has been achieved with NLWJ-01, its performance could surely be improved with further study. Based on the current results, this junction should be recommended for implementation barring any additional design iterations. Further investigation of LWJ-01's performance, particularly with smooth blending of the junction into the other wetted areas, should be completed.

CHAPTER 6

CONCLUSION

6.1 Overview

In this study, the design and development of a wingtip device was completed in an attempt to decrease overall drag in all flight conditions and coincidentally enhance aircraft performance in all areas. A “no penalties” approach was taken. Similarly, the design and development of a wing-fuselage junction was completed in an effort to decrease overall drag in all flight conditions.

In the design of both of these devices, the primary objective was the decrease of overall drag in all flight attitudes. The secondary objective was the increase in lift, otherwise regarded as an increase in span efficiency.

In the case of the wingtip device, in pursuit of these objectives, two candidates were singled out and their performances compared. Given the operating Reynolds number of the aircraft, it was found that the overall surface area of the non-planar device had to be monitored closely as to not incur any losses. It was also found that as a designer of such a device, awareness of the local Reynolds number is paramount. Regions of a non-planar device which operate in a Reynolds number range that is below the recommended threshold for the airfoil it employs may adversely affect the whole of the device in the creation of laminar separation bubbles. In this case, it is better to forget about conventional wing design techniques and instead terminate the device at the last point at which it remains effective.

It was found that the efficiency of the winglets tested was very sensitive to the cant angle, in particular, along angle-of-attack. The chord distribution of the winglet was also found to be important but a careful balance must be achieved between the amount of force generated and the added wetted area, properties which are directly related.

In the case of the wing-fuselage junction, two candidates were picked out. It was found that while the gathered results initially contradicted that of the literature, several key differences were highlighted between this study and others found in the literature to effectively negate the ability to compare the results. The study shows that a non-linear profile for the junction may provide better results in the case of this particular airframe but that the improvements were relatively insignificant as angle-of-attack increased. Nonetheless, no severe penalty was incurred by the inclusion of the non-linear filleting and as thus should still be incorporated into the airframe.

Additionally, a marginal gain in lift was found with the inclusion of these junctions but this is due to the increased chord at the root. While lift production at the root is minimal, the junction's span provides enough surface area to make a contribution in the overall lift force that the plane can generate. As with the non-planar lifting devices, a careful balance between the geometry and the overall wetted area must be achieved in order for the junction to perform efficiently.

6.2 Recommendations

Barring any further design iterations or testing, NPD-02 and NLWJ-01 should be cleared for incorporation into the fabrication of the UNLV solar-powered unmanned aerial vehicle.

Future work should include further testing of these designs. While the results are believed to be accurate, actual wind tunnel testing would solidify the validity of these results. Unfortunately, this step was not concluded within the scope of this study due to the inadequate resolution found in the data acquisition system fitted to UNLV's wind tunnel. As the results of this study shows, the gains or losses observed can be minute. The wind tunnel facility available on campus is certainly suitable for such testing, and with an upgraded DAQ further data could be gathered on these designs.

Furthermore, the new Cray CX-1 and its ability to run COMSOL Multiphysics 3.5 should be utilized. Models with a higher element and degree of freedom count could be employed, enabling a higher degree of accuracy in the solution of the problems. At this point, several additional features available in COMSOL could be put to use, such as advanced boundary layer meshing. While the results obtained in this study are considered satisfactory, there is no question that

running these simulations using finite element analysis has its limitations, the main of which is the breakdown of the geometries into triangular or tetrahedral elements, which may lead to poor mesh quality if not enough attention is paid to the process. Indeed, with the complex geometries included within this study, mesh generation took up a significant amount of time and every problem had to be specifically handled. On the other hand, if a denser mesh all around was allowable, mesh generation may have required a lesser time allocation. Simply put, the increased computing power and COMSOL's newly acquired ability to parallel-process should be utilized.

Further design iterations could and should yield perhaps even greater results. The usage of a different airfoil for the winglet may also alleviate the laminar separation bubble issue and would be of great interest.

APPENDIX A

VIRTUAL WIND TUNNEL CALIBRATION AND WING CONTROL SPECIMEN DATA

WING CONTROL SPECIMEN MODEL STATISTICS (LOITER, LEVEL FLIGHT)	Value
Number of Elements	86240
Degrees of Freedom	672224
Number of Boundary Elements Over Wing	14756
Time to Solution ($k-\epsilon$) [s]	2495.648
Time to Solution ($k-\omega$) [s]	2710.388

Table A.1 Model statistics for Wing Control Specimen in loiter, level flight.

WING CONTROL SPECIMEN (LOITER, LEVEL FLIGHT)	Test Section ($k-\epsilon$)	Test Section ($k-\omega$)
Test Flight Condition	Loiter Speed, Level Flight	
Test Condition Freestream Velocity [m/s]	15.59	
Wing Surface Area [m ²]	0.795	
Root Chord [m]	0.3	
Subdomain Fluid Density [kg/m ³]	1.2	
Subdomain Fluid Absolute Viscosity [Pa/s]	1.70E-05	
Root Reynolds Number	330141	
Measurement Plane Cross-Sectional Area [m ²]	1.65	
Flowrate (x-direction, in-bound) [m ³ /s]	25.7235	
Flowrate (x-direction, out-bound) [m ³ /s]	25.663691	25.664351
Total Drag Force [N]	2.2352	2.2106
Pressure Integration Over Top Wing Surface [N]	-35.254850	-35.337443
Pressure Integration Over Bottom Wing Surface [N]	15.510542	15.530123
Total Lift Force [N]	50.7654	50.8676
Overall Drag Coefficient	0.0386	0.0382
Overall Lift Coefficient	0.8762	0.8780
Lift-to-Drag Ratio	22.7117	23.0110

Table A.2 Raw and processed data from the Wing Control Specimen, loiter and level flight.

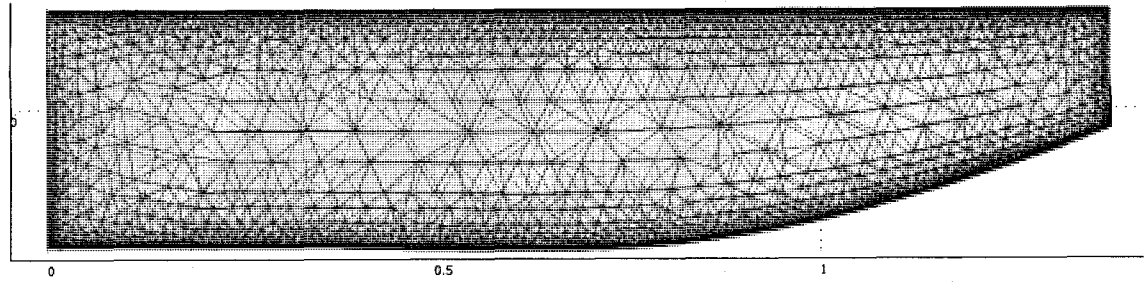


Figure A.1 Close-up of the mesh arrangement over the surface of the wing.

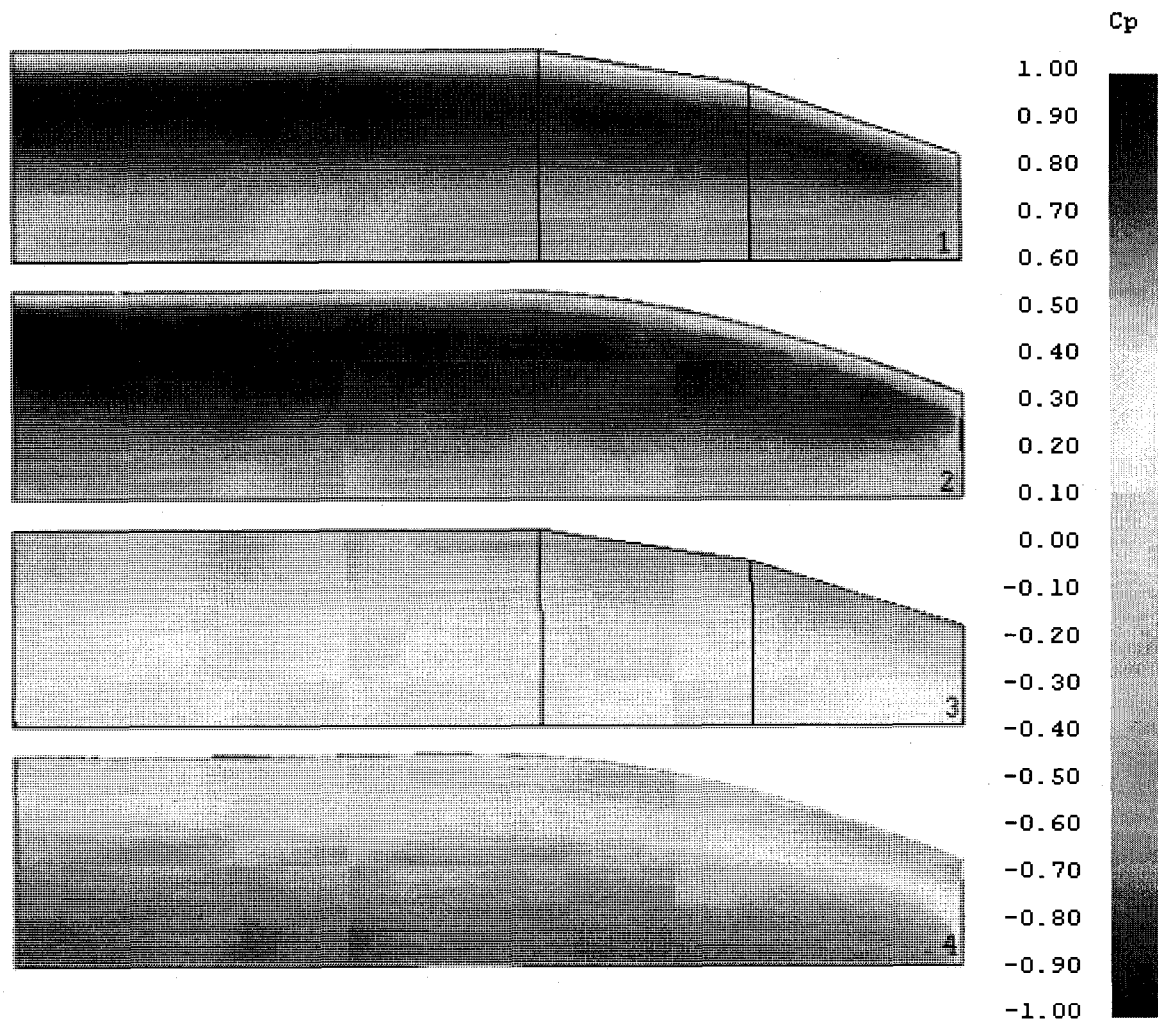


Figure A.2 Comparison of COMSOL Multiphysics 3.5 and 3-D Panel results from XFLR5 for boundary pressure distribution over the wing surface. From the top: Wing top surface, 3-D Panel (1), COMSOL (2); Wing bottom surface, 3-D Panel (3), COMSOL (4) (loiter, level flight).

WING CONTROL SPECIMEN MODEL STATISTICS (LOITER, -2° AOA)	Value
Number of Elements	86138
Degrees of Freedom	672601
Number of Boundary Elements Over Wing	15118
Time to Solution ($k-\epsilon$) [s]	6570.793
Time to Solution ($k-\omega$) [s]	7053.381

Table A.3 Model statistics for Wing Control Specimen in loiter, -2° angle-of-attack.

WING CONTROL SPECIMEN (LOITER, -2° AOA)	Test Section ($k-\epsilon$)	Test Section ($k-\omega$)
Test Flight Condition	Loiter Speed, -2° AOA	
Test Condition Freestream Velocity [m/s]	15.59	
Wing Surface Area [m ²]	0.795	
Root Chord [m]	0.3	
Subdomain Fluid Density [kg/m ³]	1.2	
Subdomain Fluid Absolute Viscosity [Pa/s]	1.70E-05	
Root Reynolds Number	330141	
Measurement Plane Cross-Sectional Area [m ²]	1.65	
Flowrate (x-direction, in-bound) [m ³ /s]	25.7235	
Flowrate (x-direction, out-bound) [m ³ /s]	25.663478	25.664172
Total Drag Force [N]	2.2432	2.2173
Pressure Integration Over Top Wing Surface [N]	-29.280676	-29.359765
Pressure Integration Over Bottom Wing Surface [N]	10.761790	10.782271
Total Lift Force [N]	40.0181	40.1176
Overall Drag Coefficient	0.0387	0.0383
Overall Lift Coefficient	0.6907	0.6925
Lift-to-Drag Ratio	17.8397	18.0930

Table A.4 Raw and processed data from the Wing Control Specimen, loiter, -2° angle-of-attack.

WING CONTROL SPECIMEN MODEL STATISTICS (LOITER, +2° AOA)	Value
Number of Elements	86427
Degrees of Freedom	675360
Number of Boundary Elements Over Wing	15130
Time to Solution ($k-\epsilon$) [s]	3987.897
Time to Solution ($k-\omega$) [s]	4931.859

Table A.5 Model statistics for Wing Control Specimen in loiter, +2° angle-of-attack.

WING CONTROL SPECIMEN (LOITER, +2° AOA)	Test Section ($k-\epsilon$)	Test Section ($k-\omega$)
Test Flight Condition	Loiter Speed, +2° AOA	
Test Condition Freestream Velocity [m/s]	15.59	
Wing Surface Area [m ²]	0.795	
Root Chord [m]	0.3	
Subdomain Fluid Density [kg/m ³]	1.2	
Subdomain Fluid Absolute Viscosity [Pa/s]	1.70E-05	
Root Reynolds Number	330141	
Measurement Plane Cross-Sectional Area [m ²]	1.65	
Flowrate (x-direction, in-bound) [m ³ /s]	25.7235	
Flowrate (x-direction, out-bound) [m ³ /s]	25.660345	25.661056
Total Drag Force [N]	2.3601	2.3336
Pressure Integration Over Top Wing Surface [N]	-41.942845	-42.02454
Pressure Integration Over Bottom Wing Surface [N]	19.597703	19.609942
Total Lift Force [N]	61.5031	61.5969
Overall Drag Coefficient	0.0407	0.0403
Overall Lift Coefficient	1.0616	1.0632
Lift-to-Drag Ratio	26.0589	26.3955

Table A.6 Raw and processed data from the Wing Control Specimen, loiter, +2° angle-of-attack.

WING CONTROL SPECIMEN MODEL STATISTICS (LOITER, +4° AOA)	Value
Number of Elements	85470
Degrees of Freedom	667230
Number of Boundary Elements Over Wing	15112
Time to Solution ($k-\epsilon$) [s]	6102.392
Time to Solution ($k-\omega$) [s]	7124.238

Table A.7 Model statistics for Wing Control Specimen in loiter, +4° angle-of-attack.

WING CONTROL SPECIMEN (LOITER, +4° AOA)	Test Section ($k-\epsilon$)	Test Section ($k-\omega$)
Test Flight Condition	Loiter Speed, +4° AOA	
Test Condition Freestream Velocity [m/s]	15.59	
Wing Surface Area [m ²]	0.795	
Root Chord [m]	0.3	
Subdomain Fluid Density [kg/m ³]	1.2	
Subdomain Fluid Absolute Viscosity [Pa/s]	1.70E-05	
Root Reynolds Number	330141	
Measurement Plane Cross-Sectional Area [m ²]	1.65	
Flowrate (x-direction, in-bound) [m ³ /s]	25.7235	
Flowrate (x-direction, out-bound) [m ³ /s]	25.643265	25.644320
Total Drag Force [N]	2.9974	2.9580
Pressure Integration Over Top Wing Surface [N]	-47.818781	-47.819820
Pressure Integration Over Bottom Wing Surface [N]	22.931661	22.941142
Total Lift Force [N]	70.5781	70.7610
Overall Drag Coefficient	0.0517	0.0511
Overall Lift Coefficient	1.2182	1.2214
Lift-to-Drag Ratio	23.5460	23.9211

Table A.8 Raw and processed data from the Wing Control Specimen, loiter, +4° angle-of-attack.

APPENDIX B

WINGTIP DEVICE SMULATIONS - COLLECTED DATA AND MODEL INFORMATION

B.1 Planar Device 01 (PD-01)

PLANAR DEVICE 01 MODEL STATISTICS (LOITER, LEVEL FLIGHT)	Value
Number of Elements	84407
Degrees of Freedom	658783
Number of Boundary Elements Over Wing	14860
Time to Solution ($k-\epsilon$) [s]	3114.959
Time to Solution ($k-\omega$) [s]	4839.306

Table B.1 Model statistics for PD-01 in loiter, level flight.

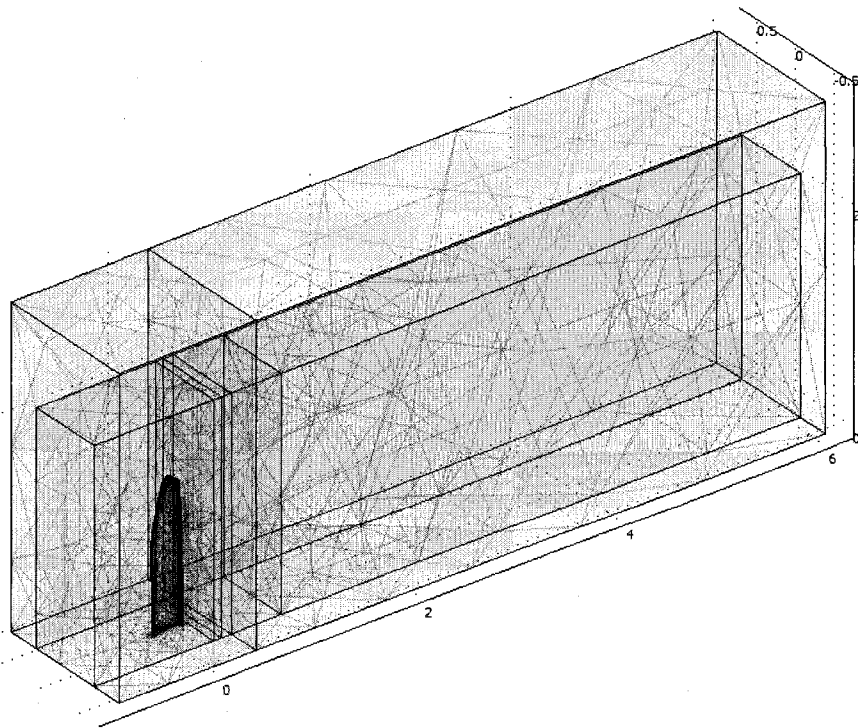


Figure B.1 Mesh overview of the model.

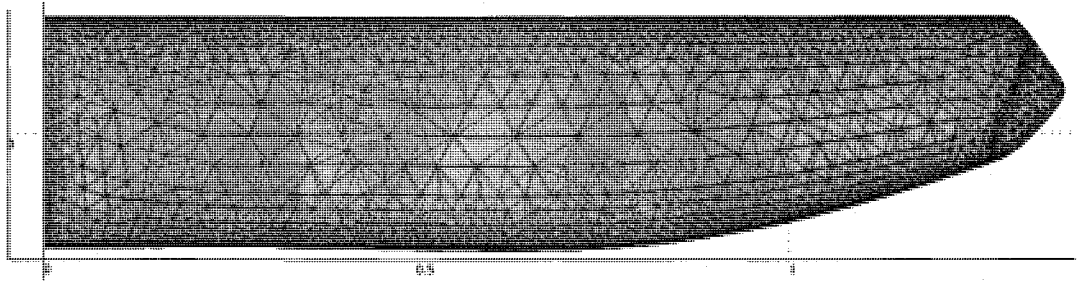


Figure B.2 Mesh detail for Planar Device 01.

PLANAR DEVICE 01 (LOITER, LEVEL FLIGHT)	Test Section ($k-\epsilon$)	Test Section ($k-\omega$)
Test Flight Condition	Loiter Speed, Level Flight	
Test Condition Freestream Velocity [m/s]	15.59	
Wing Surface Area [m ²]	0.783	
Root Chord [m]	0.3	
Subdomain Fluid Density [kg/m ³]	1.2	
Subdomain Fluid Absolute Viscosity [Pa/s]	1.70E-05	
Root Reynolds Number	330141	
Measurement Plane Cross-Sectional Area [m ²]	1.65	
Flowrate (x-direction, in-bound) [m ³ /s]	25.7235	
Flowrate (x-direction, out-bound) [m ³ /s]	25.664343	25.665028
Total Drag Force [N]	2.2109	2.1853
Pressure Integration Over Top Wing Surface [N]	-34.318544	-34.395427
Pressure Integration Over Bottom Wing Surface [N]	15.019533	15.038325
Total Lift Force [N]	49.3381	49.4338
Overall Drag Coefficient	0.0387	0.0383
Overall Lift Coefficient	0.8638	0.8654
Lift-to-Drag Ratio	22.3161	22.6210
Percent Change Drag Coefficient Over Control	0.32%	0.27%
Percent Change Lift Coefficient Over Control	-1.43%	-1.43%
Percent Change Lift-to-Drag Ratio Over Control	-1.74%	-1.69%

Table B.2 Collected data from the model simulation for Planar Device 01.

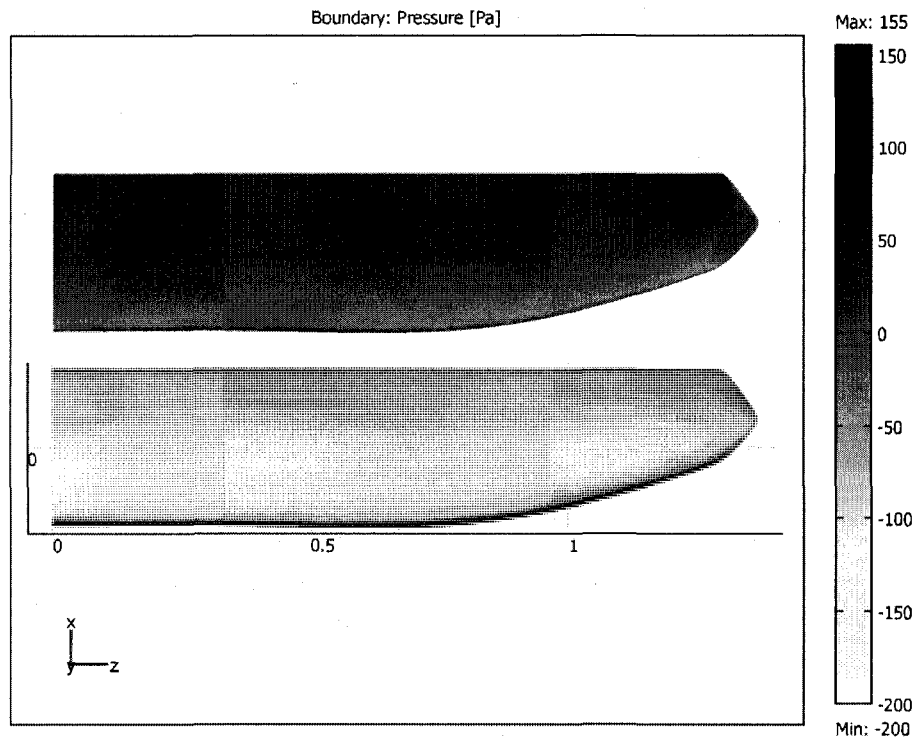


Figure B.3 Boundary pressure distribution over the bottom and top surfaces of the wing in loiter flight, zero degree angle of attack. Notice the lack of a useful pressure gradient over the wingtip surface.

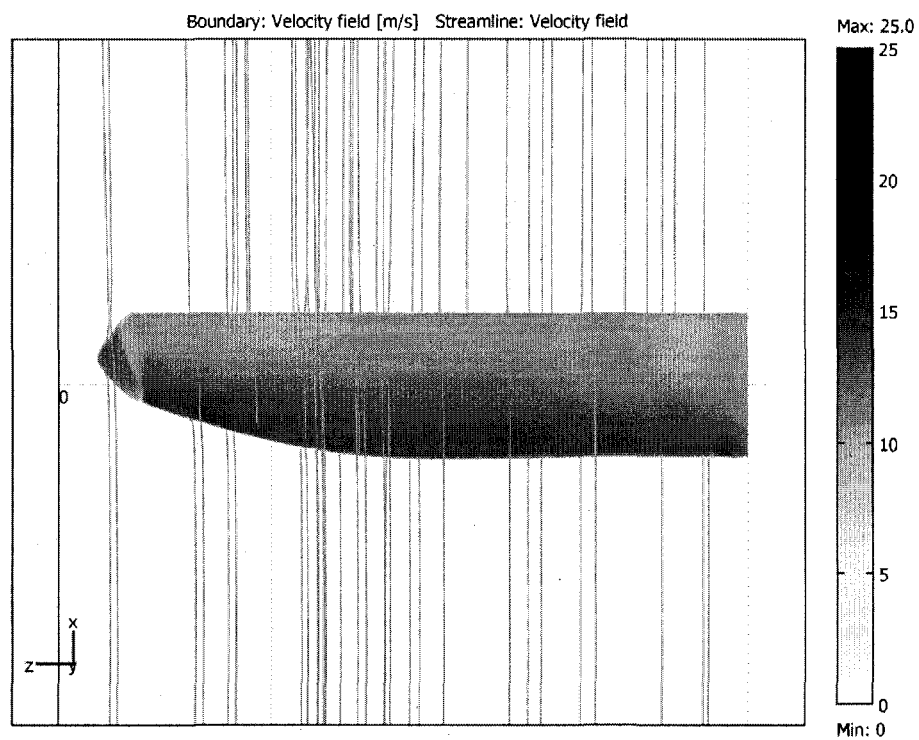


Figure B.4 Velocity distribution with velocity streamlines in loiter and level flight (bottom surface).

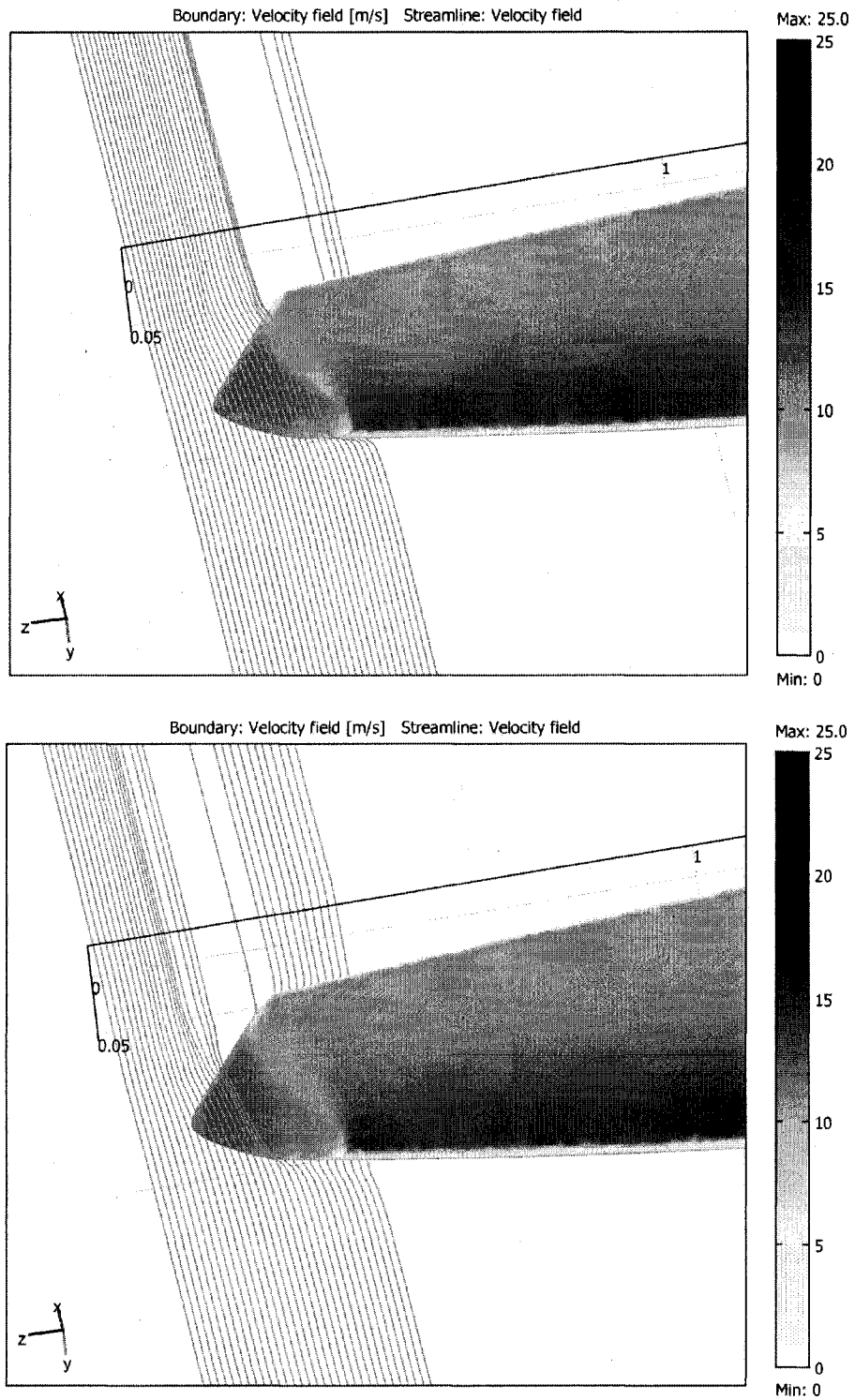


Figure B.5 Streamline detail for PD-01 with streamlines at two levels. Notice the slight streamline deflection and overall inefficiency of the device to produce any type of useful aerodynamic force: this device results in useless added wetted area.

B.2 Planar Device 02 (PD-02)

PLANAR DEVICE 02 MODEL STATISTICS (LOITER, LEVEL FLIGHT)		Value
Number of Elements		86309
Degrees of Freedom		674020
Number of Boundary Elements Over Wing		15036
Time to Solution ($k-\epsilon$) [s]		3816.212
Time to Solution ($k-\omega$) [s]		4902.290

Table B.3 PD-02 Model statistics for loiter, level flight.

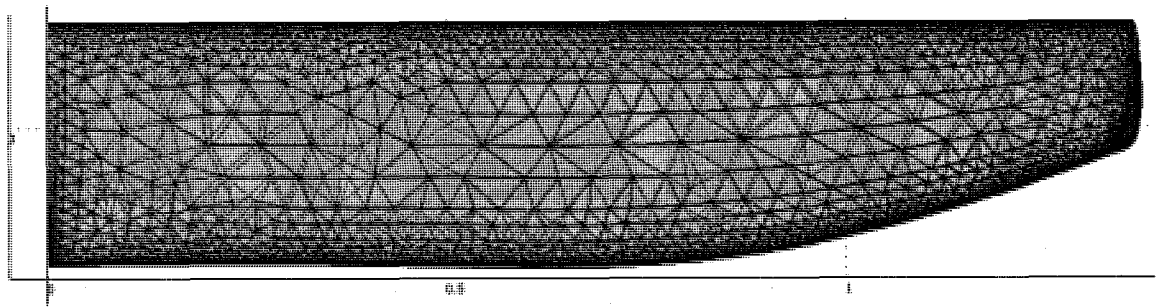


Figure B.6 Mesh detail of the coarse mesh for Planar Device 02.

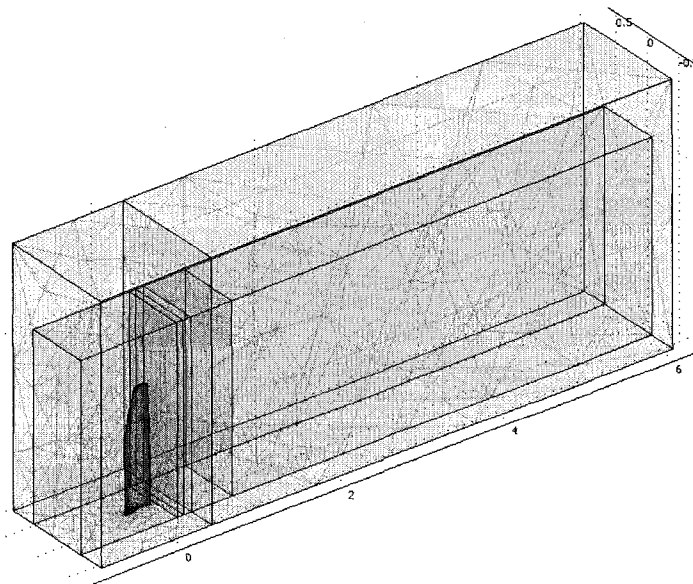


Figure B.7 Mesh overview of the model for PD-02.

PLANAR DEVICE 02 (LOITER, LEVEL FLIGHT)	Test Section ($k-\epsilon$)	Test Section ($k-\omega$)
Test Flight Condition	Loiter Speed, Level Flight	
Test Condition Freestream Velocity [m/s]	15.59	
Wing Surface Area [m ²]	0.793	
Root Chord [m]	0.3	
Subdomain Fluid Density [kg/m ³]	1.2	
Subdomain Fluid Absolute Viscosity [Pa/s]	1.70E-05	
Root Reynolds Number	330141	
Measurement Plane Cross-Sectional Area [m ²]	1.65	
Flowrate (x-direction, in-bound) [m ³ /s]	25.7235	
Flowrate (x-direction, out-bound) [m ³ /s]	25.665229	25.665856
Total Drag Force [N]	2.1778	2.1544
Pressure Integration Over Top Wing Surface [N]	-35.469524	-35.548944
Pressure Integration Over Bottom Wing Surface [N]	15.512021	15.532055
Total Lift Force [N]	50.9815	51.0810
Overall Drag Coefficient	0.0377	0.0373
Overall Lift Coefficient	0.8818	0.8836
Lift-to-Drag Ratio	23.4097	23.7102
Percent Change Drag Coefficient Over Control	-2.36%	-2.34%
Percent Change Lift Coefficient Over Control	0.64%	0.63%
Percent Change Lift-to-Drag Ratio Over Control	3.07%	3.04%

Table B.4 Collected data from the model simulation for Planar Device 02.

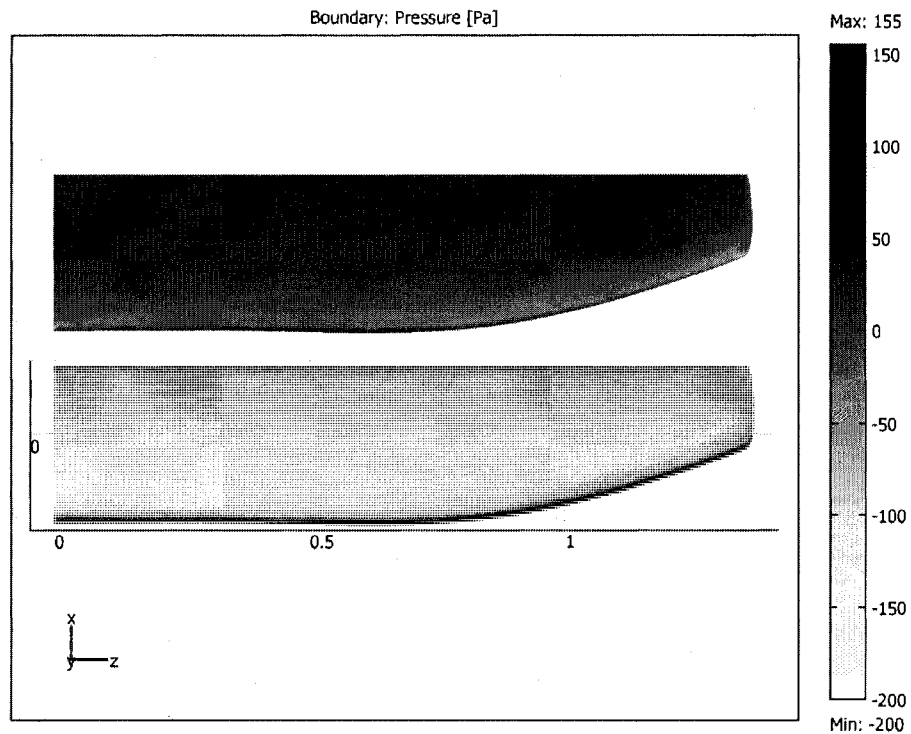


Figure B.8 Boundary pressure distribution over Planar Device 02, bottom and top surfaces. Notice the complete use of the wing for useful pressure gradient.

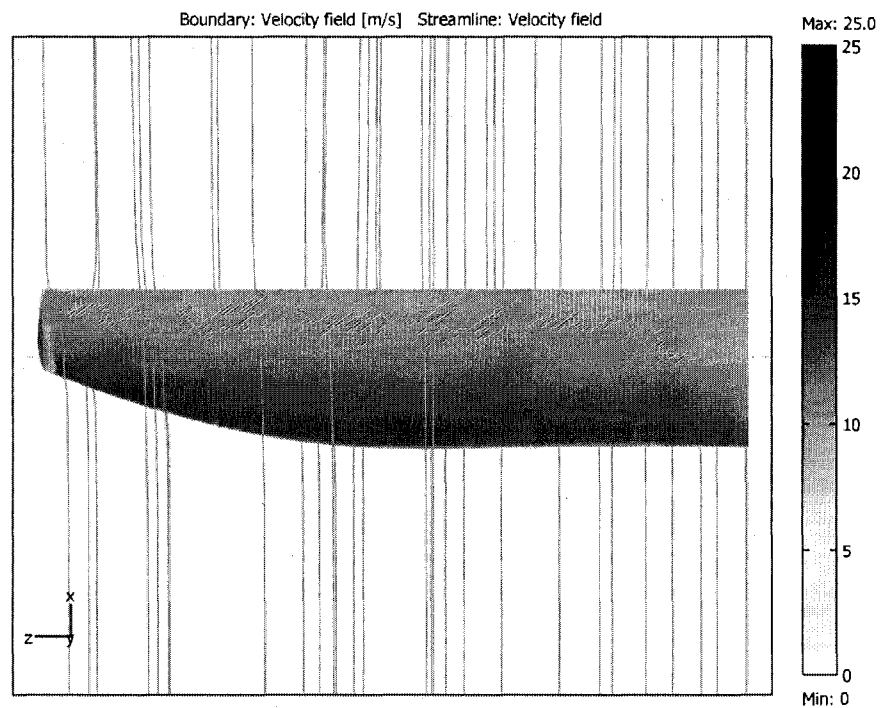


Figure B.9 Boundary velocity distribution over the bottom wing surface. Notice the wingtip vortex getting kicked outwards.

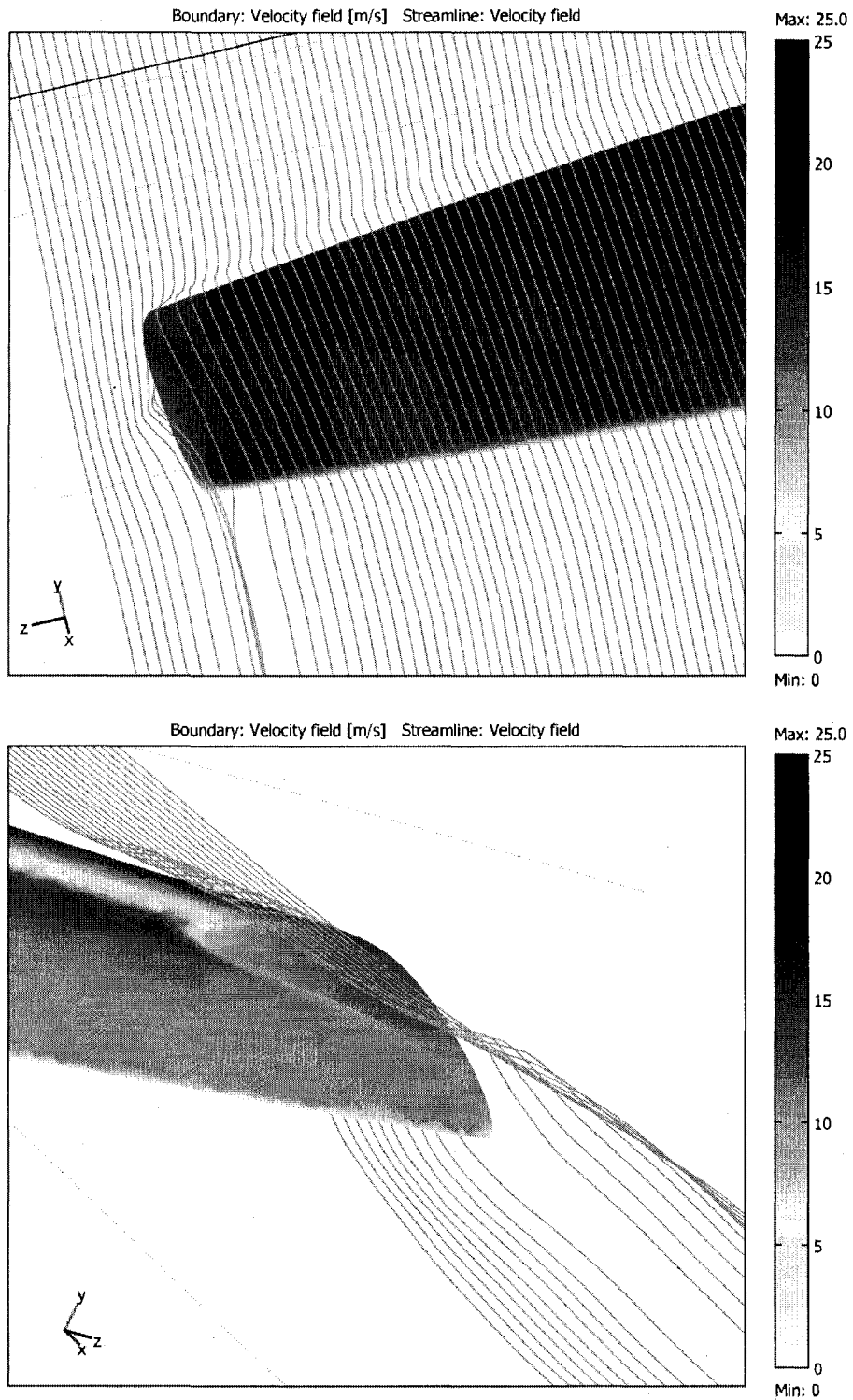


Figure B.10 Streamline details for PD-02 overseeing the top surface and a plan view from the front. Notice how the pressure gradient on the top surface is kept intact in great part due to the sharp edge of the device. In the front view, notice how the shape of the tip anticipates the formation of the vortices and dampens their effect.

B.3 Non-Planar Device 01 (NPD-01)

NON-PLANAR DEVICE 01 MODEL STATISTICS (LOITER, LEVEL FLIGHT)	Value
Number of Elements	101234
Degrees of Freedom	789384
Number of Boundary Elements Over Wing	14620
Number of Boundary Elements Over Winglet	3024
Time to Solution ($k-\epsilon$) [s]	5167.346
Time to Solution ($k-\omega$) [s]	6573.373

Table B.5 NPD-01 model statistics for loiter, level flight.

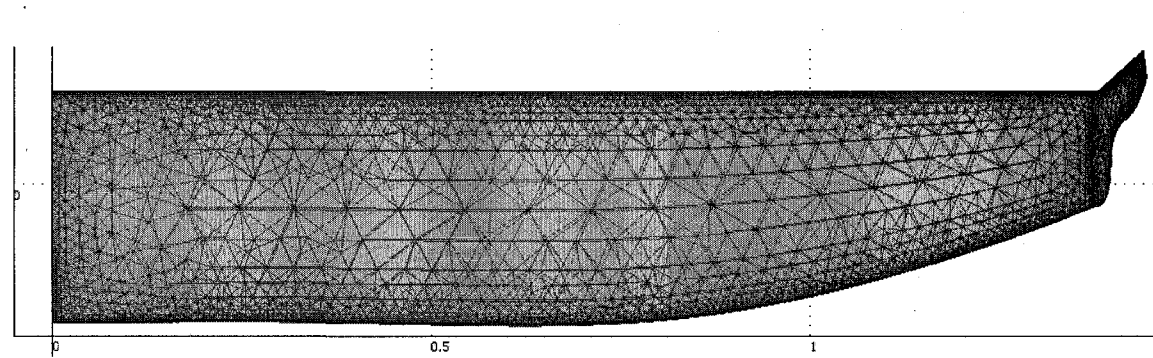


Figure B.11 Mesh detail for Non-Planar Device 01.

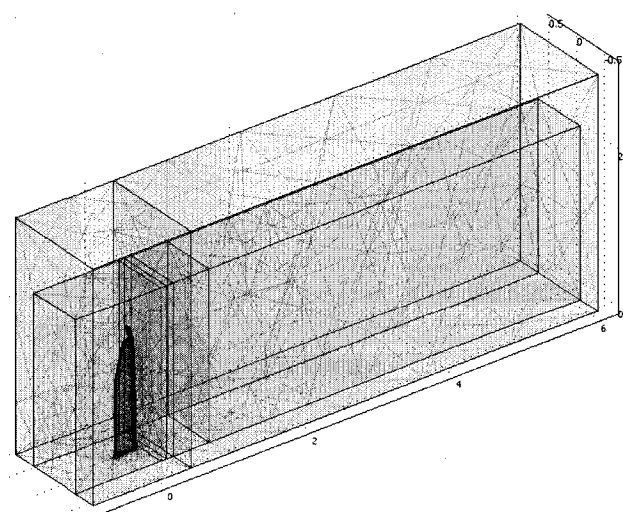


Figure B.12 Mesh overview of the model.

NON-PLANAR DEVICE 01 (LOITER, LEVEL FLIGHT)	Test Section ($k-\epsilon$)	Test Section ($k-\omega$)
Test Flight Condition	Loiter Speed, Level Flight	
Test Condition Freestream Velocity [m/s]	15.59	
Wing Surface Area [m ²]	0.795	
Winglet Surface Area [m ²]	0.012940	
Wing and Winglet Combined Surface Area [m ²]	0.807	
Root Chord [m]	0.3	
Subdomain Fluid Density [kg/m ³]	1.2	
Subdomain Fluid Absolute Viscosity [Pa/s]	1.70E-05	
Root Reynolds Number	330141	
Measurement Plane Cross-Sectional Area [m ²]	1.65	
Flowrate (x-direction, in-bound) [m ³ /s]	25.7235	
Flowrate (x-direction, out-bound) [m ³ /s]	25.662397	25.662991
Total Drag Force [N]	2.2835	2.2613
Pressure Integration Over Top Wing Surface [N]	-36.121021	-36.198014
Pressure Integration Over Bottom Wing Surface [N]	15.825819	15.843848
Pressure Integration Over Top Winglet Surface [N]	-0.815228	-0.818005
Pressure Integration Over Bottom Winglet Surface [N]	0.058846	0.059309
Winglet Surface Cant Angle [degrees]	15	
Winglet Surface Toe-Twist Angle Average [degrees]	4.5	
Wing Lift Force [N]	51.94684	52.041862
Winglet Lift Force [N]	0.844290651	0.84742025
Winglet Thrust Force [N]	0.068579056	0.068833263
Total Lift Force [N]	52.7911	52.8893
Overall Drag Coefficient	0.0388	0.0384
Overall Lift Coefficient	0.8966	0.8983
Lift-to-Drag Ratio	23.1184	23.3884
Percent Change Drag Coefficient Over Control	0.52%	0.66%
Percent Change Lift Coefficient Over Control	2.32%	2.31%
Percent Change Lift-to-Drag Ratio Over Control	1.79%	1.64%

Table B.6 Collected data from the model simulation for Non-Planar Device 01.

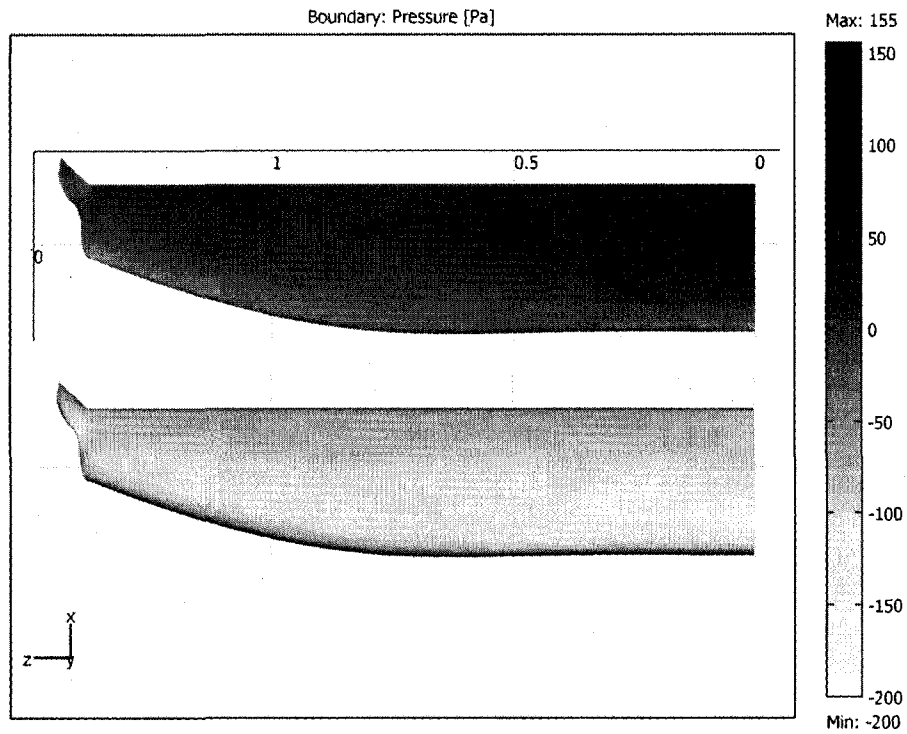


Figure B.13 Boundary pressure distribution over the bottom and top surfaces of the wing in loiter flight, zero degree angle of attack. Notice the complete usage of the wingspan in producing a useful pressure gradient.

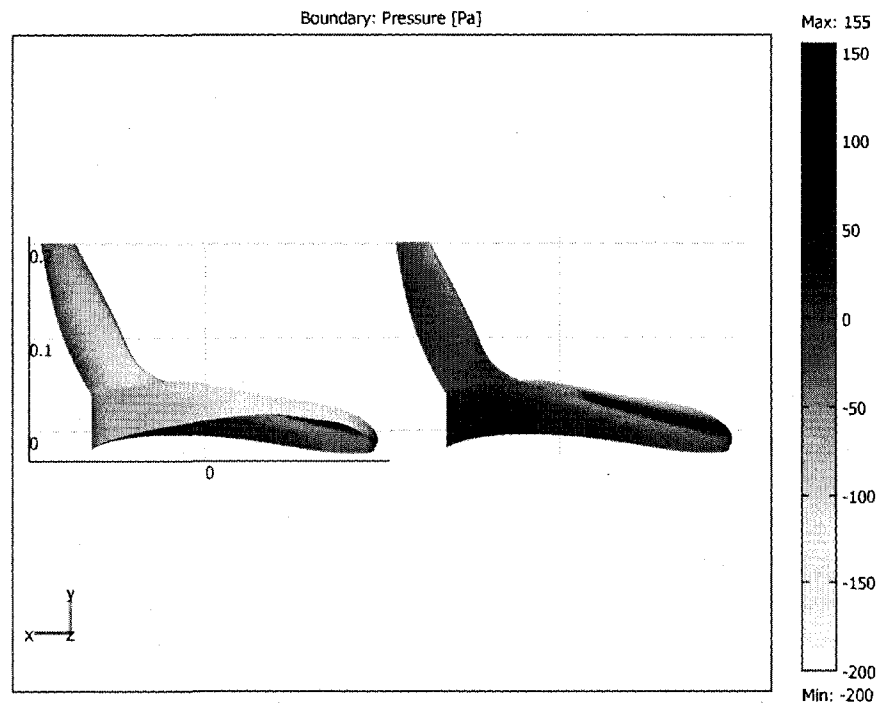


Figure B.14 Boundary pressure distribution over the inside and outside faces of the winglet. Notice the dissipation of useful pressure gradients at about two-thirds of the device span.

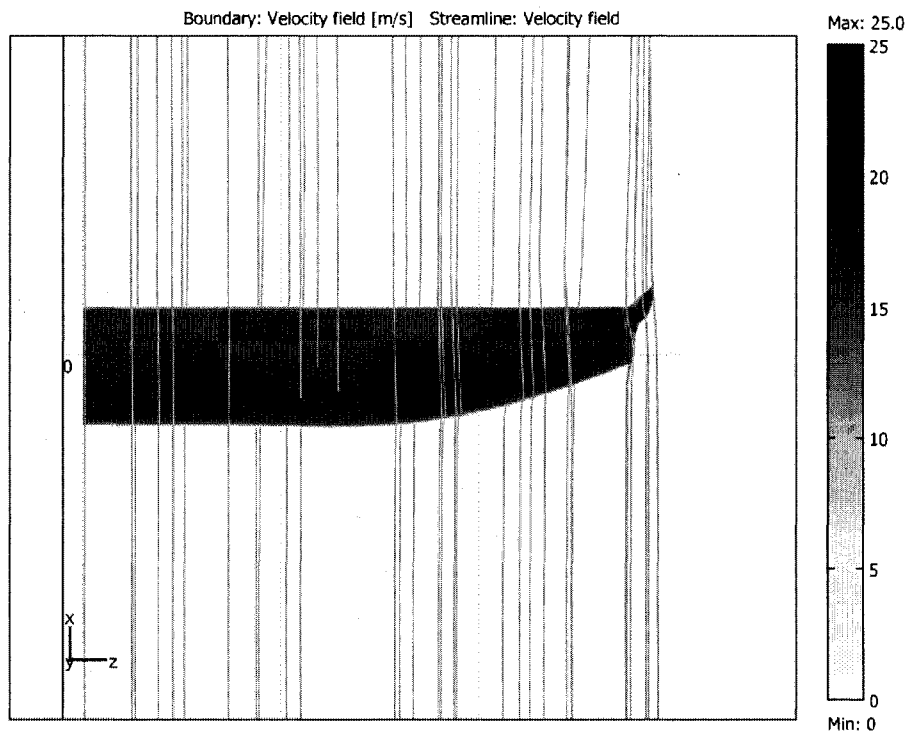
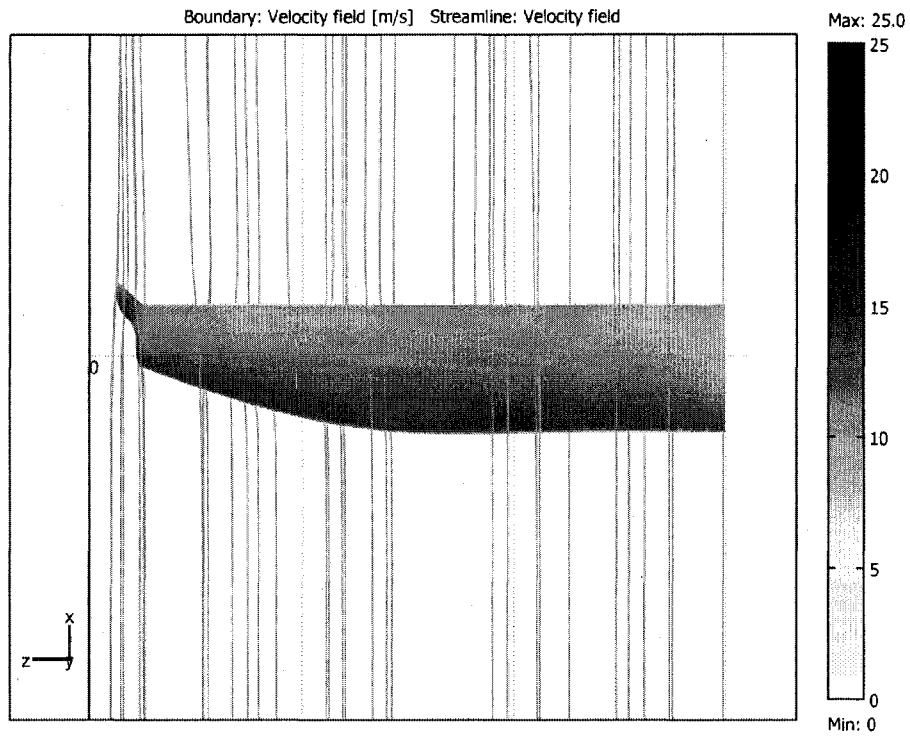


Figure B.15 Velocity boundary distribution and streamlines over the bottom and top surfaces of the wing. On the bottom surface, notice that the streamlines are still getting pulled out to the wingtip but perhaps not as strongly. On the top surface, we notice a more linear trend in the streamlines.

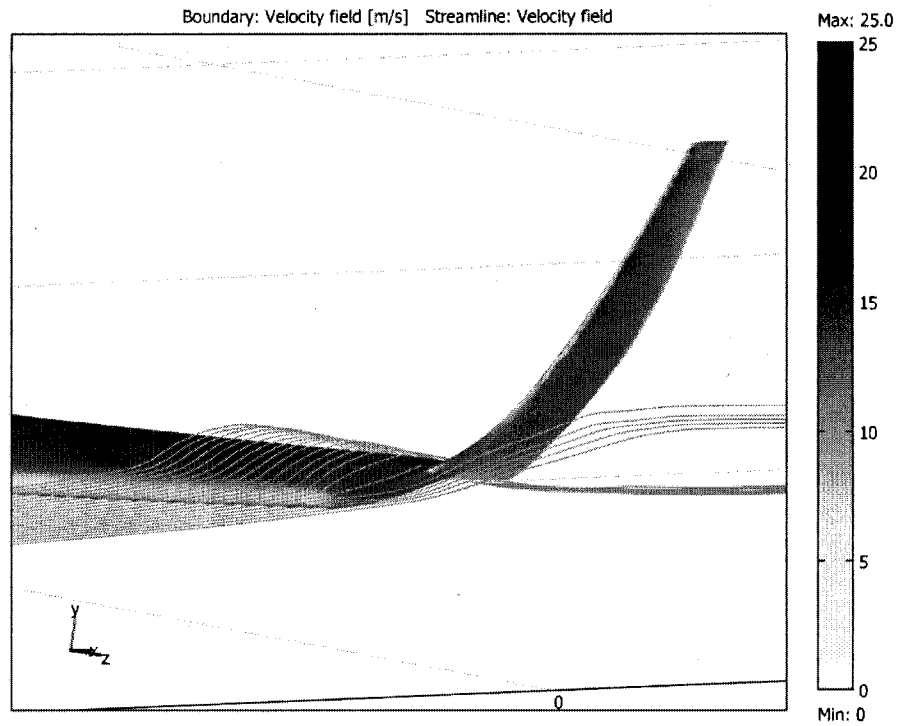


Figure B.16 Streamline details in-close for NPD-01. Notice the use of the vortice by the winglet to produce useful aerodynamic forces.

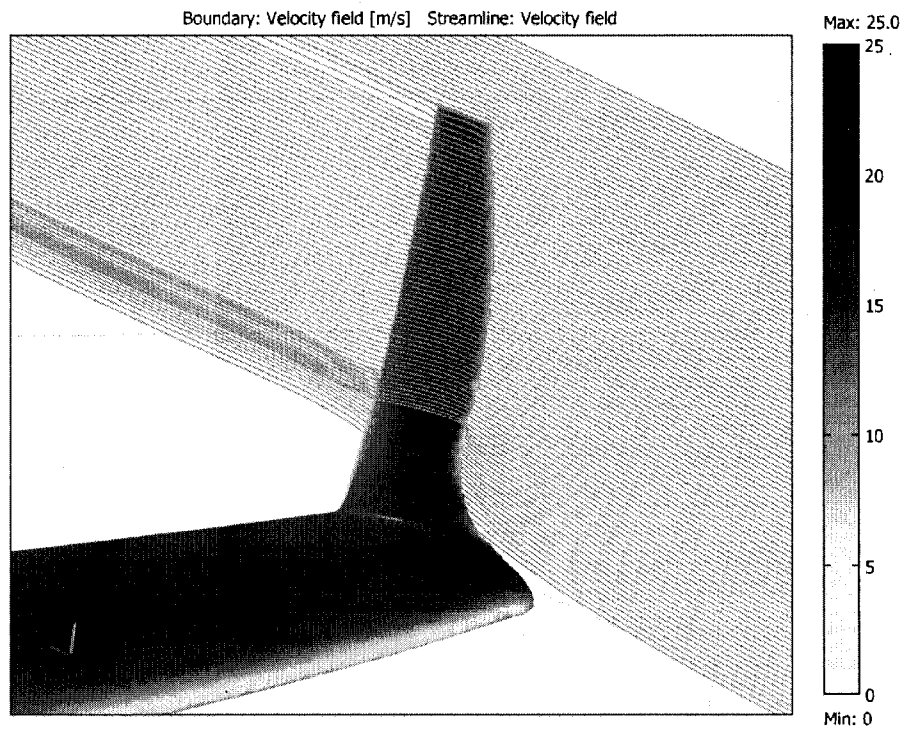


Figure B.17 Streamline details in-close for NPD-01. Notice the overlapping of streamlines and the clean nature of the flow around the winglet.

B.4 Non-Planar Device 02 (NPD-02)

NON-PLANAR DEVICE 02 MODEL STATISTICS (LOITER, LEVEL FLIGHT)	Value
Number of Elements	101574
Degrees of Freedom	792363
Number of Boundary Elements Over Wing	14654
Number of Boundary Elements Over Winglet	3076
Time to Solution ($k-\epsilon$) [s]	Not Recorded
Time to Solution ($k-\omega$) [s]	6399.413

Table B.7 Model statistics for NPD-02 in loiter, level flight.

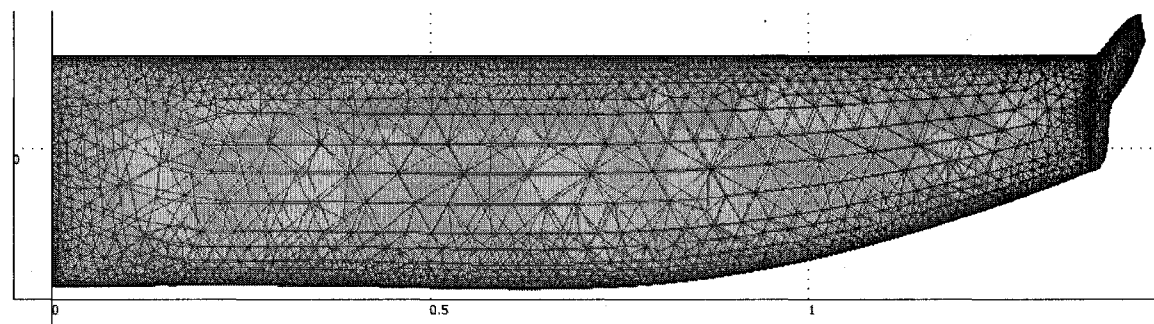


Figure B.18 Mesh detail for Non-Planar Device 02.

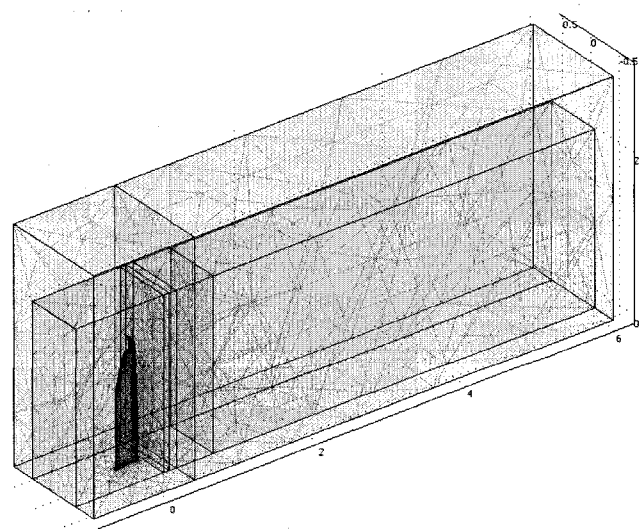


Figure B.19 Mesh overview of the model for NPD-02 in loiter, level flight.

NON-PLANAR DEVICE 02 (LOITER, LEVEL FLIGHT)	Test Section ($k-\epsilon$)	Test Section ($k-\omega$)
Test Flight Condition	Loiter Speed, Level Flight	
Test Condition Freestream Velocity [m/s]	15.59	
Wing Surface Area [m ²]	0.795	
Winglet Surface Area [m ²]	0.013764	
Wing and Winglet Combined Surface Area [m ²]	0.8083	
Root Chord [m]	0.3	
Subdomain Fluid Density [kg/m ³]	1.2	
Subdomain Fluid Absolute Viscosity [Pa/s]	1.70E-05	
Root Reynolds Number	330141	
Measurement Plane Cross-Sectional Area [m ²]	1.65	
Flowrate (x-direction, in-bound) [m ³ /s]	25.7235	
Flowrate (x-direction, out-bound) [m ³ /s]	25.666605	25.667207
Total Drag Force [N]	2.1264	2.1040
Pressure Integration Over Top Wing Surface [N]	-36.367289	-36.451322
Pressure Integration Over Bottom Wing Surface [N]	15.880051	15.901527
Pressure Integration Over Top Winglet Surface [N]	-0.860592	-0.863768
Pressure Integration Over Bottom Winglet Surface [N]	0.073533	0.074054
Winglet Surface Cant Angle Average [degrees]	18	
Winglet Surface Toe-Twist Angle Average [degrees]	4.5	
Wing Lift Force [N]	52.24734	52.352849
Winglet Lift Force [N]	0.888405668	0.891921724
Winglet Thrust Force [N]	0.073290603	0.073580666
Total Lift Force [N]	53.1357	53.2448
Overall Drag Coefficient	0.0361	0.0357
Overall Lift Coefficient	0.9016	0.9034
Lift-to-Drag Ratio	24.9883	25.3070
Percent Change Drag Coefficient Over Control	-6.49%	-6.44%
Percent Change Lift Coefficient Over Control	2.89%	2.89%
Percent Change Lift-to-Drag Ratio Over Control	10.02%	9.98%

Table B.8 Collected data from the model simulation for Non-Planar Device 02 in loiter, level flight.

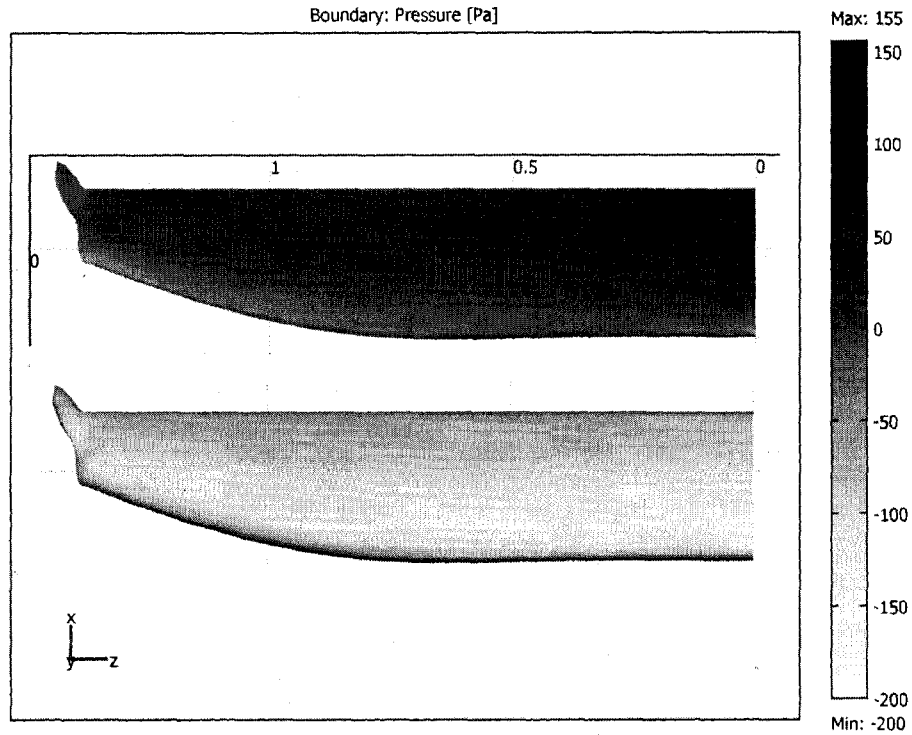


Figure B.20 Boundary pressure distribution over the bottom and top surfaces of the wing in loiter flight, zero degree angle of attack. Notice the complete usage of the wingspan in producing a useful pressure gradient, to an even greater extent than NDP-01.

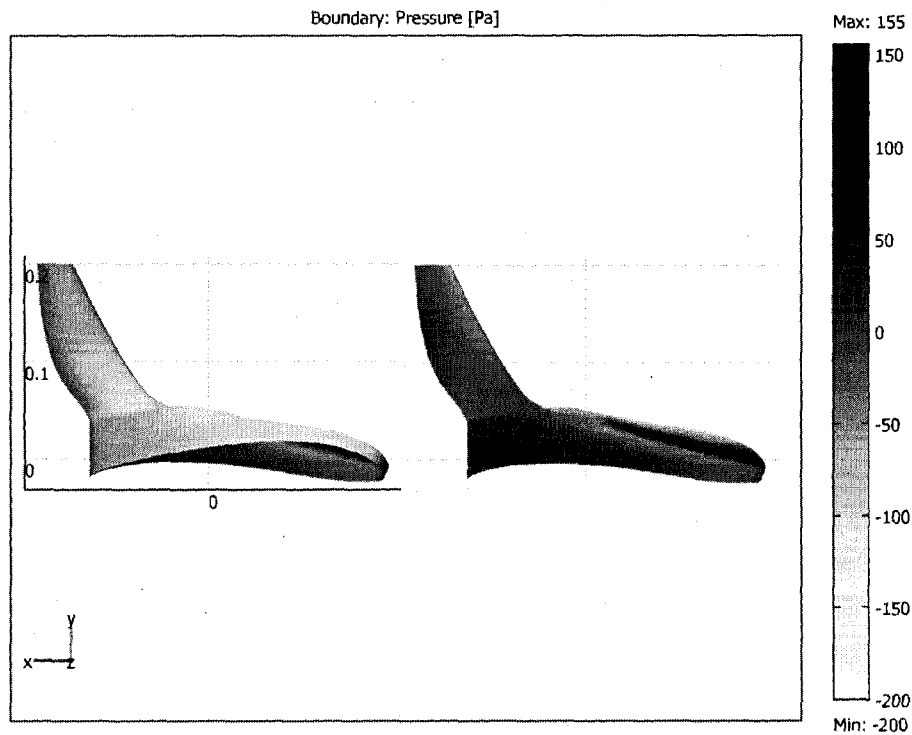


Figure B.21 Boundary pressure distribution over the inside and outside faces of the winglet in loiter, level flight. Useful pressure gradients stay active slightly longer than on NDP-01.

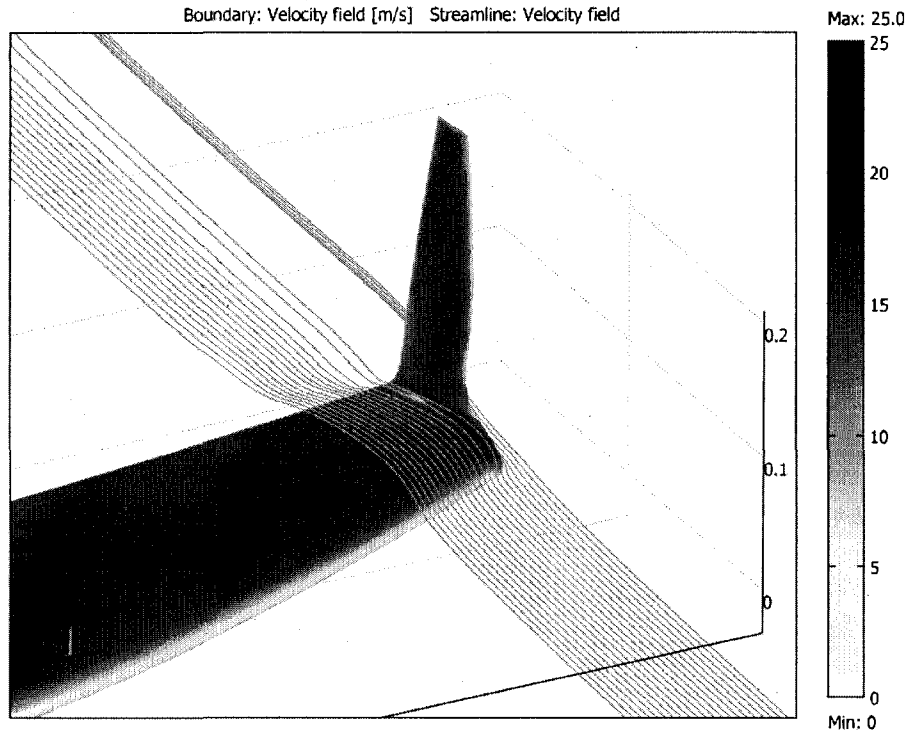


Figure B.22 Streamline detail at the winglet's base, the geometry of which remains largely unchanged from NDP-01, in loiter and level flight.

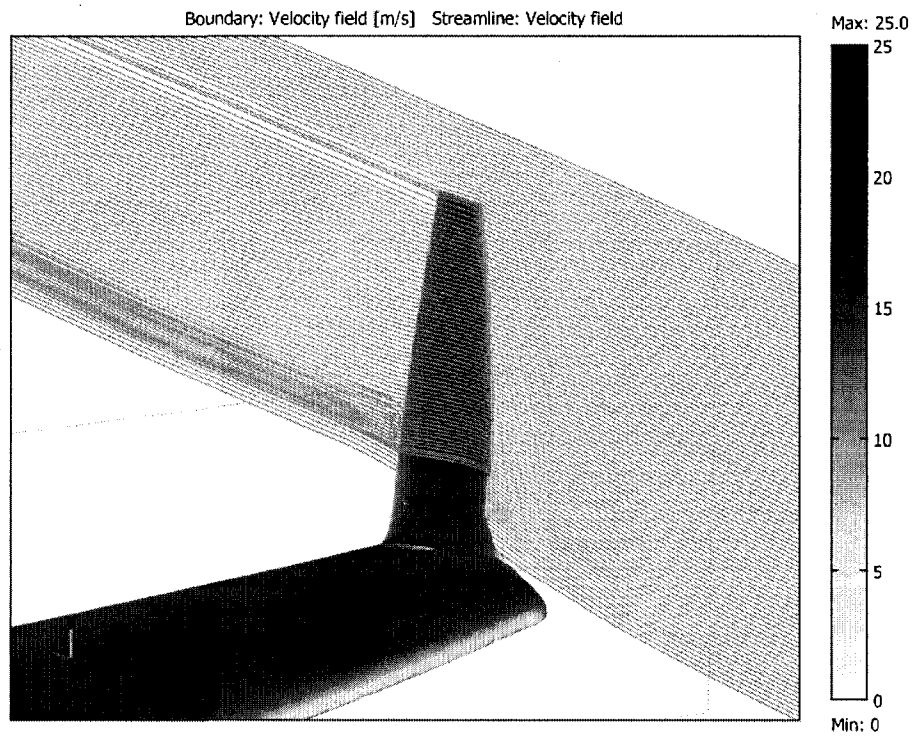


Figure B.23 Streamline detail along NDP-02's span in loiter, level flight. Notice the flow's laminar quality around the winglet and the minute amount of mixing after flow reconciliation.

NON-PLANAR DEVICE 02 MODEL STATISTICS (LOITER, -2° AOA)	Value
Number of Elements	101660
Degrees of Freedom	793574
Number of Boundary Elements Over Wing	14800
Number of Boundary Elements Over Winglet	3176
Time to Solution ($k-\epsilon$) [s]	5025.931
Time to Solution ($k-\omega$) [s]	7012.241

Table B.9 Model statistics for NPD-02 in loiter at -2° AOA.

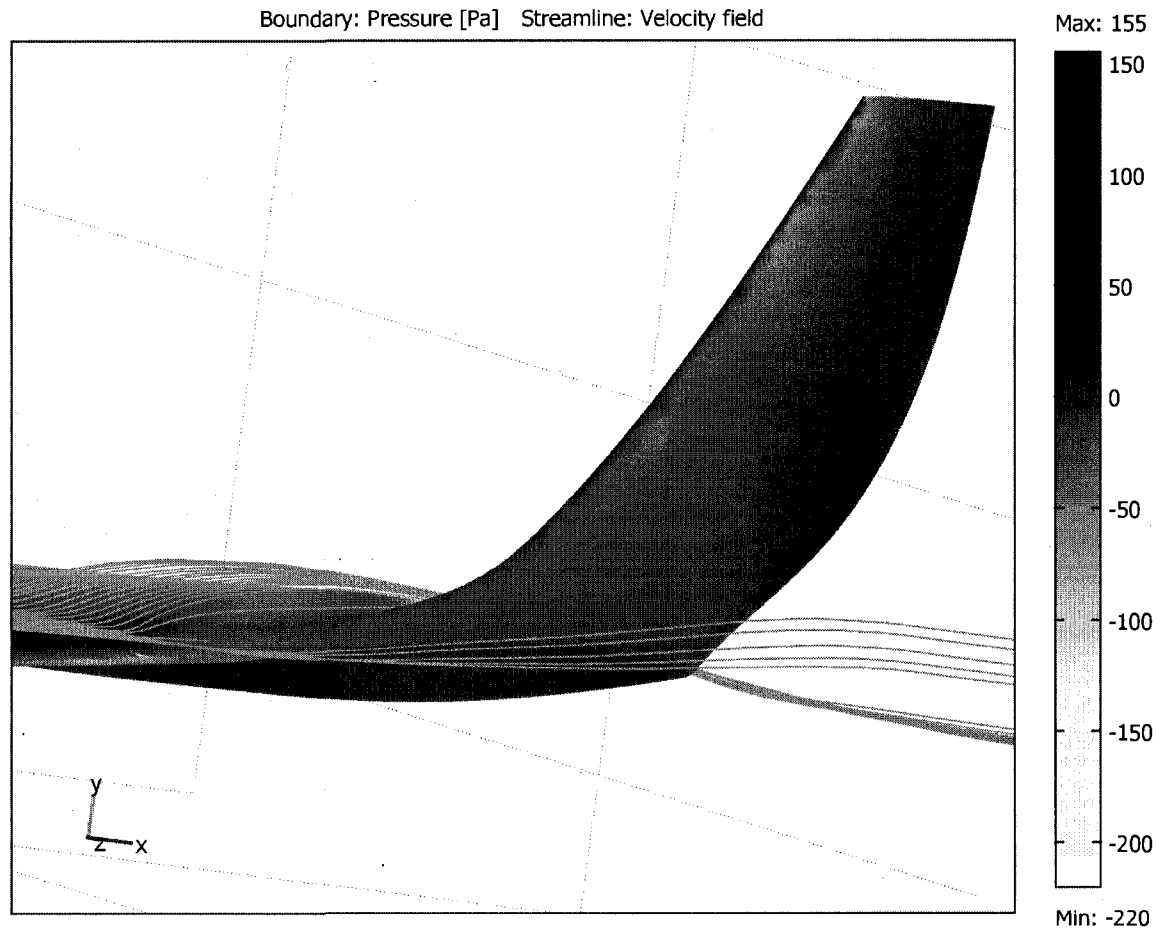


Figure B.24 Pressure and streamline detail near NPD-02 at -2° AOA. For the wing's airfoil, lift coefficient drops off slightly after -1° AOA. This results in a weakening of the wingtip vortices and thus a slightly reduced winglet efficiency. Notice the more pronounced pressure fronts on the leading and trailing edges of the winglet, a possible onset to adverse performance.

NON-PLANAR DEVICE 02 (LOITER, -2° AOA)	Test Section ($k-\epsilon$)	Test Section ($k-\omega$)
Test Flight Condition	Loiter Speed, -2° AOA	
Test Condition Freestream Velocity [m/s]	15.59	
Wing Surface Area [m ²]	0.795	
Winglet Surface Area [m ²]	0.013764	
Wing and Winglet Combined Surface Area [m ²]	0.8083	
Root Chord [m]	0.3	
Subdomain Fluid Density [kg/m ³]	1.2	
Subdomain Fluid Absolute Viscosity [Pa/s]	1.70E-05	
Root Reynolds Number	330141	
Measurement Plane Cross-Sectional Area [m ²]	1.65	
Flowrate (x-direction, in-bound) [m ³ /s]	25.7235	
Flowrate (x-direction, out-bound) [m ³ /s]	25.665427	25.666012
Total Drag Force [N]	2.1704	2.1486
Pressure Integration Over Top Wing Surface [N]	-29.281676	-29.30019
Pressure Integration Over Bottom Wing Surface [N]	10.732910	10.740191
Pressure Integration Over Top Winglet Surface [N]	-0.860592	-0.890124
Pressure Integration Over Bottom Winglet Surface [N]	0.073533	0.074558
Winglet Surface Cant Angle Average [degrees]	18	
Winglet Surface Toe-Twist Angle Average [degrees]	4.5	
Wing Lift Force [N]	40.014586	40.040381
Winglet Lift Force [N]	0.888405668	0.917467102
Winglet Thrust Force [N]	0.073290603	0.075688077
Total Lift Force [N]	40.8781	40.9329
Overall Drag Coefficient	0.0368	0.0365
Overall Lift Coefficient	0.6936	0.6945
Lift-to-Drag Ratio	18.8343	19.0513
Percent Change Drag Coefficient Over Control	-4.89%	-4.75%
Percent Change Lift Coefficient Over Control	0.41%	0.30%
Percent Change Lift-to-Drag Ratio Over Control	5.58%	5.30%

Table B.10 Collected data from the model simulation for Non-Planar Device 02 in loiter, -2° AOA.

NON-PLANAR DEVICE 02 MODEL STATISTICS (LOITER, +2° AOA)	Value
Number of Elements	113375
Degrees of Freedom	868075
Number of Boundary Elements Over Wing	14688
Number of Boundary Elements Over Winglet	3064
Time to Solution ($k-\epsilon$) [s]	5066.490
Time to Solution ($k-\omega$) [s]	7410.132

Table B.11 Model statistics for NPD-02 in loiter at +2° AOA.

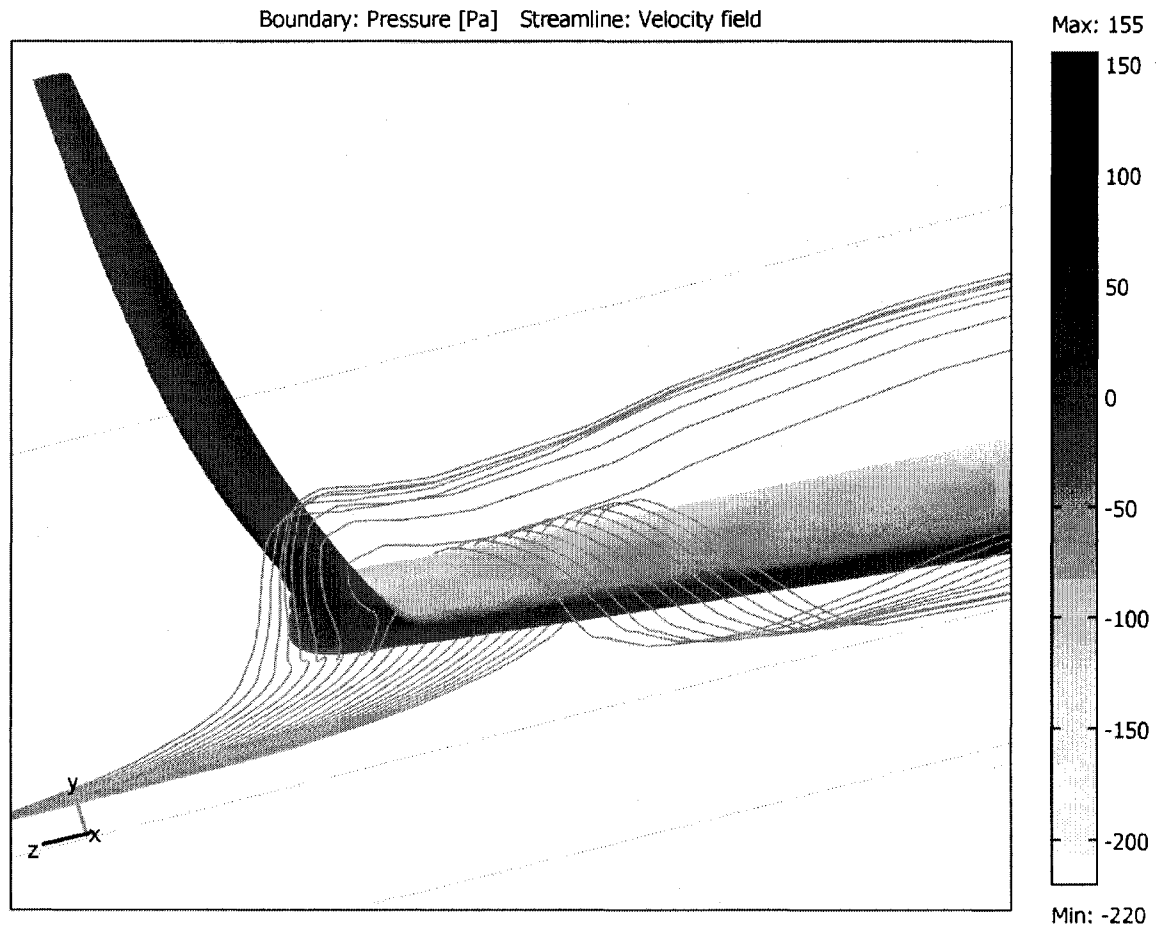


Figure B.25 Pressure and streamline detail near NPD-02 as the streamlines fly past the viewpoint, at +2° AOA. The increased angle-of-attack results in a stronger upwash at the tip and enables the winglet to operate closer to its full potential.

NON-PLANAR DEVICE 02 (LOITER, +2° AOA)	Test Section ($k-\epsilon$)	Test Section ($k-\omega$)
Test Flight Condition	Loiter Speed, +2° AOA	
Test Condition Freestream Velocity [m/s]	15.59	
Wing Surface Area [m ²]	0.795	
Winglet Surface Area [m ²]	0.013764	
Wing and Winglet Combined Surface Area [m ²]	0.8083	
Root Chord [m]	0.3	
Subdomain Fluid Density [kg/m ³]	1.2	
Subdomain Fluid Absolute Viscosity [Pa/s]	1.70E-05	
Root Reynolds Number	330141	
Measurement Plane Cross-Sectional Area [m ²]	1.65	
Flowrate (x-direction, in-bound) [m ³ /s]	25.7235	
Flowrate (x-direction, out-bound) [m ³ /s]	25.661201	25.662510
Total Drag Force [N]	2.3282	2.2793
Pressure Integration Over Top Wing Surface [N]	-42.797962	-43.00151
Pressure Integration Over Bottom Wing Surface [N]	19.928877	19.909915
Pressure Integration Over Top Winglet Surface [N]	-1.097377	-1.112853
Pressure Integration Over Bottom Winglet Surface [N]	0.119103	0.125156
Winglet Surface Cant Angle Average [degrees]	18	
Winglet Surface Toe-Twist Angle Average [degrees]	4.5	
Wing Lift Force [N]	62.726839	62.911425
Winglet Lift Force [N]	1.156941231	1.177416527
Winglet Thrust Force [N]	0.095443921	0.097133067
Total Lift Force [N]	63.8449	64.0498
Overall Drag Coefficient	0.0395	0.0387
Overall Lift Coefficient	1.0833	1.0867
Lift-to-Drag Ratio	27.4229	28.1007
Percent Change Drag Coefficient Over Control	-3.03%	-3.99%
Percent Change Lift Coefficient Over Control	2.04%	2.21%
Percent Change Lift-to-Drag Ratio Over Control	5.23%	6.46%

Table B.12 Collected data from the model simulation for Non-Planar Device 02 in loiter, -2° AOA.

NON-PLANAR DEVICE 02 MODEL STATISTICS (LOITER, +4° AOA)	Value
Number of Elements	97107
Degrees of Freedom	756829
Number of Boundary Elements Over Wing	14364
Number of Boundary Elements Over Winglet	2454
Time to Solution ($k-\epsilon$) [s]	5066.490
Time to Solution ($k-\omega$) [s]	7410.132

Table B.13 Model statistics for NPD-02 in loiter at +4° AOA.

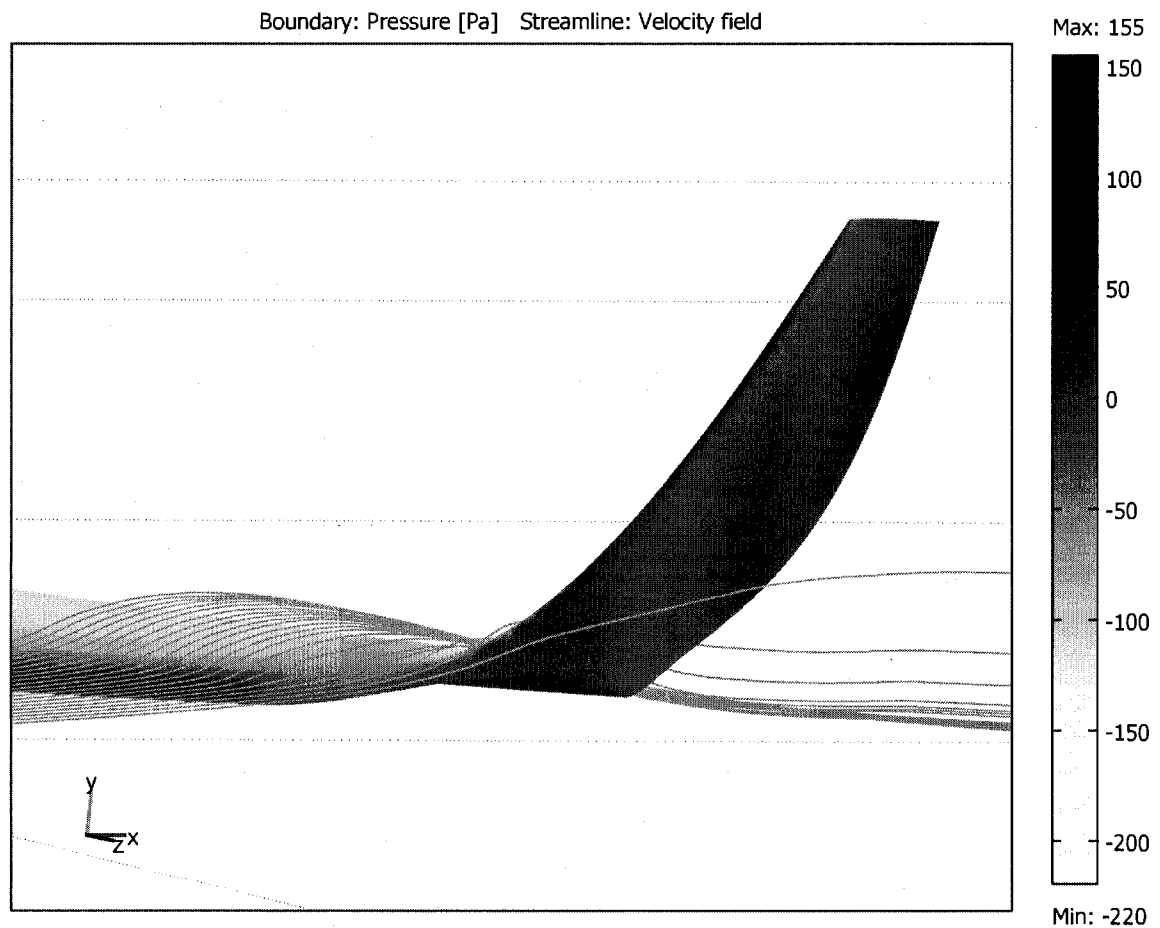


Figure B.26 Pressure distribution and streamline detail on NPD-02 at +4° AOA. The flow in the area near the winglet root still displays outstanding adherence. Notice how the fluid spills from underneath the bottom of the leading edge into the bottom surface of the winglet.

NON-PLANAR DEVICE 02 (LOITER, +4° AOA)	Test Section (k-ε)	Test Section (k-ω)
Test Flight Condition	Loiter Speed, +4° AOA	
Test Condition Freestream Velocity [m/s]	15.59	
Wing Surface Area [m ²]	0.795	
Winglet Surface Area [m ²]	0.013764	
Wing and Winglet Combined Surface Area [m ²]	0.8083	
Root Chord [m]	0.3	
Subdomain Fluid Density [kg/m ³]	1.2	
Subdomain Fluid Absolute Viscosity [Pa/s]	1.70E-05	
Root Reynolds Number	330141	
Measurement Plane Cross-Sectional Area [m ²]	1.65	
Flowrate (x-direction, in-bound) [m ³ /s]	25.7235	
Flowrate (x-direction, out-bound) [m ³ /s]	25.644610	25.646014
Total Drag Force [N]	2.9472	2.8948
Pressure Integration Over Top Wing Surface [N]	-48.942532	-49.981541
Pressure Integration Over Bottom Wing Surface [N]	22.958101	23.098631
Pressure Integration Over Top Winglet Surface [N]	-1.071289	-1.09841
Pressure Integration Over Bottom Winglet Surface [N]	0.14215	0.140832
Winglet Surface Cant Angle Average [degrees]	18	
Winglet Surface Toe-Twist Angle Average [degrees]	4.5	
Wing Lift Force [N]	71.900633	73.080172
Winglet Lift Force [N]	1.154049068	1.178589179
Winglet Thrust Force [N]	0.095205327	0.097229807
Total Lift Force [N]	73.0102	74.2135
Overall Drag Coefficient	0.0500	0.0491
Overall Lift Coefficient	1.2388	1.2592
Lift-to-Drag Ratio	24.7725	25.6364
Percent Change Drag Coefficient Over Control	-3.35%	-3.80%
Percent Change Lift Coefficient Over Control	1.69%	3.10%
Percent Change Lift-to-Drag Ratio Over Control	5.21%	7.17%

Table B.14 Collected data from the model simulation for Non-Planar Device 02 in loiter, +4° AOA.

B.5 Non-Planar Device 03 (NPD-03)

NON-PLANAR DEVICE 03 MODEL STATISTICS (LOITER, LEVEL FLIGHT)	Value
Number of Elements	97612
Degrees of Freedom	761913
Number of Boundary Elements Over Wing	14796
Number of Boundary Elements Over Winglet	2316
Time to Solution ($k-\epsilon$) [s]	5198.532
Time to Solution ($k-\omega$) [s]	Not Recorded

Table B.15 Model statistics for NPD-03 in loiter, level flight.

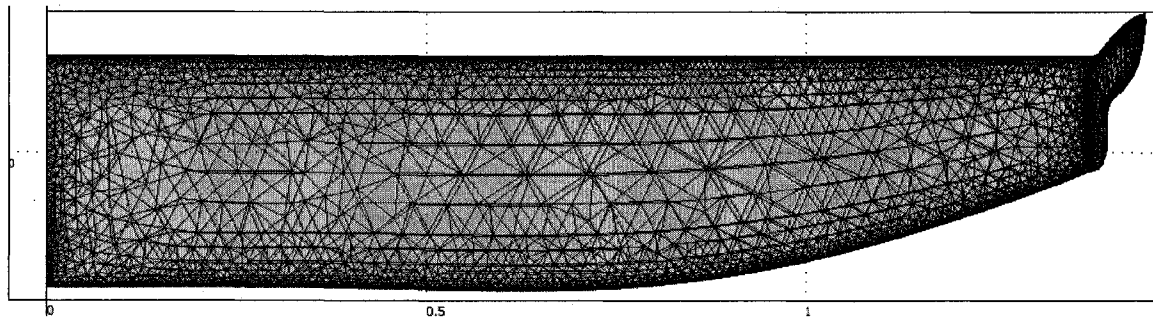


Figure B.27 Mesh detail for Non-Planar Device 03.

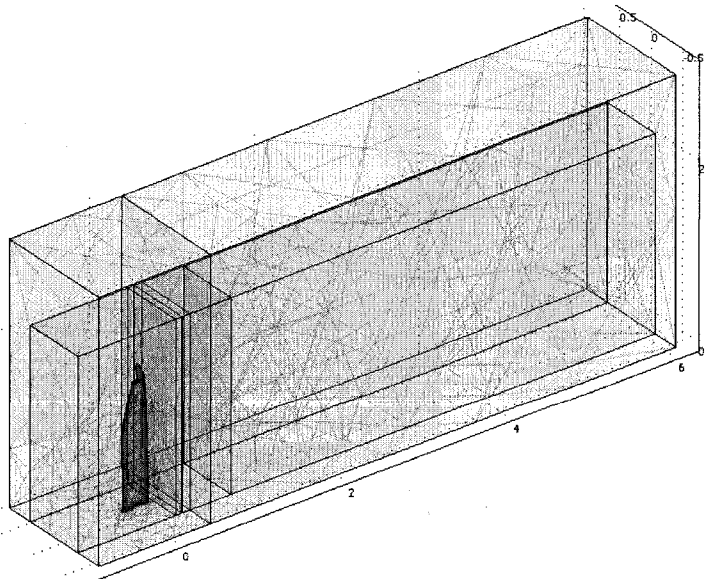


Figure B.28 Mesh overview of the model for NPD-03.

NON-PLANAR DEVICE 03 (LOITER, LEVEL FLIGHT)	Test Section ($k-\epsilon$)	Test Section ($k-\omega$)
Test Flight Condition	Loiter Speed, Level Flight	
Test Condition Freestream Velocity [m/s]	15.59	
Wing Surface Area [m ²]	0.795	
Winglet Surface Area [m ²]	0.015403	
Wing and Winglet Combined Surface Area [m ²]	0.8099	
Root Chord [m]	0.3	
Subdomain Fluid Density [kg/m ³]	1.2	
Subdomain Fluid Absolute Viscosity [Pa/s]	1.70E-05	
Root Reynolds Number	330141	
Measurement Plane Cross-Sectional Area [m ²]	1.65	
Flowrate (x-direction, in-bound) [m ³ /s]	25.7235	
Flowrate (x-direction, out-bound) [m ³ /s]	25.664996	25.665702
Total Drag Force [N]	2.1865	2.1601
Pressure Integration Over Top Wing Surface [N]	-36.323449	-36.325422
Pressure Integration Over Bottom Wing Surface [N]	15.897607	15.887123
Pressure Integration Over Top Winglet Surface [N]	-0.89723	-0.898124
Pressure Integration Over Bottom Winglet Surface [N]	0.056815	0.057646
Winglet Surface Cant Angle Average [degrees]	18	
Winglet Surface Toe-Twist Angle Average [degrees]	4.5	
Wing Lift Force [N]	52.221056	52.212545
Winglet Lift Force [N]	0.907350714	0.908991287
Winglet Thrust Force [N]	0.074853508	0.07498885
Total Lift Force [N]	53.1284	53.1215
Overall Drag Coefficient	0.0370	0.0366
Overall Lift Coefficient	0.8996	0.8995
Lift-to-Drag Ratio	24.2984	24.5917
Percent Change Drag Coefficient Over Control	-4.04%	-4.14%
Percent Change Lift Coefficient Over Control	2.67%	2.45%
Percent Change Lift-to-Drag Ratio Over Control	6.99%	6.87%

Table B.16 Collected data from the model simulation for Non-Planar Device 03 (loiter, level).

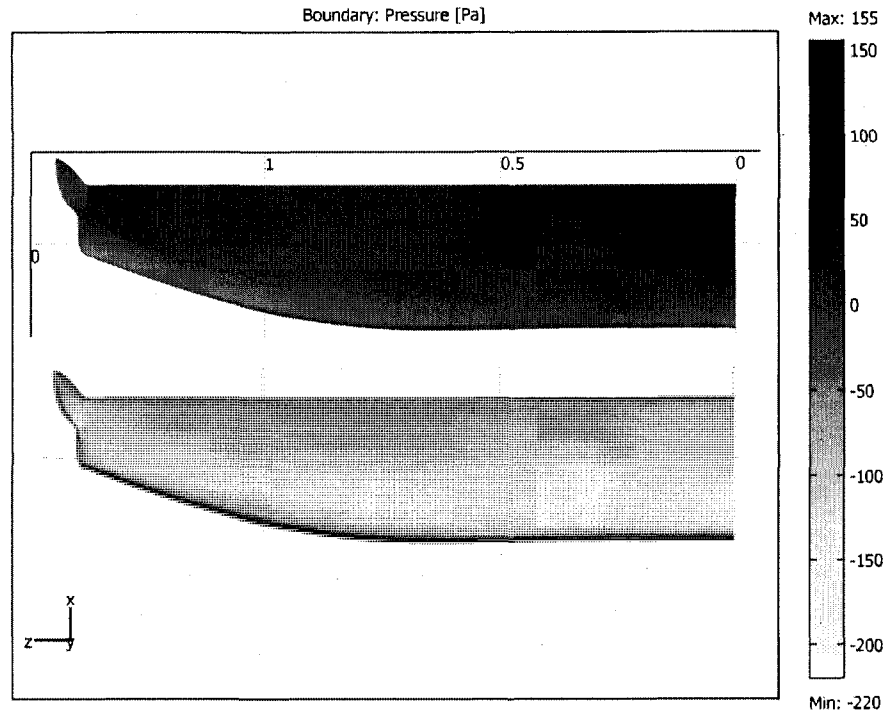


Figure B.29 Boundary pressure distribution over NPD-03 in loiter, level flight. This looks very similar to NPD-02 and as a matter of fact it is nearly identical. The real issue is with the non-planar surface itself, although the performance decrease was not so significant.

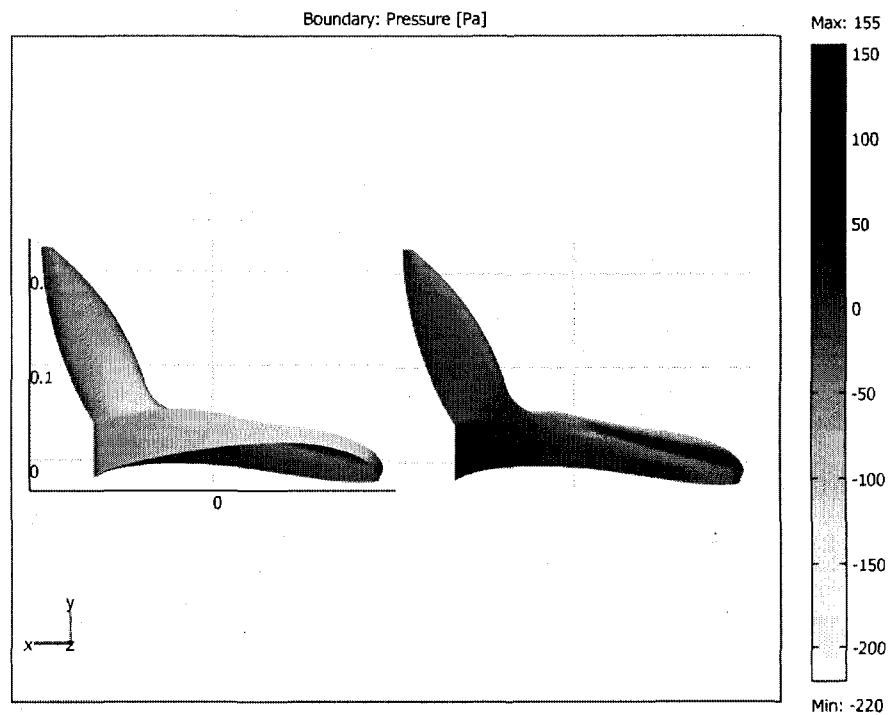


Figure B.30 Boundary pressure distribution over NPD-03's inner and outer surfaces. Notice the lack of useful aerodynamic forces at the tip.

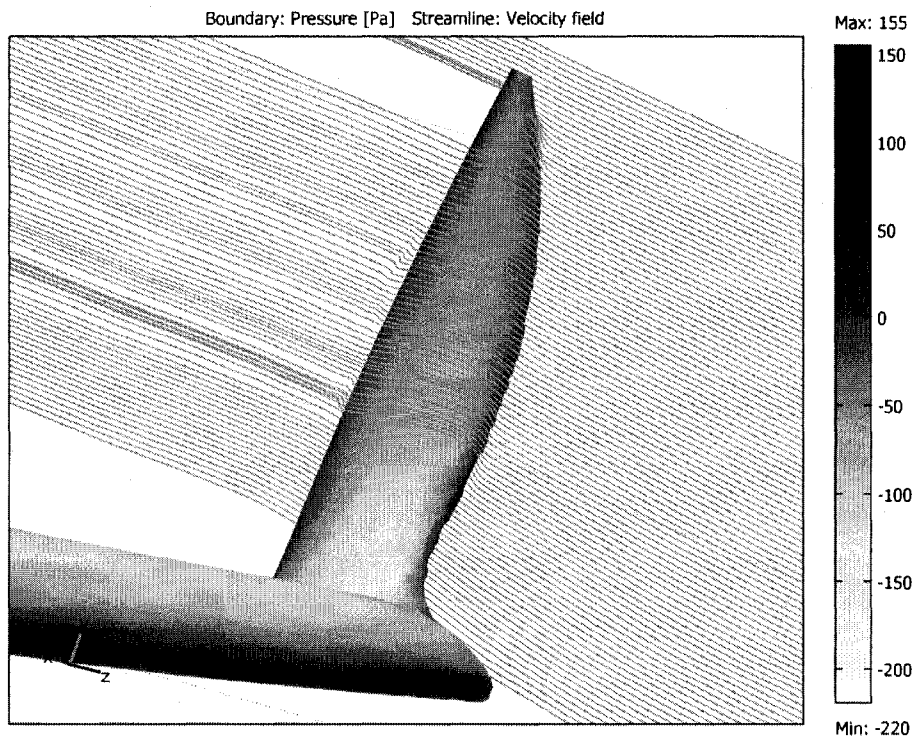
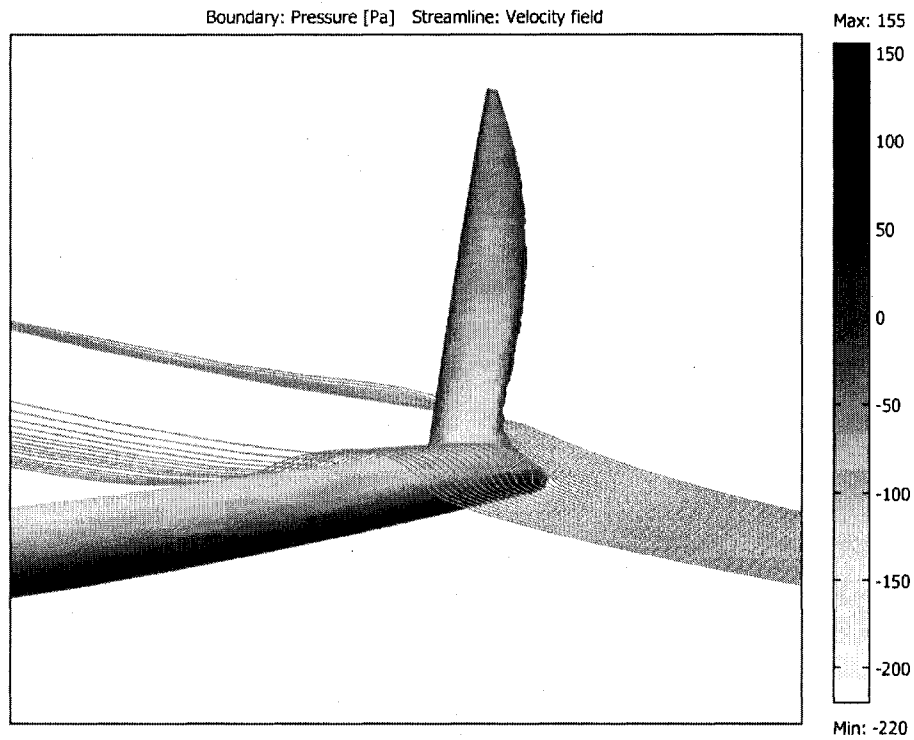


Figure B.31 Streamline detail around NPD-03 in loiter, level flight. At the winglet's root, the flow conditions seem to be typical of what had been seen with NPD-02. However at the tip we notice a strange pattern with the streamlines, most likely attributable to a laminar separation bubble, common to airfoils operating at low Reynolds numbers.

B.6 Non-Planar Device 04 (NPD-04)

NON-PLANAR DEVICE 04 MODEL STATISTICS (LOITER, LEVEL FLIGHT)	Value
Number of Elements	99735
Degrees of Freedom	777021
Number of Boundary Elements Over Wing	14660
Number of Boundary Elements Over Winglet	2610
Time to Solution ($k-\epsilon$) [s]	3682.518
Time to Solution ($k-\omega$) [s]	4091.532

Table B.17 Model statistics for NPD-04 in loiter, level flight.

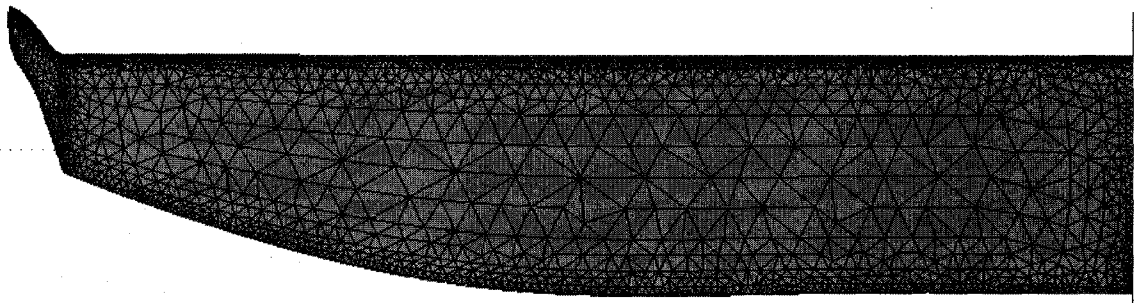


Figure B.32 Mesh detail for Non-Planar Device 04.

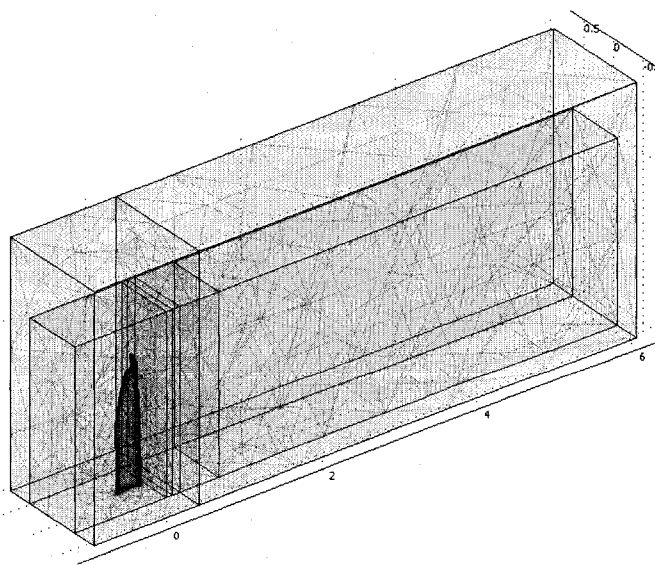


Figure B.33 Mesh overview of the model for NPD-04.

NON-PLANAR DEVICE 04 (LOITER, LEVEL FLIGHT)	Test Section ($k-\epsilon$)	Test Section ($k-\omega$)
Test Flight Condition	Loiter Speed, Level Flight	
Test Condition Freestream Velocity [m/s]	15.59	
Wing Surface Area [m ²]	0.795	
Winglet Surface Area [m ²]	0.014391	
Wing and Winglet Combined Surface Area [m ²]	0.8089	
Root Chord [m]	0.3	
Subdomain Fluid Density [kg/m ³]	1.2	
Subdomain Fluid Absolute Viscosity [Pa/s]	1.70E-05	
Root Reynolds Number	330141	
Measurement Plane Cross-Sectional Area [m ²]	1.65	
Flowrate (x-direction, in-bound) [m ³ /s]	25.7235	
Flowrate (x-direction, out-bound) [m ³ /s]	25.665666	25.666691
Total Drag Force [N]	2.1615	2.1232
Pressure Integration Over Top Wing Surface [N]	-36.176523	-36.291034
Pressure Integration Over Bottom Wing Surface [N]	15.823724	15.90192
Pressure Integration Over Top Winglet Surface [N]	-0.900852	-0.911421
Pressure Integration Over Bottom Winglet Surface [N]	0.04248	0.03294
Winglet Surface Cant Angle Average [degrees]	18	
Winglet Surface Toe-Twist Angle Average [degrees]	4.5	
Wing Lift Force [N]	52.000247	52.192954
Winglet Lift Force [N]	0.897162046	0.8981407
Winglet Thrust Force [N]	0.074012976	0.0740937
Total Lift Force [N]	52.8974	53.0911
Overall Drag Coefficient	0.0366	0.0360
Overall Lift Coefficient	0.8968	0.9001
Lift-to-Drag Ratio	24.4727	25.0050
Percent Change Drag Coefficient Over Control	-5.02%	-5.66%
Percent Change Lift Coefficient Over Control	2.35%	2.52%
Percent Change Lift-to-Drag Ratio Over Control	7.75%	8.67%

Table B.18 Collected data from the model simulation for Non-Planar Device 04 (loiter, level).

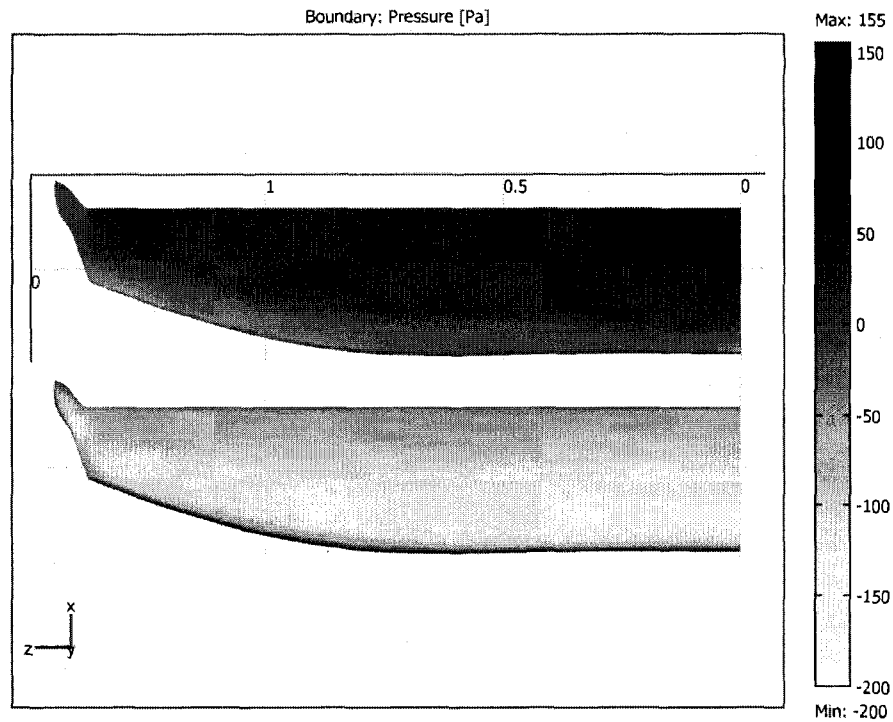


Figure B.34 Bottom and top surface boundary pressure distribution. As with NPD-02 and NPD-03, not a lot different here.

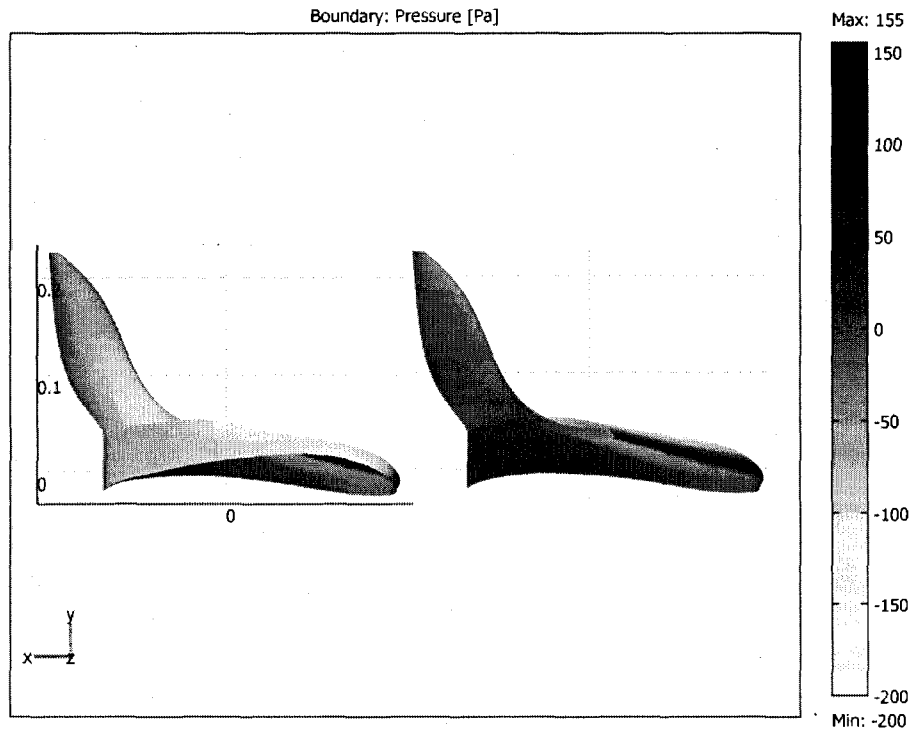


Figure B.35 Inside and outside surfaces for NPD-04, showcasing the boundary pressure distribution. The pressure gradient at the tip is more conducive to the production of useful aerodynamic forces.

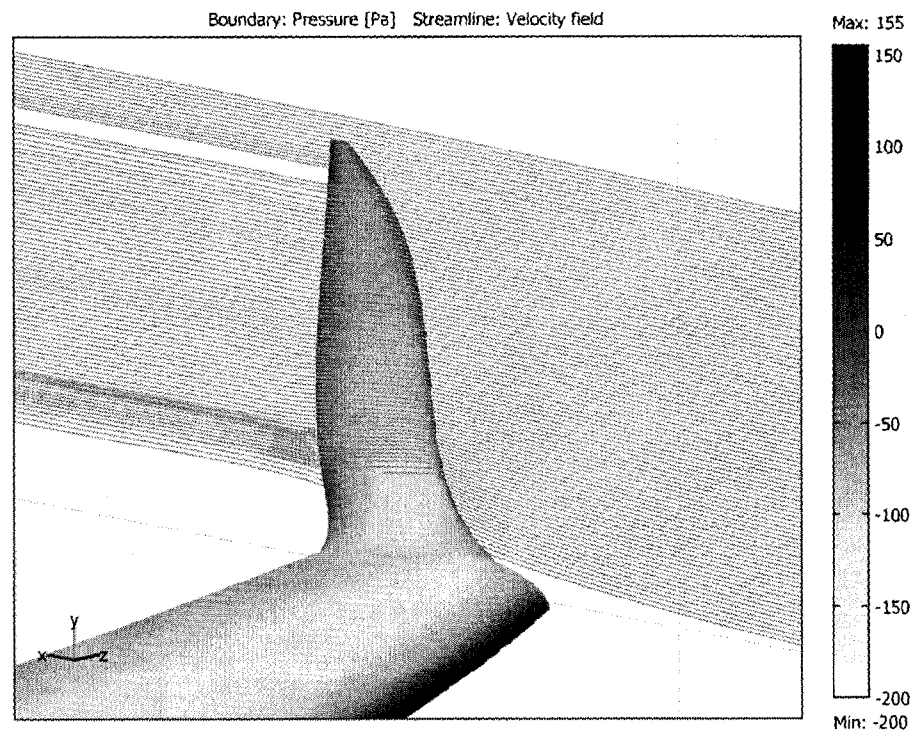
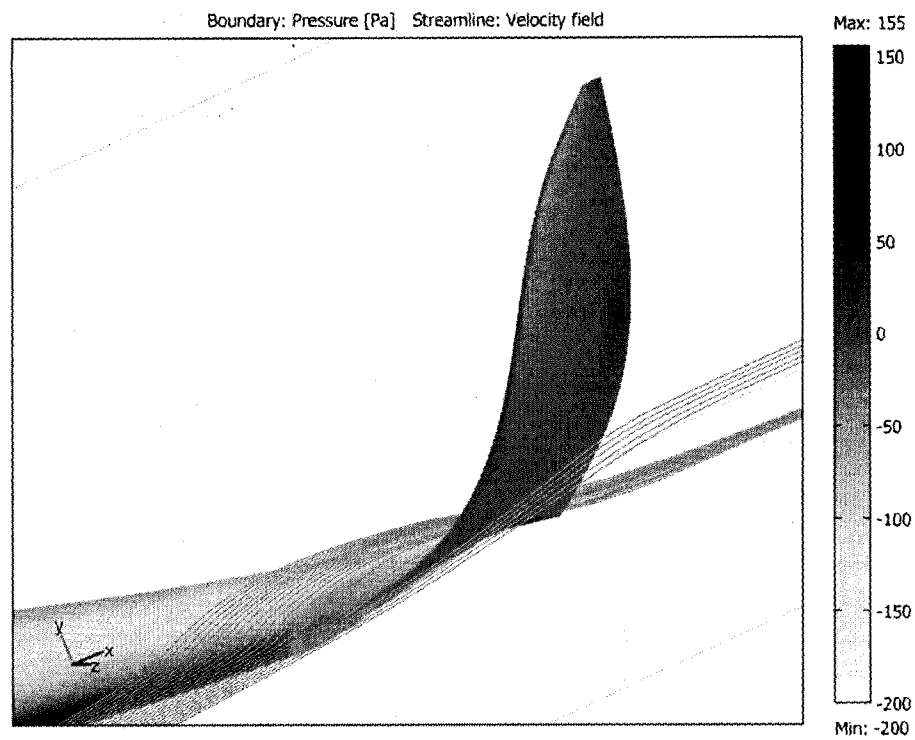


Figure B.36 Boundary pressure distribution and streamline detail near NPD-04 in loiter, level flight. Unfortunately, the same issues as with NPD-03 manifest themselves here at the winglet tip. The local Reynolds number is simply too low for that part of the winglet to produce any useful aerodynamic forces.

NON-PLANAR DEVICE 04 MODEL STATISTICS (LOITER, -2° AOA)	Value
Number of Elements	98930
Degrees of Freedom	771692
Number of Boundary Elements Over Wing	14676
Number of Boundary Elements Over Winglet	2688
Time to Solution ($k-\epsilon$) [s]	5175.893
Time to Solution ($k-\omega$) [s]	6713.537

Table B.19 Model statistics for NPD-04 in loiter, -2° AOA.

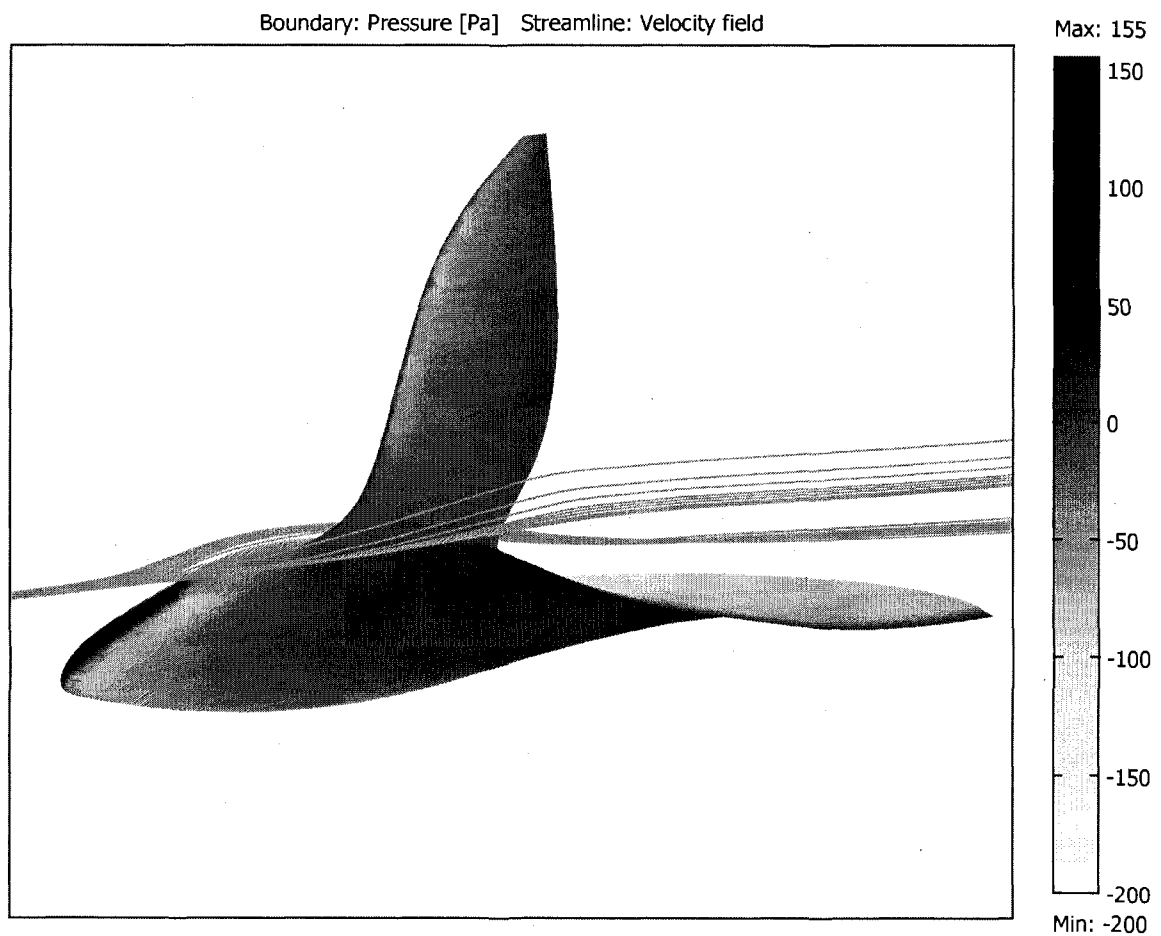


Figure B.37 Boundary pressure distribution and streamline detail near NPD-04 in loiter at -2° AOA. As in Figure B.24 we notice a decrease in the strength of the wingtip vortices, due to the lessened lift coefficient, but the winglet is still effective at the root.

NON-PLANAR DEVICE 04 (LOITER, -2° AOA)	Test Section ($k-\epsilon$)	Test Section ($k-\omega$)
Test Flight Condition	Loiter Speed, -2° AOA	
Test Condition Freestream Velocity [m/s]	15.59	
Wing Surface Area [m ²]	0.795	
Winglet Surface Area [m ²]	0.014391	
Wing and Winglet Combined Surface Area [m ²]	0.8089	
Root Chord [m]	0.3	
Subdomain Fluid Density [kg/m ³]	1.2	
Subdomain Fluid Absolute Viscosity [Pa/s]	1.70E-05	
Root Reynolds Number	330141	
Measurement Plane Cross-Sectional Area [m ²]	1.65	
Flowrate (x-direction, in-bound) [m ³ /s]	25.7235	
Flowrate (x-direction, out-bound) [m ³ /s]	25.660811	25.662131
Total Drag Force [N]	2.3427	2.2934
Pressure Integration Over Top Wing Surface [N]	-29.613004	-29.90125
Pressure Integration Over Bottom Wing Surface [N]	11.037146	11.10014
Pressure Integration Over Top Winglet Surface [N]	-0.618188	-0.622418
Pressure Integration Over Bottom Winglet Surface [N]	0.041106	0.051082
Winglet Surface Cant Angle Average [degrees]	18	
Winglet Surface Toe-Twist Angle Average [degrees]	4.5	
Wing Lift Force [N]	40.65015	41.00139
Winglet Lift Force [N]	0.627025855	0.6405366
Winglet Thrust Force [N]	0.051727611	0.0528422
Total Lift Force [N]	41.2520	41.6166
Overall Drag Coefficient	0.0397	0.0389
Overall Lift Coefficient	0.6994	0.7056
Lift-to-Drag Ratio	17.6087	18.1459
Percent Change Drag Coefficient Over Control	2.58%	1.60%
Percent Change Lift Coefficient Over Control	1.25%	1.89%
Percent Change Lift-to-Drag Ratio Over Control	-1.29%	0.29%

Table B.20 Collected data from the model simulation for Non-Planar Device 04 (loiter, -2° AOA).
Notice the increase in drag while still maintaining a lift increase.

NON-PLANAR DEVICE 04 MODEL STATISTICS (LOITER, +2° AOA)	Value
Number of Elements	100107
Degrees of Freedom	780407
Number of Boundary Elements Over Wing	14712
Number of Boundary Elements Over Winglet	2688
Time to Solution ($k-\epsilon$) [s]	5763.592
Time to Solution ($k-\omega$) [s]	8720.532

Table B.21 Model statistics for NPD-04 in loiter, +2° AOA.

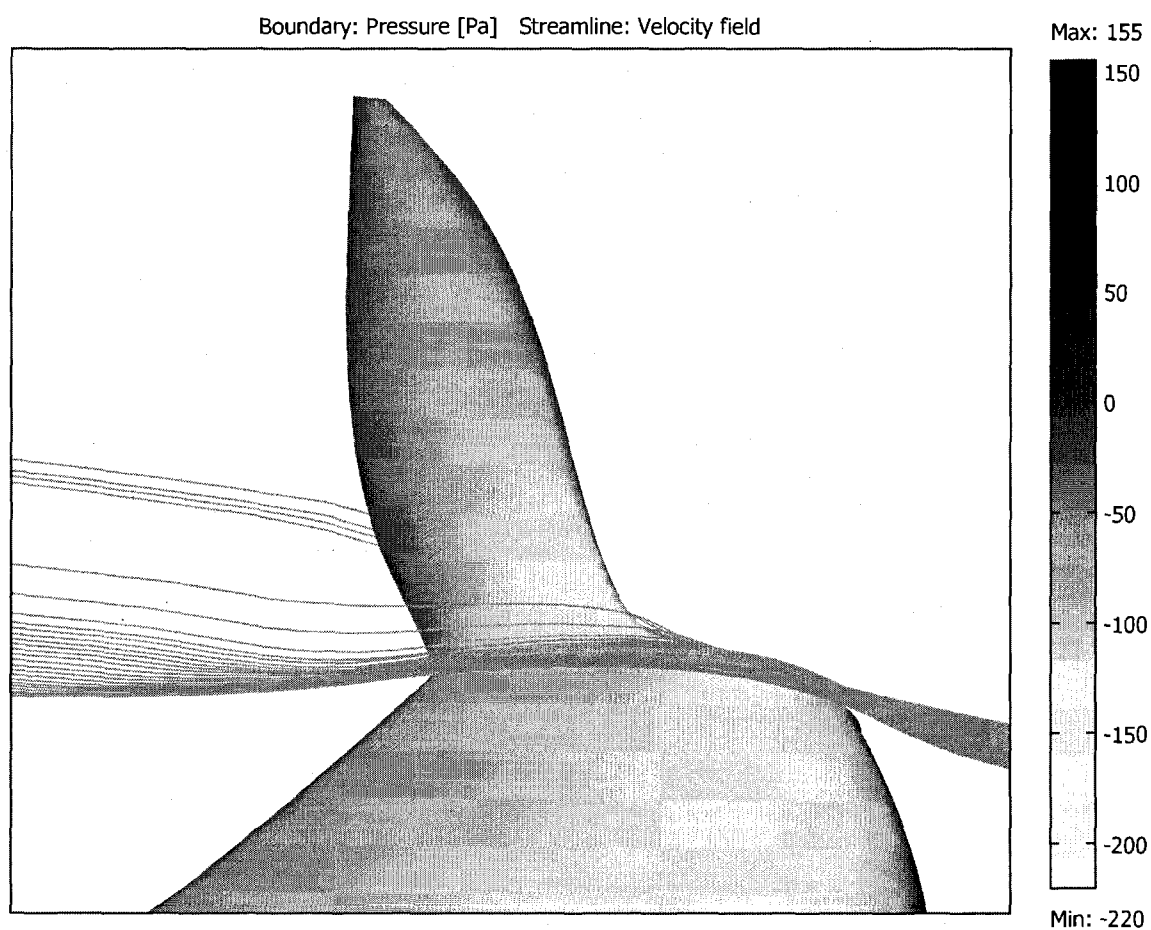


Figure B.38 Boundary pressure distribution and streamline detail on the inside face of NPD-04 in loiter at +2° AOA. Again, adherence of the flow at the root is still excellent. Notice the progressive dissipation of the useful pressure gradient, starting nearly one third of the way up the winglet.

The reason for this drop off in performance is likely due to the formation of a laminar separation bubble, propagating down the span of the device.

NON-PLANAR DEVICE 04 (LOITER, +2° AOA)	Test Section (<i>k-ε</i>)	Test Section (<i>k-ω</i>)
Test Flight Condition	Loiter Speed, +2° AOA	
Test Condition Freestream Velocity [m/s]	15.59	
Wing Surface Area [m ²]	0.795	
Winglet Surface Area [m ²]	0.014391	
Wing and Winglet Combined Surface Area [m ²]	0.8089	
Root Chord [m]	0.3	
Subdomain Fluid Density [kg/m ³]	1.2	
Subdomain Fluid Absolute Viscosity [Pa/s]	1.70E-05	
Root Reynolds Number	330141	
Measurement Plane Cross-Sectional Area [m ²]	1.65	
Flowrate (x-direction, in-bound) [m ³ /s]	25.7235	
Flowrate (x-direction, out-bound) [m ³ /s]	25.658102	25.659915
Total Drag Force [N]	2.4438	2.3762
Pressure Integration Over Top Wing Surface [N]	-42.659718	-42.661332
Pressure Integration Over Bottom Wing Surface [N]	19.905014	19.99092
Pressure Integration Over Top Winglet Surface [N]	-1.168404	-1.171092
Pressure Integration Over Bottom Winglet Surface [N]	0.107957	0.091995
Winglet Surface Cant Angle Average [degrees]	18	
Winglet Surface Toe-Twist Angle Average [degrees]	4.5	
Wing Lift Force [N]	62.564732	62.652252
Winglet Lift Force [N]	1.213891446	1.2012671
Winglet Thrust Force [N]	0.10014213	0.0991007
Total Lift Force [N]	63.7398	63.8146
Overall Drag Coefficient	0.0414	0.0403
Overall Lift Coefficient	1.0806	1.0819
Lift-to-Drag Ratio	26.0820	26.8562
Percent Change Drag Coefficient Over Control	1.70%	0.01%
Percent Change Lift Coefficient Over Control	1.80%	1.76%
Percent Change Lift-to-Drag Ratio Over Control	0.09%	1.75%

Table B.22 Collected data from the model simulation for Non-Planar Device 04 (loiter, +2° AOA).

NON-PLANAR DEVICE 04 MODEL STATISTICS (LOITER, +4° AOA)	Value
Number of Elements	134789
Degrees of Freedom	930930
Number of Boundary Elements Over Wing	14688
Number of Boundary Elements Over Winglet	2956
Time to Solution ($k-\epsilon$) [s]	71679.255
Time to Solution ($k-\omega$) [s]	73841.420

Table B.23 Model statistics for NPD-04 in loiter, +4° AOA.

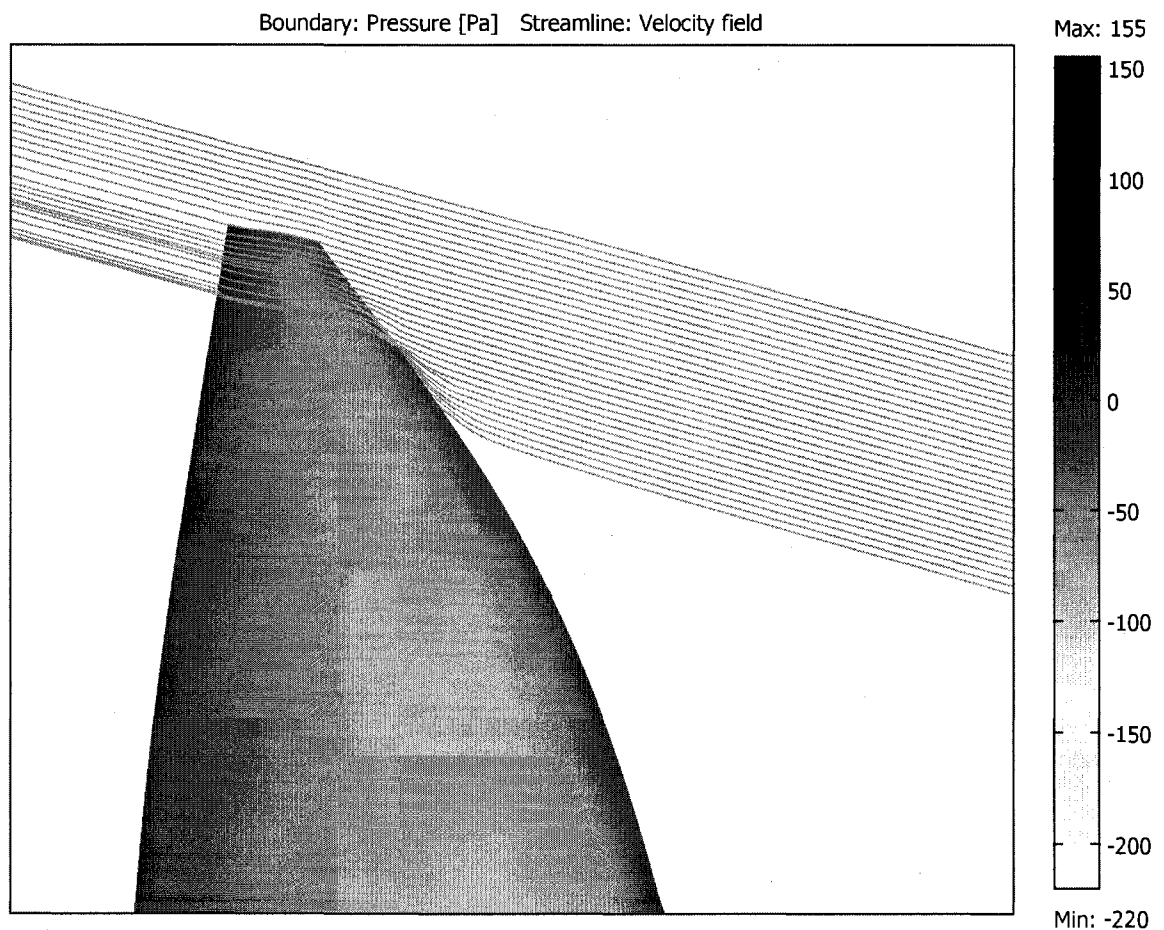


Figure B.39 Boundary pressure distribution and streamline detail near NPD-04's tip in loiter at +4° AOA. Notice the bunching up of streamlines around that particular area, near the leading edge. This coincides with the winglet tip extension that was put in play with NPD-03 and NPD-04.

NON-PLANAR DEVICE 04 (LOITER, +4° AOA)	Test Section ($k-\epsilon$)	Test Section ($k-\omega$)
Test Flight Condition	Loiter Speed, +4° AOA	
Test Condition Freestream Velocity [m/s]	15.59	
Wing Surface Area [m ²]	0.795	
Winglet Surface Area [m ²]	0.014391	
Wing and Winglet Combined Surface Area [m ²]	0.8089	
Root Chord [m]	0.3	
Subdomain Fluid Density [kg/m ³]	1.2	
Subdomain Fluid Absolute Viscosity [Pa/s]	1.70E-05	
Root Reynolds Number	330141	
Measurement Plane Cross-Sectional Area [m ²]	1.65	
Flowrate (x-direction, in-bound) [m ³ /s]	25.7235	
Flowrate (x-direction, out-bound) [m ³ /s]	25.642161	25.643561
Total Drag Force [N]	3.0386	2.9864
Pressure Integration Over Top Wing Surface [N]	-48.022616	-48.23148
Pressure Integration Over Bottom Wing Surface [N]	24.515157	24.80164
Pressure Integration Over Top Winglet Surface [N]	-0.90541	-1.035199
Pressure Integration Over Bottom Winglet Surface [N]	0.072527	0.099151
Winglet Surface Cant Angle Average [degrees]	18	
Winglet Surface Toe-Twist Angle Average [degrees]	4.5	
Wing Lift Force [N]	72.537773	73.03312
Winglet Lift Force [N]	0.930073356	1.078831
Winglet Thrust Force [N]	0.076728053	0.0890001
Total Lift Force [N]	73.4231	74.0668
Overall Drag Coefficient	0.0515	0.0506
Overall Lift Coefficient	1.2448	1.2557
Lift-to-Drag Ratio	24.1637	24.8018
Percent Change Drag Coefficient Over Control	-0.43%	-0.84%
Percent Change Lift Coefficient Over Control	2.18%	2.81%
Percent Change Lift-to-Drag Ratio Over Control	2.62%	3.68%

Table B.24 Collected data from the model simulation for Non-Planar Device 04 (loiter, +4° AOA).

APPENDIX C

WING-FUSELAGE JUNCTION CONTROL SPECIMEN DATA

WING-FUSELAGE JUNCTION CONTROL SPECIMEN MODEL STATISTICS (LOITER, LEVEL FLIGHT)	Value
Number of Elements	70263
Degrees of Freedom	562542
Number of Boundary Elements Over Geometry	7970
Time to Solution ($k-\varepsilon$) [s]	1762.289
Time to Solution ($k-\omega$) [s]	1804.634

Table C.1 Model statistics for Wing-Fuselage Junction Control Specimen in loiter, level flight.

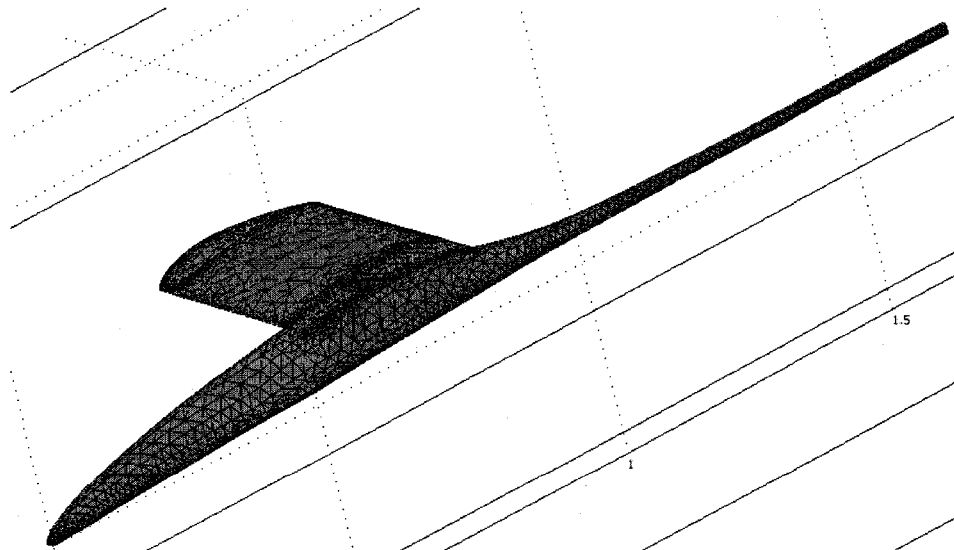


Figure C.1 Mesh detail of the Wing-Fuselage Junction Control Specimen model.

WING-FUSELAGE JUNCTION CONTROL SPECIMEN (LOITER, LEVEL FLIGHT)	Test Section ($k-\epsilon$)	Test Section ($k-\omega$)
Test Flight Condition	Loiter Speed, Level Flight	
Test Condition Freestream Velocity [m/s]	15.59	
Wing Section Surface Area [m ²]	0.088226	
Total Wing-Fuselage Junction Surface Area [m ²]	0.049466	
Overall Wetted Area [m ²]	0.368297	
Root Chord [m]	0.3	
Subdomain Fluid Density [kg/m ³]	1.2	
Subdomain Fluid Absolute Viscosity [Pa/s]	1.70E-05	
Root Reynolds Number	330141	
Measurement Plane Cross-Sectional Area [m ²]	0.285	
Flowrate (x-direction, in-bound) [m ³ /s]	4.44315	
Flowrate (x-direction, out-bound) [m ³ /s]	4.426710	4.426875
Total Drag Force [N]	0.6140	0.6078
Pressure Integration Over Junction Surface [N]	-4.173612	-4.18534
Pressure Integration Over Top Wing Surface [N]	-10.37768	-10.41908
Pressure Integration Over Bottom Wing Surface [N]	4.389015	4.405489
Junction Lift Force [N]	4.173612	4.185340
Junction Lift Coefficient	0.578578	0.580204
Wing Section Lift Force [N]	14.7667	14.8246
Wing Section Lift Coefficient	1.1477	1.1522
Overall Model Drag Coefficient	0.011432	0.011317
Overall Model Lift Coefficient	0.352651	0.353947

Table C.2 Raw and processed data for Wing-Fuselage Junction Control Specimen in loiter, level flight.

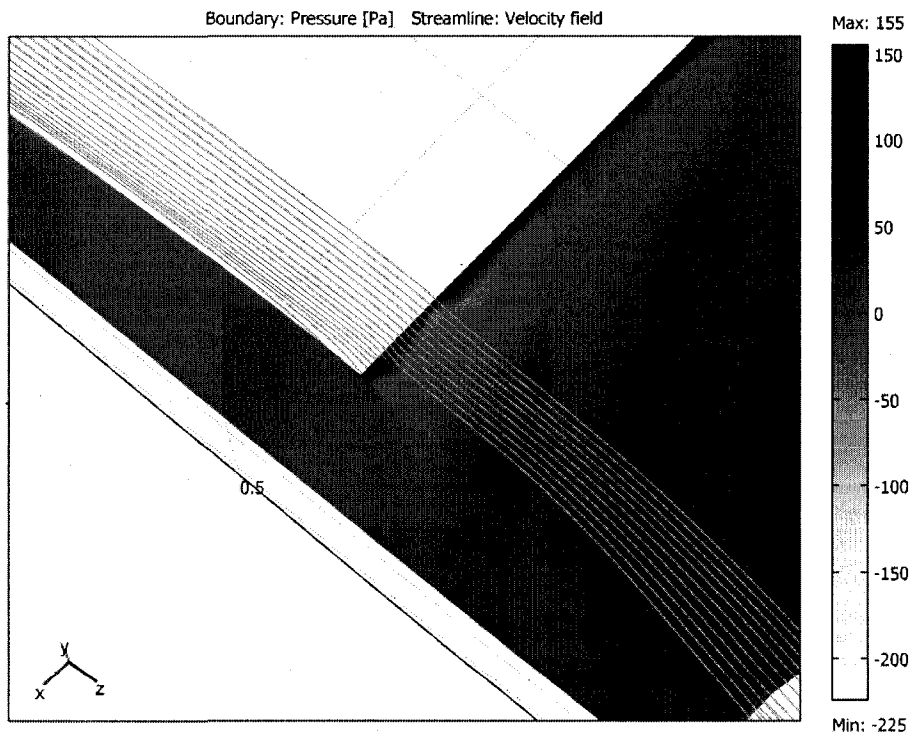
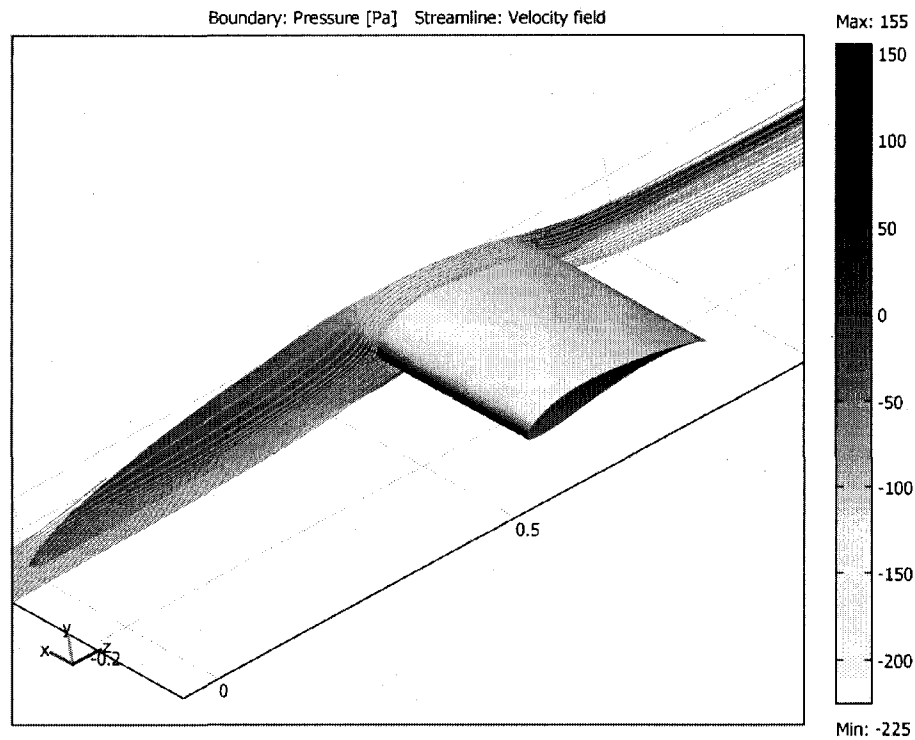


Figure C.2 Streamline detail and boundary pressure distribution for loiter, level flight in a top plan view and a view of the underside. Notice, on the bottom figure, the varying pressure gradient around the wing root. This is one of the few aspects a better wing-fuselage junction can help improve.

WING-FUSELAGE JUNCTION CONTROL SPECIMEN MODEL STATISTICS (LOITER, +2° AOA)	Value
Number of Elements	68884
Degrees of Freedom	551580
Number of Boundary Elements Over Geometry	7682
Time to Solution ($k-\epsilon$) [s]	1820.978
Time to Solution ($k-\omega$) [s]	1910.421

Table C.3 Model statistics for Wing-Fuselage Junction Control Specimen in loiter, level flight.

WING-FUSELAGE JUNCTION CONTROL SPECIMEN (LOITER, +2° AOA)	Test Section ($k-\epsilon$)	Test Section ($k-\omega$)
Test Flight Condition	Loiter Speed, +2° AOA	
Test Condition Freestream Velocity [m/s]	15.59	
Wing Section Surface Area [m ²]	0.088226	
Total Wing-Fuselage Junction Surface Area [m ²]	0.049466	
Overall Wetted Area [m ²]	0.368297	
Root Chord [m]	0.3	
Subdomain Fluid Density [kg/m ³]	1.2	
Subdomain Fluid Absolute Viscosity [Pa/s]	1.70E-05	
Root Reynolds Number	330141	
Measurement Plane Cross-Sectional Area [m ²]	0.285	
Flowrate (x-direction, in-bound) [m ³ /s]	4.44315	
Flowrate (x-direction, out-bound) [m ³ /s]	4.424689	4.424854
Total Drag Force [N]	0.6893	0.6832
Pressure Integration Over Junction Surface [N]	-4.595392	-4.597592
Pressure Integration Over Top Wing Surface [N]	-12.042286	-12.123413
Pressure Integration Over Bottom Wing Surface [N]	5.370252	5.384860
Junction Lift Force [N]	4.595392	4.597592
Junction Lift Coefficient	0.637048	0.637353
Wing Section Lift Force [N]	17.4125	17.5083
Wing Section Lift Coefficient	1.3534	1.3608
Overall Model Drag Coefficient	0.012834	0.012720
Overall Model Lift Coefficient	0.409768	0.411591

Table C.4 Raw and processed data for Wing-Fuselage Junction Control Specimen in loiter at +2° AOA.

WING-FUSELAGE JUNCTION CONTROL SPECIMEN MODEL STATISTICS (LOITER, +4° AOA)	Value
Number of Elements	71263
Degrees of Freedom	569412
Number of Boundary Elements Over Geometry	6859
Time to Solution ($k-\epsilon$) [s]	1823.625
Time to Solution ($k-\omega$) [s]	1912.326

Table C.5 Model statistics for Wing-Fuselage Junction Control Specimen in loiter, level flight.

WING-FUSELAGE CONTROL SPECIMEN (LOITER, +4° AOA)	Test Section ($k-\epsilon$)	Test Section ($k-\omega$)
Test Flight Condition	Loiter Speed, +4° AOA	
Test Condition Freestream Velocity [m/s]	15.59	
Wing Section Surface Area [m ²]	0.088226	
Total Wing-Fuselage Junction Surface Area [m ²]	0.049466	
Overall Wetted Area [m ²]	0.368297	
Root Chord [m]	0.3	
Subdomain Fluid Density [kg/m ³]	1.2	
Subdomain Fluid Absolute Viscosity [Pa/s]	1.70E-05	
Root Reynolds Number	330141	
Measurement Plane Cross-Sectional Area [m ²]	0.285	
Flowrate (x-direction, in-bound) [m ³ /s]	4.44315	
Flowrate (x-direction, out-bound) [m ³ /s]	4.420240	4.420405
Total Drag Force [N]	0.8550	0.8488
Pressure Integration Over Junction Surface [N]	-5.109418	-5.123418
Pressure Integration Over Top Wing Surface [N]	-13.692448	-13.693580
Pressure Integration Over Bottom Wing Surface [N]	6.192029	6.193497
Junction Lift Force [N]	5.109418	5.123418
Junction Lift Coefficient	0.708306	0.710247
Wing Section Lift Force [N]	19.8845	19.8871
Wing Section Lift Coefficient	1.5455	1.5457
Overall Model Drag Coefficient	0.015919	0.015805
Overall Model Lift Coefficient	0.465363	0.465673

Table C.6 Raw and processed data for Wing-Fuselage Junction Control Specimen in loiter at +4° AOA.

APPENDIX D

WING-FUSELAGE JUNCTION SIMULATIONS – COLLECTED DATA AND MODEL INFORMATION

D.1 Linear Wing-Fuselage Junction 01

LINEAR WING-FUSELAGE JUNCTION 01 (LOITER, LEVEL FLIGHT)		Value
Number of Elements		79087
Degrees of Freedom		633122
Number of Boundary Elements Over Geometry		9583
Time to Solution ($k-\varepsilon$) [s]		1963.325
Time to Solution ($k-\omega$) [s]		2003.556

Table D.1 Model statistics for LWJ-01 in loiter, level flight.

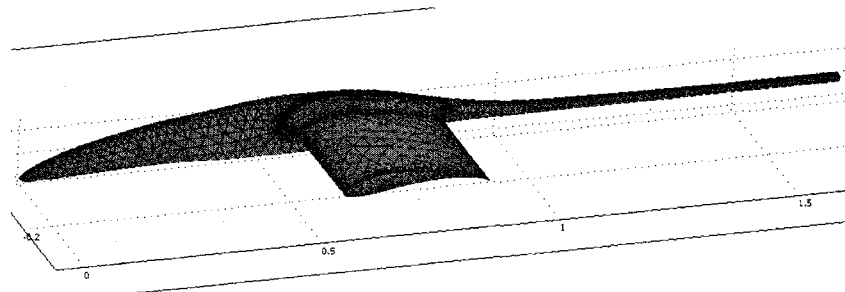


Figure D.1 Mesh detail for LWJ-01.

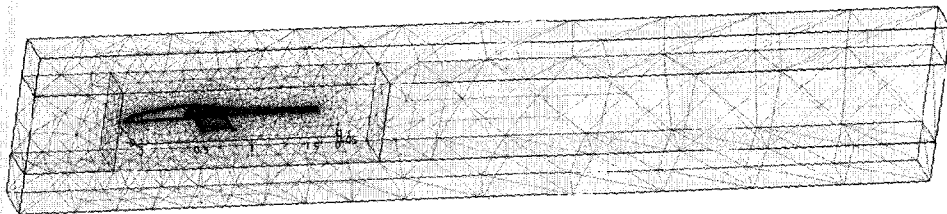


Figure D.2 Mesh model for Linear Wing-Fuselage Junction 01.

LINEAR WING-FUSELAGE JUNCTION 01 (LOITER, LEVEL FLIGHT)	Test Section ($k-\epsilon$)	Test Section ($k-\omega$)
Test Flight Condition	Loiter Speed, Level Flight	
Test Condition Freestream Velocity [m/s]	15.59	
Wing Section Surface Area [m ²]	0.088226	
Total Wing-Fuselage Junction Surface Area [m ²]	0.053749	
Surface Area Increase Over Control [m ²]	0.004283	
Overall Wetted Area [m ²]	0.370470	
Root Chord [m]	0.3	
Subdomain Fluid Density [kg/m ³]	1.2	
Subdomain Fluid Absolute Viscosity [Pa/s]	1.70E-05	
Root Reynolds Number	330141	
Measurement Plane Cross-Sectional Area [m ²]	0.285	
Flowrate (x-direction, in-bound) [m ³ /s]	4.44315	
Flowrate (x-direction, out-bound) [m ³ /s]	4.426852	4.426999
Total Drag Force [N]	0.6087	0.6032
Pressure Integration Over Junction Surface [N]	-4.475430	-4.497314
Pressure Integration Over Top Wing Surface [N]	-10.683577	-10.72601
Pressure Integration Over Bottom Wing Surface [N]	4.541957	4.558567
Junction Lift Force [N]	4.475430	4.497314
Junction Lift Coefficient	0.570980	0.573772
Wing Section Lift Force [N]	15.2255	15.2846
Wing Section Lift Coefficient	1.1834	1.1880
Overall Model Drag Coefficient	0.011267	0.011165
Overall Model Lift Coefficient	0.364662	0.366160
Percent Change Wing Section Lift Coefficient Over Control	3.11%	3.10%
Percent Change Junction Lift Coefficient Over Control	-1.31%	-1.11%
Percent Change Overall Drag Coefficient Over Control	-1.44%	-1.34%
Percent Change Overall Lift Coefficient Over Control	3.41%	3.45%

Table D.2 Collected data from the model simulation for LWJ-01 in loiter, level flight.

LINEAR WING-FUSELAGE JUNCTION 01 (LOITER, +2° AOA)		Value
Number of Elements		79829
Degrees of Freedom		566528
Number of Boundary Elements Over Geometry		7801
Time to Solution ($k-\epsilon$) [s]		1802.245
Time to Solution ($k-\omega$) [s]		2412.981

Table D.3 Model statistics for LWJ-01 in loiter at +2° angle-of-attack.

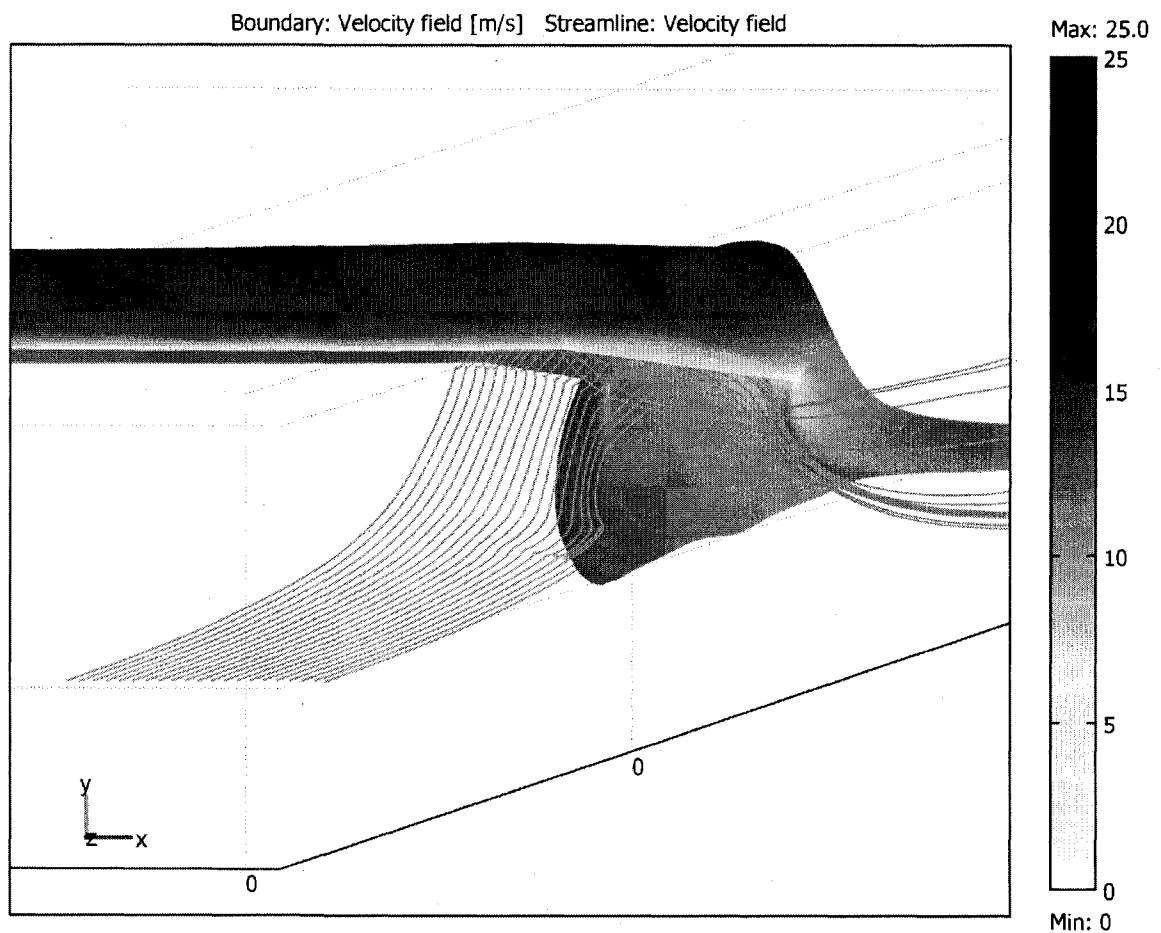


Figure D.4 Streamline detail and boundary velocity distribution over LWJ-01 at +2° AOA. Notice the contraction in the aft part of the fuselage, designed to mimic the downwash created by the streamlines. In this picture we notice an interesting trend at the trailing edge where flow seems to be mixing. This is probably caused by the unrounded edge where the junction meets the fuselage face.

LINEAR WING-FUSELAGE JUNCTION 01 (LOITER, +2° AOA)	Test Section ($k-\epsilon$)	Test Section ($k-\omega$)
Test Flight Condition	Loiter Speed, +2° AOA	
Test Condition Freestream Velocity [m/s]	15.59	
Wing Section Surface Area [m ²]	0.088226	
Total Wing-Fuselage Junction Surface Area [m ²]	0.053749	
Junction Surface Area Increase Over Control [m ²]	0.000979	
Overall Wetted Area [m ²]	0.369304	
Root Chord [m]	0.3	
Subdomain Fluid Density [kg/m ³]	1.2	
Subdomain Fluid Absolute Viscosity [Pa/s]	1.70E-05	
Root Reynolds Number	330141	
Measurement Plane Cross-Sectional Area [m ²]	0.285	
Flowrate (x-direction, in-bound) [m ³ /s]	4.44315	
Flowrate (x-direction, out-bound) [m ³ /s]	4.423456	4.423603
Total Drag Force [N]	0.7352	0.7298
Pressure Integration Over Junction Surface [N]	-4.947655	-4.946657
Pressure Integration Over Top Wing Surface [N]	-12.292668	-12.300190
Pressure Integration Over Bottom Wing Surface [N]	5.470484	5.491020
Junction Lift Force [N]	4.947655	4.946657
Junction Lift Coefficient	0.631227	0.631100
Wing Section Lift Force [N]	17.7523	17.7804
Wing Section Lift Coefficient	1.3798	1.3820
Overall Model Drag Coefficient	0.013609	0.013508
Overall Model Lift Coefficient	0.420174	0.420674
Percent Change Wing Section Lift Coefficient Over Control	1.95%	1.55%
Percent Change Junction Lift Coefficient Over Control	-0.91%	-0.98%
Percent Change Overall Drag Coefficient Over Control	6.04%	6.20%
Percent Change Overall Lift Coefficient Over Control	2.54%	2.21%

Table D.4 Collected data from the model simulation for LWJ-01 in loiter at +2° AOA.

LINEAR WING-FUSELAGE JUNCTION 01 (LOITER, +4° AOA)		Value
Number of Elements		70568
Degrees of Freedom		564364
Number of Boundary Elements Over Geometry		7807
Time to Solution ($k-\epsilon$) [s]		1823.625
Time to Solution ($k-\omega$) [s]		2483.211

Table D.5 Model statistics for LWJ-01 in loiter at +4° angle-of-attack.

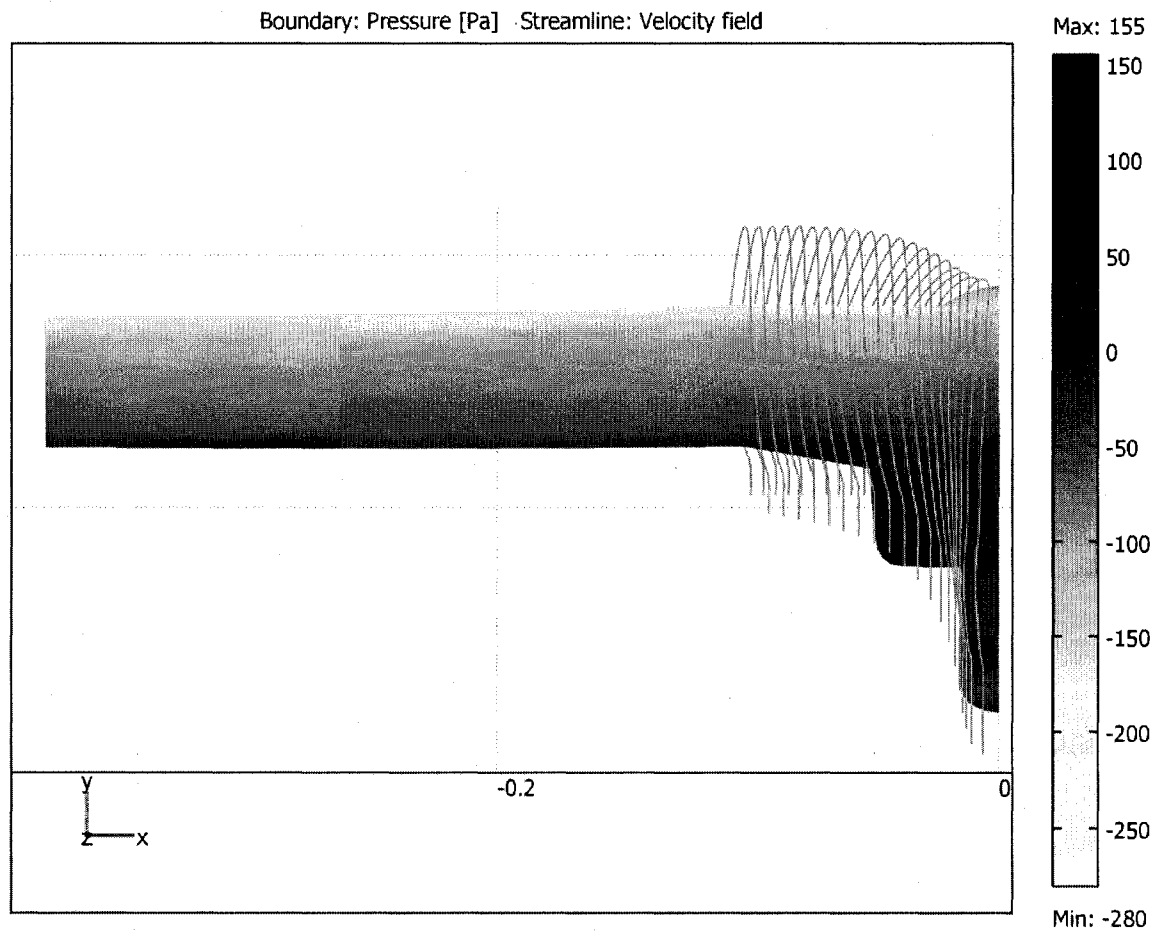


Figure D.5 Streamline detail and boundary pressure distribution over LWJ-01 at +4° AOA as viewed from behind the aircraft. Notice the adherence of the streamlines to the fuselage shape and the gradual progression over to the wing's lifting area.

LINEAR WING-FUSELAGE JUNCTION 01 (LOITER, +4° AOA)	Test Section ($k-\epsilon$)	Test Section ($k-\omega$)
Test Flight Condition	Loiter Speed, +4° AOA	
Test Condition Freestream Velocity [m/s]	15.59	
Wing Section Surface Area [m ²]	0.088226	
Total Wing-Fuselage Junction Surface Area [m ²]	0.053749	
Junction Surface Area Increase Over Control [m ²]	0.000979	
Overall Wetted Area [m ²]	0.369304	
Root Chord [m]	0.3	
Subdomain Fluid Density [kg/m ³]	1.2	
Subdomain Fluid Absolute Viscosity [Pa/s]	1.70E-05	
Root Reynolds Number	330141	
Measurement Plane Cross-Sectional Area [m ²]	0.285	
Flowrate (x-direction, in-bound) [m ³ /s]	4.44315	
Flowrate (x-direction, out-bound) [m ³ /s]	4.418701	4.418848
Total Drag Force [N]	0.9123	0.9068
Pressure Integration Over Junction Surface [N]	-5.498680	-5.523052
Pressure Integration Over Top Wing Surface [N]	-13.872457	-13.912910
Pressure Integration Over Bottom Wing Surface [N]	6.221186	6.232567
Junction Lift Force [N]	5.498680	5.523052
Junction Lift Coefficient	0.701527	0.704637
Wing Section Lift Force [N]	20.0936	20.1455
Wing Section Lift Coefficient	1.5618	1.5658
Overall Model Drag Coefficient	0.016886	0.016785
Overall Model Lift Coefficient	0.473711	0.475121
Percent Change Wing Section Lift Coefficient Over Control	1.05%	1.30%
Percent Change Junction Lift Coefficient Over Control	-0.96%	-0.79%
Percent Change Overall Drag Coefficient Over Control	6.07%	6.20%
Percent Change Overall Lift Coefficient Over Control	1.79%	2.03%

Table D.6 Collected data from the model simulation for LWJ-01 in loiter at +4° AOA.

D.2 Linear Wing-Fuselage Junction 02

LINEAR WING-FUSELAGE JUNCTION 02 (LOITER, LEVEL FLIGHT)		Value
Number of Elements		73209
Degrees of Freedom		584431
Number of Boundary Elements Over Geometry		8189
Time to Solution (k - ϵ) [s]		1821.961
Time to Solution (k - ω) [s]		1912.202

Table D.7 Model statistics for LWJ-02 in loiter, level flight.

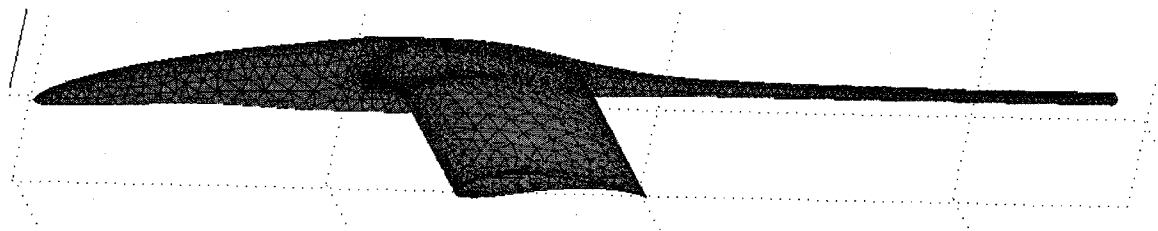


Figure D.6 Mesh detail for LWJ-02.

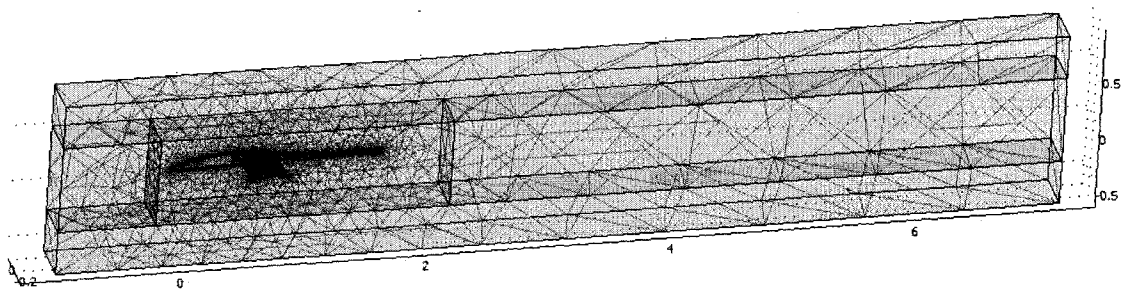


Figure D.7 Mesh detail for LWJ-02.

LINEAR WING-FUSELAGE JUNCTION 02 (LOITER, LEVEL FLIGHT)	Test Section ($k-\epsilon$)	Test Section ($k-\omega$)
Test Flight Condition	Loiter Speed, Level Flight	
Test Condition Freestream Velocity [m/s]	15.59	
Wing Section Surface Area [m ²]	0.088226	
Total Wing-Fuselage Junction Surface Area [m ²]	0.050655	
Surface Area Increase Over Control [m ²]	0.001189	
Overall Wetted Area [m ²]	0.368282	
Root Chord [m]	0.3	
Subdomain Fluid Density [kg/m ³]	1.2	
Subdomain Fluid Absolute Viscosity [Pa/s]	1.70E-05	
Root Reynolds Number	330141	
Measurement Plane Cross-Sectional Area [m ²]	0.285	
Flowrate (x-direction, in-bound) [m ³ /s]	4.44315	
Flowrate (x-direction, out-bound) [m ³ /s]	4.426903	4.42702
Total Drag Force [N]	0.6068	0.6024
Pressure Integration Over Junction Surface [N]	-4.280066	-4.300009
Pressure Integration Over Top Wing Surface [N]	-10.767509	-10.807313
Pressure Integration Over Bottom Wing Surface [N]	4.566043	4.581871
Junction Lift Force [N]	4.280066	4.300009
Junction Lift Coefficient	0.579408	0.582108
Wing Section Lift Force [N]	15.3336	15.3892
Wing Section Lift Coefficient	1.1918	1.1961
Overall Model Drag Coefficient	0.011298	0.011217
Overall Model Lift Coefficient	0.365202	0.366610
Percent Change Wing Section Lift Coefficient Over Control	3.84%	3.81%
Percent Change Junction Lift Coefficient Over Control	0.14%	0.33%
Percent Change Overall Drag Coefficient Over Control	-1.17%	-0.89%
Percent Change Overall Lift Coefficient Over Control	3.56%	3.58%

Table D.8 Collected data from the model simulation for LWJ-02.

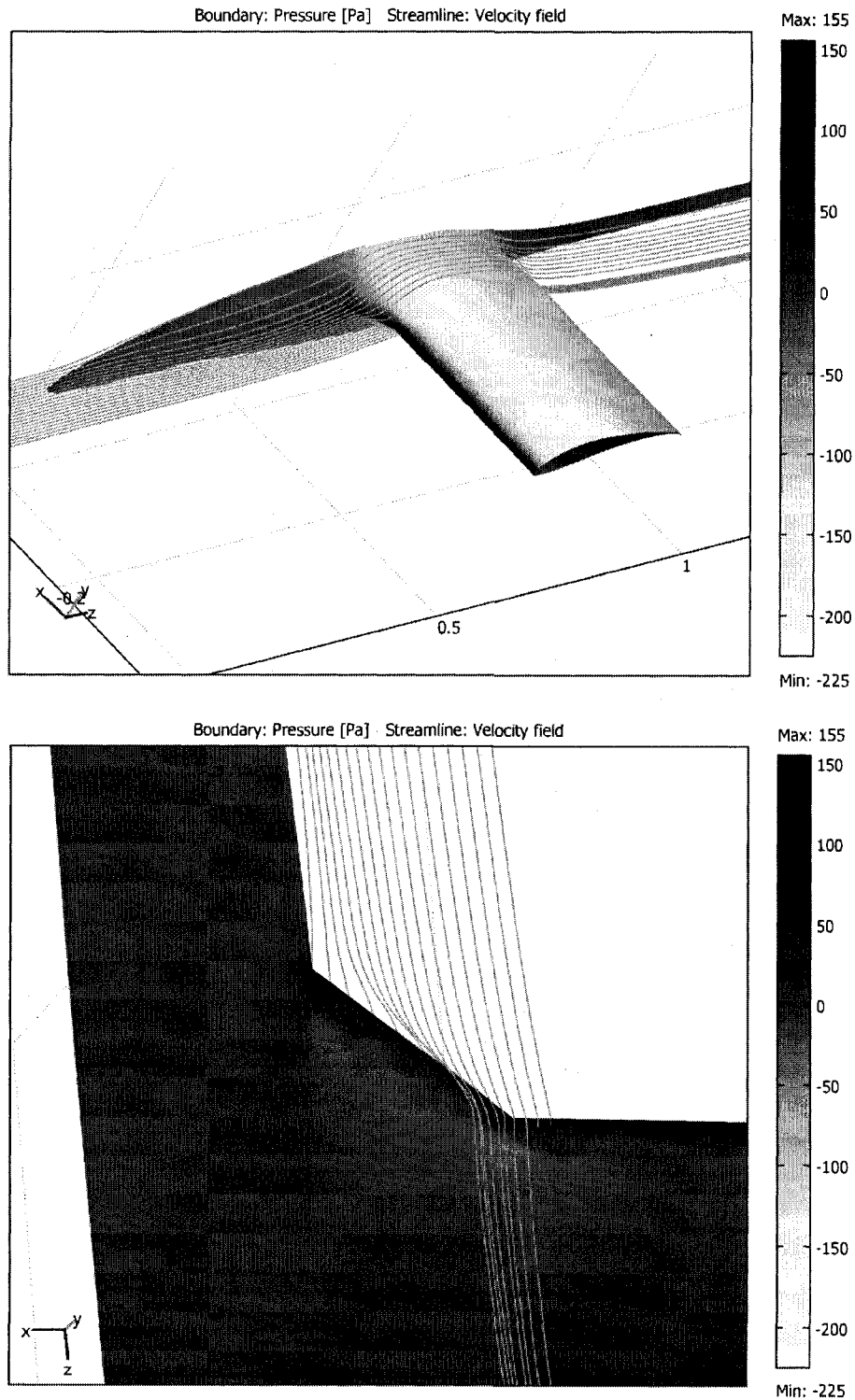


Figure D.8 Boundary pressure distribution and streamline detail near the wing-fuselage junction for loiter, level flight. The sweep angle of the junction is too great, as illustrated in the view from under the fuselage, where the flow is pushed outwards, a condition remedied downstream by the fuselage contraction.

D.3 Non-Linear Wing-Fuselage Junction 01

NON-LINEAR WING-FUSELAGE JUNCTION 01 (LOITER, LEVEL FLIGHT)		Value
Number of Elements		74030
Degrees of Freedom		589936
Number of Boundary Elements Over Geometry		8129
Time to Solution (k - ϵ) [s]		1818.363
Time to Solution (k - ω) [s]		1847.623

Table D.9 Model statistics for NLWJ-01 in loiter, level flight.

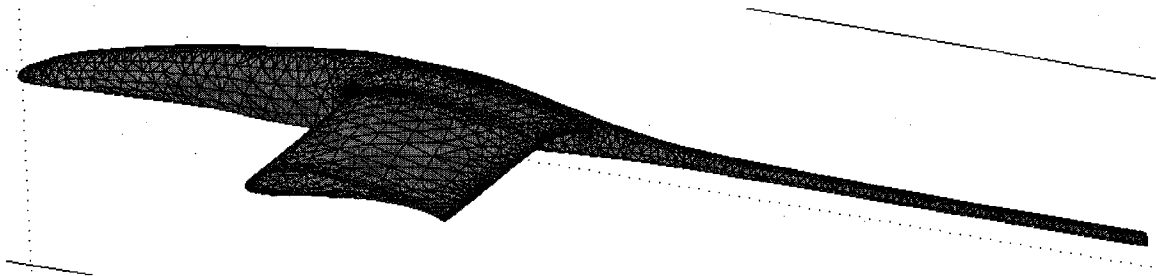


Figure D.9 Mesh detail for NLWJ-01.

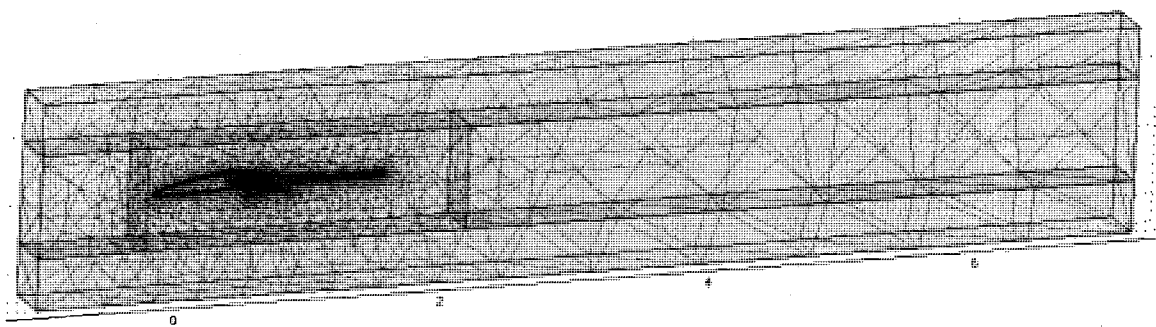


Figure D.10 Mesh overview for NLWJ-01 in loiter, level flight.

NON-LINEAR WING-FUSELAGE JUNCTION 01 (LOITER, LEVEL FLIGHT)	Test Section ($k-\epsilon$)	Test Section ($k-\omega$)
Test Flight Condition	Loiter Speed, Level Flight	
Test Condition Freestream Velocity [m/s]	15.59	
Wing Section Surface Area [m ²]	0.088226	
Total Wing-Fuselage Junction Surface Area [m ²]	0.050445	
Junction Surface Area Increase Over Control [m ²]	0.000979	
Overall Wetted Area [m ²]	0.369304	
Root Chord [m]	0.3	
Subdomain Fluid Density [kg/m ³]	1.2	
Subdomain Fluid Absolute Viscosity [Pa/s]	1.70E-05	
Root Reynolds Number	330141	
Measurement Plane Cross-Sectional Area [m ²]	0.285	
Flowrate (x-direction, in-bound) [m ³ /s]	4.44315	
Flowrate (x-direction, out-bound) [m ³ /s]	4.427273	4.427382
Total Drag Force [N]	0.5930	0.5889
Pressure Integration Over Junction Surface [N]	-4.354720	-4.374483
Pressure Integration Over Top Wing Surface [N]	-10.707479	-10.745871
Pressure Integration Over Bottom Wing Surface [N]	4.540839	4.555385
Junction Lift Force [N]	4.354720	4.374483
Junction Lift Coefficient	0.591969	0.594655
Wing Section Lift Force [N]	15.2483	15.3013
Wing Section Lift Coefficient	1.1852	1.1893
Overall Model Drag Coefficient	0.011011	0.010935
Overall Model Lift Coefficient	0.363995	0.365345
Percent Change Wing Section Lift Coefficient Over Control	3.26%	3.22%
Percent Change Junction Lift Coefficient Over Control	2.31%	2.49%
Percent Change Overall Drag Coefficient Over Control	-3.68%	-3.37%
Percent Change Overall Lift Coefficient Over Control	3.22%	3.22%

Table D.10 Collected data from the model simulation for NLWJ-01 in loiter, level flight.

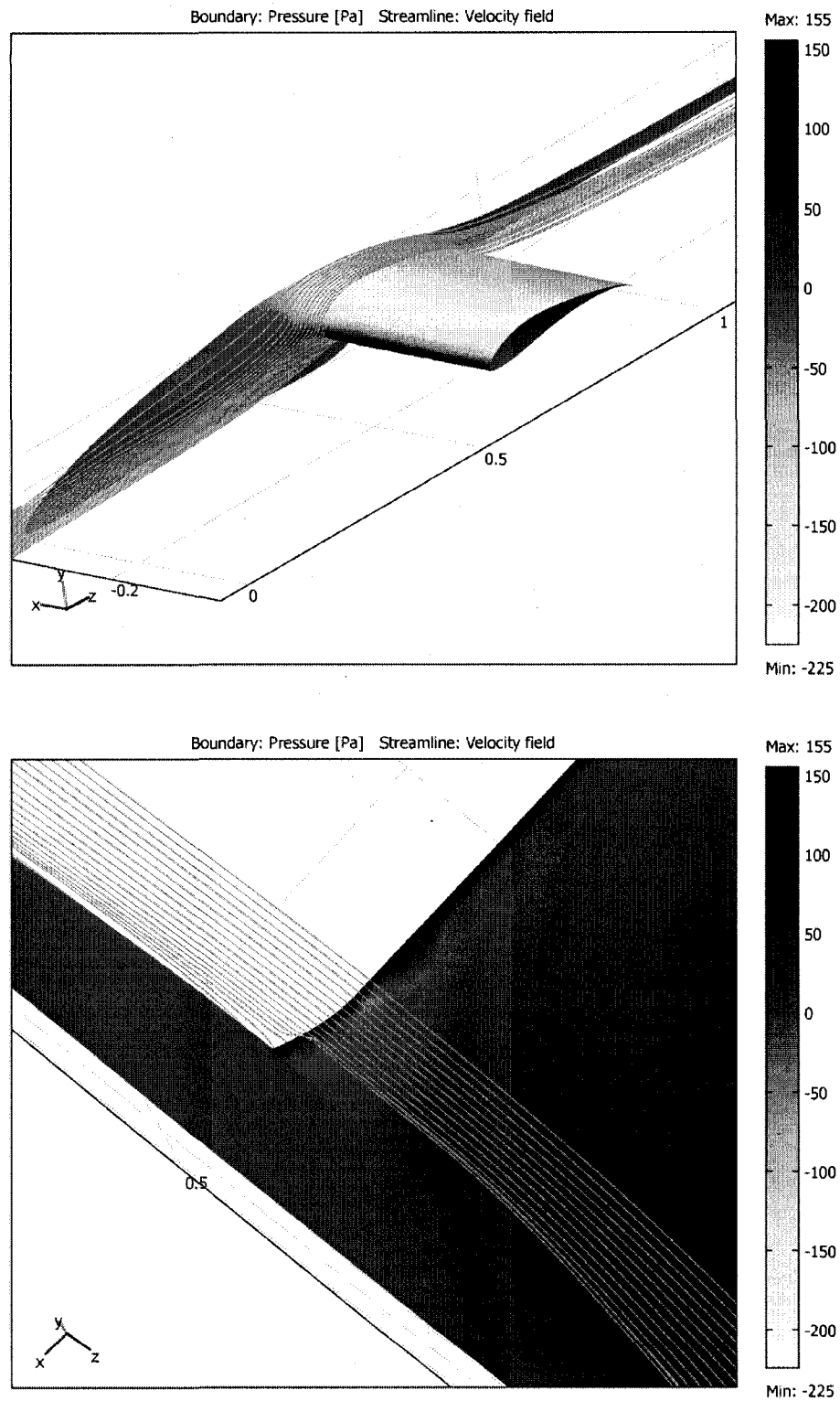


Figure D.11 Boundary pressure distribution and streamline detail near the wing-fuselage junction for loiter, level flight. The subtle leading edge fairing performs well here but the targeted pressure gradient for elimination is still present, although the flow is much more docile in that region. Notice that the flow reconciles well just downstream of the trailing edge.

NON-LINEAR WING-FUSELAGE JUNCTION 01 (LOITER, +2° AOA)		Value
Number of Elements		70802
Degrees of Freedom		566522
Number of Boundary Elements Over Geometry		7851
Time to Solution ($k-\epsilon$) [s]		1802.716
Time to Solution ($k-\omega$) [s]		2389.212

Table D.11 Model statistics for NLWJ-01 in loiter at +2° angle-of-attack.

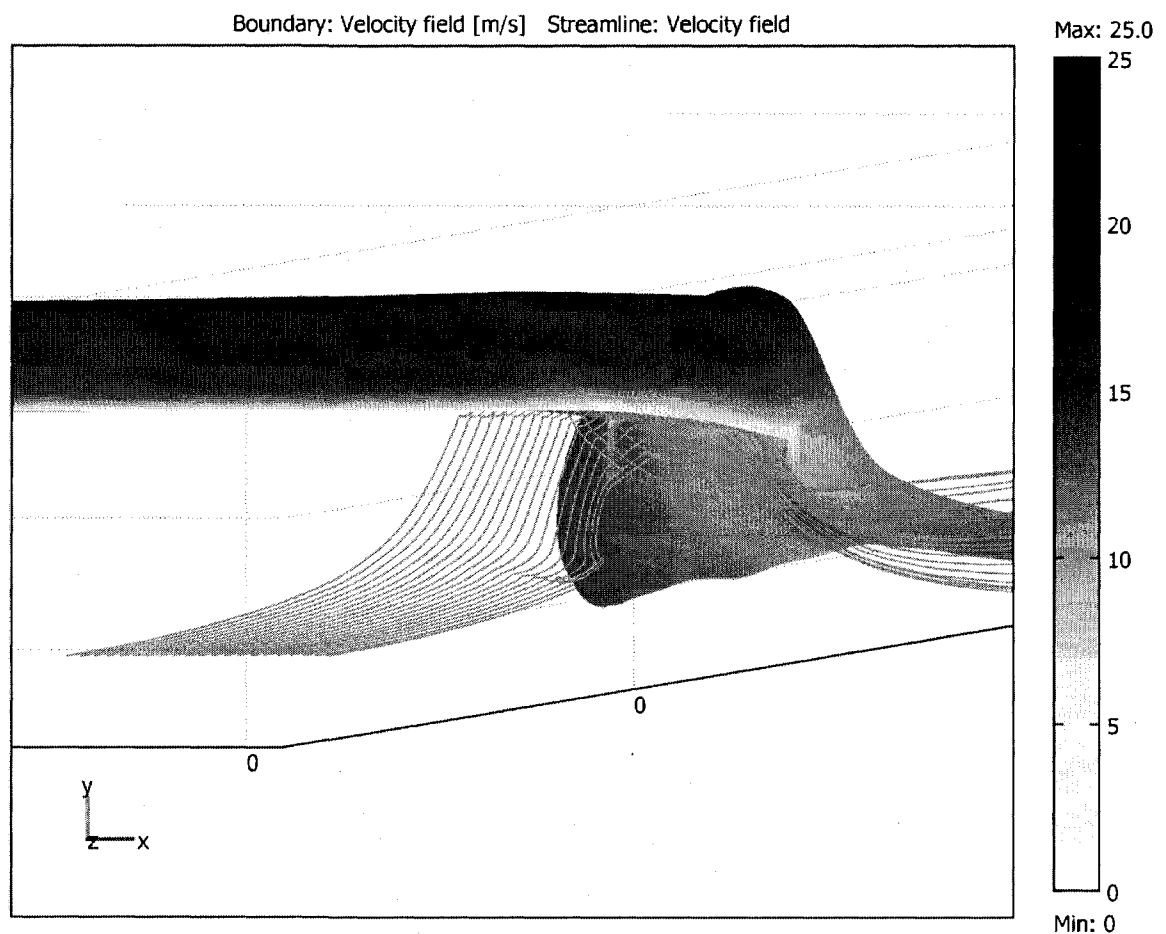


Figure D.12 Streamline detail and boundary velocity distribution over NLWJ-01 at +2° AOA. Comparing to Figure D.4, we notice slightly less mixing in the streamlines due to a smoother progression from the junction into the wing root profile.

NON-LINEAR WING-FUSELAGE JUNCTION 01 (LOITER, +2° AOA)	Test Section ($k-\epsilon$)	Test Section ($k-\omega$)
Test Flight Condition	Loiter Speed, +2° AOA	
Test Condition Freestream Velocity [m/s]	15.59	
Wing Section Surface Area [m ²]	0.088226	
Total Wing-Fuselage Junction Surface Area [m ²]	0.050445	
Junction Surface Area Increase Over Control [m ²]	0.000979	
Overall Wetted Area [m ²]	0.369304	
Root Chord [m]	0.3	
Subdomain Fluid Density [kg/m ³]	1.2	
Subdomain Fluid Absolute Viscosity [Pa/s]	1.70E-05	
Root Reynolds Number	330141	
Measurement Plane Cross-Sectional Area [m ²]	0.285	
Flowrate (x-direction, in-bound) [m ³ /s]	4.44315	
Flowrate (x-direction, out-bound) [m ³ /s]	4.424920	4.425110
Total Drag Force [N]	0.6807	0.6736
Pressure Integration Over Junction Surface [N]	-4.770364	-4.791201
Pressure Integration Over Top Wing Surface [N]	-12.184525	-12.20002
Pressure Integration Over Bottom Wing Surface [N]	5.451233	5.45098
Junction Lift Force [N]	4.770364	4.791201
Junction Lift Coefficient	0.648470	0.651303
Wing Section Lift Force [N]	17.6250	17.6402
Wing Section Lift Coefficient	1.3699	1.3711
Overall Model Drag Coefficient	0.012639	0.012508
Overall Model Lift Coefficient	0.415844	0.416514
Percent Change Wing Section Lift Coefficient Over Control	1.22%	0.75%
Percent Change Junction Lift Coefficient Over Control	1.79%	2.19%
Percent Change Overall Drag Coefficient Over Control	-1.52%	-1.67%
Percent Change Overall Lift Coefficient Over Control	1.48%	1.20%

Table D.12 Collected data from the model simulation for NLWJ-01 in loiter at +2° angle-of-attack.

NON-LINEAR WING-FUSELAGE JUNCTION 01 (LOITER, +4° AOA)		Value
Number of Elements		71490
Degrees of Freedom		571609
Number of Boundary Elements Over Geometry		7873
Time to Solution ($k-\epsilon$) [s]		1906.410
Time to Solution ($k-\omega$) [s]		2536.128

Table D.13 Model statistics for NLWJ-01 in loiter at +4° angle-of-attack.

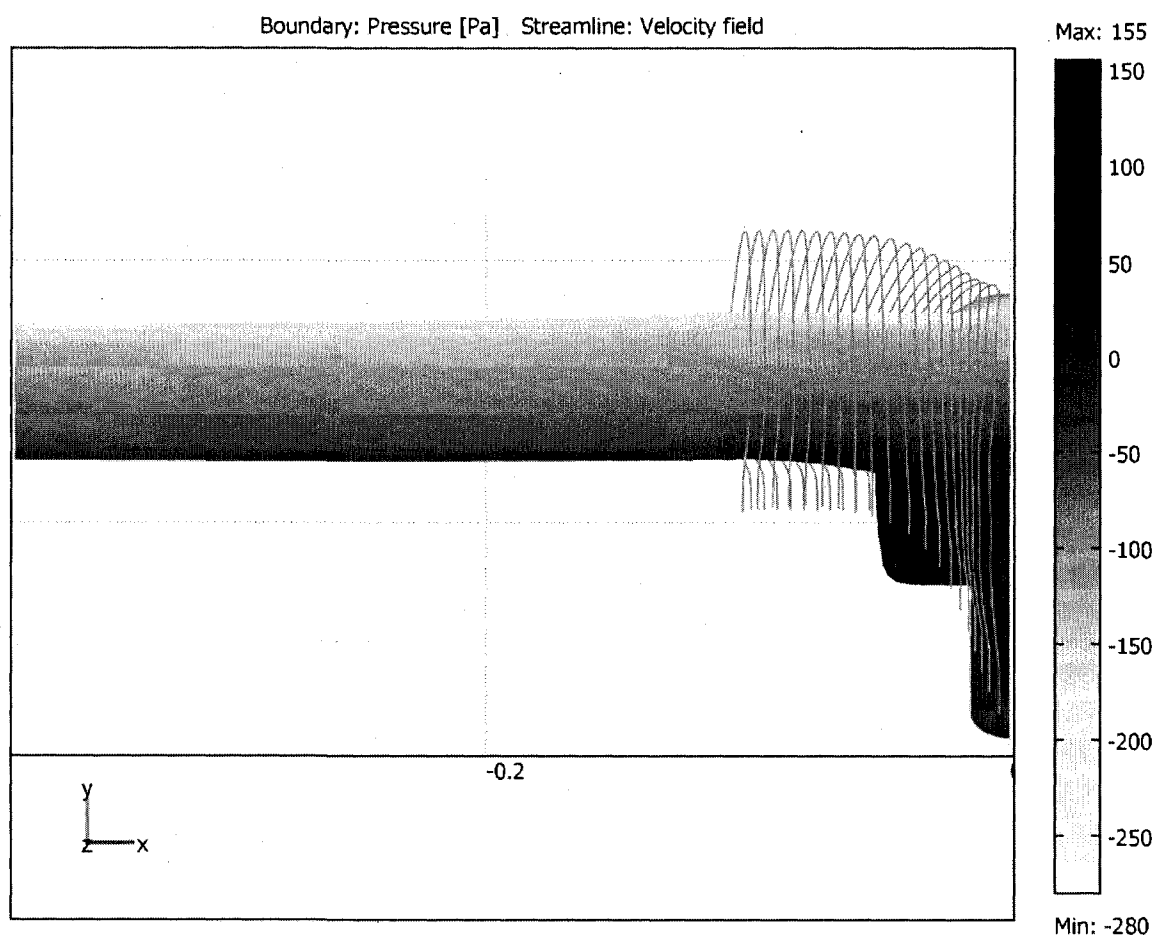


Figure D.13 Streamlines and boundary pressure distribution over the wing junction as seen from behind the plane. This figure is very similar to Figure D.5 (they use the same streamline start points) but there is one major difference to see here: the smooth flow downstream near the tail area, an improvement over LWJ-01.

NON-LINEAR WING-FUSELAGE JUNCTION 01 (LOITER, +4° AOA)		Test Section ($k-\epsilon$)	Test Section ($k-\omega$)
Test Flight Condition		Loiter Speed, +4° AOA	
Test Condition Freestream Velocity [m/s]		15.59	
Wing Section Surface Area [m ²]		0.088226	
Total Wing-Fuselage Junction Surface Area [m ²]		0.050445	
Junction Surface Area Increase Over Control [m ²]		0.000979	
Overall Wetted Area [m ²]		0.369304	
Root Chord [m]		0.3	
Subdomain Fluid Density [kg/m ³]		1.2	
Subdomain Fluid Absolute Viscosity [Pa/s]		1.70E-05	
Root Reynolds Number		330141	
Measurement Plane Cross-Sectional Area [m ²]		0.285	
Flowrate (x-direction, in-bound) [m ³ /s]		4.44315	
Flowrate (x-direction, out-bound) [m ³ /s]		4.419983	4.420221
Total Drag Force [N]		0.8646	0.8557
Pressure Integration Over Junction Surface [N]		-5.326078	-5.33001
Pressure Integration Over Top Wing Surface [N]		-13.774775	-13.7761
Pressure Integration Over Bottom Wing Surface [N]		6.205279	6.205371
Junction Lift Force [N]		5.326078	5.330010
Junction Lift Coefficient		0.724012	0.724547
Wing Section Lift Force [N]		19.9801	19.9815
Wing Section Lift Coefficient		1.5529	1.5531
Overall Model Drag Coefficient		0.016053	0.015889
Overall Model Lift Coefficient		0.469892	0.469992
Percent Change Wing Section Lift Coefficient Over Control		0.48%	0.47%
Percent Change Junction Lift Coefficient Over Control		2.22%	2.01%
Percent Change Overall Drag Coefficient Over Control		0.84%	0.53%
Percent Change Overall Lift Coefficient Over Control		0.97%	0.93%

Table D.14 Collected data from the model simulation for NLWJ-01 in loiter at +4° angle-of-attack.

D.4 Non-Linear Wing-Fuselage Junction 02

NON-LINEAR WING-FUSELAGE JUNCTION 02 (LOITER, LEVEL FLIGHT)		Value
Number of Elements		74473
Degrees of Freedom		593948
Number of Boundary Elements Over Geometry		8235
Time to Solution ($k-\epsilon$) [s]		1810.213
Time to Solution ($k-\omega$) [s]		1901.704

Table D.15 Model statistics for NLWJ-02 in loiter, level flight.

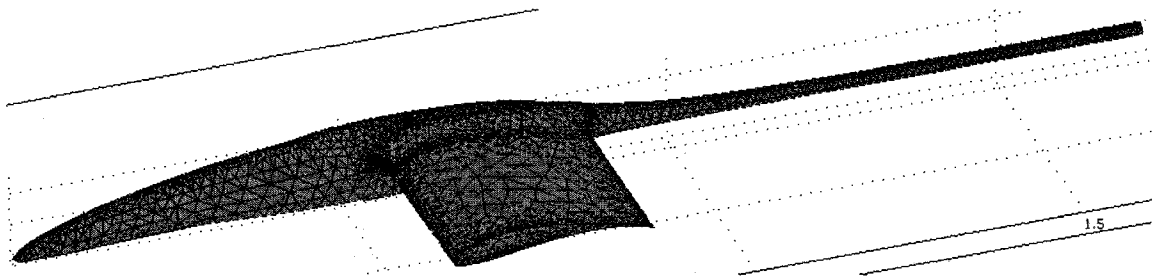


Figure D.14 Mesh detail for NLWJ-02.

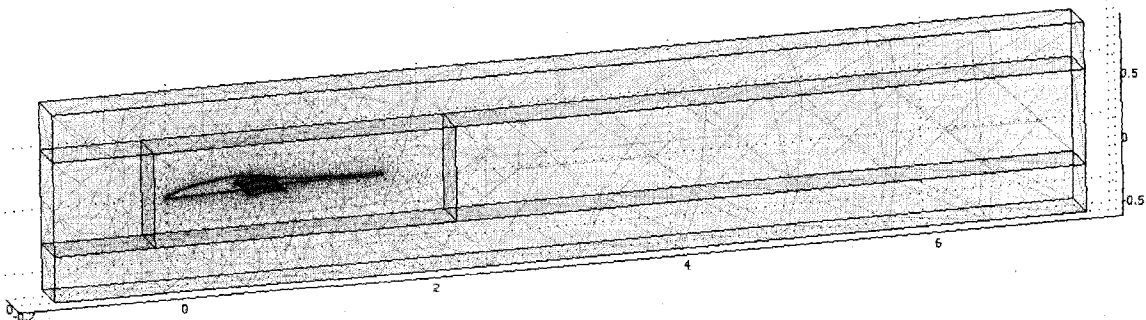


Figure D.15 Mesh overview of the model for NLWJ-02.

NON-LINEAR WING-FUSELAGE JUNCTION 02 (LOITER, LEVEL FLIGHT)	Test Section ($k-\epsilon$)	Test Section ($k-\omega$)
Test Flight Condition	Loiter Speed, Level Flight	
Test Condition Freestream Velocity [m/s]	15.59	
Wing Section Surface Area [m ²]	0.088226	
Total Wing-Fuselage Junction Surface Area [m ²]	0.050106	
Junction Surface Area Increase Over Control [m ²]	0.000640	
Overall Wetted Area [m ²]	0.370470	
Root Chord [m]	0.3	
Subdomain Fluid Density [kg/m ³]	1.2	
Subdomain Fluid Absolute Viscosity [Pa/s]	1.70E-05	
Root Reynolds Number	330141	
Measurement Plane Cross-Sectional Area [m ²]	0.285	
Flowrate (x-direction, in-bound) [m ³ /s]	4.44315	
Flowrate (x-direction, out-bound) [m ³ /s]	4.426748	4.426851
Total Drag Force [N]	0.6126	0.6087
Pressure Integration Over Junction Surface [N]	-4.227247	-4.245681
Pressure Integration Over Top Wing Surface [N]	-10.596286	-10.634248
Pressure Integration Over Bottom Wing Surface [N]	4.499341	4.51376
Junction Lift Force [N]	4.227247	4.245681
Junction Lift Coefficient	0.578528	0.581051
Wing Section Lift Force [N]	15.0956	15.1480
Wing Section Lift Coefficient	1.1733	1.1774
Overall Model Drag Coefficient	0.011338	0.011267
Overall Model Lift Coefficient	0.357664	0.358975
Percent Change Wing Section Lift Coefficient Over Control	2.23%	2.18%
Percent Change Junction Lift Coefficient Over Control	-0.01%	0.15%
Percent Change Overall Drag Coefficient Over Control	-0.82%	-0.44%
Percent Change Overall Lift Coefficient Over Control	1.42%	1.42%

Table D.16 Collected data from the model simulation for NLWJ-02 in loiter, level flight.

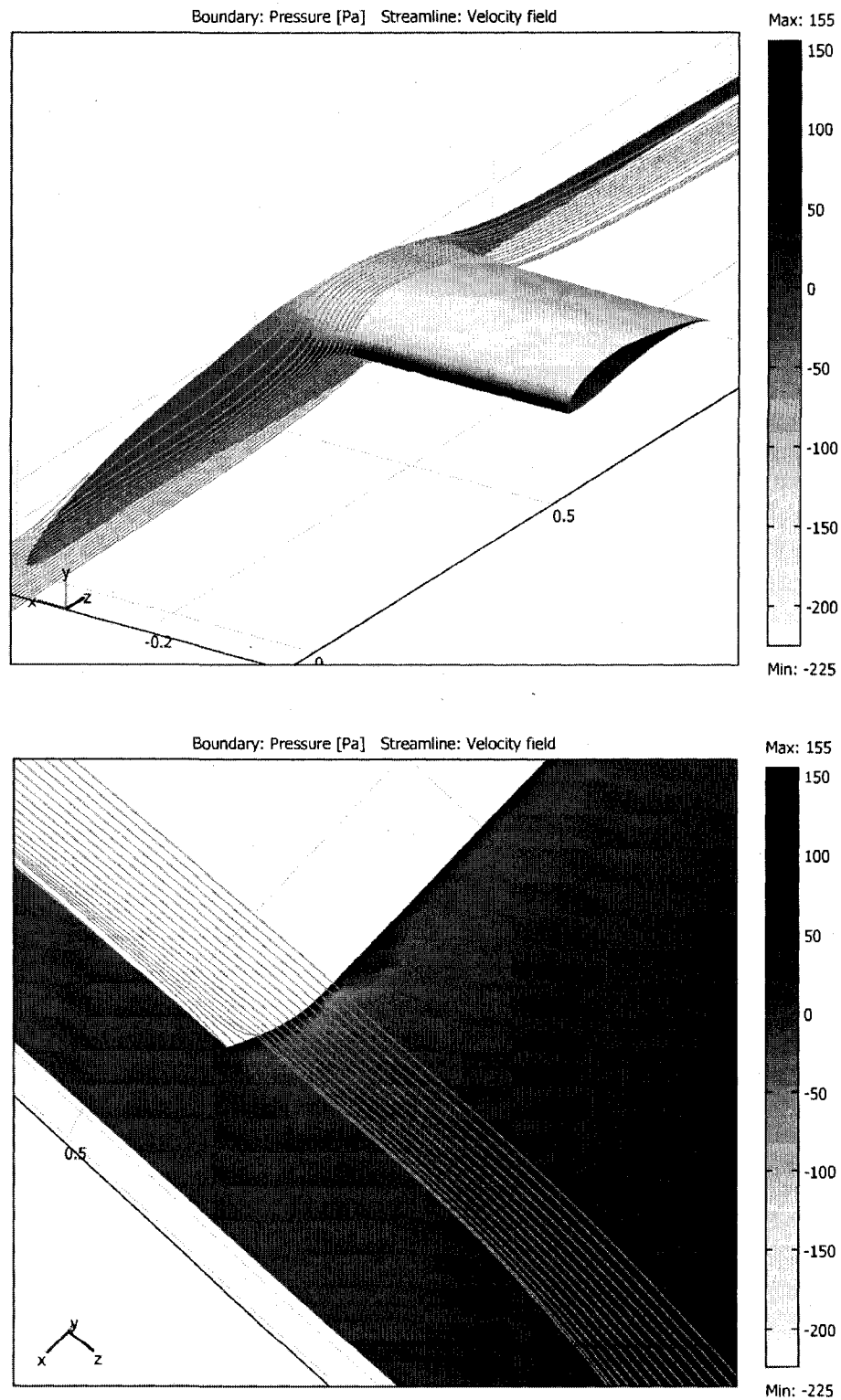


Figure D.16 Boundary pressure distribution and streamline detail near the wing-fuselage junction. The main reason for the decrease in performance observed with NLWJ-02 is not the change in placement but rather the twist angle, which turned out to have an overall negative effect in loiter, level flight.

APPENDIX E

ON THE INDUCED DRAG OF REAL WINGS

E.1 A Brief Discussion on Induced Drag

A wing of infinite length can be otherwise represented as an airfoil. It has a constant cross-section and the pressure distribution is thus constant along its span. On the other hand, a finite wing will have a varying pressure gradient which dissipates as it nears the wingtip. Since the airfoil is generating lift through the use of a greater pressure on the bottom surface, some of the fluid will tend to recirculate at the tips, creating trailing vortices which are illustrated in Figure E.1 (see also Figure 1.4). The fluid's tendency to "spill" and curl off the edges translates into spanwise flow. This and the generation of the tip vortices constitute the induced drag, the wing's energy cost for lift production.

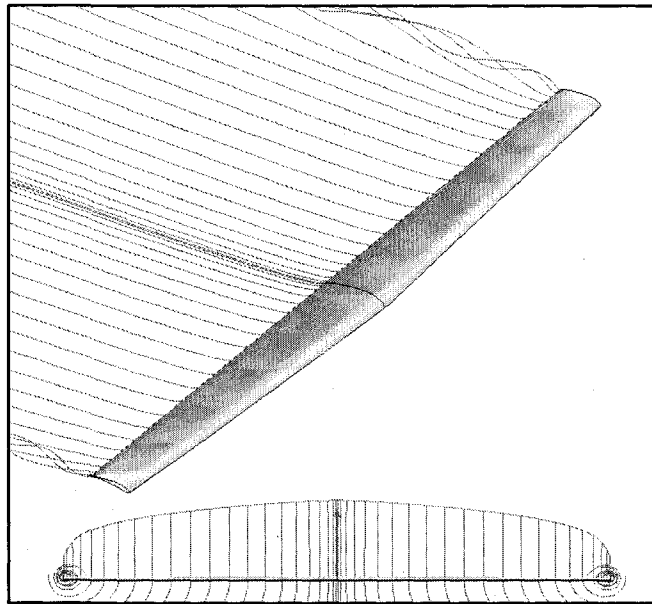


Figure E.1 Wingtip vortices are illustrated in both the isometric and front view. Also of interest is the lift distribution (and thus pressure distribution) on the front view, showing a gradual decline in the overall efficiency of the airfoil as it nears the wingtips

Prandtl's wing theory idealizes this complex phenomenon using a horseshoe vortex system, as described by Tietjens [41], which simply states that for the production of lift must come "an equal and opposite reaction" [21] where the air is given a downward velocity (downwash). This explains why the trailing edge streamlines in Figure E.1 seem to be moving down and away from the wing.

Induced drag is the dominant drag at low speeds, whereas profile drag ("parasitic" drag) is dominant at higher speeds, since it increases as a function of velocity squared. We can thus deduce that induced drag is a function of the inverse of the velocity squared.

Induced drag also varies with span. If the wingtips are pushed as far apart as possible, a greater percentage of the wing will perform at its peak efficiency, since the pressure gradients merge at the tips. For a given weight, the aspect ratio will be the controlling factor, as given by Eq. (E.1). However it may be more intuitive to think in terms of modified wing loading, that is, the weight of the plane squared over the wingspan squared. The aspect ratio is particularly important when speaking about lift distribution and is given by Eq. (E.1).

$$AR = \frac{b^2}{S} \quad \text{Eq. (E.1)}$$

Finally, induced drag also depends on wing design aspects for which Prandtl's Lifting-Line Theory cannot account without modification, such as wingtip devices, non-planar lifting surfaces (wing dihedral or winglets), wing sweep and taper. These design practices are often employed to reduce induced drag by modifying the lift distribution over the span.

E.2 Wing Design and Induced Drag

As stated previously, Prandtl's theory points to an elliptical planform for optimal lift distribution. Very few airplanes have been designed with such a planform due to the difficulty in manufacturing, but it is interesting to note that Great Britain's most famous airplane, the Supermarine Spitfire (Figure E.2), employed such a wing geometry and performed both brilliantly

and elegantly. Still, there are other ways to obtain a near-elliptical lift distribution without the use of a complex elliptic wing geometry.



Figure E.2 The Supermarine Spitfire Mk II. The elliptical planform is clearly observed in this picture.

E.2.1 Aspect Ratio

As discussed previously, aspect ratio has a marked effect on lift distribution and wingtip circulation. As aspect ratio increases, a reduction in induced drag can be observed. When the aspect ratio reaches infinity, the wing becomes two-dimensional and induced drag goes to zero. This can be clearly observed in the proceedings of lifting-line theory, which states the following equation for induced drag of an elliptical untwisted wing:

$$C_{D,i} = \frac{C_L^2}{\pi AR} \quad \text{Eq. (E.2)}$$

For a non-elliptical wing, a factor 'k' must be introduced to adjust the induced drag, so that Eq. (C.2) becomes:

$$C_{D,i} = k \frac{C_L^2}{\pi AR}, \quad \text{where } k = \frac{1}{\pi A R e} \quad \text{Eq. (E.3)}$$

The factor 'e' is the Oswald span efficiency factor [28]. It can be measured retroactively on an airframe but can only be predicted to an approximation, the equations for which are derived from empirical data and can be found in [32]. This factor is often expressed as a percentage or as a fraction and is widely regarded as an indication of how well a wing's potential to produce lift is realized. The Oswald span efficiency is affected most by aspect ratio and taper. It can be tricky to approximate and due to its high sensitivity to the previously mentioned parameters, its theoretical maximum value of one is often exceeded (although it can never be physically surpassed).

E.2.2 Taper

Wing sections are much more easily made in straight sections, where two airfoil profiles are lined up and the body of the wing is effectively lofted linearly about these profiles. If the root and tip airfoils have different chord lengths, then the designer is "tapering" the wing. A value can be defined here as the taper ratio, λ , which is the ratio between the tip and root chords. For a primer on airfoil anatomy, please refer to [32] or [39].

$$\lambda = \frac{C_{tip}}{C_{root}} \quad \text{Eq. (E.4)}$$

An untapered (or rectangular) wing is the simplest case and has a taper ratio of one. These are most easily manufactured but provide a less than ideal lift distribution. On the other hand, a taper ratio of zero refers to a triangular wing shape and provides less-than-optimal lift at the tips. Figure E.3 illustrates lift distributions for various taper ratios. A taper ratio of about 0.45 fairly approximates elliptic lift distribution.

Modern sailplanes often employ multi-tapered wings. This method allows the designer to approach elliptic lift distribution to a further degree while maintaining relative ease of construction. A well-engineered wing can usually approach elliptical lift distribution by a proper combination of taper and aspect ratios.

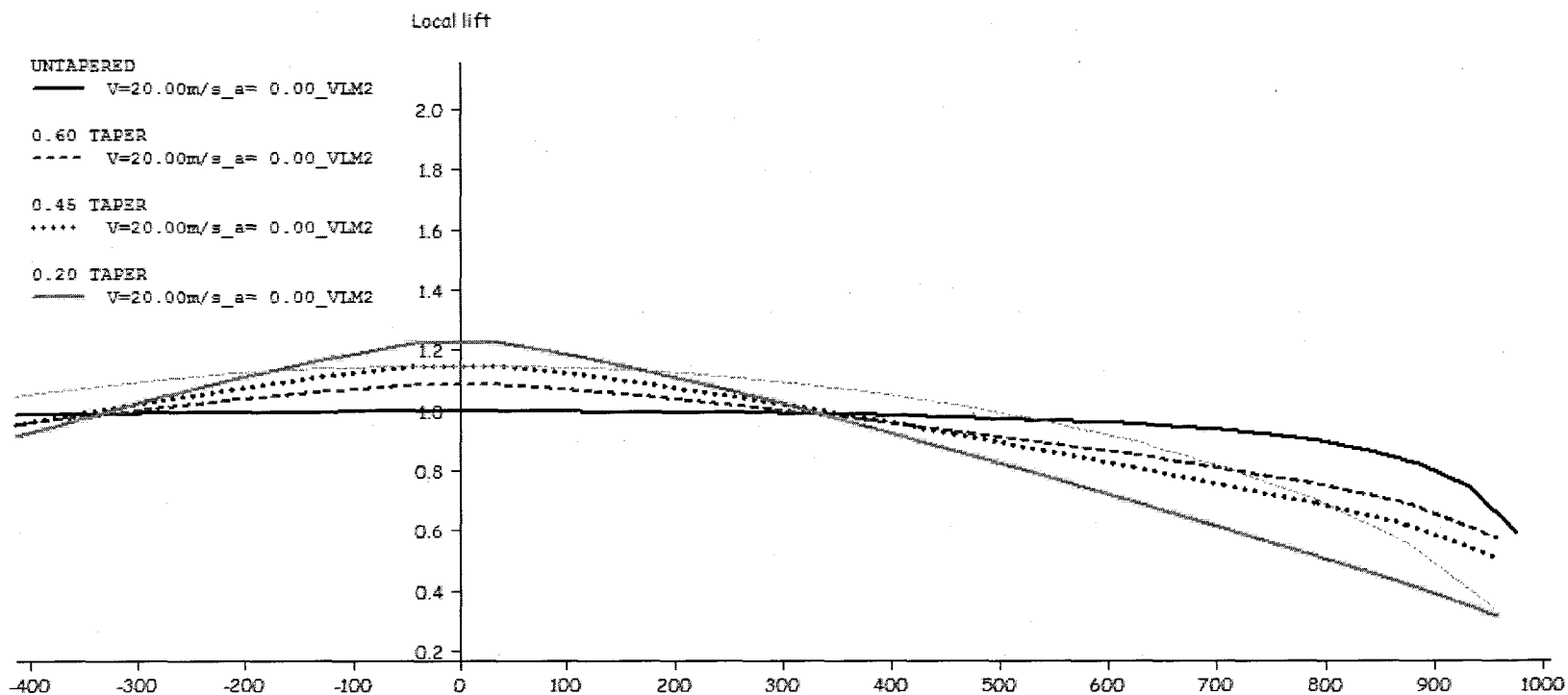


Figure E.3 Local lift distribution of various taper ratio wings. The very light dotted line (not present in the legend) is the elliptical lift distribution. As the taper ratio nears 0.45, the lift distribution begins to approximate the elliptical load. With proper combination of taper and aspect ratio, a nearly elliptical spanload can be achieved.

In certain cases, however, design requirements put constraints on the designer's ability to use these tools to enhance the lift distribution of a given planform. An increase in aspect ratio may result in an increase in wingspan, at which point ground handling may become difficult. An increase in taper ratio may result in wasted surface area on the wings with respect to the solar panels, since most are rectangular laminates. The list of examples is practically endless and the designer needs to keep the mission requirements in mind when making any and all design decisions.

E.3 Wingtip Devices – Planar Surfaces

To further enhance lift distribution on a wing when other design methods may not be appropriate, wingtip devices may be used. These can be generalized into two categories, planar and non-planar surfaces, the latter of which are usually called winglets.

To try to soften the impact of the wingtip vortices, planar surfaces may be used to improve the flow conditions around them. These surfaces lie in the plane of the wing and usually consist of a more intricate way to terminate the wing than just chopping it off. Various philosophies surround these devices: some seek to delay the transition between the top and bottom pressure gradients while others seek to harness the strength of these vortices to produce useful aerodynamic forces [32].

While a rounded wing tip may seem more elegant than a square cut-off, it is actually less efficient. Rounded tips actually ease the transition of the gradients and are detrimental in their purpose. For this reason, most low-drag planar wing tip devices use sharp edges, which delay the reconciliation of the top and bottom pressure gradients, thus ensuring a more efficient lift production over the span of the wing.

According to [32], among numerous other sources, the most popular planar tip device is the Hoerner wing tip. Although the wingtip may parabolically guide the bottom edge of the airfoil to meet the top at a sharp edge, it can produce a parabolic downscaling of the airfoil section, aligned at the trailing edge and at the top. A typical example of a Hoerner-style tip can be seen in Figure E.4. This tip configuration always features a sharp edge and a resulting "recirculation"

zone where the vortices' strength is harnessed to produce useful aerodynamic forces. Such a configuration is often seen on general aviation aircraft and other relatively inexpensive flying machines.

Various other planar wingtip types have been developed. A few examples of these are included in [32], the most common of which are the rounded and cut-off tips. Some tips are designed for specific flight conditions, such as the cut-off forward swept tip which allows for the formation of a Mach cone along the wing's tip.

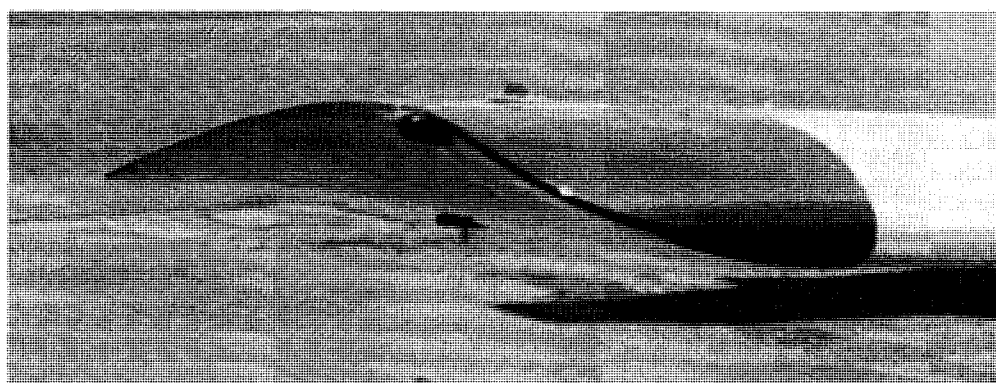


Figure E.4 Close-up of the Hoerner wingtip on a general aviation aircraft.

E.4 Wingtip Devices – Non-Planar Surfaces

In an effort to further reduce induced drag, non-planar wingtip devices may be employed. For more information on the history of such devices, please consult Chapter Two.

Non-planar lifting devices, or winglets, have standard geometric parameters that facilitate the discussion of such devices. Please consult Chapter Three for more information on these parameters.

The basic premise of a winglet is not necessarily to act as an endplate. Usually it is rather to harness to weaken the wingtip vortices, as shown in Figure E.1. The term weaken is used loosely here – the total strength of the trailing vortices cannot be changed but it can be redistributed in a more efficient way, effectively weakening its adverse contribution. To be effective, a winglet must produce enough side force (the winglet's own lift component) so that the circulation about the

wing's tip is impeded. In effect, the basic goal of a winglet is to vertically diffuse the tip vortex flow further away from the tip, resulting in a drag reduction.

A winglet is more effective for a wing which has greater loads at the tips. It is one of the reasons why a winglet can be incorporated into the UNLV solar-powered UAV. The airfoil selected for the UAV is a high-lift airfoil, and thus the tip load is quite high, even though the wing design already has a lift distribution that approaches an ideal one.

By diffusing the vortex flow away from the main wing surface, an increase in span efficiency can usually be achieved. This leads to an overall greater lift production. While giving the winglet some cant angle will allow the non-planar surface to contribute to the lift production of the aircraft, this contribution is usually minor. The cant angle instead regulates the wing root bending moment provided by the winglet. Additionally, it can be modified to provide adaptable dihedral depending on the flight condition.

APPENDIX F

ON THE USE OF THIN-FILM SOLAR CELLS TO POWER AN UNMANNED AERIAL VEHICLE

F.1 A Brief Discussion on Thin-Film Solar Cells

As briefly discussed in Chapter One, recent advances in thin-film solar cells have resulted in increased interest in solar flight. Thin-film solar cells promise to be much more cost effective than wafer-based cells, with increasing efficiency. As industry demands for silicon ramps up, so has the cost of photovoltaic wafer-based cells, which employ a high content of the material. In an attempt to swap the expensive element for an equivalent substitute, several new classes of photovoltaic materials were created, the majority of which fall under the classification of thin-film photovoltaic materials.

Most thin-film solar cells use less than one percent of silicon than their wafer ancestors. This results in a significant drop in the cost per watt, and in turn an increased availability and usability. While the efficiency of these new thin-film cells is lower than wafer-based cells, the technology is still maturing and their cost per watt now makes them a viable alternative to other sources of power.

Another interesting quality of thin-film solar cells is that most of the compounds that have been developed so far are printable through a process akin to screen printing. The compound can be printed onto a substrate in various patterns, in layers, to build a photovoltaic surface on nearly any kind of backing. The finished product is also very thin, as the name describes, usually about the thickness of two sheets of paper. Most compounds are also flexible, meaning they can conform to most surfaces.

Finally, most thin-film cells are produced in a laminate format with a protective clear face that allows for simple maintenance, usually limited to wiping them clean. While they are susceptible to

damage such as puncturing or scratching, they are generally much more resilient than wafer-based cells and also require much less care when being handled.

The most common type of thin-film solar cells are the amorphous silicon type. These are not printable and the industry trend is trying to phase them out in favor of other compounds. Cadmium telluride (CdTe) cells are the second most widespread. These cells are printable but some controversy has arisen regarding the toxicity in the manufacturing and usage of these photovoltaic cells. They are widely used since CdTe is easily deposited onto most surfaces. The debates regarding the environmental consequences of CdTe rage on.

Lesser-used cells, mainly due to their maturity, include the CIS and CIGS thin-films. Copper indium selenide (CIS) cells are printable. They represent one of the first real attempts at driving the cost of solar cells down. Copper indium gallium selenide (CIGS) attempts to further decrease the cost by subtracting as much expensive indium as possible and substituting in gallium. Both types are printable and have a promising future for a multitude of applications, including solar-powered flight. Because of this, large amounts of capital are being pumped into these two compounds for research.

F.2 Thin-Film Solar Cells and Aircraft Design

As briefly explored in Chapter One, solar flight is relatively new and mostly the object of experimental studies. However, with these new photovoltaic technologies on the rise, the ability to loiter indefinitely is becoming a reality, and for a reasonable cost. Furthermore, increasing efficiency translate into platforms that can become much smaller. While NASA's Pathfinder had a 121 foot wingspan, most solar airplanes have a span of about 15 feet. The reason for this lies primarily in the amount of surface areas it provides to lay solar cells on. Secondly, it provides a decent aspect ratio, which in turn usually translates into a high lift-to-drag ratio and a low sink rate. However, a fifteen foot wingspan UAV is still quite unwieldy for one man to operate and is sure to cause some issues in terms of ground handling. Thus, a smaller wingspan is yet desired.

Brandt and Gilliam [2] derived several relationships to relate such values as wing loading and weight to available surface area. Solar intensity is generally averaged at 1000 watts per meter

area. The efficiency of a solar cell is thus given as the percentage of that intensity which it can convert into electricity. An average efficiency for thin-film solar cells today is around 10%. As a designer tries to downsize an airframe, two options present themselves: either have higher efficiency cells or further optimize the airframe so that less power is required to fly.

As with most engineering problems, the design of a solar airplane becomes a careful balance of, and sometimes a compromise between, power management and aerodynamic efficiency. The efficiency of the solar cells is not the only deciding factor in the power issue: there are also question marks with respect to power storage, power allocation and power usage. These factors, coupled with the unusual demands of solar flight (as with know it for now), in terms of flight legs, combine to make solar flight one of the more challenging design problems in the subsonic, incompressible regime. For further information on the design of aircrafts for solar flight, please refer to [1], [2], [23] or [28].

APPENDIX G

COPYRIGHT PERMISSION FORM

Permission to Use Copyrighted Material

University of Nevada, Las Vegas

I, André Noll holder

of copyrighted material entitled Design of solar powered airplanes for
continuous flight

authored by André Noll

and originally published in at ETHZ (Swiss Federal Institute of
Technology Zurich)

hereby give permission for the author to use the above described material in total or in part
for inclusion in a master's thesis/doctoral dissertation at the University of Nevada, Las
Vegas.

I also agree that the author may execute the standard contract with University Microfilms,
Inc. for microform reproduction of the completed dissertation, including the materials to
which I hold copyright.

Signature

10.11.2007

Date

André Noll

Name (typed)

Dr.

Title

Representing

BIBLIOGRAPHY

- [1] AC Propulsion. (2006, February 2). *Technology - SoLong UAV*. Retrieved August 10, 2007, from <http://www.acpropulsion.com/solong/>
- [2] Boermans, L. (2006). *Research on sailplane aerodynamics at Delft University of Technology. Recent and present developments*. Presentation, Delft University of Technology, Delft.
- [3] Boermans, L., Kubrynski, K., & Nicolosi, F. (1997). Wing-Fuselage Design of High-Performance Sailplanes. In R. Henkes, & P. Bakker (Ed.), *Boundary-Layer Separation in Aircraft Aerodynamics* (pp. 23-41). Delft: Delft University Press.
- [4] Brandt, S. A., & Gilliam, F. T. (1995). Design Analysis Methodology for Solar-Powered Aircraft. *Journal of Aircraft* , 32 (4), 703-709.
- [5] Cebeci, T. (1999). *An Engineering Approach to the Calculation of Aerodynamic Flows*. Long Beach: Horizons Publishing.
- [6] COMSOL Multiphysics. (2008). COMSOL Multiphysics 3.5 User's Guide.
- [7] Dube, L. & Ohnstad, C. (2006). *MEG 498 Final Written Report: Solar Powered UAV Prototype Log and Results*. Unpublished paper, University of Nevada Las Vegas, Las Vegas, Nevada, 2006.
- [8] Gratzel, L. B. (1994). *Patent No. 5,348,253*. United States of America.
- [9] Green, B. E., & Whitesides, J. L. (2003, March-April). Method for Designing Leading-Edge Fillets to Eliminate Flow Separation. *Journal of Aircraft* , 40 (2), pp. 282-289.
- [10] Heller, G., Maisel, M., & Kreuzer, P. (2004). *Patent No. 6,722,615 B2*. United States of America.
- [11] Irving, J., & Davies, R. (2007). *Patent No. 7,275,722*. United States of America.
- [12] Ishimitsu, K. K., & Van Devender, N. R. (1981). *Patent No. 4,245,804*. United States of America.
- [13] Jupp, J. A., & Rees, P. H. (1987). *Patent No. 4,714,215*. United States of America.
- [14] Kuethe, A. M., & Chow, C.-Y. (1986). *Foundations of Aerodynamics* (Fourth Edition ed.). New York: John Wiley & Sons.
- [15] Mann, A., & Elscholz, D. I. (2005). The M-DAW Project. *43rd AIAA Aerospace Sciences Meeting and Exhibit*. Reno: American Institute of Aeronautics and Astronautics.
- [16] Maughmer, M. D. (2002, June). About Winglets. *Soaring Magazine* .

- [17] Maughmer, M. D. (2003). Design of Winglets for High-Performance Sailplanes. *Journal of Aircraft* , 40 (6), 1099-1106.
- [18] Maughmer, M. D., Swan, T. S., & Willits, S. M. (2002). Design and Testing of a Winglet Airfoil for Low-Speed Aircraft. *Journal of Aircraft* , 39 (4), 654-661.
- [19] Maughmer, M., Hallman, D., Ruszkowski, R., Chappel, G., & Waitz, I. (1989, August). Experimental Investigation of Wing/Fuselage Integration Geometries. *Journal of Aircraft* , 26 (8), pp. 705-711.
- [20] Montoya, L. C. (1980). *KC-135 Winglet Flight Results*. Report, NASA, Dryden Flight Research Center.
- [21] Munk, M. M. (1923). *The Minimum Induced Drag of Aerofoils*. NACA Report No. 121.
- [22] NASA. (1990, May 4). *EL-1996-00130*. Retrieved 2008, from NASA Image Exchange: <http://nix.ksc.nasa.gov/info?id=EL-1996-00130&orgid=1>
- [23] NASA. (2005, February 10). *NASA - NASA Dryden Fact Sheet - Solar-Power Research*. Retrieved June 02, 2008, from <http://www.nasa.gov/centers/dryden/news/FactSheets/FS-054-DFRC.html>
- [24] Noth, A. (2008). *Design of Solar Airplanes for Continuous Flight*. Zürich: Autonomous Systems Laboratory, Swiss Federal Institute of Technology (ETHZ).
- [25] Noth, A. (2008). *History of Solar flight*. Electronic Report, Swiss Federal Institute of Technology Zürich, Autonomous Systems Lab, Zürich.
- [26] Pajno, V. (2006). *Sailplane Design*. Varese, Italy: Macchione Editore.
- [27] Rae, W. H., & Pope, A. (1984). *Low-Speed Wind Tunnel Testing* (Second Edition ed.). New York: John Wiley & Sons.
- [28] Raymer, D. P. (1999). *Aircraft Design: A Conceptual Approach* (Third Edition ed.). Reston, Virginia, United States of America: American Institute of Aeronautics and Astronautics, Inc.
- [29] Schlichting, H., & Gersten, K. (1999). *Boundary Layer Theory* (8th Revised and Enlarged Edition ed.). (K. Mayes, Trans.) New York: Springer.
- [30] Selig, M. (2008, February 19). *UIUC Airfoil Data Site*. Retrieved 2007, from UIUC Airfoil Data Site: <http://www.ae.uiuc.edu/m-selig/ads.html>
- [31] Shelton, A., Tomar, A., Prasad, J., Smith, M. J., & Komerath, N. (2006). Active Multiple Winglets for Improved Unmanned-Aerial-Vehicle Performance. *Journal of Aircraft* , 43 (1), 110-116.
- [32] Shepelev, A., & Ottens, H. (2006). *Horten Ho 229 Spirit of Thuringia*. Surrey, England: Ian Allane Publishing Ltd.
- [33] Simons, M. (1994). *Model Aircraft Aerodynamics*. Herts: Argus Books.
- [34] Slingerland, R., & Verstraeten, J. G. (2008). Drag Characteristics for Optimally Span-loaded Planar, Wingletted, and C-wings. *46th AIAA Aerospace Sciences Meeting and Exhibit*. Reno: American Institute of Aeronautics and Astronautics.

- [35] Tennekes, H. (1996). *The Simple Science of Flight*. Cambridge: The MIT Press.
- [36] Thomas, F. (1999). *Fundamentals of Sailplane Design*. (J. Milgram, Trans.) College Park, Maryland: College Park Press.
- [37] Thwaites, B. (1960). *Incompressible Aerodynamics*. New York: Oxford University Press.
- [38] Tietjens, O. (1934). *Applied Hydro- and Aeromechanics*. (J. D. Hartog, Trans.) Toronto: General Publishing Company.
- [39] van Oudheusden, B. W., Steenaert, C. B., & Boermans, L. M. (2004). Attachment-Line Approach for Design of a Wing-Body Leading-Edge Fairing. *Journal of Aircraft*, 41 (2), 238-246.
- [40] Vogt, R. (1951). *Patent No. 2,576,981*. United States of America.
- [41] Von Mises, R. (1959). *Theory of Flight*. New York: McGraw-Hill Book Company.
- [42] Whitcomb, R. T. (1976). *A Design Approach and Selected Wind-Tunnel Results at High Subsonic Speeds for Wing-Tip Mounted Winglets*. NASA, Langley Research Center. Hampton: NASA.
- [43] Wilcox, D. C. (2006). *Turbulence Modeling for CFD* (Third Edition ed.). La Canada: DCW Industries, Inc.
- [44] XFLR5 . (2008, July). Guidelines for XFLR5 V4.07.

VITA

Graduate College
University of Nevada, Las Vegas

Louis Dube

Home Address:

5405 Progresso St.
Las Vegas, NV 89135

Degrees:

Bachelor of Science, Mechanical Engineering, 2006
University of Nevada, Las Vegas

Special Honors and Awards:

Phi Eta Sigma National Honor Society member, 2001
NASA Fellowship, 2008

Publications:

Dube, L., McElroy, W. & Pepper, D.W., Use of COMSOL in Aerodynamic Optimization of the UNLV Solar-Powered Unmanned Aerial Vehicle, COMSOL '08 Conference, Boston, MA, Oct.9-12, 2008.

Thesis Title:

Aerodynamic Optimization for Low Reynolds Number Flight of a Solar Unmanned Aerial Vehicle

Thesis Examination Committee:

Chairperson, Dr. Darrell Pepper, Ph.D.
Committee Member, Dr. William Culbreth, Ph.D.
Committee Member, Dr. Brendan O'Toole, Ph.D.
Graduate Faculty Representative, Dr. Evangelos Yfantis, Ph.D.